Characterization of CMOS Sensors for Particle Physics Applications

Patrick Freeman

May 4, 2022

Abstract

This thesis summarizes work on the development of silicon sensor technologies for use in high energy physics experiments. This work has been focused on the characterization of passive strip sensors for hybrid devices as well as two novel monolithic active pixel sensors (MAPS) in the TowerJazz 180 nm CMOS imaging sensor process, MALTA and DECAL, for experiments at particle colliders. The MALTA sensor is part of a development towards a CMOS sensor based vertex detector system for use as a further upgrade by the ATLAS experiment, and the DECAL device is a more generic development suitable for use at either e^+e^- or hadron colliders as an ultra high granularity electromagnetic calorimeter. The work has served to demonstrate the performance and identify shortcomings of the latest versions of these devices in the context of high energy particle physics experiments. Passive strip sensors for hybrids in the ATLAS Inner Tracker (ITk) were irradiated at the MC40 cyclotron in Birmingham and characterized. While the characterization results with devices irradiated at Birmingham were not conclusive, the sensor performance demonstrated at other facilities is within specifications, and the work has served as part of the commissioning of the irradiation facilities at Birmingham for sensor Quality Assurance during pre-production and production, and has highlighted issues to be resolved. Both monolithic pixel sensors, DECAL and MALTA, are the subject of ongoing developments to be included in future experiments. The very latest versions of MALTA were shown to be fully efficient after irradiation to 1×10^{15} $n_{\mathrm{eq}}/\mathrm{cm}^2$ and nearly fully efficient at 2×10^{15} $n_{\mathrm{eq}}/\mathrm{cm}^2$, a significant improvement after having 78 % efficiency at 1×10^{15} $n_{\mathrm{eq}}/\mathrm{cm}^2$ in the original version of the device. Simulation for inclusion of calorimeter constructed from monolithic active pixel sensors (MAPS) in experiments shows promise to improve particle reconstruction with Particle Flow techniques. Measurements with the DECAL sensors have demonstrated the counting logic and digital configuration necessary for the proposed application in calorimetry. While both DECAL and MALTA would have to be subject to further design iteration for inclusion in experiments to improve the front-end, sensor, and readout characteristics, the demonstrated improvements show there is a clear path towards their final implementation.

Author's Contribution

While the work of this thesis is part of three collaborative efforts (ATLAS ITk Strips, MALTA, and DECAL), the results presented are my own and where they are not the contributions of others are clearly stated.

For results with the original MALTA device, I assisted with test beam data acquisition, proton irradiations, and development of the MALTA beam telescope, including simulation and implementation of NIM electronics for triggering. The efficiency results were generated with analysis in which I did not participate.

For the results with the MiniMALTA sensor, I assisted with preparation for and data acquisition at the ELSA and Diamond test beams and generated the plots from Diamond in this thesis. I also irradiated and tested the proton-irradiated MiniMALTA samples that are used in this thesis. The efficiency results were generated with analysis in which I had only minor participation. The front-end measurements of MiniMALTA presented in the thesis were not mine, but are exemplary versions of the many measurements made on MiniMALTA, including some by myself. The key results with MiniMALTA are summarized in my proceedings for the 2019 Vertex Workshop *Recent measurements on MiniMALTA, a radiation hard CMOS sensor with small collection electrodes for ATLAS* as well as in the proceedings for the 2019 INFIERI school *MALTA: a Monolithic Active Pixel Sensor for tracking in ATLAS.*

For the results with the MALTA Cz sensor I did the core test beam analysis for efficiency measurements. I did not participate in test beam data acquisition, though I did do significant testing of devices in preparation. I also measured the IV curves, ^{55}Fe amplitude spectra, and x-ray occupancy scans, although of course with the support of others in the MALTA group.

For digital electromagnetic calorimetry simulation work, I modified existing shell scripts to interface with the DD4HEP and MARLIN software packages, and modified existing XML files for reconstruction in the the CLICdet detector. The calibration and the π^0 reconstruction are based on a similar procedures and becnhmarking studies for simulations of the International Large Detector. For the testing of the DECAL chip, I relied on and modified existing software and firmware to make measurements of the analog signal and threshold scans. The results that demonstrate the counting logic on DECAL are from measurements I did not make.

For the measurement of ATLAS17 strip sensors, I irradiated the sensors at the MC40 cyclotron and measured the collected charge with the ALiBaVa system. The interstrip measurements were made by myself at Cambridge in Cavendish labs with the assistance of our collaborators in ITk strip sensor development.

Acknowledgements

I would first like to thank my supervisors, Phil Allport and Laura Gonella for giving me the opportunity to work on a variety of exciting sensor developments for particle physics and for their tireless efforts and a wealth of guidance and support along the way. I would also like to acknowledge Nigel Watson for his supervision on simulations for digital calorimetry and help putting together this thesis. My first supervisor, Steve Worm, was instrumental in bringing me over from the U.S. and helping me become integrated in the BILPA and ATLAS groups at Birmingham as well as the MALTA testing group at CERN and the DECAL team at RAL. I would of course like to thank all members of these collaborations for their hard work and patience with my occasionally obtuse presentations.

My work at the University of Birmingham would not have been possible without the support of technical staff, post docs, and fellow students, including Simon Pyatt, Juergen Thomas, Ioannis Kopsalis, and Alasdair Winter, as well as two undergraduate summer students, Paul Swallow and Sparshita Dey, who helped with ITk sensor studies with enthusiasm. I would like to thank the operators at the MC40 cyclotron, including Prof. David Parker, Amelia Hunter, and especially Ben Phoenix for his exceptional effort in help with an overnight irradiation.

I worked as a member of the MALTA testing team at CERN for nearly two years and and during this time we generated many of the key results for this thesis. I would like to thank all members of the team for their hard work, professional support, and camaraderie. I am grateful to Heinz Pernegger and Walter Soneys for allowing me to join the testing team and for in-depth discussions on sensor design and physics that have helped to guide my work. I would especially like to thank Carlos Solans, who acted as a de facto local supervisor and was always happy to teach and whose leadership I felt helped establish and maintain a friendly and productive group dynamic. I would like to thank the the Fellows in the group, Enrico Schioppa, Valerio Dao, Mateusz Dyndal, Lingxin Meng, for their aid, patience, and friendship. My work would not have been possible without the daily help of other students, in particular Florian Dachs, Abhishek Sharma, Ignacio Asensi Tortajada, Kaan Yuksel Oyulmaz, Maria Mironova, Kaloyan Metodiev, and design students Roberto Cardella, Francesco Piro, Leyre Flores, and Ivan Berdalovic.

I acknowledge Diamond Light Source for time on Beamline B16 under Proposal 22061. The measurements leading to results in this thesis have been performed at the Test Beam Facility at DESY Hamburg (Germany), a member of the Helmholtz Association (HGF). Measurements leading to these results have been performed at the E3 beam-line at the electron accelerator ELSA operated by the University of Bonn in Nordhrein-Westfalen, Germany. This work received funding from the Postgraduate Research Scholarship Fund at the University of Birmingham (UK).

Lastly, and most obviously, I would like to thank my friends and family for their love, support, and patience throughout the adventure that has been my PhD and throughout my entire life. Thanks to my brother, Chris, for his unwavering friendship and helping me keep perspective, to my cat, Looc, for his forgiveness upon my return, and to my Roz for keeping me sane throughout the writing process. I would especially like to thank my parents for their hard work and support to give me many opportunities that they did not have.

Contents

Glossary . . . iv

1 Introduction **1**

2 Particle Physics experiments **3**
2.1 The Large Hadron Collider and ATLAS experiment . . . 4
2.1.1 The ATLAS experiment . . . 5
2.1.2 The LHC upgrades . . . 8
2.2 Proposed e^+e^- and hadron colliders . . . 11
2.2.1 The ILC . . . 12
2.2.2 CLIC . . . 14

3 Particle tracking with silicon detectors **19**
3.1 Interaction of Particles with Matter . . . 19
3.1.1 Bethe Equation . . . 20
3.1.2 Photon and electron interactions in matter . . . 22
3.2 Silicon Detectors . . . 27
3.2.1 The p-n Junction . . . 28
3.2.2 Signal Formation . . . 31
3.2.3 Leakage Current, Temperature Dependence . . . 32
3.2.4 Electronic Noise . . . 33
3.2.5 Radiation Damage in Silicon . . . 33
3.3 Tracking sensors in high energy particle physics . . . 38
3.3.1 Passive Strip and Pixel Detectors . . . 38
3.3.2 MAPS in particle physics experiments . . . 42
3.3.3 Sensor characterization . . . 49

4 Radiation Damage Studies on Strip Detectors **55**
4.1 Sensors . . . 55
4.2 Irradiations . . . 57
4.2.1 Dosimetry . . . 58
4.3 Charge Collection Studies . . . 60
4.3.1 Temperature and ADC Calibration . . . 61
4.3.2 Results . . . 62
4.4 Current-voltage measurements . . . 66
4.5 Interstrip Resistance Measurements . . . 67
4.5.1 Methodology . . . 67
4.5.2 Results . . . 68

4.6 Conclusions . . . 69

5 The MALTA CMOS sensor 71
5.1 MALTA chip design . . . 71
5.1.1 Analog front-end . . . 73
5.1.2 Digital readout . . . 77
5.1.3 The MALTA readout system . . . 83
5.2 Test beam measurements of irradiated MALTA . . . 83

6 Characterization of the MiniMALTA sensor 87
6.1 Chip design . . . 87
6.2 Front-end measurements . . . 91
6.3 Efficiency Measurements in e^- test beams . . . 94
6.3.1 Development of the MALTA telescope . . . 94
6.3.2 Efficiency results . . . 98
6.4 Photon Test Beams . . . 101
6.4.1 Analysis Methods . . . 105
6.4.2 Results . . . 107
6.5 Conclusions . . . 113

7 Characterization of MALTA Cz 115
7.1 Chip design . . . 115
7.2 Laboratory Measurements . . . 117
7.2.1 Current-Voltage Measurements . . . 118
7.2.2 Gain measurements . . . 133
7.2.3 X-ray scans . . . 136
7.3 Efficiency measurements . . . 143
7.4 Results summary, comparison of prototypes . . . 147

8 Digital Electromagnetic Calorimetry for Future Colliders 151
8.1 High-Granularity Digital Electromagnetic Calorimetry . . . 152
8.1.1 Motivation for particle flow approaches . . . 152
8.1.2 High-granularity calorimetry . . . 153
8.1.3 Digital electromagnetic calorimetry . . . 155
8.2 The DECAL chip . . . 156
8.2.1 Analog pixel measurements . . . 159
8.2.2 Threshold Measurements . . . 163
8.3 Simulation Results . . . 166
8.3.1 Reconstruction calibration . . . 167
8.3.2 Energy Resolution studies . . . 169
8.3.3 π^0 reconstruction studies . . . 171
8.4 Conclusions . . . 179

9 Summary and Outlook 181

List of Figures

2.1 Schematic of the Large Hadron Collider (LHC), reproduced from [4]. 4
2.2 Cutaway view of the ATLAS detector [5]. 6
2.3 Particle identification scheme in ATLAS [5]. 7
2.4 Plan for the LHC and High-Luminosity Large Hadron Collider (HL-LHC) [9]. . . 8
2.5 Schematic drawing of the ATLAS ITk with pixel layers in red and strip layers in blue [11]. 10
2.6 The NIEL displacement damage for the ATLAS inner tracker [11]. 11
2.7 The total ionizing dose for the ATLAS inner tracker [11]. 11
2.8 Schematic of the International Linear Collider (ILC) accelerator complex [14]. . 13
2.9 Proposed detectors at the ILC and Compact Linear Collider (CLIC) [15–17] . . 15
2.10 The proposed site for the various stages of CLIC [18]. 16
2.11 Cross sections of Higgs processes at CLIC as a function of center of mass energy. [18]. 17

3.1 The stopping power as a function of $\beta\gamma$ as calculated by the Bethe equation plotted for muons on copper [23]. 21
3.2 The stopping power as a function of momentum as calculated by the Bethe equation for electrons, protons, and pions on silicon. The plot does not include the corrections for accuracy at higher energies that are in Fig. 3.1. 21
3.3 The stopping power Landau distributions for 500 MeV pions normalized to unity for the most probable value. The width w is the full width at half the maximum [23]. 22
3.4 Photon total cross sections as a function of energy in carbon and lead, showing the contributions of different processes from [23]. 24
3.5 The photon mass attenuation length (or mean free path) λ for various elemental absorbers as a function of photon energy, from [23]. 25
3.6 Fractional energies loss for electrons and positrons in lead. 25
3.7 Electron critical energy for the chemical elements, with critical energy defined as the energy at which the ionization loss per radiation length is equal to the electron energy. The fits shown are for solids and liquids (solid line) and gases (dashed line). The rms deviation is 2.2% for the solids and 4.0% for the gases [23]. 26
3.8 Schematic of the doping and resulting electric field of an unbiased p-n junction [26]. 28
3.9 The depletion voltage as a function of fluence for a 300 μm sensor [33]. 35
3.10 The effective doping concentration as a function of the annealing time. The data shown here were taken at room temperature while the annealing took place at 60 °C [34]. 35
3.11 The α parameter for the change in leakage current as a function of time for different annealing temperatures [32]. 36

3.12 The non-ionizing energy loss (NIEL) displacement damage for various particles and energies. The insert shows the energies relevant for high energy particle physics [32]. The red lines illustrate the expected damage factor of 2 to 3 for 23 MeV protons which were used for irradiation. 37
3.13 Strip modules for the ITk. 39
3.14 Hybrid pixel sensors for the ITk. 40
3.15 Schematic of a PMOS transistor. 44
3.16 Schematic of the TowerJazz 180 nm standard process used for the ALPIDE sensor. 45
3.17 Schematics of the cross section of the pixel substrate design concepts for the A Toroidal LHC ApparatuS (ATLAS) ITk inspired by schematics in [43]. 47
3.18 Schematic of the TowerJazz 180 nm processes. 48
3.19 Amplitude spectra of ^{55}Fe with the Investigator sensor in the standard and modified TowerJazz 180 nm processes, from [45]. 48
3.20 Measurements of unirradiated and neutron-irradiated TowerJazz Investigator samples in the modified process, from [45]. 49
3.21 The current–voltage characteristic for a silicon diode in the reverse bias direction. The expanded view shows the $I \propto \sqrt{V}$ dependence, while the global view shows the full scan including breakdown at higher voltages, from [51]. 51
3.22 Examples of capacitance-voltage (CV) measurements from From [51]. The two upper bands depict sensors of two different geometries with slightly different areas and same high resistivity material, both 400 μm thick. The lower CV curves describe 500 μm thick sensors, which have less capacitance at full depletion and larger $V_{FD} \propto d^2$, as would be expected based on equation 3.18. The different depletion voltages of the lower curves are due to two different resistivities $\rho 2 > \rho 1$. 51
3.23 A threshold scan of a pixel in MALTA. The vertical line is at the mean from the error function fit. 53

4.1 Photo of the box, beam pipe, and faraday cup at the MC40 cyclotron at the University of Birmingham. 57
4.2 Plot of measured versus target fluences for ATLAS17 sensors. 60
4.3 Schematic of the ALiBaVa setup used at the University of Birmingham. 61
4.4 Plot of a Landau fit to the distribution of collected charge (in ADC) of a sample irradiated to a target fluence of 5 $\times 10^{14}$ $n_{\mathrm{eq}}/\mathrm{cm}^2$ biased at 600 V and at -25 °C. 62
4.5 The collected charge as a function of fluence measured in ATLAS12 STD Mini strip sensors with minimum ionizing particle (MIP)s and bias voltage of 500 V from [11]. 63
4.6 Collected charge versus bias voltage of ATLAS17 STD Minis tested at University of California Santa Cruz (UCSC), University of Tsukuba, and Instituto de Física Corpuscular (IFIC). Sensors were irradiated at Cyric, Ljubliana, and Birmingham. The sensors irradiated at Birmingham are from a second campaign as a follow-up to the first, which had charge collection efficiency (CCE) results inconsistent with other irradiation facilities [61]. 64
4.7 The collected charge as a function of bias voltage measured in ATLAS17 STD Mini strip sensors with ^{90}Sr. Irradiated sensors have been annealed. 65
4.8 Plot of the cluster widths for ATLAS17 STD Minis biased to 900 V. 66

4.9 Plot of IV curves for ATLAS17 sensors. 67
4.10 Circuit diagram for the interstrip resistance measurement. R_b is the bias resistance, R_i the interstrip resistance, V_s the source voltage, and V the voltmeter. 68
4.11 Plot of measured interstrip resistance values for the ATLAS STD Minis. 69
4.12 The interstrip resistance measured in ATLAS12 strip sensors irradiated at CYRIC in [11]. 70

5.1 Schematic of the TowerJazz 180 nm CMOS imaging sensor processes. 72
5.2 Mapping of the eight 32×512-pixel sectors of MALTA with variations in collection electrode and p-well implant geometry. 73
5.3 Design of the MALTA pixel. 73
5.4 Block diagram of the analog front-end. 74
5.5 Schematic of the diode reset. 75
5.6 Schematic illustrating the operating principle of the amplifier. 76
5.7 Schematic of the MALTA front-end [65]. 77
5.8 Schematic of the column drain readout in MonoPix, reproduced from [66]. . . . 77
5.9 Schematic of the red and blue groups in the asynchronous readout architecture of the MALTA, reproduced from [69]. 80
5.10 Schematic of NAND buffer, reproduced from [65] 81
5.11 Bonded MALTA samples. 83
5.12 In-pixel efficiency measurements of unirradiated MALTA samples with measurements from 2×2 pixel regions combined to improve statistics. The average efficiency is written above each plot, and the average efficiency of each region contained in a 3×3 grid is written on the plot. 84
5.13 In-pixel efficiency measurements of MALTA samples irradiated to $\phi = 1 \times 10^{15}$ $n_{\mathrm{eq}}/\mathrm{cm}^2$ with measurements from 2×2 pixel regions combined to improve statistics. The average efficiency is written above each plot, and the average efficiency of each region contained in a 3×3 grid is written on the plot. 84

6.1 Schematics of the 3 pixel substrate designs in MiniMALTA [64]. 88
6.2 TCAD simulations of electrostatic potential of the three pixel designs of MiniMALTA [72]. The figures are centered on the p-well implant, not the collection electrode, and the star marks the potential minimum. The substrate is biased to -6 V, and the collection electrode to 0.8 V. 89
6.3 TCAD simulations of the induced current from a MIP for the three pixel designs of MiniMALTA before and after irradiation [72]. 89
6.4 The MiniMALTA chip. 90
6.5 Measurements from threshold scans. 92
6.6 ^{55}Fe measurements of MiniMALTA. 94
6.7 The MALTA telescope in simulation and data acquisition. 96
6.8 Residuals in AllPix^2 simulations of the MALTA telescope. 97
6.9 Efficiency measurements in the different sectors of MiniMALTA sample W2R1 with $\phi = 1 \times 10^{15}$ $n_{\mathrm{eq}}/\mathrm{cm}^2$ [73]. Each bin corresponds to a single pixel. 100
6.10 Efficiency measurements of MiniMALTA as a function of threshold [73]. 100
6.11 In-pixel efficiency measurements of sample W2R1 irradiated to 1×10^{15} $n_{\mathrm{eq}}/\mathrm{cm}^2$ with measurements from 2×2 pixel regions combined to improve statistics. . . . 102
6.12 Experimental setup at the Diamond test beam. 104

6.13 Illustration of methods to determine the pixel boundaries. 106
6.14 Relative photon pixel response maps for the different MiniMALTA samples. Each row of maps has the results for the three pixel designs for a sensor and level of irradiation. Starting from the left, the pixel designs are: the continuous n^- substrate with the standard front-end, the extra deep p-well with the modified front-end, and the n^- gap with the modified front-end. 108
6.15 Average cluster size maps for the different samples and sectors. For each sample and row, the results are shown for three pixel designs, starting from the left: the continuous n^- substrate with the standard front-end and the extra deep p-well and n^- gap with the modified front-end. 109
6.16 Photon pixel response maps of the continuous n^- sector of W2R1 1×10^{15} n_{eq}/cm^2 with the substrate biased at -20 V and -6 V. 112

7.1 Cross sections of the n^- gap sensor design in epitaxial and Czochralksi silicon. . 116
7.2 Schematic of the circuit used in the IV measurement. The PWELL and SUB currents are measured directly to infer the leakage and punch-through currents. 119
7.3 Schematic of the biasing of the pixel substrate. The electrode and PWELL voltages are kept constant, and the SUB lowered from -6 V until the operational limit with a 20 mA current compliance. The currents through the power supplies for the SUB and PWELL are measured with other supplies to act as dedicated ammeters. 119
7.4 Examples of the 3 cases of the current-voltage measurements. 122
7.5 Current-voltage measurements for the unirradiated samples with the continuous n^- substrate at different temperatures. 123
7.6 Current-voltage measurements for the unirradiated samples with the n^- gap or extra-deep p-well substrates at different temperatures. 124
7.7 Schematic of seal ring structure at the edge of the pixel matrix, from [64]. 125
7.8 current-voltage (IV) measurement of an epitaxial continuous n^- MALTA sensor with laser (instead of diamond saw) dicing to reduce the area of the periphery. The punch-through voltage is about 9 V lower in the diamond saw-diced samples. 126
7.9 Current-voltage measurements for an unirradiated n^- gap Czochralski sensor, W9R11 at p-well biases of 2, 4, and 6 V. 127
7.10 Linear fits of the difference between substrate and p-well bias at which there is 1 mA of punch-through current for different MALTA samples. 128
7.11 Current-voltage measurements for the irradiated Czochralski continuous n^- samples at different temperatures. 129
7.12 Current-voltage measurements for the irradiated samples with the n^- gap substrate at difference temperatures. The fluence is 1×10^{15} n_{eq}/cm^2 except for a single n^- gap sample. 130
7.13 Current-voltage measurements for the irradiated samples with the n^- gap or extra deep p-well substrate at difference temperatures. The fluence is 1×10^{15} n_{eq}/cm^2 except for a single n^- gap sample. [Continued from previous figure.] 131
7.14 Current-voltage measurements for the proton irradiated samples with a fluence of 8×10^{14} n_{eq}/cm^2 and total ionizing dose (TID) of 100 Mrad. 132
7.15 Output from a MALTA monitoring pixel with an ^{55}Fe X-ray source. 134
7.16 Amplitude spectra from ^{55}Fe of different MALTA devices. 135

7.17 Average amplitude of the k-α peak in ^{55}Fe measurements. 137
7.18 The X-ray setup and amplitude spectrum. 138
7.19 Occupancy as measured in the X-ray scans with the bias at 6 V. 139
7.20 Occupancy as measured in the X-ray scans near the operational limit of the substrate bias. 140
7.21 Occupancy as measured in the X-ray scans near the operational limit of the substrate bias. 141
7.22 Occupancy as measured in the X-ray scans near the operational limit of the substrate bias. 142
7.23 Track residuals of 3 GeV electrons as measured in Proteus with the MALTA telescope and the MALTA Cz DUT. 143
7.24 Efficiency and cluster size measurements of MALTA Cz as a function of substrate bias. The thresholds are listed on the legend. 144
7.25 Efficiency measurements of MALTA Cz as a function of threshold. 145
7.26 Cluster size of an unirradiated n^- continuous Czochralski sensor as a function of substrate bias. 146
7.27 In-pixel efficiency maps of irradiated Cz samples [67]. 147

8.1 The various branches of development of Particle Flow calorimetry of the CALICE collaboration. 154
8.2 Layers in the ATLAS LAr and proposed digital SiW calorimeters. 155
8.3 The DECAL sensor. 157
8.4 Schematic of the strip and pad modes in DECAL. 157
8.5 Schematic of the DECAL front-end. 158
8.6 The DECAL readout system. 159
8.7 Example of Gaussian fit to a waveform from ^{55}Fe X-rays on DECAL FD. 159
8.8 Waveforms from DECAL and DECAL FD with the clock on and off and an ^{55}Fe source present or not. Turning off the clock removes the 40 MHz oscillation, and there is a negative polarity signal from the source. 161
8.9 Fits to distributions of pulse measurements. 162
8.10 Threshold scans of DECAL. 164
8.11 Testing of the digital sector of DECAL with number injection. 165
8.12 Proposed CLICdet detector [17]. 167
8.13 Simulated data and corresponding fits used in the Pandora calibration procedure. 168
8.14 Reconstructed energy and energy resolution for single photon events the analog and digital calorimeters. 170
8.15 Photon separation angles. 173
8.16 Projected DECAL hits for single 20 GeV and 50 GeV π^0. The hits in red are from the first five layers of the electromagnetic calorimeter (ECAL). 173
8.17 Pion reconstructed mass resolution. 174
8.18 Angles between photons. 176
8.19 Efficiency of reconstruction of single photons. 178
8.20 Efficiency for photon identification in simulated π^0 decays. 179

List of Tables

2.1 Comparison of key parameters for proposed detectors at CLIC [17]. 16

3.1 Requirements for pixel modules in the Barrel 4 region of ATLAS ITk [11]. . . . 41

4.1 Table of quantities of ATLAS17 sensors of specific types and target fluences. . . 56

4.2 Radiation tolerance requirements for ITk strip sensors. A safety factor of 1.5 is included. 56

5.1 Encoding of the 40-bit words output by MALTA. 82

6.1 Summary of the AllPix^2 simulation results for the MALTA telescope. The parameters D and d are for the distances shown in the diagram in 6.7(a). 98

6.2 Table of average efficiencies and thresholds measured in MiniMALTA. The uncertainties are statistical and assume a binary distribution. 101

6.3 Table of mean photon pixel responses. 111

6.4 Table of the mean charge sharing extent. 111

6.5 Average photon pixel response at different bias voltages. 112

7.1 Difference between the sub and p-well at which the punch-through reaches 1 mA as calculated from the linear fits in Fig. 7.10 127

7.2 Operational limits and the modes of current that dominate at the limit of MALTA Cz sensors with the p-well bias at 6 V. Uncertainties are 10%. 133

7.3 Average of fit results to amplitude spectra of MALTA Cz samples. The analog signal is measured at the outputs of the preamplifiers of four monitoring pixels with the diode reset. 136

7.4 Example of how a coincidence in the intentionally masked rows, columns and diagonals results in “ghost” masking. 137

7.5 Table of masking statistics from X-ray scans at a substrate bias of 6 V. 139

7.6 Table of best efficiencies and thresholds measured in MALTA Cz in Sector 2 at different fluences. The uncertainties are statistical and assume a binary distribution. 148

7.7 Table of measurements completed with different types of MALTA samples that are presented in this chapter. The check mark indicates the measurement was completed, the lack of a check indicates it was not. The X-ray scans could not be completed for the irradiated sensors due to lack of a cooling setup for this measurement. The proton-irradiated devices with $\phi = 8 \times 10^{14}$ $n_{\mathrm{eq}}/\mathrm{cm}^2$ were not irradiated prior to the Deutsches Elektronen-Synchrotron (DESY) test beam and so did not have efficiency measurements. The unirradiated extra deep p-well sample was not available for ^{55}Fe measurement due to its use in other setups. . . 149

8.1 Typical jet composition and energy resolution of detectors for the various jet components [88]. 153
8.2 Measurements of DECAL and DECAL FD waveforms with ^{55}Fe and ^{90}Sr. Measurements are determined from Gaussian fits to distributions as in Fig 8.9. . . . 162
8.3 Measurements with X-ray source at different substrate voltages of DECAL. . . . 163

Glossary

ADC	analog to digital converter
ALICE	A Large Ion Collider Experiment
ATLAS	A Toroidal LHC ApparatuS
BCID	bunch crossing identification
CCE	charge collection efficiency
CEPC	Circular Electron Positron Collider
CERN	European Organization for Nuclear Research
CLIC	Compact Linear Collider
CMOS	complementary metal-oxide-semiconductor
CMS	Compact Muon Solenoid
CV	capacitance-voltage
DAC	digital to analog converter
DACs	digital to analog converters
DESY	Deutsches Elektronen-Synchrotron
DMAPS	depleted monolithic active pixel sensor
DUT	device under test
ECAL	electromagnetic calorimeter
ELSA	Electron Stretcher system at the Physics Institute of the Rheinische Friedrich-Wilhelms-Universität Bonn
ENC	equivalent noise charge
FCC-ee	Future Circular Collider (e^+e^- beams)
FCC-hh	Future Circular Collider (hadron-hadron beams)
FIFO	first in, first out
FMC	FPGA Mezzanine Card
GBL	General Broken Lines
HCAL	hadronic calorimeter/calorimetry
HL-LHC	High-Luminosity Large Hadron Collider
HPK	Hamamatsu Photonics

ID	Inner Detector
IFIC	Instituto de Física Corpuscular
ILC	International Linear Collider
ILD	International Large Detector
ITk	Inner Tracker
ITS	Inner Tracking System
IV	current-voltage
LEP	Large Electron-Positron Collider
LHC	Large Hadron Collider
LHCb	Large Hadron Collider Beauty
LS	Long Shutdown
LVDS	Low Voltage Differential Signal
MALTA	Monolithic ALICE To ATLAS
MAPS	monolithic active pixel sensors
Marlin	Modular Analysis and Reconstruction for LINear Collider
MIP	minimum ionizing particle
MOS	metal-oxide-semiconductor
MOSFET	metal-oxide-silicon field effect transistor
NIEL	non-ionizing energy loss
NIM	Nuclear Instrumentation Module
NMOS	n-type MOSFET
PandoraPFA	Pandora Particle Flow Analysis
PDG	Particle Data Group
PMOS	p-type MOSFET
PMT	photomultipler tube
RAL	Rutherford Appleton Laboratory
ROI	region of interest
RTS	random telegraph signal
SiD	Silicon Detector
SPS	Super Proton Synchrotron
TCAD	Technology Computer Assisted Drafting
TID	total ionizing dose
TLU	trigger logic unit
ToT	Time over Threshold
UCSC	University of California Santa Cruz

Chapter 1

Introduction

The Standard Model has been established in the last half-century through experiments at particle accelerator facilities. These experiments have required technological advances for higher collision energies and greater precision measurements. A key tool has been silicon detectors, which have been used in particle physics experiments in the form of patterned microstrip and pixel detectors since the 1980s. Modern experiments have to meet even more demanding requirements in terms of event rate, luminosity, radiation exposure and other constraints, and silicon sensors must undergo development to maximize the physics potential of these experiments. This thesis is concerned with silicon sensor technologies for the next generation of particle experiments, including strip sensors for the next upgrade to the ATLAS experiment at CERN's LHC and MAPS for calorimetry and tracking in high-radiation environments. Through the work of this thesis, the feasibility of such approaches is demonstrated, and the potential for further development and applications of this technology is discussed. The contents of this thesis are as follows:

- Chapter 2 describes future physics experiments and the proposed detector systems for them relevant to this thesis: the ATLAS experiment at the HL-LHC and the potential circular and linear collider experiments (FCC and CEPC, ILC and CLIC).

- Chapter 3 gives an introduction to silicon detector technologies including working principles and specific technologies in this thesis: hybrid strip sensors and monolithic active

pixel sensors in CMOS imaging processes.

- Chapter 4 describes characterization of strip sensors for the ATLAS Inner Tracker upgrade, a new tracking system that will replace the current ATLAS Inner Detector.
- Chapter 5 describes the MALTA device and results with the first prototype.
- Chapter 6 summarizes characterization of the MinMALTA prototype.
- Chapter 7 summarizes characterization of MALTA Cz.
- Chapter 8 summarizes characterization of the DECAL chip and simulations for performance of a digital electromagnetic calorimeter made with monolithic pixel sensors.
- Chapter 9 summarizes the key results of the thesis and discusses the outlook for the development of CMOS silicon sensors.

Chapter 2

Particle Physics experiments

The upgrades to the existing LHC and construction of new accelerators are essential to the future of particle physics, both to increase the precision in current measurements and search for new phenomena that may only be revealed at higher luminosity and center of mass of energy. The HL-LHC will generate nearly 20 times as many collisions in Runs 4 and 5 as in Run 2 followings upgrades during Long Shutdown (LS) 3 [1], offering the potential to make unprecedented precision measurements, studies of Higgs properties, and searches for new physics. Future facilities include proposed linear accelerators to collide electrons and positrons (the ILC and the CLIC), circular colliders also for e^+e^- experiments, and finally circular colliders for hadron-hadron interactions with center of mass energies up to 100 TeV, about seven times the current reach of the LHC. With these new and upgraded experiments, unprecedented physics opportunities and corresponding experimental challenges will arise including the requirements for the silicon sensors used for particle detection. In this chapter, these experiments are described including the requirements for the proposed implementation of silicon sensor technologies studied in this work. The MALTA device, characterized in this thesis, is being developed as a possible route to a longer-term upgrade of the ATLAS experiment, while the DECAL sensor targets calorimetry in future e^+e^- experiments and higher energy hadron-hadron colliders.

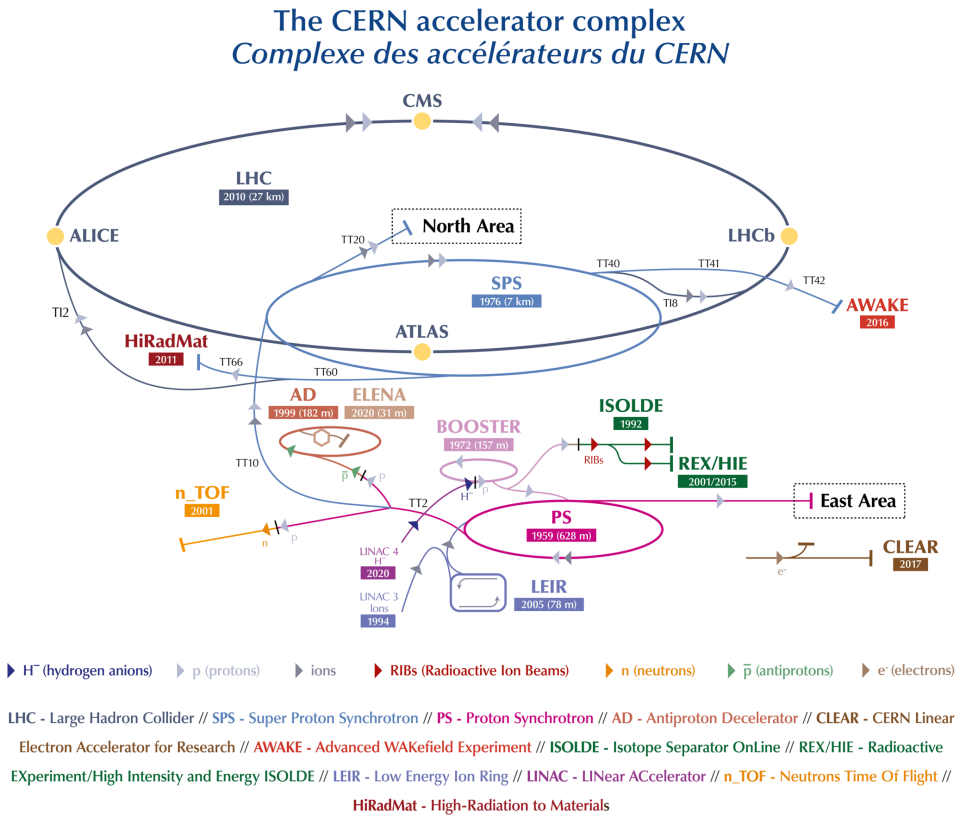

Figure 2.1: Schematic of the LHC, reproduced from [4].

2.1 The Large Hadron Collider and ATLAS experiment

The LHC is a 27-km circumference circular collider straddling the French-Swiss border west of Geneva. It is the largest and highest energy particle accelerator in the world and has been the key tool to advancing particle physics, especially in its primary initial intended scientific goal of discovering of the Higgs boson, which was achieved in 2012 [2, 3].

At the LHC, a schematic of which is shown in Fig. 2.1, protons (or in some cases heavy ions) are accelerated to high energies and made to collide at specific interaction points along the 27-km ring where large detector systems are set up to measure these interactions. The protons begin their journey as hydrogen gas stored in a bottle at LINAC 4. The machine comprises a H- ion source and four types of accelerating structure: the particles are accelerated in several stages, first to 3 MeV by a radio-frequency quadrupole (RFQ), then to 50 MeV by drift tube linacs (DTLs), then to 100 MeV by coupled-cavity drift tube linacs (CCDTLs), and finally to

160 MeV by Pi-mode structures (PIMS). After leaving LINAC 4, particles are injected in the Proton Synchrotron Booster (BOOSTER), the Proton Synchrotron (PS), the Super Protons Synchrotron (SPS) and finally into the LHC where they are accelerated up to 6.5 TeV in two opposite traveling, synchronized beams. These two beams are such that two bunches of protons cross at interaction points every 25 ns, resulting in center-of-mass energies up to 13 TeV at four interaction points where experiments are placed. The experiments at the four interaction points are:

ATLAS A general-purpose detector [5]. The unique toroidal muon spectrometer system sets the overall dimensions of the experiment.

Compact Muon Solenoid (CMS) A general-purpose detector. The key difference with ATLAS is the inclusion of the calorimeter within the solenoid and that the return yoke is instrumented for muon momentum measurement [6].

A Large Ion Collider Experiment (ALICE) A detector to study the collisions of heavy ions such as Pb-Pb and the quark-gluon plasma formed in strongly interacting matter at extreme energy densities [7].

Large Hadron Collider Beauty (LHCb) The LHCb experiment is optimized for the studies of particles containing bottom and charm quarks to investigate a number of decay characteristics such as those relating to CP-violation. In contrast to CMS and ATLAS, which measure over a large fraction of the solid angle, LHCb is in the forward region, close to the beam axis [8].

In the context of the LHC, this thesis is concerned with the development of silicon sensors for the ATLAS experiment, which is described in greater detail in the next section.

2.1.1 The ATLAS experiment

The ATLAS detector is a cylindrical, general purpose detector concentric to the LHC beam line 25 m in diameter and 44 m in length as shown in the schematic of the detector in Fig. 2.2 [5].

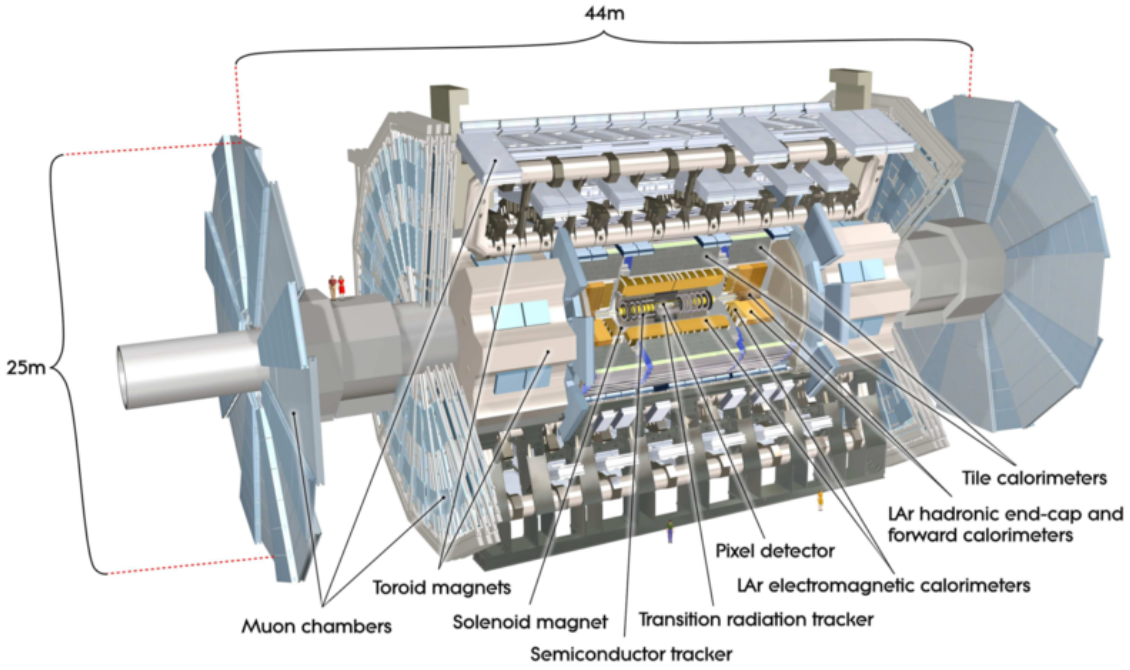

Figure 2.2: Cutaway view of the ATLAS detector [5].

Going out in radius from the interaction point, ATLAS consists of silicon tracking layers with pixel and strip detectors and a Transition Radiation Tracker contained within a superconducting solenoid magnet and together known as the Inner Detector (ID). Outside the ID are the electromagnetic and hadronic calorimeters, and a muon spectrometer to measure deflections through superconducting toroidal magnets.

Particles resulting from the proton-proton collisions are identified in ATLAS based on the measurements in these detector systems as illustrated in Fig. 2.3. The tracking layers measure the paths of charged particles and are key to measurement of their origin (primary or secondary vertex), momentum and charge. For electrons, a curved track will be recorded in the tracker and an electromagnetic shower in the ECAL. High-energy photons usually do not result in a track in the tracker, but do create an electromagnetic shower in the ECAL. Photons do occasionally pair produce in a layer of the tracker or its support or service structures and the resulting e^+e^- pair creates tracks and electromagnetic showers. Protons and other charged hadrons leave a track in the ID but do not produce substantial electromagnetic showers and instead deposit most of their energy through nuclear interactions, with this being mostly in the

hadronic calorimeter/calorimetry (HCAL). Neutrons and neutral kaons generally only interact in the HCAL. Muons interact minimally with all detector systems and leave a track through all regions of ATLAS with momentum measured in both the ID and the muon spectrometer (unless the momentum is too low to escape the ID solenoid). Neutrinos are not detected, and their presence has to be inferred from missing reconstructed energy and transverse momentum. The identification of individual particles allows for the full reconstruction of events for precision measurements or searches for new phenomena in ATLAS.

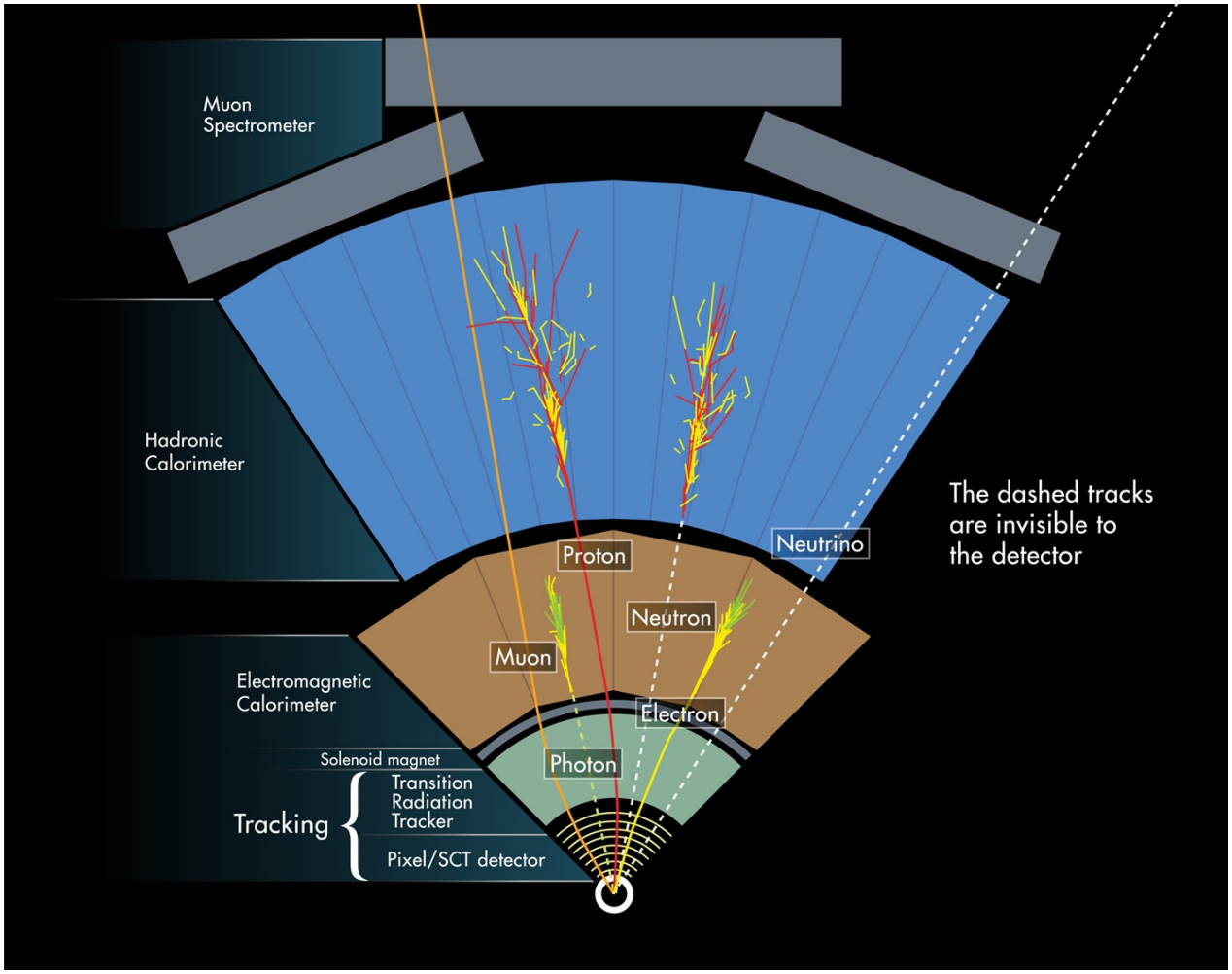

Figure 2.3: Particle identification scheme in ATLAS [5].

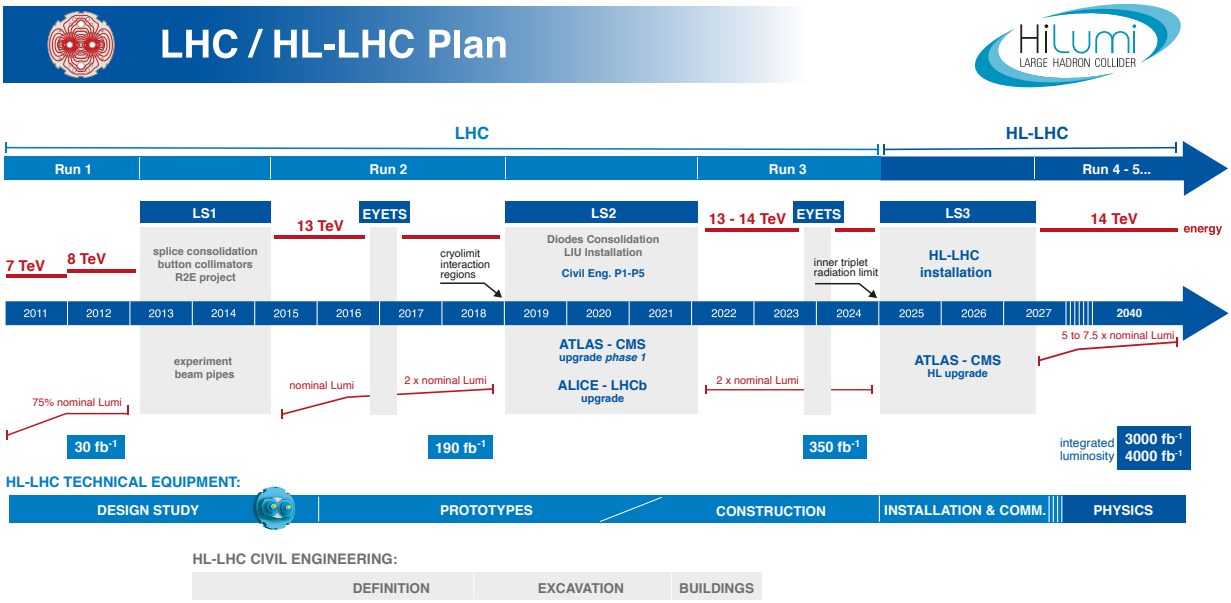

Figure 2.4: Plan for the LHC and HL-LHC [9].

2.1.2 The LHC upgrades

In order to study rare phenomena, it is necessary to have many particle interactions. The number of interactions corresponding to a particular process at the LHC is given by

$$n = L\sigma, \tag{2.1}$$

where L is the integrated luminosity of the LHC and σ is the interaction cross-section of the phenomenon of interest. The instantaneous luminosity depends on beam parameters and can be written as:

$$\mathcal{L} = \frac{N_b^2 n_b f_{rev}}{4\pi\sigma_x\sigma_y}, \tag{2.2}$$

where N_b is the number of particles per bunch, n_b the number of bunches per beam, f_{rev} the revolution frequency, and σ_x, σ_y represent the RMS beam sizes in the horizontal and vertical directions at the interaction point[1].

[1]This formulation assumes that transverse density profiles are Gaussian, identical for all bunches, uniform along the length of each bunch, and not affected during crossing of bunches.

For the HL-LHC [1], the instantaneous luminosity will be gradually increased over the course of several periods of operation and upgrade. As shown in Fig. 2.4 of the plan for the LHC, in Run 2 from 2015 through 2019, the instantaneous luminosity was gradually increased to twice the nominal value of 10^{34} $\mathrm{cm}^{-2}\mathrm{s}^{-1}$. Following the HL-LHC Upgrade to be installed during Long Shutdown 3 ending in 2027, the luminosity will be increased to between five and seven times the nominal value. The integrated luminosity for the HL-LHC is predicted to be between 3000 fb^{-1} and 4000 fb^{-1}, nearly ten times the value for Run 3. As a result of the increased instantaneous luminosity, there has been an increase in the mean number of events (pileup) per bunch crossing from $\langle\mu\rangle \sim 20$ in Run 1 to nearly $\langle\mu\rangle = 40$ in the end of Run 2. The pileup is predicted to increase to $\langle\mu\rangle \sim 200$ with an average of 1.8 vertices per mm along the beam axis during HL-LHC operation [10]. This increase in particle interactions presents exciting opportunities to search for rare phenomena and make higher precision measurements, but also presents an unprecedented challenge for the operation of experiments. In general, detectors will have to cope with higher radiation, higher data rates, and more complicated pattern recognition problems due to the greater number and higher density of interactions per bunch crossing. To this end there are great efforts to upgrade the experiments, including the development of novel particle detection technologies, the focus of the work in this thesis.

2.1.2.1 ATLAS Inner tracker upgrade

For the HL-LHC, the ID of ATLAS will be replaced with an all-silicon ITk during Long Shutdown 3 (LS3) beginning in 2024 [11]. There will not be a transition radiation tracker. The geometry for a single quadrant of the ITk is illustrated in Fig. 2.5, with pixel sensors represented by red lines and strips by blue, and the barrel and endcap regions by lighter and darker tones of these colors, respectively. In the barrel region are five layers of pixel sensors and four layers of strips. Sensors in the pixel region will be "hybrid" sensors consisting of passive silicon sensors coupled via bump bonds to readout chips containing amplification and electronics. For the pixel region, an alternative solution initially considered was monolithic pixel sensors, where the readout electronics and sensor are contained within the same silicon chip. If it had proved suffi-

ciently mature to adopt, this technology would have resulted in much less multiple scattering in the layers closest to the interaction region, greatly improving the sensitivity to secondary vertices associated with decays of short-lived particles. There were other potential advantages in terms of performance, cost, and construction which are discussed in greater detail in Sec. 3.3.2. This thesis covers a number of developments in terms of radiation hardness relating to strip detectors (Chapter 4); but it is primarily focused on MAPS, initially considered as a possible technology for the outer barrel region, but now (if radiation tolerance can be improved) as an alternative replacement for the inner pixels after Run 4 (Chapters 5, 6, 7). MAPS have also been considered for calorimetry in experiments other than ATLAS as discussed in Chapter 8.

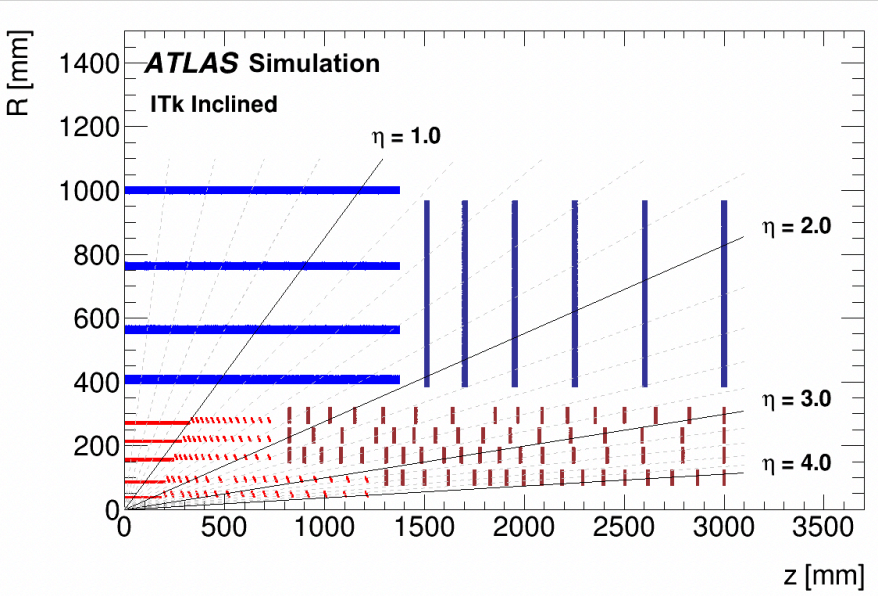

Figure 2.5: Schematic drawing of the ATLAS ITk with pixel layers in red and strip layers in blue [11].

For the HL-LHC, the radiation exposure within the tracking volume will increase along with the integrated luminosity to the levels shown in Figs. 2.6 and 2.7 in "heat maps" of the simulated integrated radiation dosage for the ITk with an integrated luminosity of 2000 fb^{-1} [11]. The damage due to NIEL, which generally affects the performance of the sensor and not the readout electronics, is shown in Sec. 2.6, and the total ionizing dose, which mostly affects the electronics, is shown in Fig. 2.7. Sensors are also vulnerable to single event upsets (SEU) and single event latch ups (SEL). These occur when a particle passes through a transistor in the detector and

causes a change of state. In the case of SELs, the result is unusually high current in a CMOS structure which can lead to permanent damage of the device. Sensors for the majority of the ITk must operate reliably over the course of twice this exposure to high levels of radiation, and undergo stringent development and characterization to ensure they do so. In Section 3.3.1, further detail of the ITk strip and pixel sensors are discussed in the context of the silicon sensor technologies under development. After the initial 2000 fb^{-1}, or approximately half of the expected integrated luminosity for the HL-LHC, the inner layers will need and are planned to be replaced due to radiation damage. For the initially installed ITk, the pixel layers will be made of hybrid 3D pixel sensors due to their superior radiation hardness and low power dissipation. At the time of replacement, other technologies such as MAPS may have improved radiation hardness and be a viable option that offers a number of advantages, depending on success of sensor research and development such as that of MALTA.

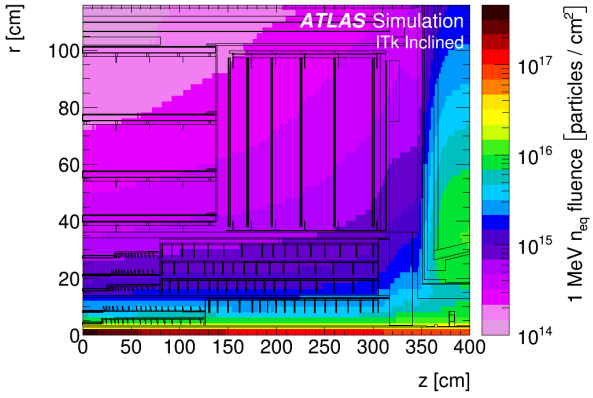

Figure 2.6: The NIEL displacement damage for the ATLAS inner tracker [11].

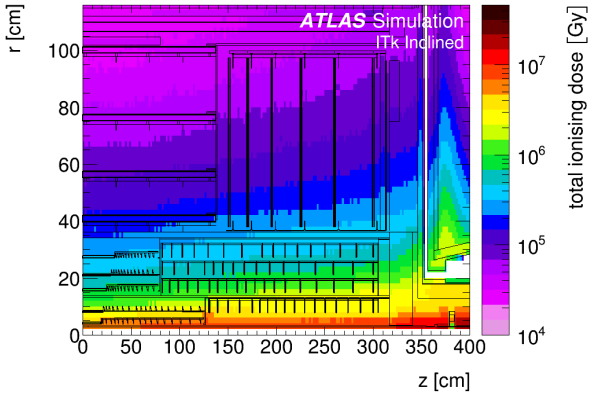

Figure 2.7: The total ionizing dose for the ATLAS inner tracker [11].

2.2 Proposed e^+e^- and hadron colliders

The next generation of of particle colliders will be likely to include an e^+e^- machine for precision measurements and later in the future a hadron collider that will reach a center-of-mass energy of ∼100 TeV. Historically, e^+e^- machines have been used to make precision measurements while hadron colliders have been used for discovery of new particles. With an e^+e^- collision, the two particles annihilate and all of the energy can be used for particle creation. A linear e^+e^- collider

avoids the issue of synchrotron radiation, and the center-of-mass energy is only limited by the gradient of the electric field and overall length of the linear accelerator. As a result, the center-of-mass energy of all collisions is well defined[2] and depends only on the machine operation. In hadronic collisions, the energies carried by the constituent parts of the stable hadron are not well defined, leading to large background rates of much lower energy interactions that can limit the precision of results. However, in hadronic collisions higher energies have been achieved since e^+e^- collision energies are limited by the higher synchrotron radiation due to their smaller masses. For the same size of ring and magnetic field, a much higher energy can be achieved with hadronic collisions. As an example, the Higgs boson was discovered in $\sqrt{s} = 13$ TeV proton-proton collisions at the LHC after a lower limit of 114 GeV was set on the Higgs mass based on analysis of e^+e^- collisions in the same tunnel in the Large Electron-Positron Collider (LEP) [13].

2.2.1 The ILC

One such proposed e^+e^- machine, which has been the subject of thorough development for nearly two decades, is the ILC, a linear collider approximately 31 km in length that will collide e^+e^- at center-of-mass energies between 91 and 1000 GeV. The ILC would be used to provide very high statistics on key processes of critical importance in challenging the detailed predictions of the Standard Model with unprecedented sensitivity. Of particular interest are specific high-precision studies of the Higgs boson which are not possible at the LHC due to the very large backgrounds [14].

A schematic of the ILC is shown in Fig 2.8. The electron source's design is based on a DC gun and feeds polarized electrons to linacs where they are accelerated to 5 GeV prior to entering the damping rings, where the beam is stored and released in precise bunches to maximize the luminosity of the experiment and ensure appropriate matching of bunch train length with the power transfer from the superconducting RF accelerating cavities. The 5 GeV electrons are used to generate positrons in the positron source, which are then accelerated to 5 GeV and

[2]In each event, there will be variation from nominal center-of-mass energy due to beamstrahlung losses [12].

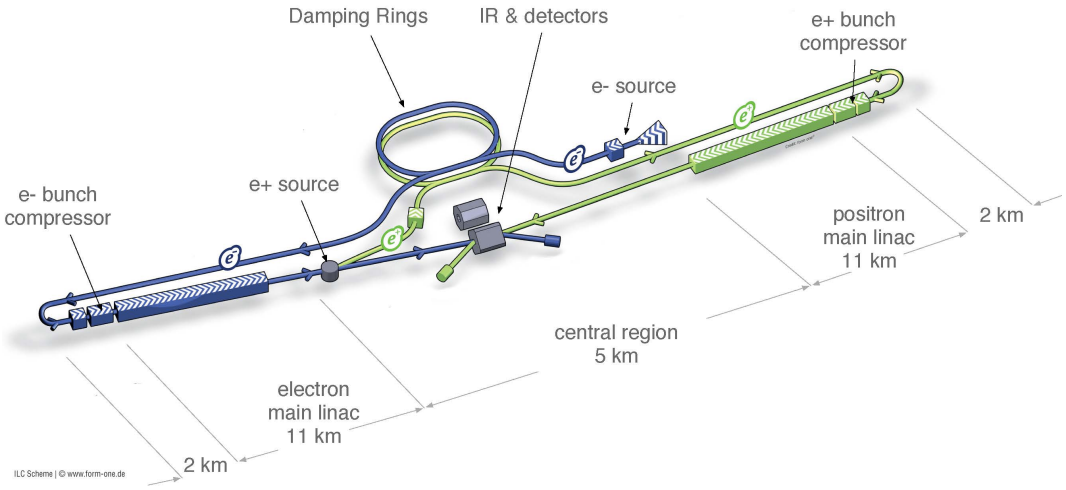

Figure 2.8: Schematic of the ILC accelerator complex [14].

also stored in the damping rings. From the damping rings, beams of positrons and electrons are accelerated in the main linac to the desired energy and made to collide at the interaction point and then dumped.

The detection system has a "push-pull" scheme such that two different detectors can be interchanged at the interaction point: the International Large Detector (ILD) and a largely silicon based version appropriately called the Silicon Detector (SiD), illustrated in Fig. 2.9. The key difference between the two is the choice of technology for the tracker: in the ILD, a time projection chamber is used with additional silicon detectors for vertexing and tracking (and ECAL). Going radially outward from the interaction point in the SiD, there is the all-silicon vertex detector and tracker with pixel and strip sensors, respectively, followed by the electromagnetic and hadronic calorimeters, all of which is contained in a solenoid with a 5 T magnetic field. Outside of this, muon detectors are interlaced in the return yoke for the solenoid. For the ECAL, a sampling calorimeter constructed from alternating layers of tungsten absorbers and silicon sensors, referred to as SiW technology, was selected and is the technology used in simulations in Chapter 8. In the forward direction are systems for beam and luminosity calibration, which will also use SiW technology.

The ILC detectors are designed such that the jet energy resolution, on which precision Higgs measurements can heavily depend, can be minimized through use of Particle Flow algorithms. Particle Flow associates tracks in the tracker to clusters in the calorimeters, allowing for the

measurements to be made with the most suitable detectors: the momenta of charged particles are measured in the tracker and the energy of neutral particles is measured in the calorimeters and the two are combined in the end. The challenge of a Particle Flow approach is identifying which hits in the calorimeter are from neutral particles and which are associated with charged tracks. Particle Flow techniques with the SiD have been shown to have superior jet energy resolution in simulation, and this approach is being considered for the circular hadron-hadron experiments and at other proposed e^+e^- experiments described in this chapter, such as CLIC [15].

2.2.2 CLIC

CLIC would be constructed near the LHC at European Organization for Nuclear Research (CERN) in three stages with increasing center of mass energy as shown in Fig. 2.10. The accelerator would reach energies of up to 3 TeV with a total length of approximately 48 km. CLIC began development after the ILC and as such has been able to apply many of the concepts and studies from the ILC. As shown in Fig. 2.11 of the cross-sections of various Higgs processes, at 3 TeV, the relative cross-section of ZH processes is less than at lower energies, allowing probing of other Higgs processes and searching for beyond-Standard-Model processes [18]. However, at 3 TeV the overall backgrounds will be considerably greater than at 1 TeV, and even more so than at the ILC due to a shorter duration between bunches in CLIC. While originally a push-pull scheme with both an ILD-like and SiD-like detector was considered, studies to optimize performance at 3 TeV found that a time-projection chamber was not favorable in the higher background environment, and that as a result the two CLIC detector concepts would be very similar. This, combined with the lost beam time from exchanging detectors, motivated the design of a single detector of intermediate dimensions, CLICdet [17]. The key parameters of the three CLIC detector designs are shown in Table 2.1. For the simulation work in Chapter 8, the CLICdet model was selected, though the work is general enough to be equally applicable to either any proposed e^+e^- or Future Circular Collider (hadron-hadron beams) (FCC-hh) [19] accelerator.

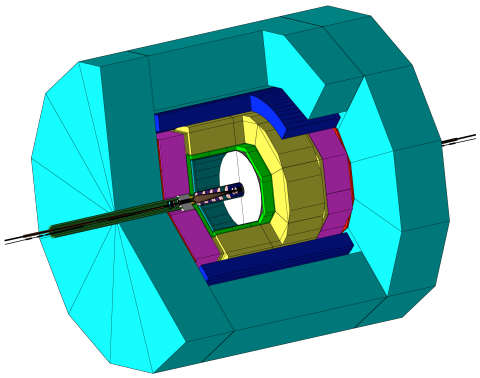

(a) Rendering of the ILD.

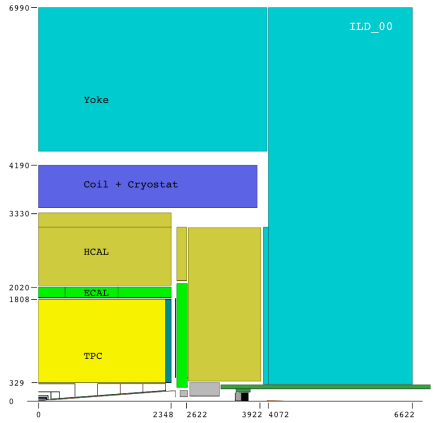

(b) A quadrant of the ILD.

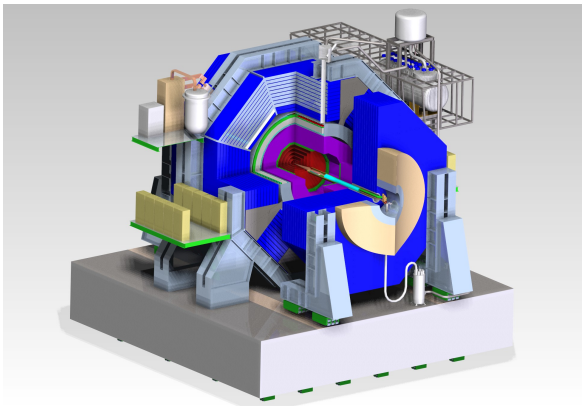

(c) Rendering of the SiD.

(d) A quadrant of the SiD.

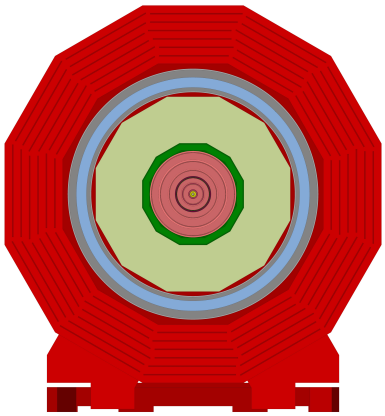

(e) Front view of CLICdet.

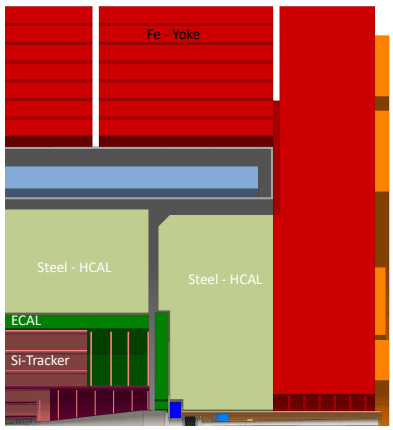

(f) A quadrant of CLICdet.

Figure 2.9: Proposed detectors at the ILC and CLIC [15–17]

In addition to linear colliders, under consideration are circular colliders that would run e^+e^- prior to the tunnel being used to house ∼100 TeV hadron-hadron collider: the Circular Electron Positron Collider (CEPC) in China and the Future Circular Collider (e^+e^- beams) (FCC-ee)

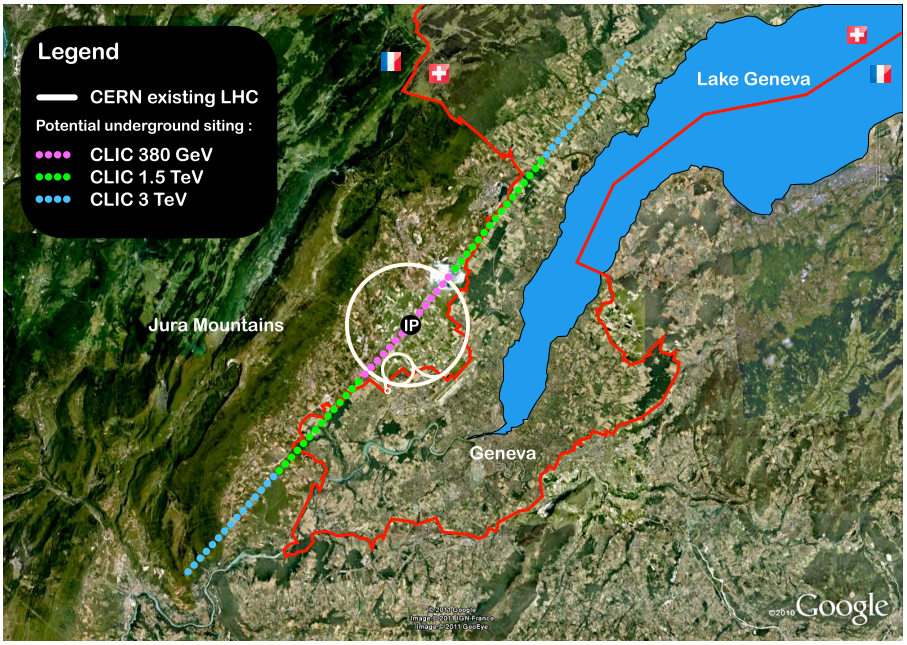

Figure 2.10: The proposed site for the various stages of CLIC [18].

Concept	CLICdet	CLIC_ILD	CLIC_SiD
Vertex inner radius [mm]	31	31	27
Tracker technology	Silicon	TPC/Silicon	Silicon
Tracker half length [m]	2.2	2.3	1.5
ECAL absorber	W	W	W
ECAL X_0	22	23	23
ECAL barrel r_{min} [m]	1.5	1.8	1.3
ECAL barrel δ_r [mm]	202	172	139
ECAL endcap z_{min} [m]	2.31	2.45	1.66
ECAL endcap δ_z [mm]	202	172	139
Overall height [m]	12.9	14.0	14.0
Overall length [m]	11.4	12.8	12.8
Overall weight [t]	8100	10800	12500

Table 2.1: Comparison of key parameters for proposed detectors at CLIC [17].

at CERN [19–21]. Either would be a massive undertaking and require the construction of the largest machine ever, a 50 to 100-km circumference circular collider, that would not be completed until well into the middle of the century. For e^+e^- circular colliders, the synchrotron radiation will limit the center-of-mass energies to several hundred GeV and call for a smaller detector than FCC-hh similar to the LEP experiments [22]. For the higher energy of the hadron-hadron collisions, a similar detector design to ATLAS or CMS could possibly work, assuming a number of significant R&D challenges can be addressed (not least in terms of radiation

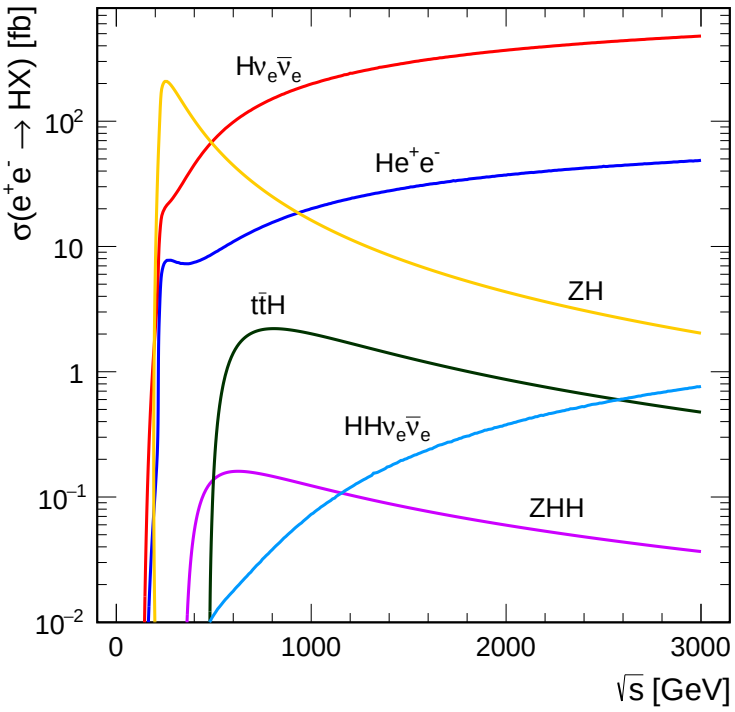

Figure 2.11: Cross sections of Higgs processes at CLIC as a function of center of mass energy. [18].

hardness). However, for the barrel calorimeter, due to the distance from the interaction point, the same SiW technology should be suitably radiation hard for 1 TeV e^+e^- and 100 TeV h-h. While there will be unprecedented challenges in terms of radiation hardness (requiring survival to doses a hundred times HL-LHC) for vertexing and tracking sensors near the interaction point, the focus of studies in this thesis has been on developing sensors for digital ECAL for such future experiments. The simulation studies and measurements of the DECAL sensor in Chapter 8 are relevant to the inclusion of a digital calorimeter constructed from devices similar to the DECAL prototype in these proposed physics experiments. For these studies the simulation framework of CLICdet was adopted for convenience and because of its relative sophistication and maturity.

Chapter 3

Particle tracking with silicon detectors

As described in Chapter 2, particle physics experiments make extensive use of silicon detectors for tracking of charged particles and they are also being explored for applications in calorimetry. In this chapter, the working principles of silicon detectors and their application in particle physics are described. There is special attention paid to the development of MAPS and the TowerJazz 180 nm process since this technology was used for both devices characterized for the work of this thesis, the MALTA and DECAL sensors. Also included are a brief discussion of radiation damage in silicon and a description of typical characterization measurements used for silicon sensors in particle physics.

3.1 Interaction of Particles with Matter

ATLAS and other experiments rely on the understanding of the interaction of incident particles passing through large bodies of matter, such as planes of silicon in the tracker. Photons interact through predominantly pair production at high energies (above a few MeV) and Compton scattering and the photoelectric effect at lower energies. Neutrons interact through the strong force and scatter or undergo nuclear interactions. Neutrinos have such small cross sections that their presence is usually inferred through missing energy. Electrically charged particles predominantly interact through ionization, Cherenkov radiation, bremsstrahlung, or transition radiation, with ionization by charged particles as the main mode by which signal is created in

silicon detectors.

3.1.1 Bethe Equation

For a heavy charged particle (with mass greater than that of an electron), as the particle passes through matter, it will interact with that matter through a series of single collisions, depositing energy with each interaction [23]. For thin absorbers used in tracking detectors, there are few interactions, and therefore significant variance in the total deposited energy. The Bethe equation estimates the mean rate of energy loss per unit length of a heavy charged particle

$$-\frac{dE}{dx} = Kz^2\frac{Z}{A}\frac{1}{\beta^2}\left[\frac{1}{2}\ln\frac{2m_ec^2\beta^2\gamma^2W_{max}}{I^2} - \beta^2 - \frac{\delta(\beta\gamma)}{2}\right] \tag{3.1}$$

where I is the mean excitation potential (characteristic of the material), z is the charge number of the incident particle, Z is the atomic number of the absorber, A is the atomic mass of the absorber, K is $4\pi N_A r_e m_e c^2/\alpha$ with r_e as the classical electron radius, α as the fine structure constant, and N_A is Avogadro's number [23]. The term $\delta(\beta\gamma)$ is the density correction and W_{max} is the maximum energy deposited in single interaction, calculated as:

$$W_{max} = \frac{2m_ec^2\beta^2\gamma^2}{1 + 2\gamma m_e/M + (m_e/M)^2} \tag{3.2}$$

The matter which the particle passes through is characterized by the mean excitation energy I which is determined from previous stopping power experiments.

Figure 3.1 shows the mean stopping power for muons on copper and labels regions of the plot, with the point of minimum ionization highlighted. Particles at this energy are known as minimum ionizing particles (MIPs). When characterizing sensors, it is important to test that a sensor has the sensitivity to detect MIPs since many relativistic particles at the LHC have mean energy loss rates close to their minima. The Bethe equation is accurate to a few percent in the region $0.1 < \beta\gamma < 1000$ for intermediate-Z materials.

For electrons, the stopping power is a less useful quantity than for heavy particles because the energy loss in any single collision can be very large, leading to a highly scattered path for

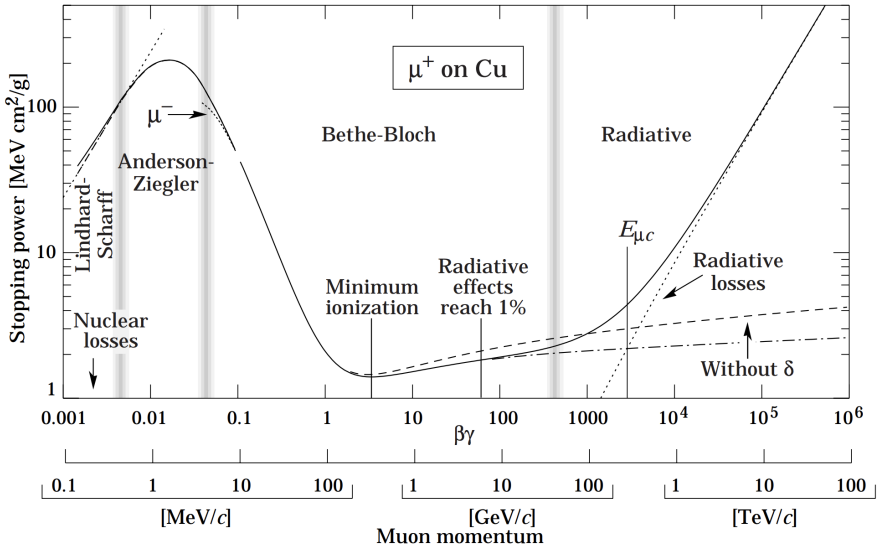

Figure 3.1: The stopping power as a function of $\beta\gamma$ as calculated by the Bethe equation plotted for muons on copper [23].

all but the highest energies. For electrons, W_{max} should be the kinetic energy of the electron, $m_e c^2(\gamma - 1)$, though due to the scattering being of electrons by electrons, the maximum energy transfer is actually $W_{max}/2 = m_e c^2(\gamma - 1)/2$ [23]. This value was used, along with the Bethe equation, to generate the plot in Fig. 3.2 of the stopping power of electrons, protons, and pions for silicon (the three charged particles used for sensor characterization in this thesis). The plot does not include the corrections for accuracy at higher energies that are in Fig. 3.1.

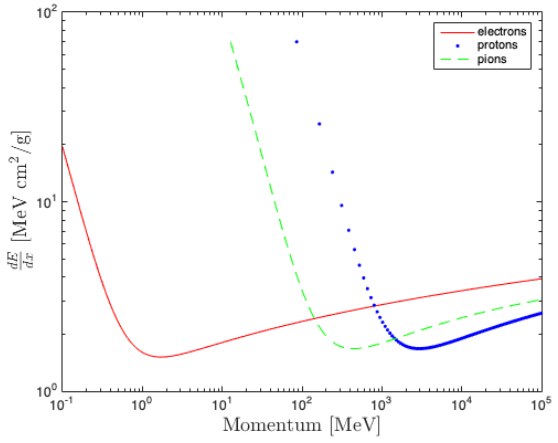

Figure 3.2: The stopping power as a function of momentum as calculated by the Bethe equation for electrons, protons, and pions on silicon. The plot does not include the corrections for accuracy at higher energies that are in Fig. 3.1.

While the Bethe equation describes the mean energy loss at a given incident particle energy,

the energy loss from a single particle's passage is distributed according to a skewed Landau distribution as shown in Fig. 3.3 from [23]. The most probable value of the stopping power dE/dx is typically used to characterize the distribution and the sensor. This most probable value is less than the mean energy loss, and depends on the absorber thickness: thinner layers of silicon will tend to have a lower most probable value of the stopping power than thicker ones have, as shown in the figure via the Landau distributions for sensors of various thickness.

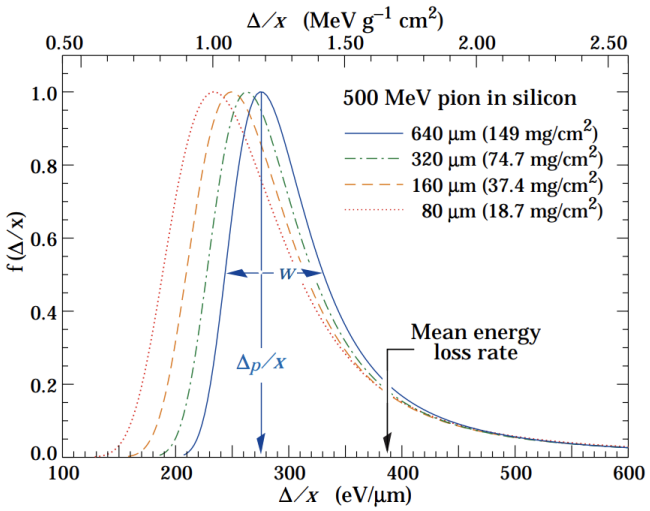

Figure 3.3: The stopping power Landau distributions for 500 MeV pions normalized to unity for the most probable value. The width w is the full width at half the maximum [23].

3.1.2 Photon and electron interactions in matter

The cross-sections for the various processes for photon interaction with matter are shown in Fig. 3.4 for carbon and lead. The photoelectric effect, which dominates at low energies, is characterized by the absorption edges for photoionization of atomic energy levels. In particular, the rest mass of the electron and positron is 511 keV, so photons with energies below 1.022 MeV cannot undergo pair production. Depending on the material, Compton scattering becomes the dominant effect for photons near 1 MeV.

For high-energy photons and electrons, pair production and bremsstrahlung are dominant processes for energy loss in matter, with the dominance of bremsstrahlung over ionization beginning at around 10 MeV in lead and 40 MeV in silicon (as shown in Fig. 3.6 and 3.7, described in detail ahead). The probability that a photon or electron will interact after traveling

a given distance in a medium is characterized by the radiation length of the medium, X_0. It is both the average distance over which an electron loses all but $1/e$ of its energy to bremsstralhung and $\frac{7}{9}$ of the mean free path for pair production by a high energy photon, λ [23].

In Fig. 3.5, the photon absorption length λ is plotted as a function of the photon energy for various materials. The intensity I remaining after traversal of thickness t (in mass/unit area) is given by

$$I = I_0 e^{-t/\lambda} \tag{3.3}$$

Low energy photons may not penetrate past the silicon oxide in a sensor and avoid detection, and high energy photons are unlikely to interact with the silicon at all. X-rays can be useful for characterization since at the energies near that of a MIP in a thin sensing layer (O(keV) to O(10keV)) the mean absorption length (O(10μm) to O(100μm)) results in a reasonable acquisition rate, as can been estimated from Fig. 3.5.

For electrons and positrons, bremsstrahlung dominates at high energies, as shown in Fig. 3.6 of the fractional energy loss of electrons or positrons in lead as a function of their energy. At lower energies, most of the electron energy is lost to ionization. The critical energy E_C of a material is the energy below which ioniziation dominates. The critical energy for various materials as a function of their atomic number is plotted in Fig. 3.7. There are several useful definitions for E_C, for this plot it is the energy at which the ionization loss per radiation length is equal to the electron energy (that is, when the ionization curve is above 1 in Fig. 3.6).

Given these cross sections for photons and electrons and positrons, a high energy (above a few MeV and E_C) photon or electron/positron incident on a thick absorber will produce a shower of electrons, positrons, and photons through subsequent pair production and bremsstrahlung. As more interactions occur the energy of the particles will decrease until they reach a critical energy E_C below which ionization dominates and a particle is absorbed by the medium. Eventually, (if the medium is deep enough) the total number of particles falls to zero. The mean number of particles N generated in a shower is proportional to E, the energy of the incident particle. The shower evolution is governed by Poisson statistics so the variance of the mean N is also N and the standard deviation of the mean is $1/\sqrt{N}$. Hence, the energy of a shower can be estimated

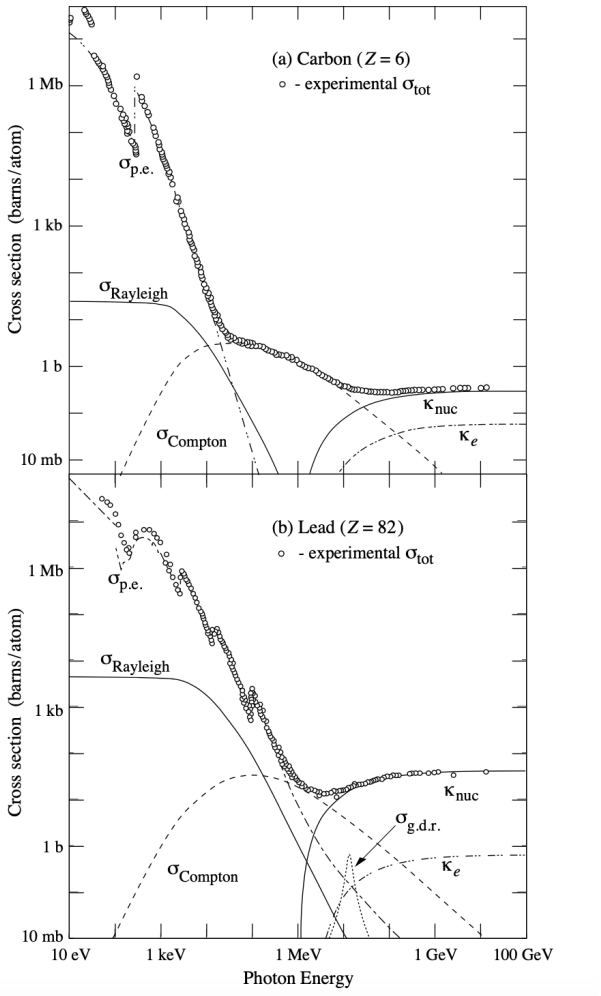

Figure 3.4: Photon total cross sections as a function of energy in carbon and lead, showing the contributions of different processes from [23].

from the number of particles, and this is the underlying concept of digital electromagnetic calorimetry, the subject of Chapter 8.

The profile of the shower can be estimated as a gamma distribution:

$$\frac{dE}{dt} = E_0 b \frac{(bt)^{a-1} e^{-bt}}{\Gamma(a)} \tag{3.4}$$

where E_0 is the initial energy of the incident particle, $t = X/X_0$ is the number of radiation lengths traversed, and a and b are properties of the material [23]. The depth at which the

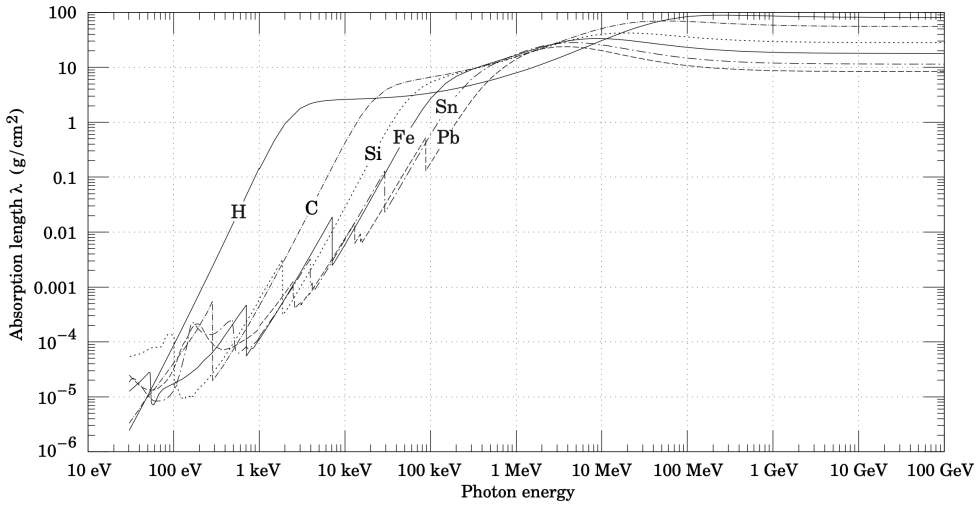

Figure 3.5: The photon mass attenuation length (or mean free path) λ for various elemental absorbers as a function of photon energy, from [23].

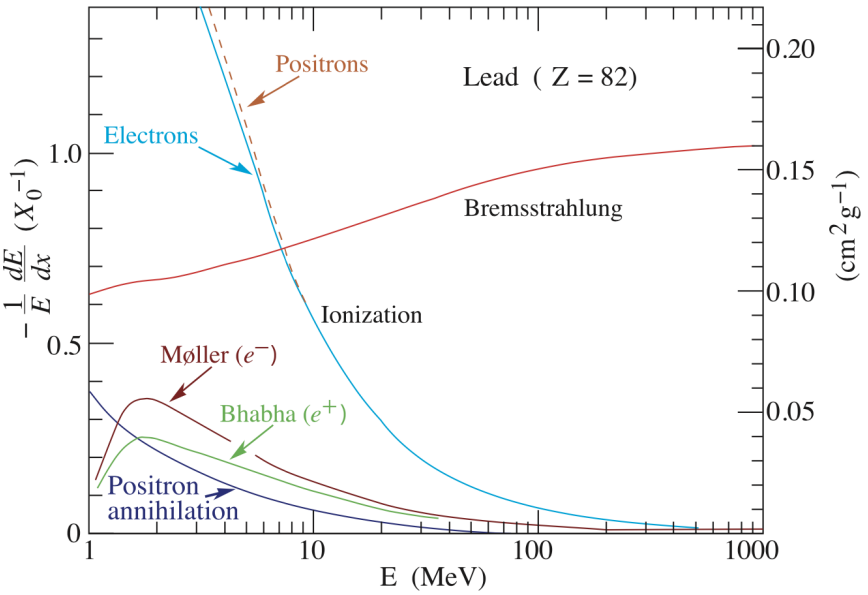

Figure 3.6: Fractional energies loss for electrons and positrons in lead.

number of particles is maximized, known as the shower max, is

$$t_{max} = \frac{a-1}{b} = \ln y + C \tag{3.5}$$

where $y = \frac{E_0}{E_C}$.

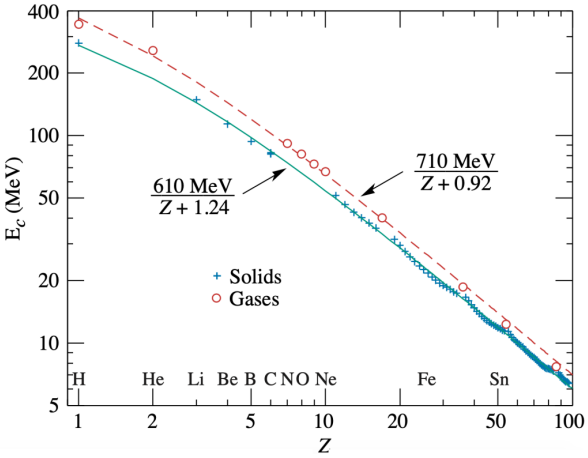

Figure 3.7: Electron critical energy for the chemical elements, with critical energy defined as the energy at which the ionization loss per radiation length is equal to the electron energy. The fits shown are for solids and liquids (solid line) and gases (dashed line). The rms deviation is 2.2% for the solids and 4.0% for the gases [23].

Coloumb Scattering

As a charged particle passes through matter, it is deflected in a series of small-angle scatters, mostly due to Coulomb scattering. The distribution of angular deflections can be modeled as Gaussian with an RMS width of [23]

$$\theta_0 = \frac{13.6 \text{ MeV}}{\beta cp}\sqrt{\frac{x}{X_0}}\left[1 + 0.038 \ln(\frac{xz^2}{X_0\beta^2})\right] \tag{3.6}$$

In tracking applications, it is usually desirable to minimize the radiation length of sensors and thereby the effect on the tracked particle and uncertainty in reconstructed tracks. The accuracy of the reconstructed momentum depends on measuring the curvature of the track of charged particles in a magnetic field and will be better with less multiple scattering. The impact parameter resolution depends on the multiple scattering in the first layers of the detector. The resolution of lower energy particles is affected even more, and for their reconstruction, minimizing multiple scattering is especially important.

3.2 Silicon Detectors

Silicon sensors have long been a cornerstone of particle detection in physics experiments, first developed as planar pad and strip sensors in the 1980s and then as pixel detectors for LEP and the innermost detection layers at the LHC [24, 25]. The ATLAS Inner Detector contains thousands of silicon sensors with millions of signal channels, and the continued use of silicon is proposed in future upgrades and will have even larger sensors areas with more channels.

Silicon is a semiconductor material that converts the ionizing energy deposited by an incident particle into mobile charge carriers, that is, electrons and holes. In the presence of an external field, for example, due to biased electrodes on either side of a silicon chip, these charges will drift and can be collected and the induced current on electrodes can be read out as signal, making silicon an effective detector. In the absence of an applied field, charges will move due to diffusion and can still be collected. However, the charge collection by diffusion is much slower and so is not as well suited for particle physics applications where the charge must be collected quickly. Devices with diffusion are also more susceptible to radiation damage since the collection time and carrier lifetime become comparable as the detector becomes more damaged. Silicon diodes formed from p-n junctions are operated in reverse bias to expand the region in which there is an electric field, and thereby increase the signal current. The p-n junction and the working principles are discussed in more detail in the sections below.

There are a number of advantages to silicon that have led to its wide use in high energy physics. It is widely available as one of the most abundant elements on earth. The number of charge carriers generated is proportional to the energy deposited (on average, 3.6 eV per electron-hole pair created). Silicon can be manufactured with structures having nanometer-level precision, though for particle physics sensors, a spatial resolution on the order of microns is sufficient. Silicon chips are developed for many other applications in industry by multi-billion pound foundries, meaning that there is a breadth of technologies such as CMOS that are potentially applicable to particle physics which can be produced affordably in large numbers relatively quickly (that is, with high throughput) from an array of potential manufacturers. The

structural rigidity of silicon, good energy and spatial resolution, and the availability of advanced silicon technologies due to its popularity in industry and natural abundance on earth have made it a natural choice for tracking applications.

3.2.1 The p-n Junction

A p-n junction is a junction between silicon doped with group-III elements such as boron (p-type silicon) and silicon doped with group-V elements such as phosphorous (n-type silicon) as shown in the schematic in Fig. 3.8. Due to the concentration gradient, electrons diffuse from the n-doped region to the p-doped, and holes from p-doped to n-doped. When crossing the junction the charge carriers recombine, leaving a space charge on the two sides: positive on the n-doped side (due to group-V dopant atoms that have lost an electron), and negative on the p-doped side (due to group-III atoms that have lost a hole). This space charge region depleted of charge carriers is called the depletion region. The space charges result in an electric field in the depletion region and a potential difference across it called the built-in voltage.

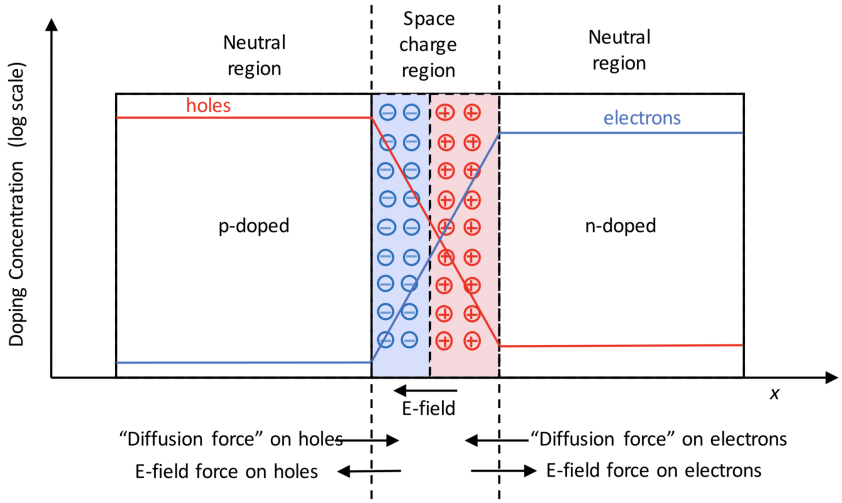

Figure 3.8: Schematic of the doping and resulting electric field of an unbiased p-n junction [26].

The application of an external field in the same direction as the built-in voltage, known as reverse biasing, results in the depletion region becoming wider. In particle physics applications, the reverse bias voltage is typically much greater than the built-in voltage, and so the built-in

voltage is neglected. The Poisson equation (in one dimension) can be used to estimate the relationship between the width of the depletion region and the bias voltage:

$$\frac{\partial^2\phi}{\partial x^2} = -\frac{\rho(x)}{\epsilon} = -\frac{Ne}{\epsilon} \tag{3.7}$$

where ρ is the charge density and N is the doping concentration. Then in the n-type region, the potential is

$$\phi_n = -\frac{N_D e x_n^2}{2\epsilon} \tag{3.8}$$

and for the p-type region

$$\phi_p = \frac{N_A e x_p^2}{2\epsilon} \tag{3.9}$$

where N_A is the concentration of acceptors (p-type dopants), N_D is the concentration of donors (n-type dopants), and x_n and x_p are the distances from the junction. The zero of potential is defined such that $\phi(x = 0) = 0$. Using the equilibrium condition that no charge carriers have been added to the silicon, only exchanged between the doped regions

$$N_D x_n = N_A x_p \tag{3.10}$$

Then for $x_n = X_n$, the depth of the n-type depletion region, (and $x_p = X_p$, for the p-type depletion region), the voltage drop across the depleted region can be written as

$$\phi_p - \phi_n = V = \frac{e}{2\epsilon}(X_n^2 N_D + X_p^2 N_A) = \frac{e N_D X_n^2}{2\epsilon}\left(1 + \frac{N_D}{N_A}\right) = \frac{e N_A X_p^2}{2\epsilon}\left(1 + \frac{N_A}{N_D}\right) \tag{3.11}$$

On each side of the junction, the depletion width is:

$$X_p = \sqrt{\frac{2V\epsilon}{eN_A(1 + N_A/N_D)}} \tag{3.12}$$

and

$$X_n = \sqrt{\frac{2V\epsilon}{eN_D(1 + N_D/N_A)}} \tag{3.13}$$

To get the full width, w the two depths are summed:

$$w = X_p + X_n \tag{3.14}$$

In the case where one doping concentration is significantly greater, it can be approximated that the depletion region extends only into the other region with lower doping concentration. Let it be assumed that $N_D >> N_A$. Then,

$$w \approx X_p \approx \sqrt{\frac{2V\epsilon}{eN_A}} \tag{3.15}$$

If the resistivity, $\rho = 1/(Ne\mu)$, with carrier mobility μ, is substituted, then

$$w = \sqrt{2\epsilon\mu\rho V_{bias}} \tag{3.16}$$

and we derive a simple approximation for the depletion voltage of a detector given its depth, D

$$V_{full\ depletion} = \frac{D^2}{2\epsilon\mu\rho} \tag{3.17}$$

The full depletion voltage is an important characteristic of a detector; if a detector is run below full depletion the signal will be smaller than at full depletion. Equation 3.17 implies that in order to have a reasonably low depletion voltage, the resistivity ρ must be sufficiently high, which requires low impurity concentrations.

The detector capacitance also depends on the width of the depletion region and is small for large resistivity values. Assuming a planar geometry for the junction [27]

$$C = \frac{dQ}{dV} = \frac{A\ dQ}{\frac{dQ}{\epsilon}w} = \frac{A\epsilon}{w} = A\sqrt{\frac{\epsilon}{2V_{bias}\mu\rho}} \tag{3.18}$$

With Equation 3.18, from a measurement of a sensor's CV curve (Sec. 3.3.3) the doping concentration can be inferred.

In contrast, in forward biasing the polarity of the voltage source is the opposite and the

depletion region shrinks, there are more free charge carriers, and the resulting current is much greater. In the undepleted silicon, there is no field so charges will diffuse, increasing the time for charges to move towards the electrodes. For particle detection, silicon sensors are operated with reverse bias in order to have a large depletion region and thereby increased collected charge and a faster signal collected by drift instead of diffusion.

3.2.2 Signal Formation

Charge carriers in the presence of an electric field, such as electrons and holes in the depletion region, drift along the field lines [28]. The drift velocity can be modeled as the product of the electric field and carrier mobility

$$v = \mu E \tag{3.19}$$

The electrons are approximately three times more mobile than holes: for electrons $\mu = 1350$ cm^2/Vs , while for holes $\mu = 450$ cm^2/Vs.

The Shockley-Ramo theorem describes the current induced by a mobile charge carrier with charge q on an electrode

$$i = -q\vec{E}_{weight} \cdot \vec{v} \tag{3.20}$$

where E_{weight} is the weighting field, that is the electric field calculated by setting the collection electrode to one volt and all others to ground. For configurations with only two electrodes, the form of the weighting field and electric field will be the same. A sensor may be operated above depletion (be "over depleted") to increase the field strength and carrier drift velocity to improve the characteristics of the signal. The final amplitude of the voltage signal depends only on the total collected charge Q and the sensor capacitance, C:

$$V_{in} = Q/C \tag{3.21}$$

The collected charge, Q is proportionate to the energy deposited in the sensor by ionizing radiation: an electron-hole pair is formed for every 3.6 eV of deposited energy. To achieve a

large signal amplitude, the capacitance should be minimized, however, the time constants of the sensor capacitance, collection time, and amplifier have to be well-matched, and the trade-offs of thinner (higher C) sensors must also be considered. That being said, in general low capacitance designs are attractive for the high voltage signal and low noise, as discussed in Sec. 3.2.4

3.2.3 Leakage Current, Temperature Dependence

Leakage current is the current in a device that arises from charge carriers becoming thermally excited and slipping into mid-gap states and then into the conduction band (or excited from valence to conduction band through a two step process via mid-bandgap states). The leakage current of a device should go linearly with the depletion depth, that is, as $\sqrt{V_{ext}}$, until depletion is reached. The current remains relatively constant or increases gradually with voltage until breakdown is reached and the current increases greatly. Above this breakdown voltage sensors cannot be operated as effective detectors, making the measurement of the IV curves (Sec. 3.3.3) important for sensor characterization.

The current depends on the temperature as [28]:

$$I_{leakage} \propto T^2 \times e^{\frac{-E_g}{2Tk_B}} = T^2 \times e^{\frac{-0.62}{Tk_B}} \tag{3.22}$$

where E_g is the bandgap energy for silicon, 1.12 eV. This temperature dependence leads to the possibility for thermal runaway since increasing temperature leads to increasing current and vice versa. A high leakage will contribute to shot noise and could even make discerning a signal from an incident particle difficult, and sensors are often cooled during operation to limit their current, including in ATLAS where they are cooled to -30°C for operation after radiation damage.

3.2.4 Electronic Noise

The equivalent noise charge (ENC) in a silicon detector system can be modeled as the sum of three components [28]

$$Q_{noise} = i_n^2 F_i T_s + e_n^2 F_v \frac{C^2}{T_S} + F_{vf} A_f C^2 \tag{3.23}$$

The shot noise is

$$i_d^2 = 2eI_{leakage} \tag{3.24}$$

and the $1/f$ noise is modeled as

$$e_n^2 = A_f/f \tag{3.25}$$

where A_f is a device-specific noise coefficient and f is the frequency. The last term $F_{vf}A_fC^2$, is for the noise of the capacative load. T_S is the shaping time for the output signal, often determined by the integration time of the first amplifier stage. F_i, F_v, F_{vf} are shape factors calculated as:

$$F_i = \frac{1}{2T_S}\int_{-\infty}^{\infty}[W(t)]^2 dt, \qquad F_v = \frac{T_S}{2}\int_{-\infty}^{\infty}\left[\frac{dW(t)}{dt}\right]^2 dt \tag{3.26}$$

for the output waveform $W(t)$. Given Equation 3.23, detector capacitance must be kept low to avoid significant noise. The detector capacitance depends on the depth of the detector d and the area of the collection electrode A as $C = \frac{A\epsilon}{d}$, though these parameters must be balanced in the detector's design since a large electrode provides a uniform electric field and shallow depth allows for fast detection time, among other trade-offs. In strip detectors, the capacitance between strips actually dominates, and $C = \frac{A\epsilon}{d}$ is not a valid approximation.

3.2.5 Radiation Damage in Silicon

Silicon sensors are exposed to high levels of radiation that degrade sensor performance over time. One of the key and oft-limiting design requirements for any detector intended for use in an experiment is that it be sufficiently radiation hard. There are two types of radiation damage that affect silicon detectors: displacement damage, also known as bulk damage, due to

non-ionizing radiation, and surface damage due to ionizing radiation.

Displacement Damage

Bulk or displacement damage to silicon detectors comes from NIEL (non-ionizing energy loss), as opposed to ionizing energy loss used for detection. Atoms in the silicon interact with incident radiation and become displaced from their original positions and form Frenkel pairs of vacancies and interstitials. Defects migrate through the lattice and when combined with other impurity atoms form defect clusters [29]. Some of these defect clusters are electrically active and so act as mid-band-gap states between the valence and conduction bands. States near the middle of the gap facilitate the transfer of electrons from the valence to conduction band, increasing the leakage current. In diodes, the basis for detectors, the change in leakage current is modeled as

$$\delta I = \phi * \alpha * V \tag{3.27}$$

where ϕ is the fluence in $n_{\text{eq}}/\text{cm}^2$ and V is the volume of the active region in the detector [28]. The parameter α has been measured experimentally to be 4×10^{-17} for 1 MeV neutrons and $\alpha \approx 3 \times 10^{-17}$ for 650 MeV protons in [30–32].

Defect levels can trap free charge carriers from the conduction band and decrease the signal in a detector if the trapping time is comparable to the signal collection time. Defects can also lead to a change in the effective space charge and thereby the depletion voltage. The depletion voltage and effective doping concentrations of a 300 μm sensor are plotted as a function of fluence in Fig. 3.9. The increase in depletion voltage means the operation voltage of a detector is higher and combined with the increased leakage current I_d, there can be significantly more power consumption and/or relative noise in an irradiated sensor. Along with trapping, the increased leakage current and the decreased depletion depth can lead to a small signal and higher noise. In order to decrease the leakage current, and allow for higher bias voltages and more depletion, irradiated sensors are generally cooled to near -30 °C.

If the damage is great enough, the density of acceptor-like defects can be greater than the

donor density in n-type silicon (partially due to donor removal) , resulting in a negative effective space charge when depleted. This is known as "type inversion" and shown by labeled point in the plot in Fig. 3.9. Though there are still donor states present, the acceptor-like space charge of the defects dominates. This is not observed in high-resisitivity p-type silicon, which already has a negative space charge prior to the corresponding inversion fluence.

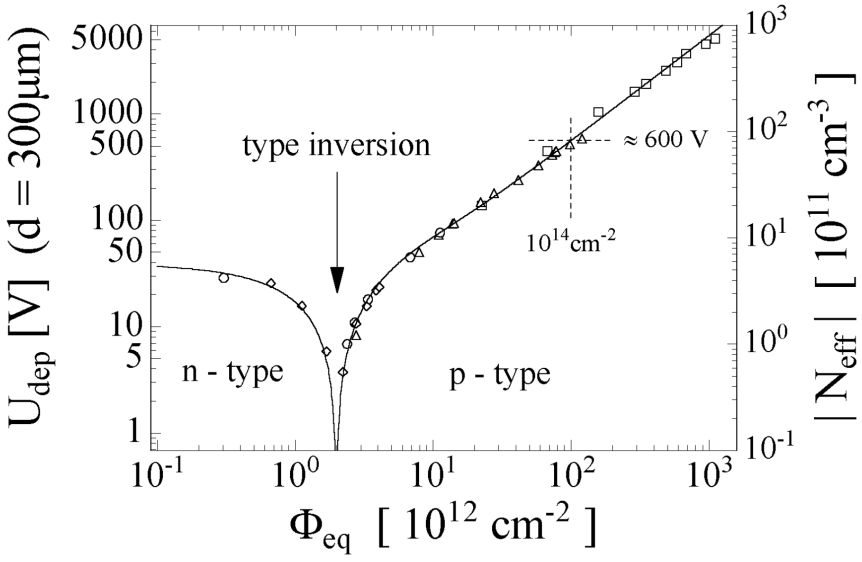

Figure 3.9: The depletion voltage as a function of fluence for a 300 μm sensor [33].

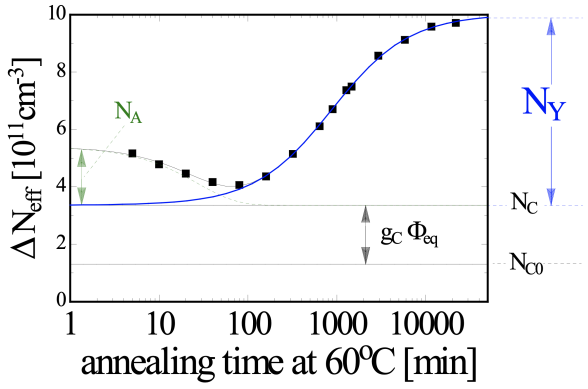

Figure 3.10: The effective doping concentration as a function of the annealing time. The data shown here were taken at room temperature while the annealing took place at 60 °C [34].

The effective doping concentration changes with time for irradiated sensors due to what is called annealing and can be slowed by cooling or sped up by warming the sensor. As shown in Fig. 3.10 of the effective doping concentration as a function of the annealing time at 60 °C, detectors can be annealed to reduce the change in effective doping concentration, though anti-

annealing effects limit this technique, that is, after too much annealing the change in doping concentration begins to increase. The working prescription for annealing detectors is 80 minutes at 60 °C [35], to allow easy comparison between sensors with differing initial annealing histories, and this was the procedure used in annealing sensors for this thesis. The leakage current also depends on the duration and temperature of annealing, as shown in Fig. 3.11, where the α parameter for various anneal times and temperatures is plotted.

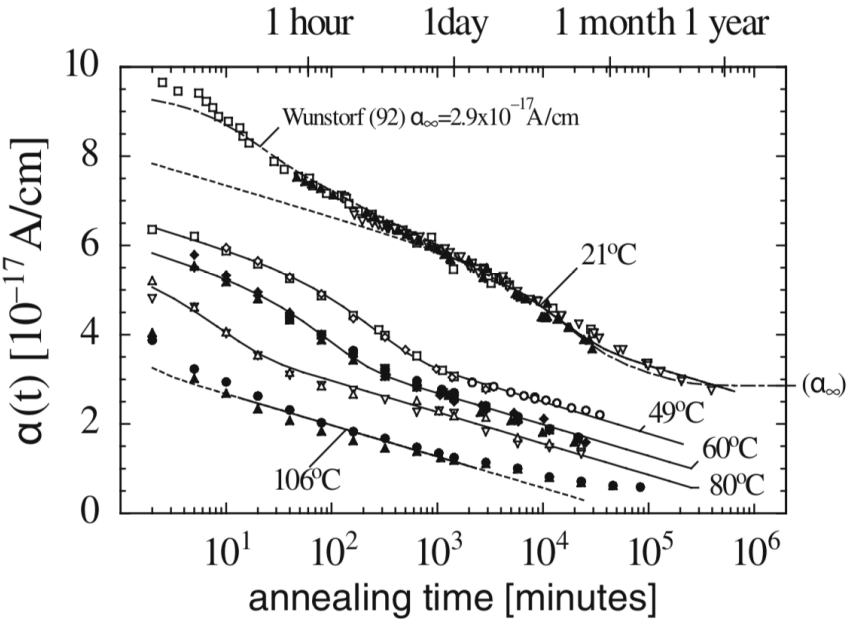

Figure 3.11: The α parameter for the change in leakage current as a function of time for different annealing temperatures [32].

Ionization (Surface) Damage

Ionizing radiation results in the creation of free charge carriers in the silicon. In depleted silicon, the charges will drift to the electrodes due to the electric field, and in these "bulk" regions ionizing radiation does not cause damage. However, in layers with no or very little field, such as the oxide on the surface of detectors, the charges will tend to build from ionization. Due to the greater mobility of electrons, they are generally collected, but holes are trapped leading to a fixed charge build-up and resulting in an electric field that can affect the flow of charges and thereby performance of a detector. The space charge can create an inversion layer in the silicon

that allows conduction between strips or pixels or other structures in a sensor. The interstrip resistance measurements discussed in Section 4.5 were done based on suspicions of the impact of ionization damage.

The space charge can also affect the operation of metal-oxide-semiconductor (MOS) transistors, the building blocks of the electronics in complementary metal-oxide-semiconductor (CMOS) sensors and readout chips. The ionizing damage can lead to changes in the threshold voltage (for setting a transistor on or off), potentially making a sensor inoperable. However, to an extent, the negative effects of ionizing radiation, such as an increase in the current in the digital electronics, have been found to be self-mitigating as the oxide charge build up saturates.

Measuring Damage

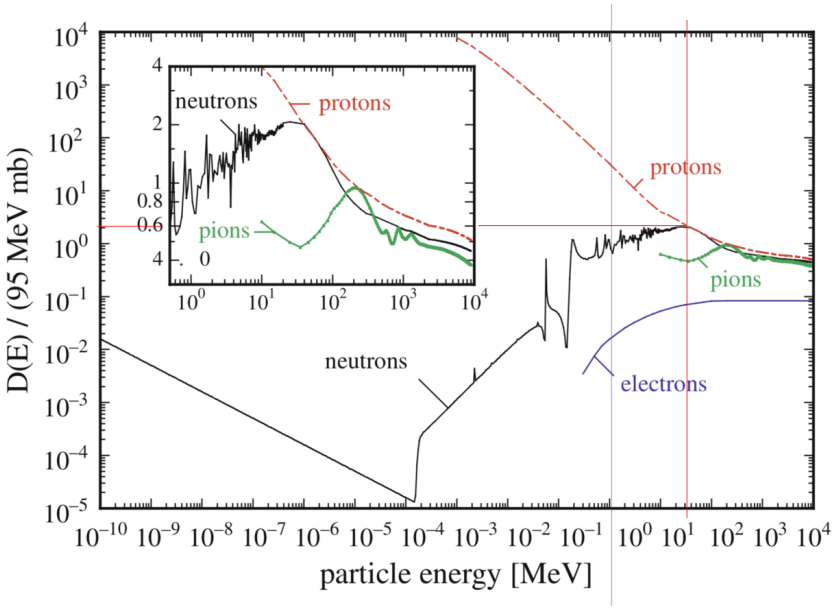

Figure 3.12: The NIEL displacement damage for various particles and energies. The insert shows the energies relevant for high energy particle physics [32]. The red lines illustrate the expected damage factor of 2 to 3 for 23 MeV protons which were used for irradiation.

For bulk damage, the amount of damage depends on NIEL which depends on the energy and type of the particle used for irradiation. For example, X-rays cause entirely ionizing damage, neutrons mostly non-ionizing, and protons significant amounts of both. For bulk damage, the damage is quantified relative to the damage done by 1 MeV neutrons. The

1 MeV neutron equivalent fluence is the fluence of 1 MeV neutrons that produces the same damage as the particles used for a given irradiation and it is typically expressed in units of 1 MeV neutron equivalent fluence per square centimeter and written as $n_{\mathrm{eq}}/\mathrm{cm}^2$. The calculated relative damage for various particles is shown in Fig. 3.12. The 23 to 28 MeV protons used in irradiations for this thesis should do 2 to 3 times the damage of 1 MeV neutrons, as can be seen with solid the red lines in the figure. For ionizing radiation, the damage depends primarily on the total ionizing energy absorbed.

3.3 Tracking sensors in high energy particle physics

3.3.1 Passive Strip and Pixel Detectors

Silicon strip and pixel detectors are planar detectors patterned with strips of implants at regular intervals, usually on the order of tens of microns. Each strip has an electrode to read out the signal, thus giving position information for the interaction. Power and readout electronics are provided for passive sensors, typically via one or more PCBs and direct bump or wire bonding to a readout chip. For pixel sensors, this "hybridization" process can be especially challenging due to the high number and spatial density of channels.

Passive silicon sensors do not contain readout electronics such as amplification and discrimination that are built into active silicon sensors. Passive sensors have been used extensively in particle physics experiments, including in the current ATLAS Inner Detector and other LHC experiments. For the ITk, the inner and outer layers will be constructed from hybrid pixel and strip sensors, respectively, though CMOS pixel sensors were originally considered for some of the inner layers and may still be used as a replacement in the future.

3.3.1.1 ITk Strip Modules

The ITk strip detector consists of arrays of strip sensors arranged in four concentric cylinders in the barrel region and six parallel discs in each endcap region. The main mechanical components are 'stave' and 'petal' mechanical supports for the barrel and endcap regions, respectively. Each

endcap disc is covered by 32 petals, and the number of staves increases further from the beam. On these supports strip sensor modules are placed and supplied with local services such as cooling and power. To more precisely determine the track positions, two strip detectors are placed back-to-back on either side of the central support with a small angle (26 millirad) between.

A strip module consists of a sensor coupled to one or more low-mass PCBs called "hybrids" hosting readout electronics. In the barrel, for regions close to the beam (L0-L1), the occupancy will be higher and it is advantageous to use shorter strips in these regions. Hence, there are two designs of modules: Short Strip and Long Strip. In Fig. 3.13(a) is the design concept for one of the Short Strip modules, and a fully assembled module is in Fig. 3.13(b). The Long Strip modules have the same components, but have longer strips and correspondingly fewer readout channels.

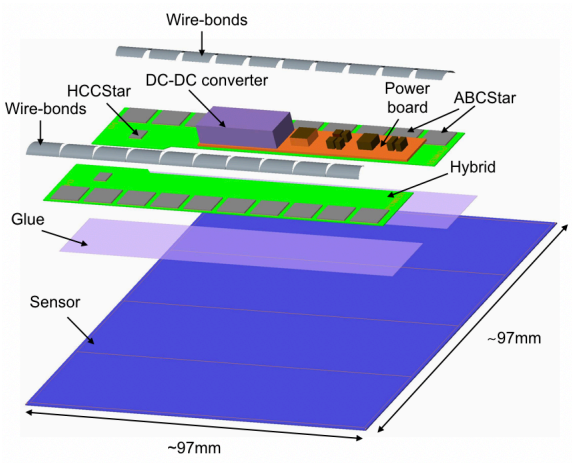

(a) Schematic of the Short Strip modules for the ITk [11].

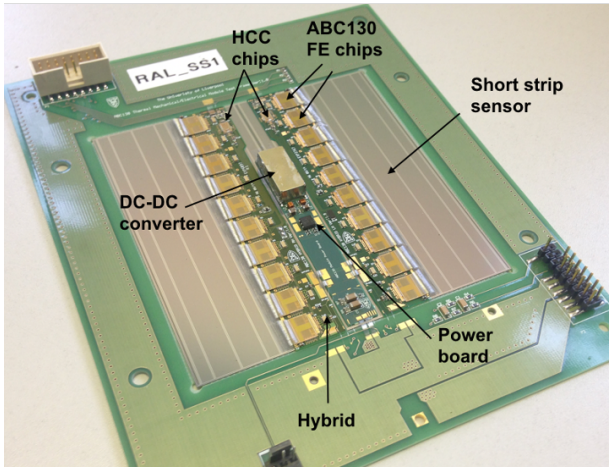

(b) A fully assembled Short Strip module [11].

Figure 3.13: Strip modules for the ITk.

To ensure that sensors meet the radiation requirements of the ITk (previously shown in Fig. 2.6 and 2.7), prototypes must be characterized, as was done in the irradiation and characterization of passive strips sensors described in Chapter 4.

3.3.1.2 ITk Pixel Modules

Pixel modules are the basic mechanical and electrical unit of the ITk Pixel Detector. A module, a schematic of which is shown in Fig. 3.14, is composed of one or more passive pixel sensors each bump bonded to a readout chip (forming a "bare module") and then glued and wire bonded to a flexible PCB (called a "PCB module flex") which provides power, means for data transfer, and other services such as cooling. Fig 3.14 shows a picture of a pixel module from the PCB side. There are three types of pixel modules for the ITk: single modules with one sensor and a 2×2 cm^2 area for the inclined region of the inner barrel layer, dual modules with two sensors and 2×4 cm^2 area for the innermost layer and inclined barrel, and quad modules with four sensors and 4×4 cm^2 area, to be used in the outer flat barrel and outer end-cap rings.

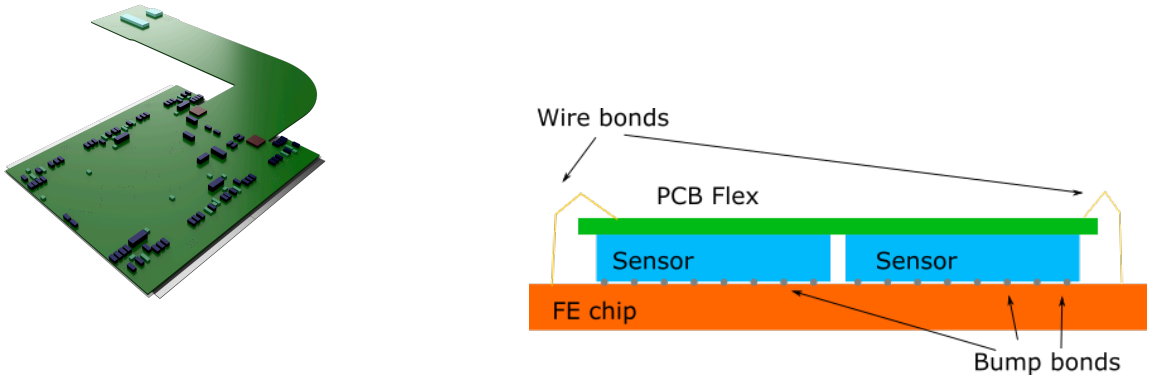

(a) An ITk pixel quad module from the PCB side.

(b) Schematic of a hybrid pixel module with the flex, sensor, and readout chip bonded.

Figure 3.14: Hybrid pixel sensors for the ITk.

The bump-bonding or "hybridization" of the sensor and front-end chips is a time-consuming process and the most expensive portion of the pixel module construction. The process can be divided into four steps: bump deposition on the readout wafer, sensor wafer processing, wafer thinning and dicing, and face-to-face bonding of the readout chip and sensor, known as "flip-chip" bonding. Each step involves qualifying vendors and quality control by the ITk team and the assembled module must undergo additional testing to ensure that only a small portion of the bump bonds will fail due over the lifetime of the module. While similar methods were used

in the construction of the Inner Barrel Layer which is currently the innermost portion of the ID, the ITk Pixel detector presents a greater technological challenge due to an increased bump density, number of bumps per chip, and wafer size. Another significant challenge is the scale of production since the area covered by silicon sensors the for the ATLAS ITk Pixel Detector is much larger (13 m^2) than for the current ATLAS pixel sub-detector (1.9 m^2) [36].

The CMOS monolithic active sensors discussed in this thesis address the challenges related to a large-area detector and hybridization since they do not require this bump bonding phase and the actual sensor production can take advantage of processes and vendors scaled and refined for the commercial sector to produce large numbers of sensors in a short amount of time. For this reason and others, discussed in greater detail in section 3.3.2, sensors in CMOS technology were considered as a option for the ITk in place of hybrid modules in the Barrel 4 region, and may still potentially be included in Runs 4 and 5.

In order for either CMOS or hybrid modules to be included in the ITk, in addition to radiation tolerance, there are several other key requirements for pixel sensors. The requirements for Layer 4 of the barrel are tabulated in Table 3.1. The time resolution and thereby rise time, effectively the collection time for a sensor, must be less than 25 ns due to the 40 MHz bunch crossing frequency of the LHC. The power consumption needs to be limited in order to limit the mass of the necessary cooling structures and material in the detector which increases multiple scattering and reduces the accuracy of reconstruction. The development and characterization of CMOS pixel sensors for the ITk Pixel Detector discussed further in Chapters 5, 6, and 7 is in light of these requirements.

ATLAS ITk Pixel Requirements	
Requirement	Value
Power consumption	0.5 W/cm^2
Time resolution	25 ns
Hit efficiency	97%
NIEL displacement damage	1×10^{15} n_{eq}/cm^2
Total ionizing dose	50 MRad
Noise	1% hit occupancy = 1 MHz/cm^2

Table 3.1: Requirements for pixel modules in the Barrel 4 region of ATLAS ITk [11].

3.3.2 MAPS in particle physics experiments

MAPS are CMOS imaging sensors modified for use as silicon pixel detectors. Unlike hybrid pixel detectors, in MAPS there is no need for bump bonding of separate devices together since the pixel matrix readout circuitry such as amplification and discrimination is built into a single monolithic device.

With their monolithic nature and link to commercial sensor production, MAPS have been developed for implementation in particle physics experiments due to a number of advantages over the hybrid pixel detectors used in ATLAS and other experiments:

Thin sensors Using a single piece of silicon instead of two in a hybrid results in thinner sensor modules and a detector with a lower material budget to improve track reconstruction, in particular of the impact parameter in vertex detectors. Furthermore, the epitaxial silicon used for charge collection in some designs is as thin as 18 μm, and sensors can be thinned to 50 μm or less. Besides the improvement in reconstruction with less material budget, at these thicknesses, it becomes possible to bend the sensor with significant curvature to be concentric to the beam line in experiments, as is proposed for the next upgrade of the Inner Tracking System (ITS) in ALICE [37] during LS3 .

Low capacitance and power The capacitance of the sensor can be far less than the inherent capacitance of a bump bonded diode contact, and allows for low capacitance and therefore noise and power consumption. The capacitance can be even lower in pixel designs with smaller collection electrodes. The overall material budget can be decreased even further if there is less infrastructure for cooling and powering as a result of lower power consumption of the sensor, and the minimum material budget is limited only by the thickness of the sensors themselves.

Stitching Stitching is a technology that allows for the manufacture of wafer-scale pixel matrices. Devices of this size would greatly improve the possibility of developing a large area silicon tracker, in particular of a curved, cylindrical detector such as in the previously

mentioned proposed ITS upgrade, though the production yield is also less for stitched sensors.

Production costs and speed "Hybridization" is an expensive and time-consuming process. MAPS are produced in commercial processes for CMOS image sensors which can offer reduced production costs and times compared to planar sensors, and even more so in comparison to the full hybrids.

These potential advantages have made CMOS imaging technology attractive for implementation in particle physics and the subject of much research and development.

3.3.2.1 MOSFET and CMOS

The metal-oxide-silicon field effect transistor (MOSFET) transistor consists of doped silicon interfaced with an insulating material (such as silicon oxide) and metal to form a cross section as shown in Fig. 3.15 of an p-type MOSFET (PMOS). (In n-type MOSFET (NMOS), the polarity of the doping is reversed.) A PMOS transistor consists of n-doped bulk substrate, p-doped source and drain terminals and an insulating layer (typically silicon dioxide in older technologies) and conductive metal to form the gate. The behavior of the transistor is dictated by the doping levels, trapped charge in the insulating layer (see discussion above on radiation damage), and biasing of the source, gate, drain, and bulk to control the depletion and flow of current between terminals. MOSFETs are typically used for switching or amplification and are the building blocks of digital and analog circuitry. CMOS logic is built with complimentary NMOS and PMOS transistors such that only one out of the pair is switched on at a given time (with the exception of a brief time when switching occurs). Circuits built in this way consume significantly less power than NMOS logic or Transistor-Transistor Logic, and CMOS logic is the dominant logic used in modern digital and electronic circuitry.

CMOS can be used to build circuitry, including amplifiers and digital logic at a scale that can be contained in a single silicon pixel. Historically, silicon sensors and readout devices have typically been developed and produced separately and then combined into hybrid sensors, however, CMOS devices with sensing components for commercial applications such as digital

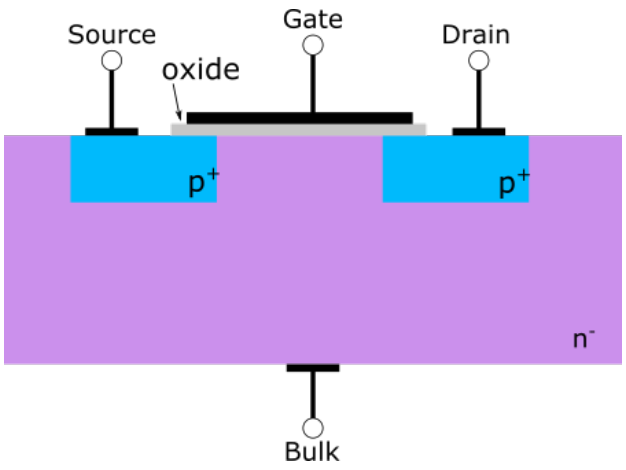

Figure 3.15: Schematic of a PMOS transistor.

cameras have been modified for implementation in particle physics and present an exciting opportunity to build all-in-one ("monolithic") devices.

3.3.2.2 Historical developments

MAPS have been developed for particle physics based on CMOS imaging sensors (CIS) for commercial digital cameras. Since the early development of MIMOSA and implementation in the STAR experiment [38, 39], there has been significant work to expand the applicability of CMOS sensors to particle physics applications as detectors of ionizing radiation. This work includes the development of readout architectures and sensor designs.

Like most CMOS imaging sensors, MIMOSA featured charge collection by diffusion in a thin ($\sim$20 μm) undepleted layer of epitaxial silicon, and a rolling shutter readout. In a rolling shutter readout, the pixels are readout one row at a time in a set sequence to the sensor periphery where there is further amplification and discrimination. While these features were suitable for STAR, they limited the speed of the readout and thereby implementation in other experiments. In later versions of MIMOSA, a zero suppression readout was implemented, allowing for readout of only pixels that registered hits [40]. These newer versions of MIMOSA have a wide array of applications in particle physics, including the KARTel telescope used for particle tracking in test beam measurements of the first MALTA device presented in this thesis [41].

Following the use of MIMOSA in STAR, other MAPS that collect charge by diffusion have

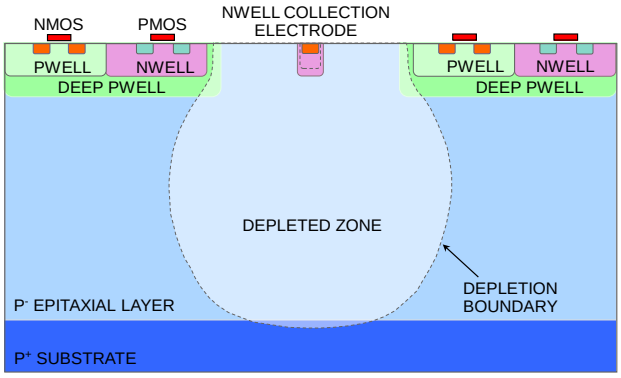

Figure 3.16: Schematic of the TowerJazz 180 nm standard process used for the ALPIDE sensor.

been developed and installed in particle physics experiments, such as the ALPIDE sensor [42], which was integrated into the ALICE Inner Tracking System upgrade during LS2 of the LHC from 2019-2021. A schematic of the pixel cross section is shown is shown in Fig. 3.16. The sensor is implemented in the TowerJazz 180 nm CMOS imaging process .The substrate is a high resisitivity (1 kΩ) 18-30 μm thick epitaxial layer and has a small n^- collection electrode outside the p-well structures shielding the electronics from charge carriers generated by particles that transverse the sensing volume. The depletion region is delineated by the dotted line in Fig. 3.16, and does not include the area under the p-well.

The collection by diffusion in MAPS results in much longer collection times than collection by drift along an electric field. This collection is too slow for many particle physics applications, such as in ATLAS where a signal must be detected in a single 25 ns bunch crossing. The long collection time also increases the likelihood of recombination and of charge being lost due to trapping, given the reduced carrier lifetime. The concentration of these traps increases after irradiation, and the radiation hardness is limited with collection by diffusion. The ALPIDE chip is radiation hard up to a NIEL fluence of 1×10^{13} $n_{\mathrm{eq}}/\mathrm{cm}^2$ [42], which is sufficient for ALICE, but two orders of magnitude below the ATLAS requirement of 1×10^{15} $n_{\mathrm{eq}}/\mathrm{cm}^2$. As with MIMOSA, this sensor's application was limited to lower rate and irradiation levels. To improve the radiation hardness, more signal needs to be collected in shorter time. This can be achieved by increasing the size of the depleted region where there is an electric field so that charge carriers will be collected by drift instead of diffusion.

Fortunately, as CMOS technology has matured, it has become feasible to design MAPS with

faster charge collection and better radiation tolerance. In general this is due to higher resistivity substrates and higher voltages that have allowed for greater depletion (the depleted volume is proportionate to $\sqrt{V\rho}$ and thereby the development of a subclass of sensors known as depleted MAPS or depleted monolithic active pixel sensor (DMAPS) [43] which could potentially be installed in the ATLAS ITk and similar environments and are the subject of ongoing development.

3.3.2.3 DMAPS for the ATLAS ITk Upgrade

The ATLAS collaboration surveyed a number of potential CMOS vendors and technologies and selected three to continue development of MAPS for the ATLAS ITk: AMS 180 nm, TowerJazz 180 nm, and LFoundry 130 nm [36]. This development of DMAPS for ATLAS has been divided into two different design approaches: "large collection electrode" and "small collection electrode."

A schematic of the large collection electrode design is shown in Fig. 3.17(a). In this design, the substrate is 50 to 100 μm thick or more and the NMOS and PMOS electronics are housed within a large deep n-well that also serves as the collection electrode. Large collection electrode devices have shown promising results, with MIP signals on the order of 7000 e and excellent detection efficiencies above 99 % in devices irradiated to 1×10^{15} $n_{\mathrm{eq}}/\mathrm{cm}^2$ 3.17(a) [36]. The main drawback of these devices is that the large area of the collection electrode leads to relatively large capacitance, near 100 fF per pixel, which affects the power consumption, signal to noise, and timing accuracy of the pixels.

A schematic of the small electrode design is shown in Fig. 3.17(b). The smaller electrode leads to a capacitance of $\sim$10 fF and therefore lower power consumption and better signal to noise, allowing for efficient hit detection despite the smaller collected charge due to the thinner depletion region. This thinner collection region also allows for faster charge collection as carriers drift a shorter distance. The main challenge of these devices is the collection of charge carriers generated under the p-well, far from the collection electrode as this region may not be depleted or have a weak electric field, especially in devices after significant NIEL damage.

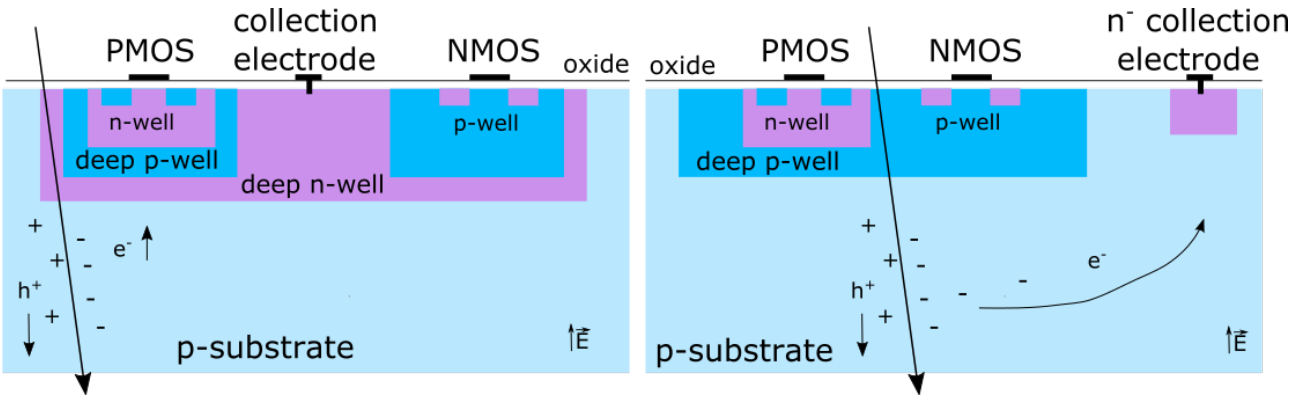

(a) Cross section of the large collection electrode pixel substrate. The resulting capacitance is ~ 100 fF.

(b) Cross section of the small collection electrode pixel substrate. The resulting capacitance is ~ 5 fF.

Figure 3.17: Schematics of the cross section of the pixel substrate design concepts for the ATLAS ITk inspired by schematics in [43].

DMAPS in the TowerJazz 180 nm modified process

A recent development to improve the radiation hardness for use in ATLAS is to modify the TowerJazz 180 nm process to include a lowly doped n^- layer throughout the substrate as shown in the Fig. 3.18(b) [44]. With this n-layer, the depletion region begins to grow from the junction of the p-substrate and n-layer and full depletion of the epitaxial layer is achieved. The TowerJazz Investigator, a sensor with only analog readout, was implemented in both the standard and modified processes [44]. It features many 'mini-matrices' with variations in pixel design such as the pixel, electrode, and p-well sizes and reset mechanism. Promising results were measured with the Investigator sensors, such as improved signal in the modified process, as demonstrated in ^{55}Fe spectra in Fig. 3.19, and a slight improvement in the rise time and signal amplitude after irradiation to 1×10^{15} $n_{\mathrm{eq}}/\mathrm{cm}^2$ as shown in Fig. 3.20 [45]. Initial test beam measurements indicated that the efficiency after irradiation was sufficient, however, closer examination of the data and characterization of later devices in the TowerJazz 180 nm process, including MALTA, would reveal that further modification to the sensor and/or front-end were necessary for radiation tolerance to 1×10^{15} $n_{\mathrm{eq}}/\mathrm{cm}^2$, at least at the sensor pitches required for ATLAS [46].

Two sensors, MALTA (Monolithic ALICE to ATLAS) and MonoPix, have been developed based on the TowerJazz Investigator designs [47, 48]. The analog front-end in each pixel is

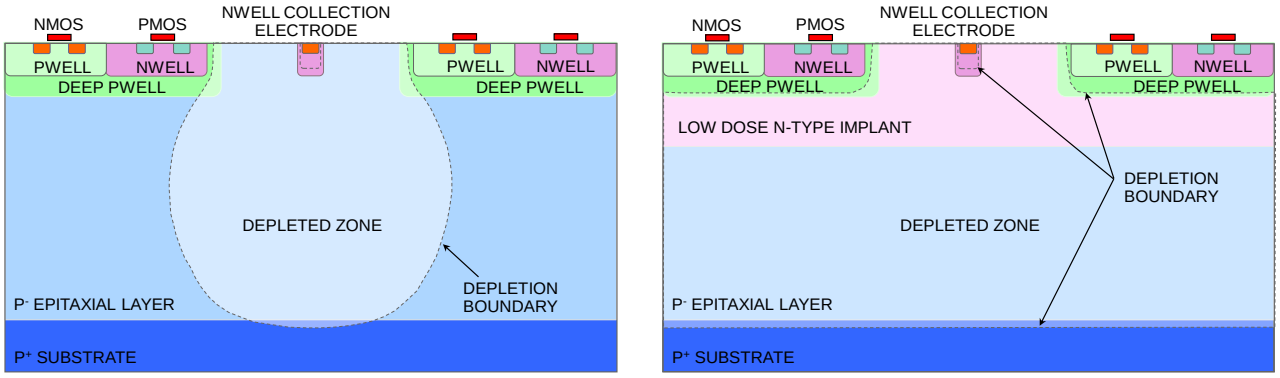

(a) The standard process used for the ALPIDE sensor.

(b) The modified process used for the MALTA and MonoPix sensors.

Figure 3.18: Schematic of the TowerJazz 180 nm processes.

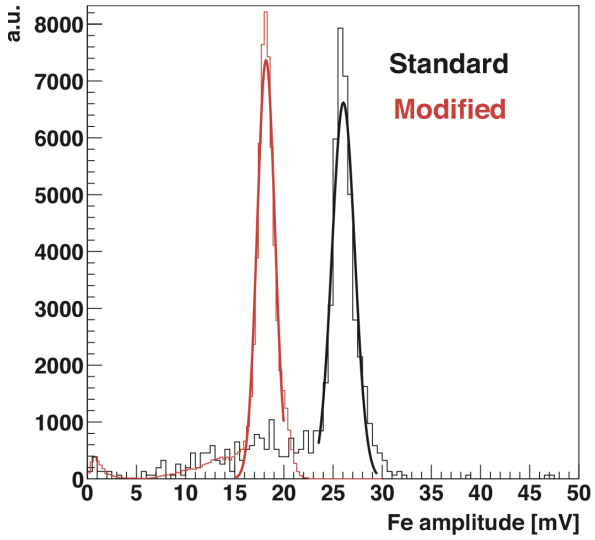

Figure 3.19: Amplitude spectra of ^{55}Fe with the Investigator sensor in the standard and modified TowerJazz 180 nm processes, from [45].

identical to the one in ALPIDE. The key difference between MALTA and MonoPix is in their readout architectures, which is synchronous for MonoPix and asynchronous for MALTA, and discussed in more detail in Chapter 5. The characterization of MALTA and subsequent versions of the sensor is the subject of Chapters 5, 6, and 7.

3.3.2.4 Applications in high-granularity calorimetry

A novel application of tracking sensors is high-granularity calorimetry for proposed e^+e^- and hadron collider experiments such as the ILC, CLIC, FCC, and CPEC. The precision of many

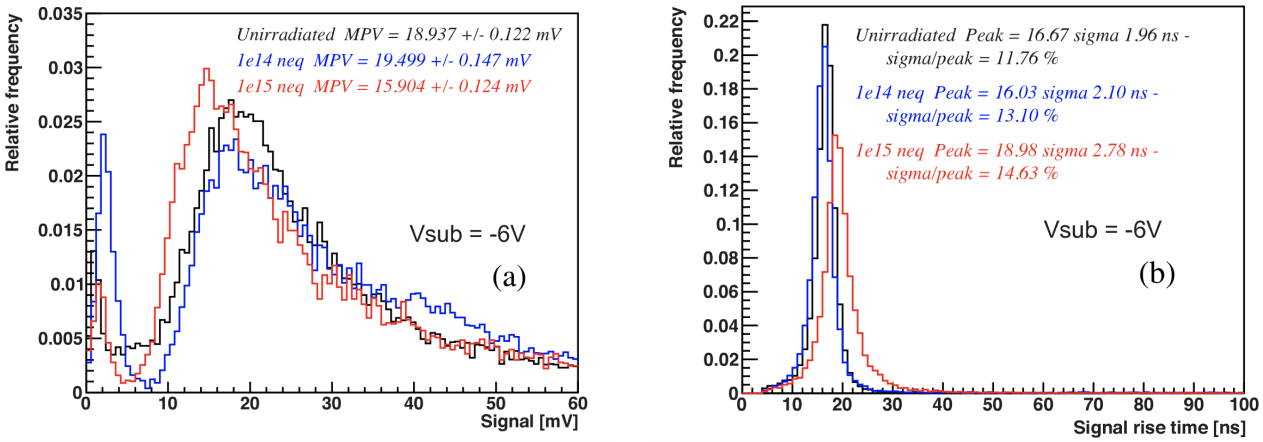

(a) Amplitude distributions.

(b) Rise time distributions.

Figure 3.20: Measurements of unirradiated and neutron-irradiated TowerJazz Investigator samples in the modified process, from [45].

measurements in these experiments depends on the jet energy resolution, which may be improved with a high-granularity calorimeter constructed from silicon sensors that allow for precise tracking and reconstruction of all particles in a jet. Both planar pad sensors and MAPS have been considered and developed in hadronic and electromagnetic calorimetry by the CALICE collaboration [49]. Chapter 8 is concerned with MAPS for electromagnetic calorimetry and contains results for the simulated single-particle event reconstruction with a MAPS-based electromagnetic calorimeter as well as characterization of DECAL, a prototype MAPS sensor for electromagnetic calorimetry [50].

3.3.3 Sensor characterization

For inclusion in physics experiments, sensors must be reliable and well-characterized. The typical measurements to understand sensor characteristics are described in this section. The exact measurements for characterizing a sensor depend on the requirements of a target experiment as well as the maturity of the experiment and the device being tested. Early versions of a sensor may be limited in functionality or have features ill-suited for a specific application or practical operation in a large-scale experiment. Likewise, the design parameters of an experiment may not yet be exactly determined and/or change at a later stage. Typical requirements for a given experiment are limits on power consumption, data transfer rate, detection efficiency,

and radiation tolerance. The characterization of irradiated devices is especially important, but is also more challenging than characterization of unirradiated devices due to the irradiations themselves and complications in testing such as the need to cool sensors.

Characterization for the ATLAS ITk is relatively mature, with a large collaboration that has agreed on a set of requirements publicly accessible in [36] and [11] and has developed standardized testing procedures for characterization prior to and during construction. The strip sensors and CMOS sensors characterized for Chapters 4, 5, 6, and 7 were targeted for inclusion in the ITk and are presented in light of the requirements and procedures of the collaboration. For the DECAL sensor in Chapter 8, the exact experiment that will be constructed is not yet clear, and so the characterization of the device is more open-ended, and simulation studies including ones such as those in Section 8.3 may influence future sensor specifications.

Current-voltage and Capacitance-voltage measurements

In current-voltage (IV) measurements, the reverse bias on a sensor is varied and the leakage current is measured. IV measurements of sensors are used to characterize the power dissipation in the substrate for the sensor, and determine the operational limits. In a typical IV measurement, an example of which is shown in 3.21, the current follows the proportionality to $\sqrt{V_{bias}}$ (since the number of charge carriers goes as the depletion depth as in Eqn. 3.16) until the sensor is depleted. At some voltage (ideally at greater reverse bias than the full depletion voltage), the sensor begins to go into electrical breakdown and the current sharply increases. When making IV measurements, precautions should be taken to avoid large current draws on the sensors, such as smaller voltage steps and low power supply current compliance. They are often the first measurement of a new device to determine the depletion voltage to be applied for reverse bias operation, the breakdown voltage, and the leakage current.

In CV measurements, the capacitance is measured as a function of the bias voltage. Examples of CV measurements are shown in Fig. 3.22. As V_{bias} is increased and the depletion region widens C decreases proportionately to $\frac{1}{\sqrt{V}}$ as in Eqn. 3.18 and with V_{bias} greater than the depletion voltage, the capacitance plateaus. CV measurements can be used to infer N as a function of w

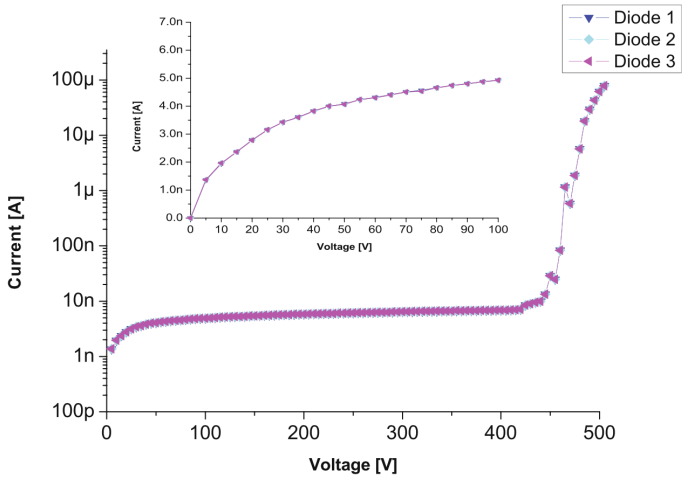

Figure 3.21: The current–voltage characteristic for a silicon diode in the reverse bias direction. The expanded view shows the $I \propto \sqrt{V}$ dependence, while the global view shows the full scan including breakdown at higher voltages, from [51].

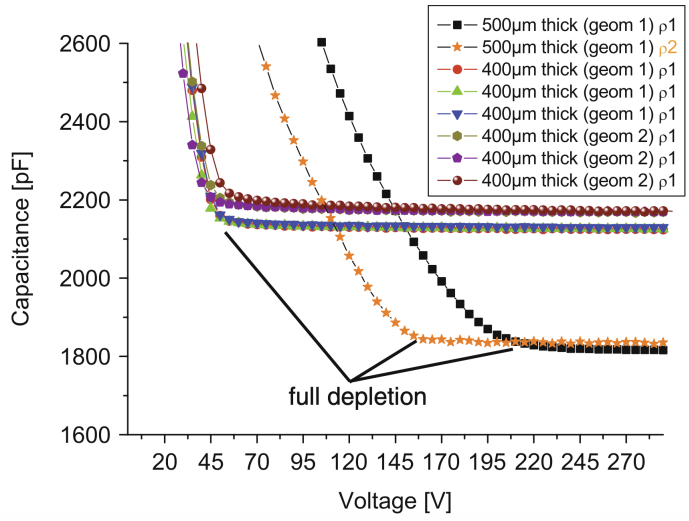

Figure 3.22: Examples of CV measurements from From [51]. The two upper bands depict sensors of two different geometries with slightly different areas and same high resistivity material, both 400 μm thick. The lower CV curves describe 500 μm thick sensors, which have less capacitance at full depletion and larger $V_{FD} \propto d^2$, as would be expected based on equation 3.18. The different depletion voltages of the lower curves are due to two different resistivities $\rho 2 > \rho 1$.

and measure a doping profile with

$$N(w) = \frac{2A}{q\epsilon} \frac{1}{d(1/C^2)/dV} \tag{3.28}$$

from [27].

Signal measurements

The sensor performance is characterized by measurement of the output signal of the sensor with particles from a radioactive or laser light source of predictable energy. Typically, an oscilloscope is used to digitize the output for offline analysis. The gain of a sensor is defined as the relative output signal for a given input, often in terms of pulse amplitude for a given input charge. ^{90}Sr and ^{55}Fe are popular choices for characterization, including in the work presented in the thesis. The energy spectrum of ^{55}Fe has a dominant k-α peak at 5.9 keV. The decay spectrum of ^{90}Sr includes a 550 keV β decay and 2.3 MeV β decay from the resulting ^{90}Y. Measurements are made by triggering on a sensor, usually a scintillator coupled to a photomultiplier tube, placed behind the device under test (DUT). The majority of the lower energy electrons do not trigger the scintillators. Hence, the main decay measured has a endpoint energy of 2.3 MeV and a spectrum of particles with ionization sufficiently similar to that of a MIP that allows for fitting of a Landau function to the amplitude or integrated charge spectrum.

Ideally, a sensor is characterized with multiple sources with known spectral peaks and has a gain which is linear over a reasonable range of energies, for example in an X-ray tube with multiple targets and energy spectra. In addition to the gain, characteristics such as the rise time, noise pedestal, and noise RMS can also be measured by signal analysis with radioactive sources.

For irradiated devices, it is important that a reasonably similar amount of charge is collected after NIEL irradiation. The CCE of a sensor is defined as the ratio of the collected charge after irradiation to the collected charge before irradiation:

$$\epsilon = \frac{Q_{irradiated}}{Q_{unirradiated}} \tag{3.29}$$

Thus, the CCE quantifies the decrease in signal after irradiation, and must be not too far below 1 for devices to be considered radiation tolerant.

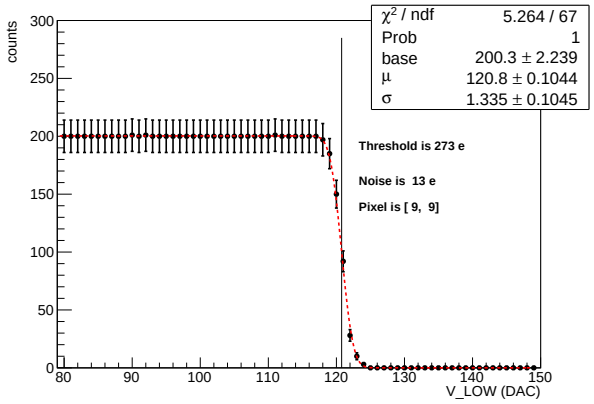

Figure 3.23: A threshold scan of a pixel in MALTA. The vertical line is at the mean from the error function fit.

Threshold measurements

The threshold is the amount of signal that must be input into the front-end of a sensor to cause the discriminator in the front-end electronics to fire. Typically, an electrical pulse of a set voltage value is injected N times into the front-end circuitry of a sensor via a calibration capacitor and the hits in the sensor are counted. The voltage value is varied from well below the threshold, where there should be no hits, to well above the threshold, where N hits should be counted. The number of hits is plotted and fit with an error function (integral of a Gaussian with mean μ and width σ) as in Fig. 3.23 of a threshold scan of a single pixel in MALTA. The threshold is the μ term of the fit (at the vertical line in the figure), and the noise is the σ term. Ideally, the threshold of each pixel is "tuned" to be as close as possible to a single value so the sensor has a uniform response, which can be gauged in noise and source scans.

Noise and source scans

A noise scan is a measurement in which the sensor is operated for a set time without a particle beam or source to characterize the noise on the sensor. If many noisy pixels register hits at a high rate, this can be problematic (particularly for MALTA with its readout architecture and masking scheme). To mitigate this, the noisiest pixels may be masked during operation. With a reasonable mask, the sensor can be exposed to a uniform beam of particles (such as one generated by an X-ray tube larger than the sensor) in a source scan to measure the uniformity

of the sensor's response. This can be used to check for dead pixels, failed bump-bonds, the effectiveness of masking, and other issues. In an ideal case, the number of hits across the pixel (or strip) matrix is uniform.

Test beams

Test beams are used to measure the detection efficiency of sensors. The efficiency is defined as

$$\epsilon = \frac{N_{detected}}{N_{total}} \tag{3.30}$$

where $N_{detected}$ is the number of tracks detected on a DUT and N_{total} is the number of incident ionizing particles that have passed through the sensor. Efficiency measurements test the core function of particle detection: if a sensor is not efficient for MIP detection at $>\sim$ 97 %, it is not useful. Measurements are made with high-energy incident charged particles (for example 180 GeV pions) which will ionize and pass through silicon with negligible change in direction and energy. Thus for a set of multiple sensors aligned and synchronized in a "beam telescope," a roughly straight track of hits will be formed and can be reconstructed in analysis. A DUT is placed between planes of this telescope, and for every reconstructed track, the readout of the DUT is checked for a corresponding hit with the same spatial and temporal location as predicted by the track. The total number of tracks in the telescope is N_{total} and the number of corresponding measurements on the DUT is $N_{detected}$. Using a high energy beam and pixel sensors (including MAPS) with excellent position and time resolution, tracks can be reconstructed with micron-level precision allowing for probing of sub-pixel structures.

Chapter 4

Radiation Damage Studies on Strip Detectors

During the 2024-26 the Phase II HL-LHC upgrade, the ATLAS Inner Detector will be replaced with the ITk. This includes the installation of four layers of strip sensors and five layers of pixel sensors. In order to characterize the radiation hardness of prototype strip sensors, an irradiation and testing campaign was carried out by a collaboration of research facilities. A number of prototype strip sensors were manufactured by Hamamatsu Photonics (HPK) in 2017. These ATLAS17 sensor wafers included miniature versions of the full-size device which were irradiated at the MC40 cyclotron at the University of Birmingham and at other facilities and then distributed throughout the collaboration for measurement. At the University of Birmingham, the CCE was measured using the ALiBaVa data acquisition system and a ^{90}Sr beta particle source, and IV curves and interstrip resistances were measured in follow-up measurements [52].

4.1 Sensors

The ATLAS17 miniature strip structures are AC-coupled n-on-p float zone[1] strip detectors with a 75.5 μm strip pitch and a thickness of 300 μm [53]. The standard (STD) sensors used for

[1]Float zone silicon is produced in a specific process for low impurity concentrations and high resistivity. [53]

characterization are miniature 1×1 cm^2 versions of the main proposed sensors, which will have an area of 10×10 cm^2. The other sensors irradiated were miniature versions of the long strip (LS), short strip (SS) sensors, 8×8 mm^2 diodes, and two sets of test structures for monitoring of specific device parameters: the "A1" structures and 4×4 mm^2 diodes. The quantities of each type at a given target fluence are tabulated in Table 4.1. In total 89 sensors were irradiated. The target fluences were selected based on the radiation requirements shown in Table 4.2, which include a safety factor of 1.5.

	Target Fluence [n_{eq}/cm^2]			
Sensor type	1×10^{14}	5×10^{14}	1×10^{15}	2×10^{15}
STD Mini	7	8	8	8
8x8 Diode	4	4	4	4
Long Strip	2	2	2	2
Short Strip	1	1	1	1
4x4 Test	4	4	3	3
A1 Test	4	4	4	4

Table 4.1: Table of quantities of ATLAS17 sensors of specific types and target fluences.

Sensor type	Fluence [n_{eq}/cm^2]	TID [MRad]
Long Strips	3.8×10^{14}	9.8
Short Strips	7.2×10^{14}	32.5
Endcap	1.2×10^{15}	50.4

Table 4.2: Radiation tolerance requirements for ITk strip sensors. A safety factor of 1.5 is included.

As previously mentioned, the irradiation and measurement campaign at the University of Birmingham was only a subset of a larger campaign to measure the ATLAS17 Minis. Only a portion of the sensors irradiated at the MC40 cyclotron were kept for testing at Birmingham: a total of 10 STD Mini sensors, one annealed and unannealed at each fluence, including two unirradiated samples. The majority were sent for testing at UCSC, Cambridge, and University of Freiburg. Samples were also irradiated with 70 MeV protons at CYRIC at the Tohoku University, 24 GeV protons at the PS-Irrad facility at CERN, and neutrons at the Ljubljana TRIGA reactor [54–56]. Charge collection characterization was performed at UCSC, University

of Tsukuba, and IFIC in addition to Birmingham, and comparison of measurements was key to interpreting the results.

4.2 Irradiations

The MC40 cyclotron provides a collimated, 1×1 cm^2 beam of 28 MeV protons to irradiate sensors with an adjustable beam current in order to prevent heating sensors during the irradiation. An aluminum plate of thickness 300 µm was placed in front of the sample within the box to absorb a portion of the low energy particles that have historically been present in the beam, resulting in an energy of 23 MeV at the sample as determined from GEANT4 simulations (also due to the kapton windows of the box, air, nickel foil). A photograph of the facility is in Fig. 4.1. A hardness factor of 2.2 (the displacement damage relative to 1 MeV neutrons) was estimated for the beam and confirmed by current measurements in diodes in [57].

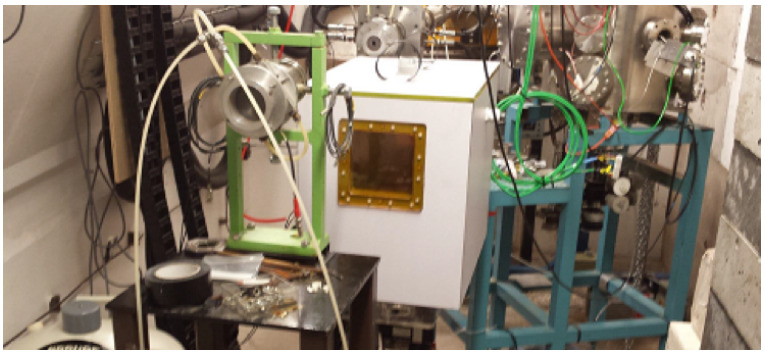

Figure 4.1: Photo of the box, beam pipe, and faraday cup at the MC40 cyclotron at the University of Birmingham.

Sensors were placed into small frames in between layers of Kapton tape and hung in a box which we could move with millimeter precision via motorized stages. Gafchromatic film (a film which will change color with radiation exposure) was attached to the front of the frames to check and accurately position the box and sensors relative to the beam. Nickel foil was attached in front of or behind a subset of the sensors for dosimetry. For the smaller sensors, that is the STD Minis, 8×8 cm^2 diodes, and the test structures, the 1×1 cm^2 beam was large enough to cover the entire sample and a 100 nA beam was used (referred to as a "point-to-point" irradiation). For the LL and SS structures, which were larger than the beam size, the beam was scanned by

gradually moving the box during the irradiation and we were able to use a 400 nA beam current since there was less risk of the beam heating the larger, moving sample. In order to prevent the sensors from heating and annealing during the irradiation, the box was temperature and humidity (to prevent condensation) controlled with a liquid nitrogen micro-dosing system, a nitrogen gas line to maintain low humidity, and a fan to improve circulation within the box. The temperature and humidity were monitored prior to and during the irradiation. The two humidity probes were placed at different locations in the box. One temperature probe measured the air near the center of the box and the other was taped to the metal frame used to mount the sensors. The temperature was kept near -27 °C and the humidity below 10 %RH during the irradiation.

4.2.1 Dosimetry

Dosimetry for the samples was computed from measurements of nickel foils placed in front of the silicon samples and a Faraday cup behind them. For samples with a nickel foil, the dosimetry was completed by measuring the energy spectrum of the irradiated foil using an Ortec High Purity Germanium Radiation Detector and the time of irradiation and dosimetry measurements [58]. For the displacement damage, the fluence was calculated by first inferring the number of ^{57}Ni atoms based on the decay rate from the spectrometer counts including corrections for the efficiency and acceptance of the detector as well as the time elapsed during and after the irradiation. From the number of ^{57}Ni atoms produced, the number of protons in the beam was calculated using the interaction cross section and the total number of nickel atoms. Finally, the 1 MeV neutron-equivalent fluence was calculated using the hardness factor and foil area. In all, the fluence is calculated as:

$$\phi = \frac{N_{counts}}{t_{dos}} \frac{1}{\epsilon \alpha f e^{-\lambda t_{elap}}} \frac{t_r}{1 - e^{-t_r}} \frac{1}{\sigma N_{Ni}} \frac{D}{A} \tag{4.1}$$

where N_{counts} and t_{dos} are the number of counts and duration of the dosimetry, respectively, λ the ^{57}Ni decay constant, ϵ the efficiency, α the acceptance, f the fraction of ^{57}Ni atoms that

will decay at the specified peak, t_{elap} the time elapsed since the irradiation, t_r the duration of the irradiation, σ the proton cross section for Ni to ^{57}Ni, N_{Ni} the surface number density of the nickel atoms, D the hardness factor, and A the area of the foil in the beam.

To estimate the total ionizing dose, the total energy deposited is calculated as the product of the proton fluence and the stopping power, dE/dx

$$E = F_{proton} * \frac{dE}{dx} = F_{neq}/D * \frac{dE}{dx} \tag{4.2}$$

for 23 MeV protons, $\frac{dE}{dx} = 1.825 * 10^7$eV cm^2/gr. For example, for a fluence of 1×10^{15} $n_{\rm eq}$/cm^2, the total ionizing dose is then

$$E = \frac{1 \times 10^{15}\ n_{\rm eq}/{\rm cm}^2}{2.2{\rm n_{eq}}} \times 1.825 \times 10^7 {\rm eV\ cm}^2/{\rm gr} = 8.3 \times 10^{21} {\rm eV/g} = 1330\ {\rm J/g} = 133\ {\rm MRad} \tag{4.3}$$

where electron volts are converted to Joules with 1 eV $= 1.6 * 10^{-19}$ J. The dose of 133 Mrad at 1×10^{15} $n_{\rm eq}$/cm^2 is significantly higher than the TID of 50.4 MRad expected for the endcap strip modules. The higher TID was not expected to effect the bulk silicon and collected charge, but gave reason to expect surface effects that could lead to a change in other factors such as the coupling between strips.

In the case where a nickel foil was not present in front of each sample, the counts in the Faraday cup behind a sample were used to approximate the fluence based on the mean ratio of Faraday counts to fluence as calculated from the nickel foils used that day.

The results of the dosimetry are presented in Fig. 4.2, where the estimated fluence is plotted as a function of the target fluence for every sample. For most samples, the measured 1 MeV equivalent fluence is within 20 % of the target fluence, which is marked with the line in the figure. Discrepancies are likely due to variance in the beam current during the run, slight misalignment of the samples, and/or inhomogeneity of the beam.

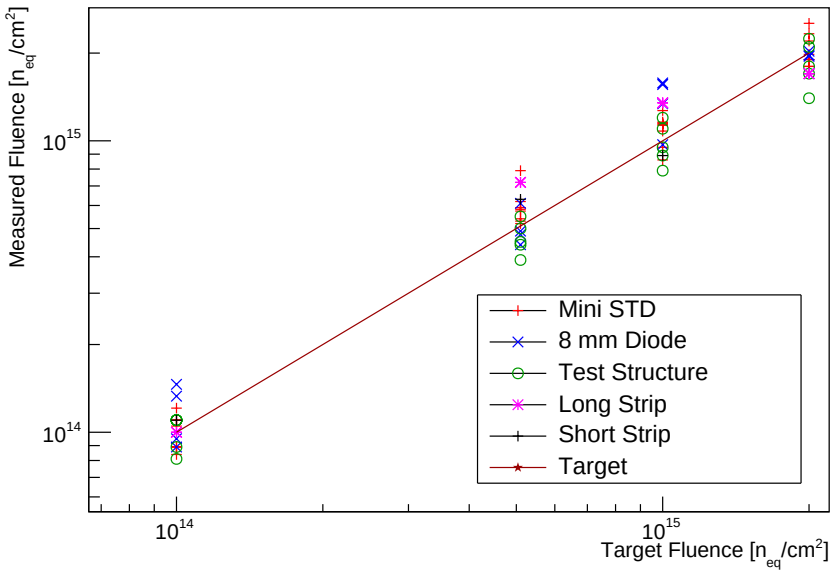

Figure 4.2: Plot of measured versus target fluences for ATLAS17 sensors.

4.3 Charge Collection Studies

The ALiBaVa readout system, a schematic of which is shown in Fig. 4.3, was used to measure the collected charge efficiency of the ATLAS17 STD Mini sensors [59]. The ALiBaVa readout system consisted of a motherboard and daughterboard on which a sensor was mounted as well as two Beetle chips for readout of up to 128 channels [60]. Two scintillators attached to photomultipler tube (PMT)s were placed beneath the daughterboard and sensor to trigger the ALiBaVa readout (though during the work of this thesis, the scintillators were not used in coincidence). The motherboard received signals from the daughterboard and scintillators and interfaced via USB connection with a PC to run the data acquisition software.

The daughterboard was placed in an aluminum box inside a consumer freezer in order to cool the sensor to approximately -30 °C. The temperature and humidity were monitored to ensure that the sensor did not reach the dew point and to later calibrate the Beetle chip's gain to the measured temperature. A small fan was placed under the daughterboard to dissipate heat from the backside mounted heat sink and nitrogen gas was fed into the aluminum box.

A ^{90}Sr radioactive source was used to inject the 2.3 MeV endpoint β particles to serve as MIP-like particles and allow for fitting of a Landau function to the collected charge spectrum

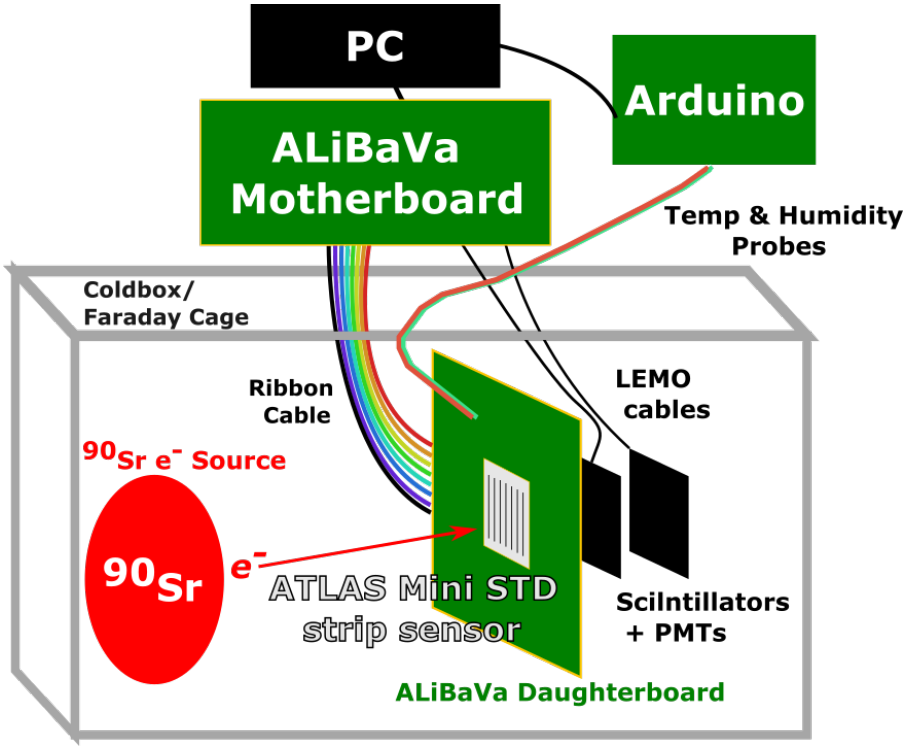

Figure 4.3: Schematic of the ALiBaVa setup used at the University of Birmingham.

and thereby measurement of the CCE.

4.3.1 Temperature and ADC Calibration

In order to account for the temperature dependence of the gain of the Beetle chip, the CCE of an unirradiated sensor was measured at two temperatures, approximately -25 °C and $+25$ °C. A linear relationship was assumed based on previous measurements at multiple temperatures in [52]. From the measurements at -25 °C and $+25$ °C, the temperature dependence was approximated to be

$$N_{ADC} = 101 - .383 * T \tag{4.4}$$

with temperature T in °C and N_{ADC} the number of analog to digital converter (ADC) counts of the readout charge value. The number of ADC counts is found after a pedestal subtraction. Assuming a depletion thickness of 300 μm and that approximately 75 e/h pairs are collected per micron in the Landau peak, 22500e/h pairs are collected in total at -25 °C, the charge calibration is 202 e per ADC count.

4.3.2 Results

The CCE of annealed ATLAS17 STD Miniature strip sensors was measured for different values of applied bias ranging from 100 to 1000 V. Events from 100,000 triggers were collected, though only a fraction of these events were selected based on several criteria. The time of arrival of the signal was selected to be within a 10 ns window as this was the approximate range in which the full signal was collected by the Beetle chip. Noise was calculated by the ALiBaVa software from pedestal runs without a source present, and the signal-to-noise was required to be greater than 3.5 in the strip with the largest signal, or "seed." Clusters are groups of signals from multiple adjacent strips, with the requirement that for channels other than the seed the signal-to-noise be greater than 1.5. For clusters, the signal charge is calculated by summing the charge from all the strips in a cluster. For events that satisfied these criteria, a Landau function was fitted to the distributions of collected charge, as in Fig. 4.4.

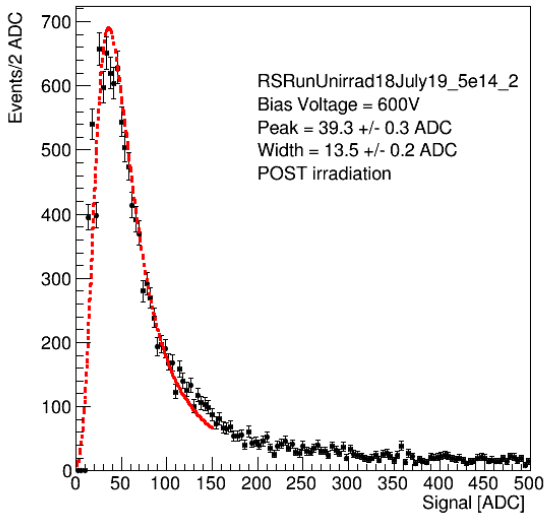

Figure 4.4: Plot of a Landau fit to the distribution of collected charge (in ADC) of a sample irradiated to a target fluence of 5 $\times 10^{14}$ $n_{\mathrm{eq}}/\mathrm{cm}^2$ biased at 600 V and at -25 °C.

Previous measurements of the Landau peak in ATLAS12 sensors at a bias voltage of 500 V are shown in Fig 4.5 as a function of fluence [11]. For these sensors, the CCE is comparable before irradiation and at 1×10^{14} $n_{\mathrm{eq}}/\mathrm{cm}^2$. There was a measurable signal above 1×10^{15} $n_{\mathrm{eq}}/\mathrm{cm}^2$, and in some cases to 1×10^{16} $n_{\mathrm{eq}}/\mathrm{cm}^2$. The ATLAS17 sensors were expected to have

similar if not better radiation tolerance.

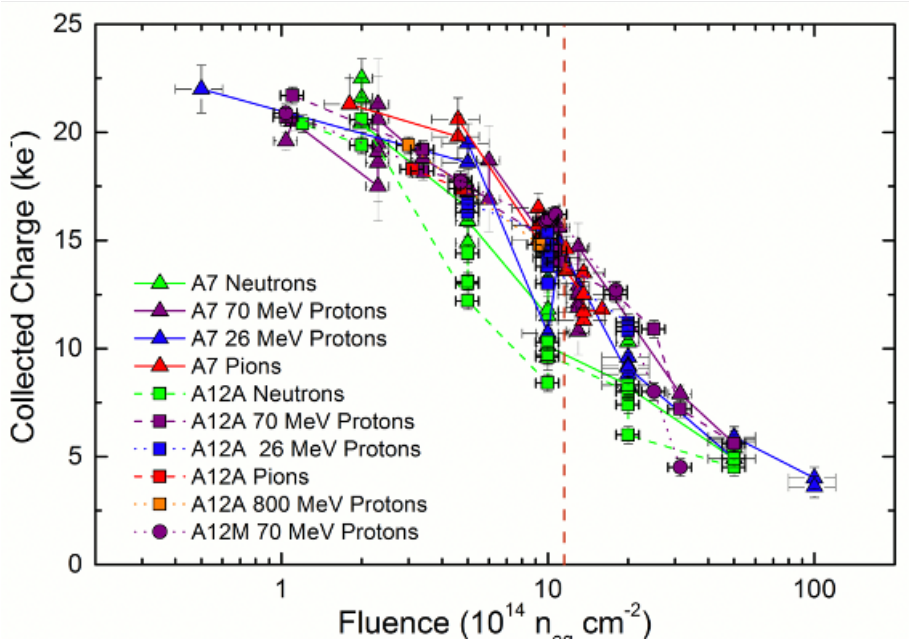

Figure 4.5: The collected charge as a function of fluence measured in ATLAS12 STD Mini strip sensors with MIPs and bias voltage of 500 V from [11].

The CCE results with ATLAS 17 sensors irradiated at various facilities (including at the MC40 Cyclotron in a later campaign) are shown in Fig. 4.6 from [61]. The samples with $\phi = 2 \times 10^{15}$ $n_{\text{eq}}/\text{cm}^2$ have comparable CCE to ATLAS12s with $\phi = 2 \times 10^{15}$ $n_{\text{eq}}/\text{cm}^2$ in Fig. 4.5 and this confirmed that the radiation tolerance was sufficient in the ATLAS17 STD Mini strips sensors, as was expected based on previous measurements of ATLAS12 sensors.

In Fig. 4.7 is a plot of the most probable value of the Landau fits after temperature correction versus the bias voltage for various sensors irradiated and measured at Birmingham. The unirradiated sensor was measured warm and cold to determine the temperature correction, and this correction results in a consistent CCE for the two temperatures as can be seen in the plot. For the unirradiated sensor, the full depletion is near 300 V since at this point the collected charge saturates. For the irradiated sensors, all of which are annealed in Fig. 4.7, the depletion voltage has increased, as expected, though perhaps not for the $\phi = 1 \times 10^{14}$ $n_{\text{eq}}/\text{cm}^2$ sensor, which depletes around the same point, though with less collected charge. Due to the smaller collected charge, Landau distributions could not be reliably fit for five of the most irradiated sensors: both sensors irradiated to 1×10^{15} $n_{\text{eq}}/\text{cm}^2$ and 2×10^{15} $n_{\text{eq}}/\text{cm}^2$, and the unannealed

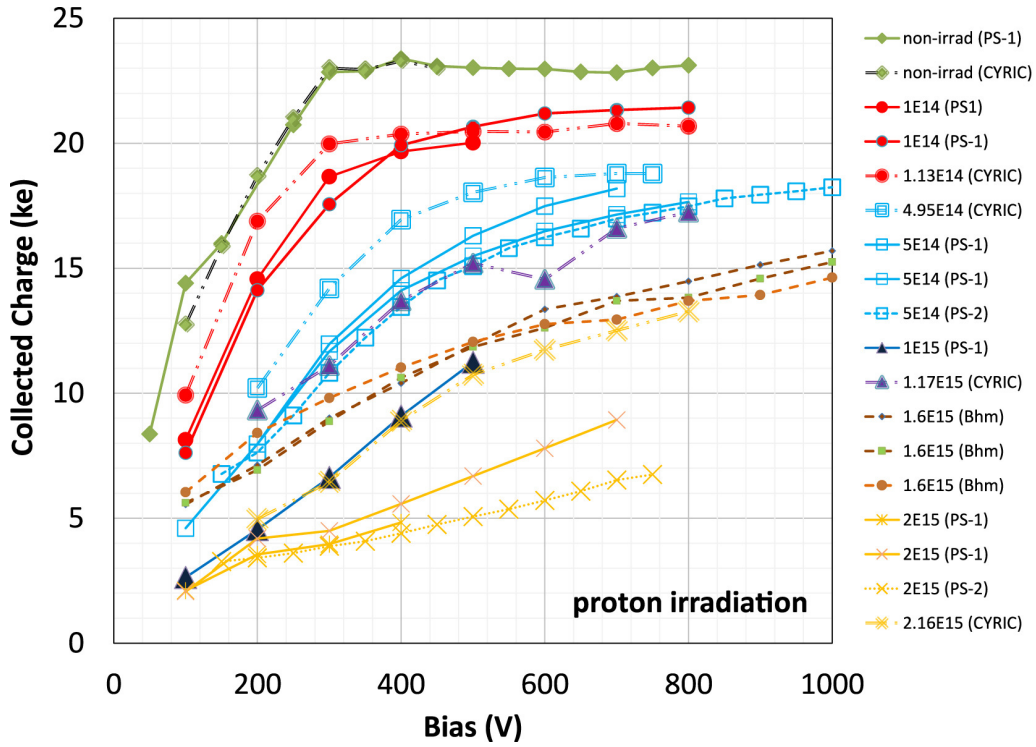

Figure 4.6: Collected charge versus bias voltage of ATLAS17 STD Minis tested at UCSC, University of Tsukuba, and IFIC. Sensors were irradiated at Cyric, Ljubliana, and Birmingham. The sensors irradiated at Birmingham are from a second campaign as a follow-up to the first, which had CCE results inconsistent with other irradiation facilities [61].

sensor irradiated to 5 $\times 10^{14}$ $n_{\text{eq}}/\text{cm}^2$. For the annealed 5 $\times 10^{14}$ $n_{\text{eq}}/\text{cm}^2$ sensor for voltages below 600 V, the fit to the signal distribution was also insufficient, and so the plotted results begin at 600 V.

In comparison to measurements at other facilities in Fig. 4.6, at the same fluences, the CCE values measured in Birmingham and shown in Fig. 4.7 are smaller. In Fig. 4.7, an ATLAS12 sensor irradiated to 3×10^{14} $n_{\text{eq}}/\text{cm}^2$ had the same collected charge as the 1×10^{14} $n_{\text{eq}}/\text{cm}^2$ ATLAS17 sensor, though a higher depletion voltage. Since the ATLAS12 sensors were previously measured to be sufficiently radiation hard, and these newer results were not inconsistent, something was either not reproducible with the irradiations, temperature history either during and after irradiations, or the measurements. That ATLAS17 Minis irradiated and tested at other facilities were measured to have sufficient CCE after irradiation (in Fig. 4.6) suggested that the discrepancy with the Birmingham results in Fig. 4.7 was due to differences in the irradiation. One concern was components of the MC40 cyclotron beam unaccounted for in dosimetry calcu-

lations. To better understand the underlying cause of the discrepancy, several more ATLAS12 sensors were irradiated to be compared to previous results with ATLAS12 Minis irradiated at Birmingham, edge transient current measurements were made with a laser to better understand the radiation damage, and different irradiation methods were tried [61]. The irradiation was made with scanning a 400 nA proton beam instead of a stationary (point-to-point) 100 nA beam for samples irradiated to 1.6×10^{15} $n_{\mathrm{eq}}/\mathrm{cm}^2$ at Birmingham and are shown in Fig. 4.6 to be consistent. The scanning should decrease the effects of heating and annealing that can occur in a stationary irradiation [62]. While these recent results are consistent with others at different irradiation facilities, there is more work being done to understand and refine the MC40 irradiations as unexplained lower CCE effects still occur intermittently.

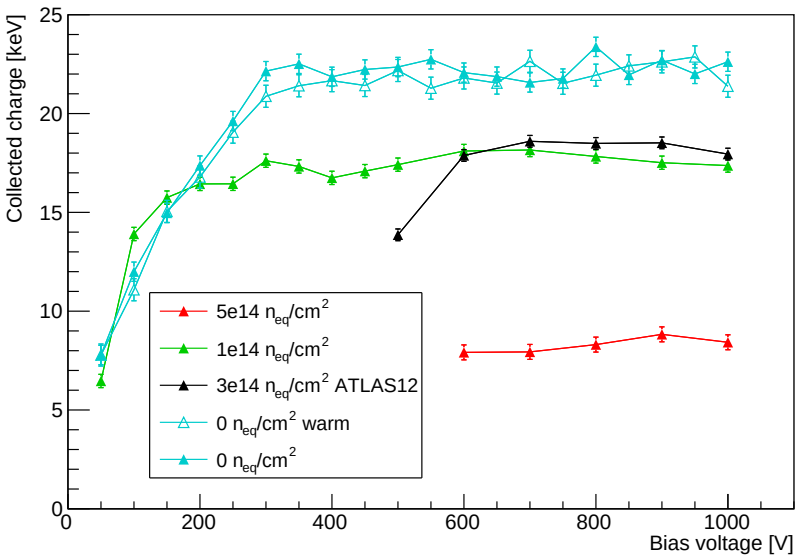

Figure 4.7: The collected charge as a function of bias voltage measured in ATLAS17 STD Mini strip sensors with ^{90}Sr. Irradiated sensors have been annealed.

4.3.2.1 Cluster Widths

The cluster width is defined as the number of strips included in a hit, and this was measured for the same sensors for which the CCE was measured, as well as an ATLAS12 unirradiated sensor for comparison. As shown in Fig. 4.8, the cluster sizes were consistent between the ATLAS12 and ATLAS17 sensors prior to irradiation, and in the ATLAS17 the clusters became wider with

increased fluence. This increase in cluster width suggested that the interstrip resistance, that is the resistance between strips which characterizes their isolation, had decreased due to surface damage from the higher total ionising dose for a corresponding fluence when using protons at Birmingham. To investigate this, interstrip resistance measurements were made at Cambridge as described in Sec. 4.5.

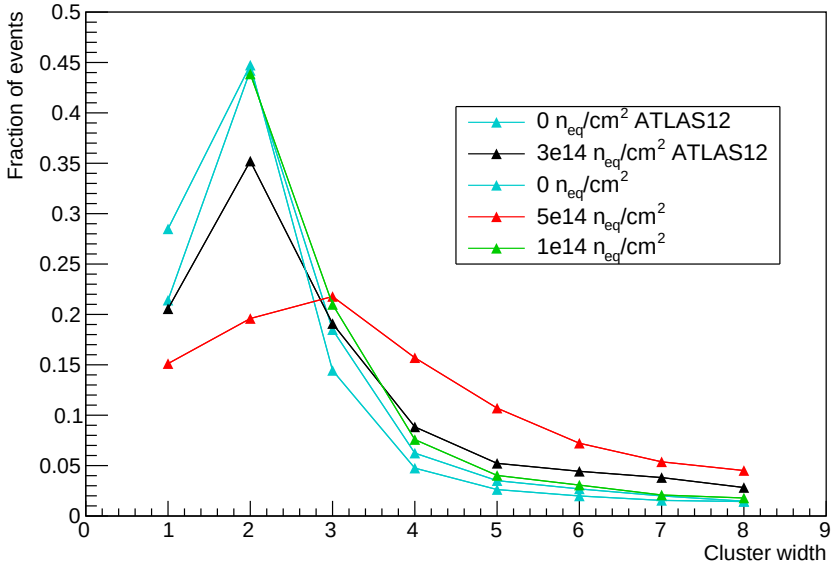

Figure 4.8: Plot of the cluster widths for ATLAS17 STD Minis biased to 900 V.

4.4 Current-voltage measurements

IV measurements were made of the same sensors used for charge collection. With the sensor wire bonded to the AliBaVa board, the voltage on the Keithley power supply used to bias the sensor was manually adjusted and the leakage current was recorded as measured by the supply. The resulting IV curves are plotted in Fig. 4.9. The current increases with fluence as expected, however, at the same fluence (color in the plot), the annealed sensors (filled symbols) have a higher current than unannealed sensors (empty symbols). Excluded from this plot are the values for the current at bias below 450 V for the unirradiated ATLAS17 since these were fluctuating due to their small size relative to the random error in the setup. Also excluded is the measurement of the unannealed 2×10^{15} $n_{\mathrm{eq}}/\mathrm{cm}^2$ sensor, for which the current reached a

compliance of 100 μA at 30 V of bias.

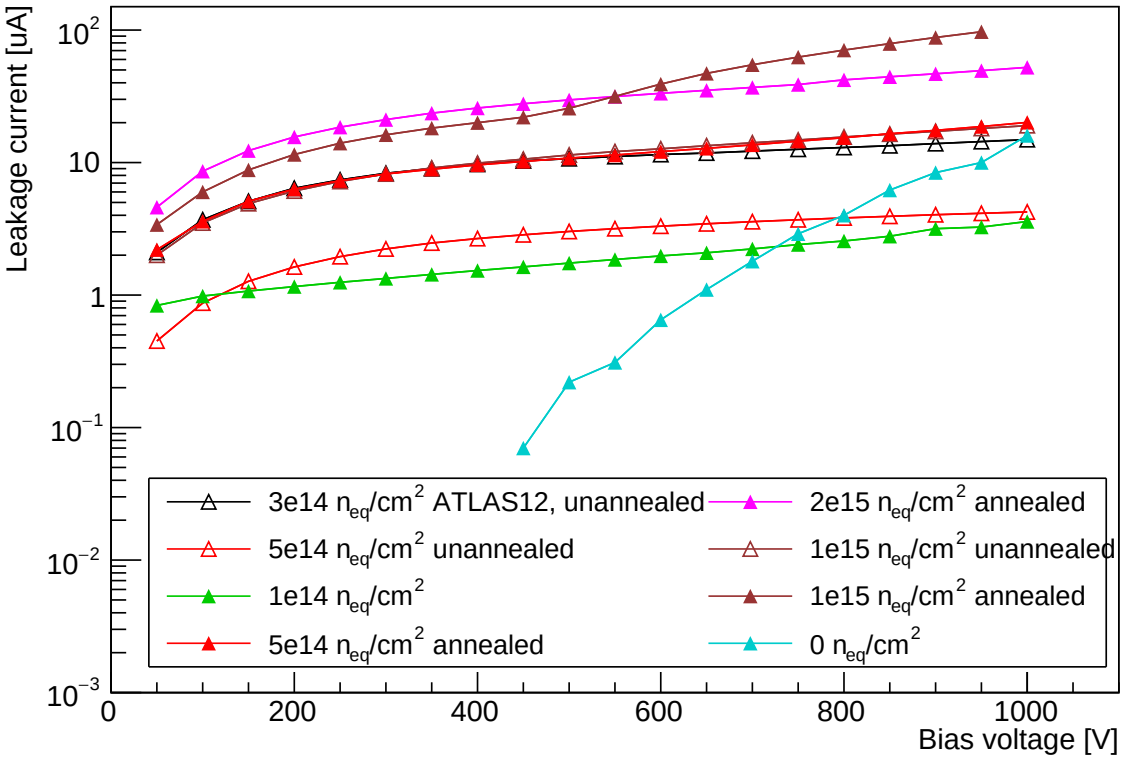

Figure 4.9: Plot of IV curves for ATLAS17 sensors.

4.5 Interstrip Resistance Measurements

Based on the increased cluster width measured in irradiated sensors, and high TID of the irradiation, it was suspected that there may be insufficient interstrip resistance, that is, less than the 1.5 MΩ of the bias resistors, due to surface damage. To investigate this, the interstrip resistance was measured at the University of Cambridge.

4.5.1 Methodology

Sensors were mounted on small boards and three adjacent strips were biased to measure the interstrip resistance. The outer two strips were connected to a power supply with bias V_s and the middle strip to ground. The supply voltage V_s was varied and a voltmeter was used to

measure the voltage on the middle strip. A circuit diagram of the setup is show in Fig. 4.10, where R_b is a 1.5 MΩ bias resistor.

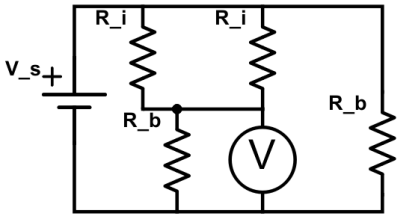

Figure 4.10: Circuit diagram for the interstrip resistance measurement. R_b is the bias resistance, R_i the interstrip resistance, V_s the source voltage, and V the voltmeter.

For this circuit, we find that

$$V = \frac{V_s R_b}{R_b + \frac{R_i}{2}} \tag{4.5}$$

then

$$\frac{dV}{dV_s} = \frac{R_b}{R_b + \frac{R_i}{2}} R_i = 2R_b \left(\frac{1}{dV/dV_s} - 1 \right) \tag{4.6}$$

and we can solve for the interstrip resistance as

$$R_i = 2R_b \left(\frac{1}{dV/dV_s} - 1 \right) \tag{4.7}$$

with V_s the low voltage output, R_i the interstrip resistance, and R_b the bias resistor resistance. In order to measure R_i, the lower voltage power supply output, V_s, was increased from -5 V and +5 V in 0.5 V steps and the voltage over the middle strip, V, was measured. A linear fit of V versus V_s was then used to determine dV/dV_s and thereby R_i. To deplete the sensor bulk, negative high voltage was sourced from the backside. Measurements were made at bias voltages of 200, 400, 600, and 800 V.

4.5.2 Results

In Fig. 4.11, the measured interstrip resistances are plotted versus the bias voltage for the 10 STD Mini sensors measured. With the exception of one unannealed $\phi = 2\times10^{15}$ $n_{\mathrm{eq}}/\mathrm{cm}^2$ sensor, the interstrip resistances are well above the bias resistor resistance of 1.5 MΩ. Furthermore,

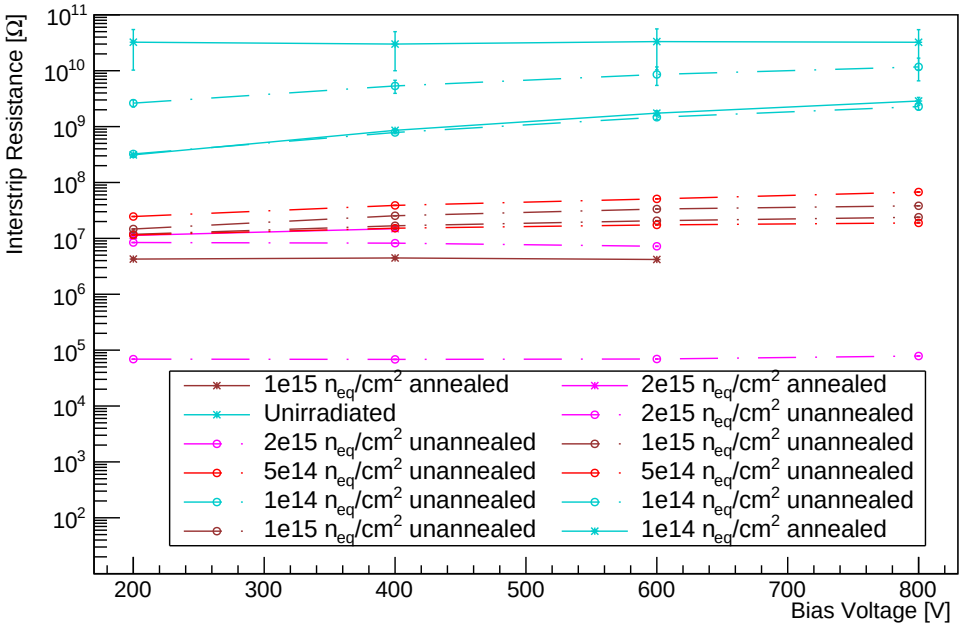

Figure 4.11: Plot of measured interstrip resistance values for the ATLAS STD Minis.

in comparison to results previous studies with ATLAS12 Minis shown in Fig. 4.12, which were measured to have sufficient radiation tolerance, the results for the annealed sensors were not anomalous [11] and showed the ATLAS17 sensors were radiation tolerant in terms of interstrip resistance and that a lack of strip isolation due to surface damage did not explain the low CCE or the anomalously high cluster sizes. measured in the ATLAS17 sensors.

4.6 Conclusions

Measurements of ATLAS17 STD Miniature strip sensors irradiated at Birmingham yielded results that were somewhat anomalous: IV measurements showed an increase in current after annealing and CCE measurements suggested that the radiation tolerance may not be sufficient and that cluster widths were increasing with irradiation. Comparison to measurements of sensors irradiated and tested at other facilities demonstrated that sensors were in fact radiation tolerant to 2×10^{15} $n_{\mathrm{eq}}/\mathrm{cm}^2$ and spurred further investigation into the MC40 beamline. The discrepancy of the Birmingham results was thought to be perhaps due to surface damage decreasing the isolation between strips, but measurements confirmed the interstrip resistance

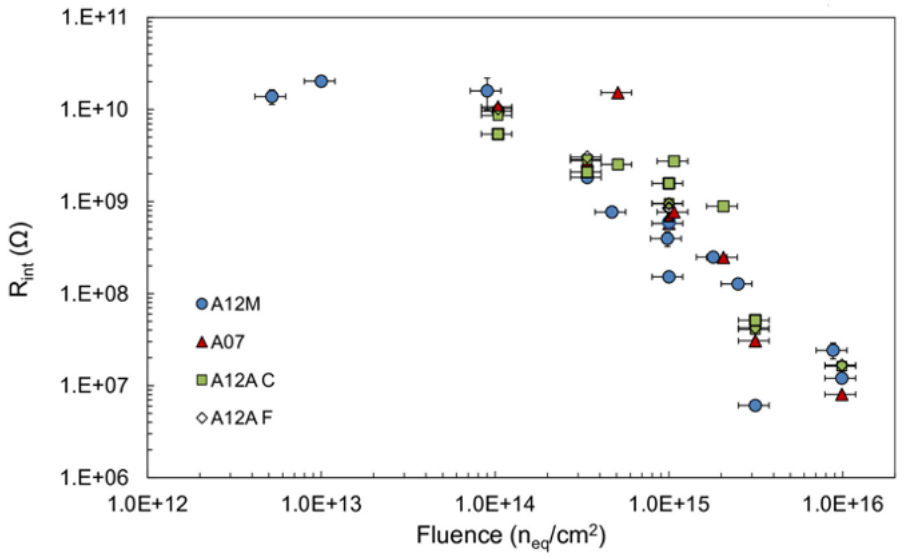

Figure 4.12: The interstrip resistance measured in ATLAS12 strip sensors irradiated at CYRIC in [11].

was sufficient to $\phi = 2 \times 10^{15}$ $n_{\text{eq}}/\text{cm}^2$ and consistent with previous results with ATLAS12 sensors. Further studies ([57,62]) remeasured the hardness factor and yielded results consistent with other facilities with scanning irradiations at Birmingham which should help mitigate the effects of sample heating. There seem to be two sources of discrepancy in the Birmingham irradiation: unaccounted for beam components and heating of the samples related to point-to-point irradiations, which can seemingly be mitigated with scanning irradiations. While these latest results with scanning irradiations are encouraging, there is further work to understand and refine the irradiation procedure to be more reproducible and allow for greater contributions towards being part of a routine quality assurance procedure for radiation hardness studies.

Chapter 5

The MALTA CMOS sensor

In this chapter, the design and characterization results of the first version of the Monolithic ALICE To ATLAS (MALTA) pixel sensor, a CMOS depleted monolithic active pixel sensor originally intended for inclusion in the pixel outer barrel of the ITk, are presented [47]. This first version of the sensor was demonstrated to have radiation tolerance to 5×10^{14} $n_{\mathrm{eq}}/\mathrm{cm}^2$, but not to the requirement for the outer layer of the ITk, 1×10^{15} $n_{\mathrm{eq}}/\mathrm{cm}^2$. As such, MALTA was not selected from a group of competing pixel technologies to construct the pixel ITk, and more recent prototypes, MiniMALTA and MALTA Cz, were developed to improve the radiation tolerance for potential installation in the ITk beyond Run 4. The design and characterization of MiniMALTA and MALTA Cz are discussed in Chapters 6 and 7, respectively. These new devices have improved radiation tolerance and have motivated and informed the design and production of further iterations of the sensor, MALTA 2 and the planned production of MALTA 3.

5.1 MALTA chip design

The MALTA sensor is a DMAPS produced in the TowerJazz 180 nm modified process as described in Section 3.3.2.3 and shown in Fig. 5.1(b) with a 25 or 30 μm epitaxial layer for charge collection and an additional low-dose n^- layer in the sensor as a modification from the standard process used for ALPIDE and shown in Fig. 5.1(a) [42]. MALTA is one of two devices produced in this technology, the other being the MonoPix sensor [48]. In the context of

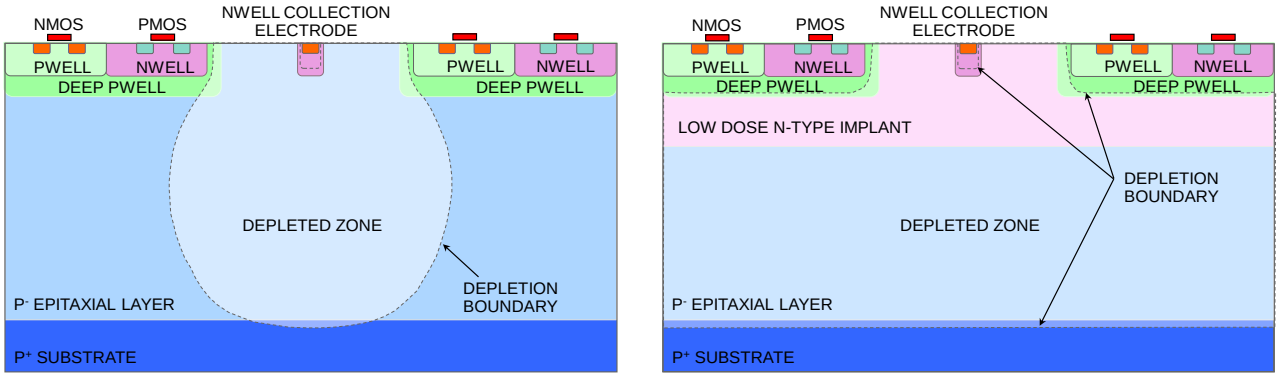

(a) The standard process used for the ALPIDE sensor.

(b) The modified process used for the MALTA and MonoPix sensors.

Figure 5.1: Schematic of the TowerJazz 180 nm CMOS imaging sensor processes.

ATLAS, they are both "small collection electrode" sensors. The key difference between them is the asynchronous readout architecture in MALTA, which is described in Sec. 5.1.2.

The MALTA chip has a 512×512 matrix of 36.4×36.4 μm^2 pixels, meaning it covers 1.87×1.87 cm^2 of the diced chip total area of 2×2.2 cm^2. As a small collection electrode DMAPS, a pixel of MALTA has a small collection electrode for low capacitance (near 5 fF) and therefore low power consumption and noise. Each pixel contains an analog front-end with a pre-amplifier and discriminator which is tuned by setting digital to analog converters (DACs) at the bottom of the pixel matrix. The digital and analog circuitry in a pixel are separated to reduce crosstalk between the two as shown in Fig. 5.3. There are also 8 monitoring pixels, 4 with the diode reset and 4 with the PMOS reset, for measurement of the analog output prior to discrimination. The asynchronous readout architecture does not require clock distribution to the matrix, reducing the power consumption of the device.

The pixel matrix is divided symmetrically into eight columns or "sectors" each 32 pixels in width with variations in the reset mechanism and size of the collection electrode and deep p-well implant, as shown in Fig. 5.2. The sectors on the left half of the device have a diode reset, and those on the right side have the PMOS reset. Test beam measurements focused on Sectors 2 and 3 of MALTA, which feature the diode reset, the slightly larger 3 μm collection electrode (for faster charge collection) and the slightly smaller 3.5 μm spacing between the electrode and deep p-well housing the electronics.

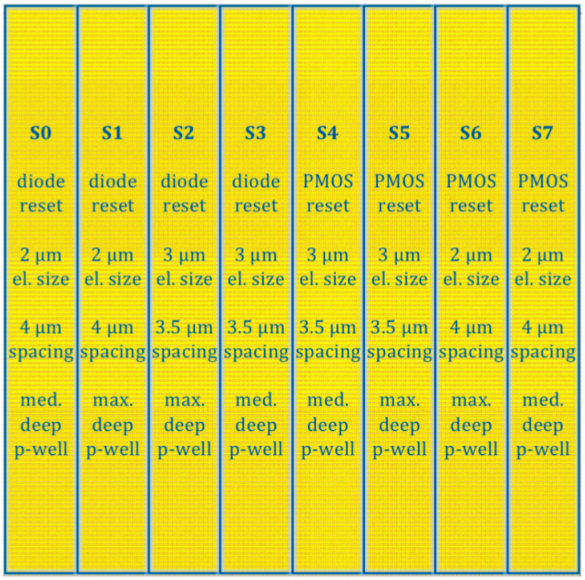

Figure 5.2: Mapping of the eight 32 × 512-pixel sectors of MALTA with variations in collection electrode and p-well implant geometry.

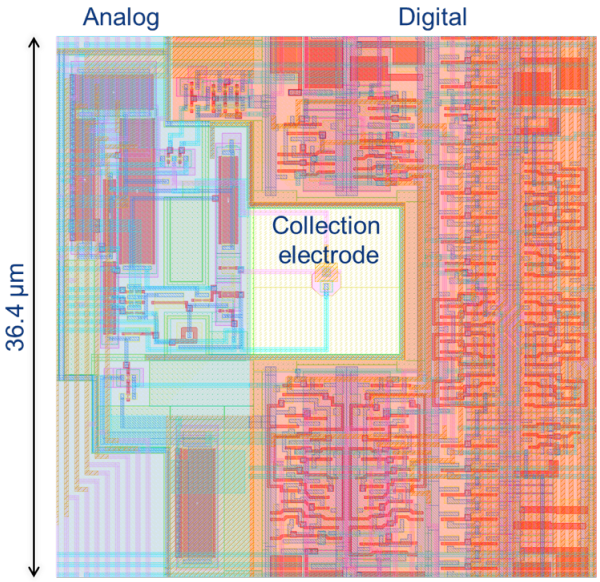

Figure 5.3: Design of the MALTA pixel.

On the periphery of the chip, below the matrix, is digital circuitry for readout and what is referred to as the Slow Control for chip configuration. For data transmission there is a 40-bit parallel psuedo-Low Voltage Differential Signal (LVDS) (called LAPA (pseudo-LVDS for the ATLAS Pixel Apparatus) [63, 64]) output capable of operation at 5 Gb/s. On the periphery on the sides are 1.8 V CMOS standard input/output pads for communication between chips.

The Slow Control block of MALTA consists of a pool of registers which configure the operation of MALTA and a finite state machine to set and read the registers in the pool. These registers set the digital to analog converter (DAC)s of MALTA. Unfortunately, in the original version of MALTA, the slow control could not be used to change the register pools from their default configuration, and the DACs were controlled with external power supplies when operating the original MALTA sensors.

5.1.1 Analog front-end

A block diagram of the analog front-end is shown in Fig. 5.4 and in Fig. 5.7 is the circuit diagram, which will be discussed in more detail below. The analog front-end in each pixel contains a voltage reset circuit, an amplifier, and discriminator. There is also a calibration

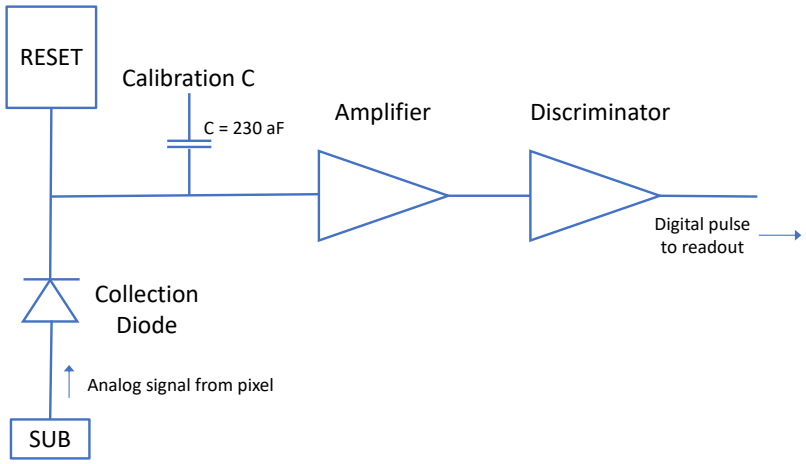

Figure 5.4: Block diagram of the analog front-end.

capacitor which can be sent a voltage pulse to inject a known charge and measure the response of the front-end. The front-end design is based on the ALPIDE front-end, but has been modified to decrease the shaping time from about 2 μs to less than 25 ns for implementation in ATLAS. After amplification, the discriminator converts analog signals which are above an adjustable threshold into digitized pulses that are sent to the digital readout.

There are two reset mechanisms in MALTA, a diode reset and a PMOS-based reset, however, only the diode reset (in Sectors 0, 1, 2, and 3) is discussed since the sensor had extremely high noise when the PMOS sector was turned on.

A schematic of the diode reset is shown in Fig. 5.5. The reset diode resets the voltage of the collection electrode, IN in the figure, after charge collection. The reset diode is forward biased by the VRESET_D DAC, which is near 1.3 V, and the leakage current of the sensor diode. The collection electrode bias is the VRESET_D voltage minus the voltage drop across the reset diode, which is around 500 mV. When the current in the sensor diode increases due to energy deposition from particle in the sensor, electrons flow to the collection electrode and the voltage drop across the reset diode increases. This results in more current flowing across the reset diode until the voltage of the collection electrode is increased to its original value. This process can take hundreds of microseconds and is slow compared to the charge collection which

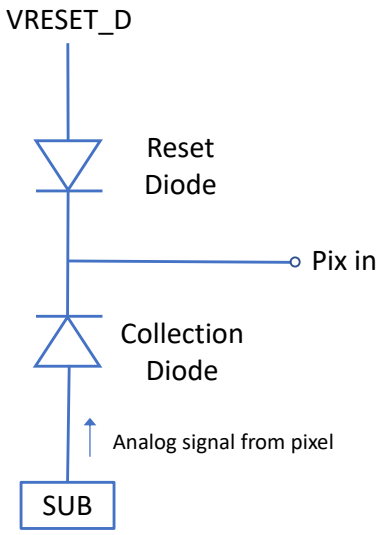

Figure 5.5: Schematic of the diode reset.

takes tens of nanoseconds. The reset is continuous, as opposed to periodic, meaning that the reset circuit is always active.

The front-end amplifier is based on the amplifier used in the ALPIDE sensor [42]. The operating principle of the amplifier is illustrated in Fig. 5.6. The PMOS transistor M1 acts as a source follower biased by the current DAC IBIAS, and has its gate connected to the collection electrode, labeled PIX IN. AVDD is the analog bias, usually 1.8 V. The gain is based on transferring the charge from the collection electrode $Q_{IN} = C_{IN}V_{IN}$ to a large capacitor C_S and then to a small capacitor C_{OUT_A} and the output can be estimated as:

$$\Delta V_{OUT\_A} = \frac{Q_S}{C_{OUT\_A}} = \frac{C_S}{C_{OUT\_A}}\Delta V_{IN} = \frac{C_S}{C_{OUT_A}}\frac{Q_{IN}}{C_{IN}} \tag{5.1}$$

where C_{IN} is the total input capacitance of the detector including the stray capacitance of the preamplifier. With the small collection electrode, the capacitance should not vary much even if the depletion depth does, and so the gain should remain relative constant for a wide range of voltage drops between the substrate and collection electrode.

The other feature of the MALTA front-end is circuitry for calibration measurements with

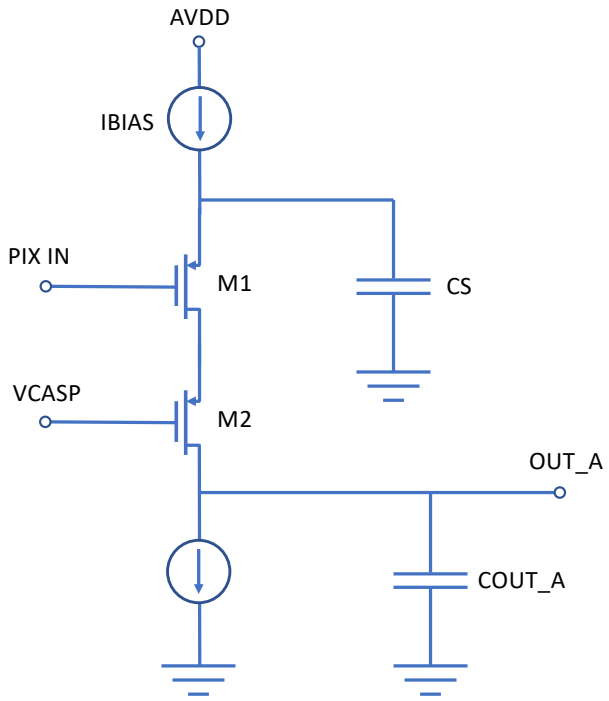

Figure 5.6: Schematic illustrating the operating principle of the amplifier.

injected pulses such as those required for threshold scans. The amount of injected charge in a calibration pulse Q_{CAL} can be calculated from the appropriate DACs as

$$Q_{CAL} = C_{IN}\Delta V_{IN} = C_{IN}\frac{C_C}{C_{IN}+C_C}\Delta V_{DAC} \approx C_C(V_{HIGH} - V_{LOW}) \tag{5.2}$$

where V_{HIGH} and V_{LOW} are voltage DACs, $V_{DAC} = V_{HIGH} - V_{LOW}$ is the voltage value set by the DACs, and C_C is the capacitance of the calibration capacitor, 230 aF. For the last approximation, C_C is assumed to be much smaller than the sensor capacitance C_{IN} that is on the order of fF.

A schematic of the actual front-end is shown in Fig. 5.7. AVDD is the analog voltage, typically 1.8 V, and AVSS is the common ground. The signal from the pixel is input onto the gate of the M1 transistor and M0 acts as a current source with current IBIAS. M2 is a cascode transistor included to increase bandwidth, the bias VCASP was generally not adjusted. M5 and M6 define the baseline voltage of OUT_A and provide feedback to return the signal to baseline, thereby reducing dead time. M7, M8, and M9 form a discriminator where the threshold is set

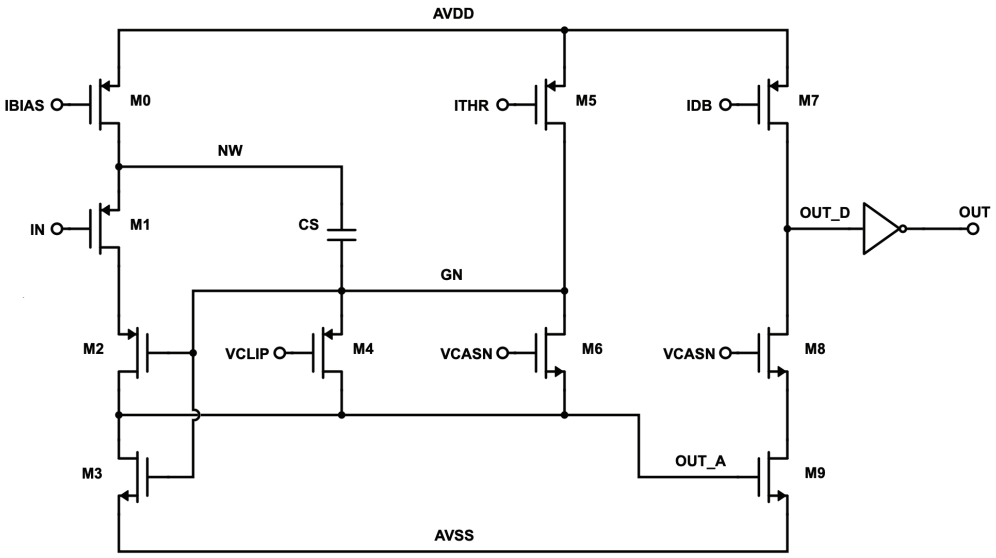

Figure 5.7: Schematic of the MALTA front-end [65].

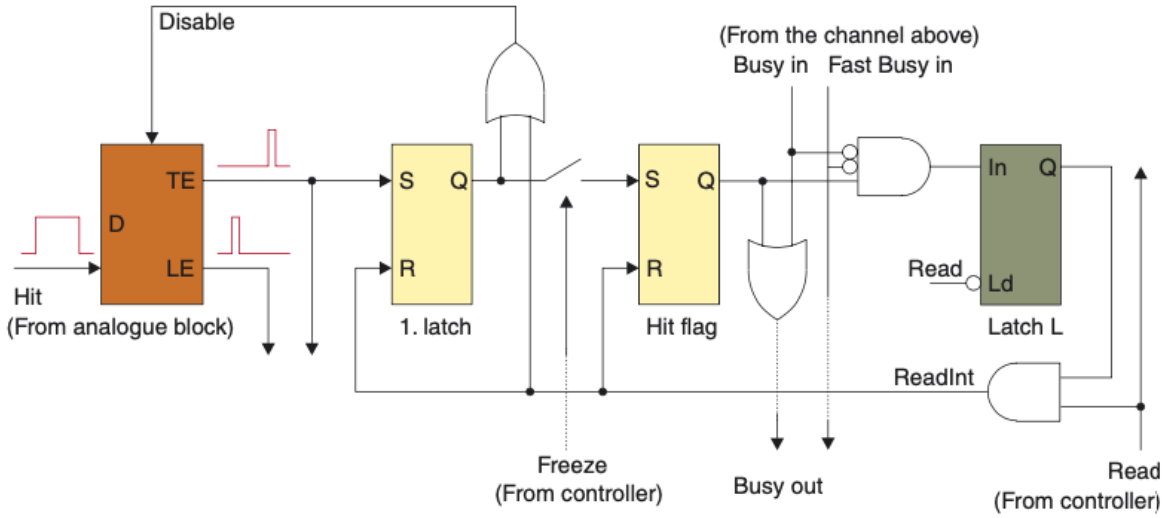

Figure 5.8: Schematic of the column drain readout in MonoPix, reproduced from [66].

by the DACs for the threshold and pedestal called "IDB" and "VCASN," respectively.

5.1.2 Digital readout

As discussed previously in Sec. 3.3.2.3, the MAPS MALTA and MonoPix were developed as tracking sensors for the ATLAS ITk based on the TowerJazz Investigator and ALPIDE designs, but have different readout architectures: synchronous for MonoPix and asynchronous for MALTA. In a simpler architecture, such as a rolling shutter readout in the original MIMOSA,

every single pixel is readout in sequence in a set order. For larger matrices and higher readout speeds this architecture is not suitable. A significant improvement can be made by reading out the columns in parallel. An additional strategy is to include a discriminator in the circuitry for each pixel so that only pixels with a hit above threshold will transfer a signal, thus achieving "zero suppression." Then, logic is used to read out the pixels such that signals from nearby pixels and close in time do not overlap, but instead have synchronization relative to each other. In an asynchronous readout, there is no order in which hits should be read, instead signals propagate directly to the bus lines as they arrive. Therefore an asynchronous readout architecture such as that of MALTA must be carefully designed relative to the application to ensure there are unlikely to be overlapping hits in time which lead to degraded performance.

The Monopix device features a synchronous "column drain" readout architecture, a schematic of which readout is shown in Fig. 5.8. In this readout, a token logic is used to only read pixels which contain a hit, making it a form of zero-suppressed readout. Hits from the analog front-end are used to generate short (∼ns) leading edge (LE) and trailing edge (TE) pulses which are time stamped by a 40 MHz clock to match the frequency of LHC bunch crossings. These time stamps are stored in in-pixel 8-bit RAM until a ReadInt signal is received, and allow for Time over Threshold (ToT) measurements, in which the time that an analog signal spends above a given voltage threshold is measured as a proxy of the pulse amplitude. The TE is used to generate a hit flag in the first latch, which disables the detection of new hits and sends a Busy signal down the column. The controller sends a "Freeze" signal through the column, preventing new hits from propagating past the first latch while still allowing new hits to be stored in the latch until the pixel is finished reading. The controller also sends a Read signal which generates the ReadInt signal through an AND gate with the hit flag as the other input. The ReadInt signal connects the RAM and ROM containing the timestamps and pixel address to a data bus to be readout. The ReadInt also resets the first and second latches, and the third is enabled once the Read signal ends. At this point, the pixel is ready to record a new hit.

In contrast, the MALTA chip has a novel asynchronous digital readout architecture, described in [64, 65, 67] and elsewhere. Unlike in the column drain readout architecture, a clock is not

propagated to the matrix for in-pixel time-stamping and ToT, significantly reducing the power consumption of the digital portion of the device, which goes as the square of the clock frequency. For the outer layer on the ITk, this results in a reduction of the digital power consumption by a factor of 20 [68]. For the inner layers, the reduction is not as drastic since on average a larger fraction of MALTA's matrix will be active due to the higher hit rates. While MALTA has a binary readout that does not provide a ToT measurement, in principle some charge information can be recovered from the cluster size and time walk information [65].

For the asynchronous readout, the 512×512 pixel matrix is organized in 256 "double columns" which are each two pixels wide. Within a double column there are alternating red and blue groups of 2 (column)×8 (row) pixels as shown in Fig. 5.9, and together the 256 double columns create a sort of checkerboard pattern of red and blue groups. The advantage of this architecture is that pixels hits from from adjacent groups are different colors and will not share a bus, therefore decreasing the likelihood of collisions on each bus and increasing the rate capabilities of the readout. Each color is coupled to its own 22-bit pixel bus, with 16 bits for the pixel hits and five for the group address (since there are 32 red groups and 32 blue groups in each double column), and one reference bit which indicates the presence of a hit. When the discriminator of a single pixel is fired, it activates signals for the reference, group number, and pixel within the 2×8 group. The signal corresponding to "1" is an electrical pulse with an adjustable width of 0.5, 1, or 2 ns. The delay in the transmission lines to the bus is matched so that the individual pulses on each of the 22 bus lines arrives at the periphery simultaneously. If the discriminators from multiple pixels in the same group fire within approximately 1 ns of each other, both corresponding signals will be included in the same word and the corresponding bits of the 16-bit address will be set to 1. If they are sufficiently separated in time, the second hit will be propagated after a short delay to be included in a separate word. Importantly, in this way, all hits that reach threshold will be read; they are not lost. The word is propagated through a buffer and reaches the periphery of the pixel matrix within 25 ns. To readout pixel hits from the same incident particle in the same word requires that the energy deposited in each pixel is comparable, otherwise, due to the time walk of the sensor, the crossing time could

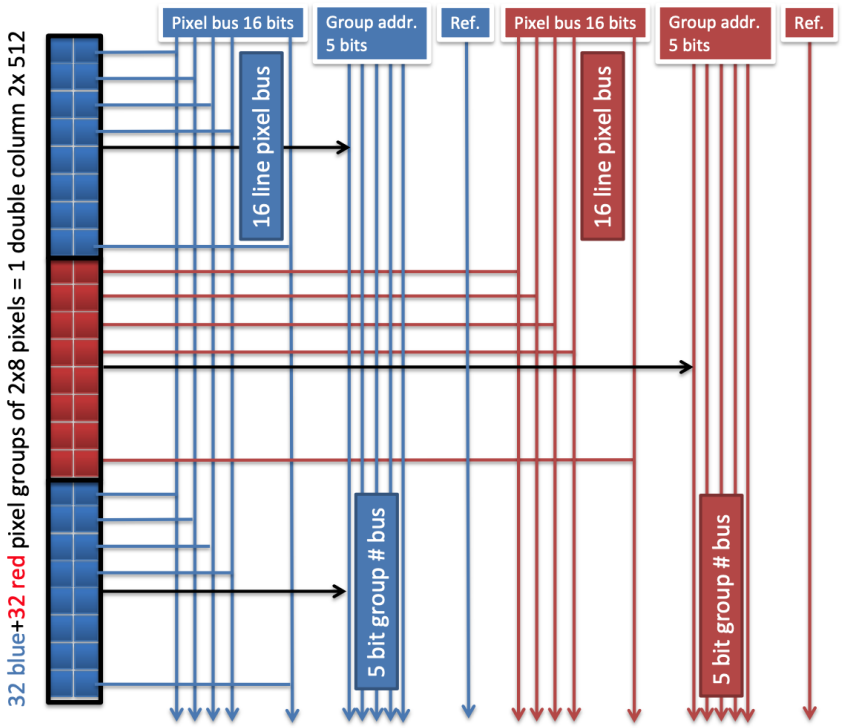

Figure 5.9: Schematic of the red and blue groups in the asynchronous readout architecture of the MALTA, reproduced from [69].

be sufficiently different and the hits not associated.

The buffer is designed to precisely maintain the duration and relative time of arrival of pulses. It is composed of a series of NAND gates as shown in Fig. 5.10. For each red group, one terminal of the NAND gate is connected to the output of the group, and the other to signals from higher in the column. This NAND gate is followed by an inverter made from a second NAND gate with one input set to 1, and the output of this is sent to the NAND gate connected to the next red group. Successive NAND gates are used instead of single OR gates to ensure the that the pulse duration is kept constant. By inverting the signal, the rising/falling edge of the input pulse becomes the falling/rising edge of the output. This protects against possible differences in the delay of the rising and falling edge that could cause pulses to become elongated or disappear entirely after many successive buffers through the same same type of gate with the same polarity. The structure of a NAND gate followed by an inverter necessitates that the pixel groups' output signals are active low.

In the case of multiple words in different groups of the same color and double-column, they

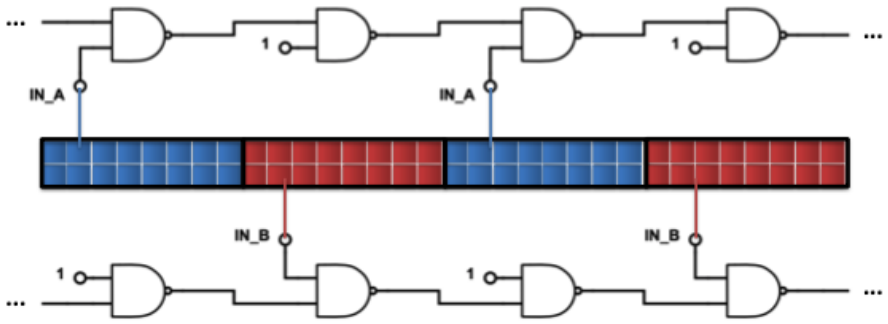

Figure 5.10: Schematic of NAND buffer, reproduced from [65]

will usually be propagated as two words in series. However, if a signal enters the buffer while one is already present, there will be an OR of the two signals, resulting in a single corrupted word instead of two correct words. This is mitigated by the alternating red and blue groups. For L4 of the ITk the hit occupancy is low enough that such corruption should be rare.

After traveling through the buffer and reaching the periphery hits undergo merging via a nine-layer binary tree structure before being read out. In the first level of merging, hits from the red and blue buses in the same double column are merged onto one bus and a bit is added to identify the hit as coming from a red or blue group. A delay bit is added to indicate if a word has arrived simultaneously with another and has been delayed via arbitration logic similar to the one used in the pixel. A 2-bit counter running at 40 MHz is used to add a bunch crossing identification (BCID). In the second step, the delay counter is expanded to three bits in order to accommodate for a word being delayed up to seven times in the entire merging process. A shortcoming of this delay structure is that a pulse may be delayed up to nine times in the nine levels of merging, though simulations show that is rare to have more than seven delays in L4 of the ITk. For environments with significantly higher occupancies, there would need to be further design considerations to achieve faster output, such as RAM for each double column that would read out to a FIFO and then to serializer at 10 Gbps. At each level of merging after the first, a bit is added to indicate if the signal comes from the left or right double column(s), resulting in an 8-bit double column address after 9 levels of merging.

An additional tenth layer merges words from multiple chips which may be connected and

four bits are added to indicate which chip hits come from, allowing for up to 16 chips to be connected in theory. In total, this results in 40-bit words, which are encoded as in Table 5.1: one reference bit, 16 bits for the pixel address, five bits for the group address, one bit for the group color, three bits for the delay counter, eight bits for the double column, two bits for the BCID, and four bits for the chip identification.

Bits	Contents
0	Reference
1-16	Pixel address
12-21	Group address
22	Group identification
23-25	DELAY counter
26-33	Double column address
34-35	BCID counter
36-39	Chip identification

Table 5.1: Encoding of the 40-bit words output by MALTA.

As a backup to the merging described above, The MALTA chip also features a simpler merging architecture that consists of a binary tree of OR gates. Instead of incrementing a delay counter, hits which arrive simultaneously are merged with OR logic, resulting in a single corrupted word instead of two separate correct words. For the test results presented in this thesis the more complicated merger could not be used and instead the simpler backup merger was used. For applications with low hit rates including these results this OR merging is sufficient, though there is evidence of the OR merger in test beam and other measurements. Future versions of the device with an operational merger can be expected to have improved results.

The 40-bit words are transmitted off chip in parallel using either the low-voltage differential signal (LVDS) or 1.8 V CMOS standard. The LVDS drivers are designed to operate up to 5 Gb/s and the the CMOS standard allows for transmission of data between multiple chips. The CMOS input/output pads are on the sides of the chip, allowing for chaining of chips in the horizontal direction with LVDS readout for up to 16 chained chips.

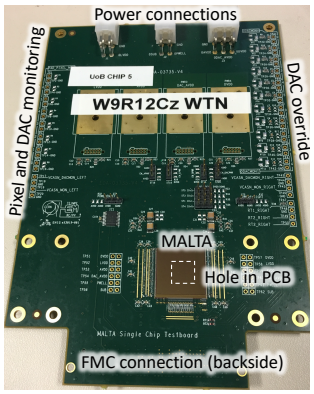

(a) The MALTA carrier board with a MALTA chip mounted and wire bonded.

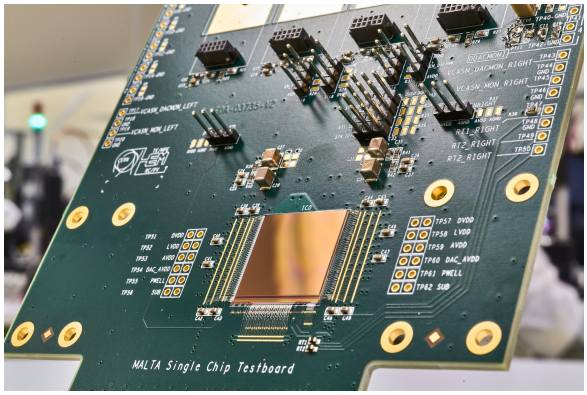

(b) Closeup of MALTA on the carrier board.

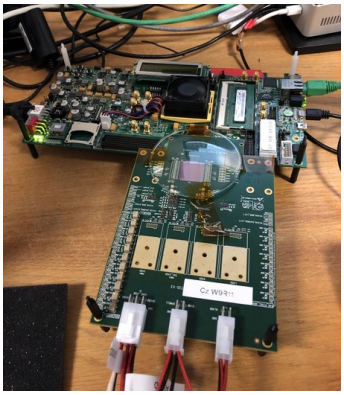

(c) The MALTA readout system, set up at CERN.

Figure 5.11: Bonded MALTA samples.

5.1.3 The MALTA readout system

For data acquisition and characterization, MALTA chips are mounted on carrier boards which allow independent powering of the substrate, p-well, analog front-end, DACs, digital pulsing, and LVDS drivers. Photographs of the board with a chip mounted are shown in Fig. 5.11(a) and 5.11(b). The board is coupled via an FPGA Mezzanine Card (FMC) connector to a VIRTEX VC707 FPGA evaluation board as shown in Fig. 5.11(c) to readout data with custom firmware. The backside of the chip (and thereby the substrate) is electrically coupled to the board using conductive glue. Pads along the sides and bottom of the chip for powering the analog, digital, and LVDS drivers are connected to the board with wire bonds. There is a $1{\times}1$ cm^2 hole in the board to allow for particles to pass through with minimal multiple scattering and attenuation, which is useful for characterization including precise track reconstruction in test beams. On the sides of the board are trimmers to override the DACs for configuring the front-end and connections to monitor selected DACs and the outputs of the 8 monitoring pixels.

5.2 Test beam measurements of irradiated MALTA

The in-pixel efficiencies of the irradiated and unirradiated MALTA devices were measured in a beam of 180 GeV pions at the Super Proton Synchrotron (SPS) test beam facility at CERN.

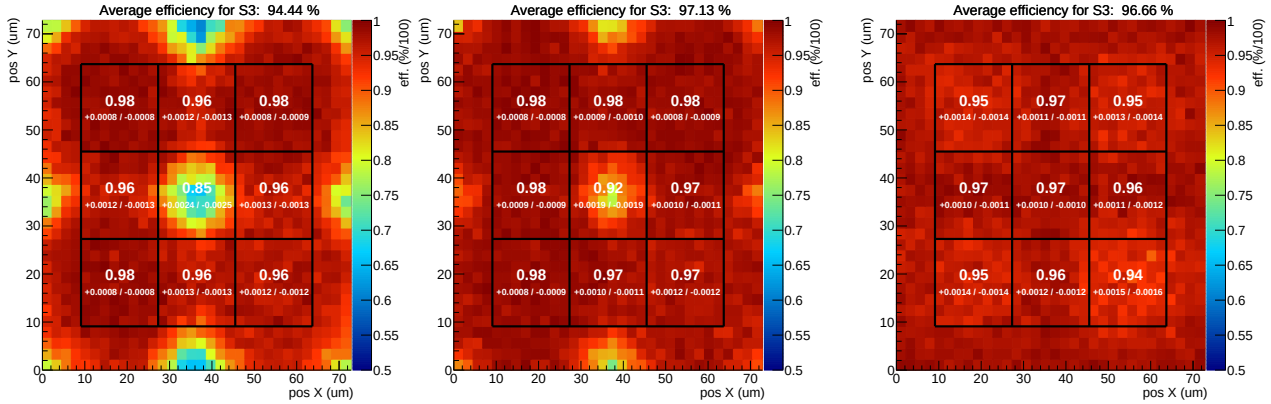

(a) Threshold of 600 e (b) Threshold of 400 e (c) Threshold of 250 e

Figure 5.12: In-pixel efficiency measurements of unirradiated MALTA samples with measurements from 2×2 pixel regions combined to improve statistics. The average efficiency is written above each plot, and the average efficiency of each region contained in a 3×3 grid is written on the plot.

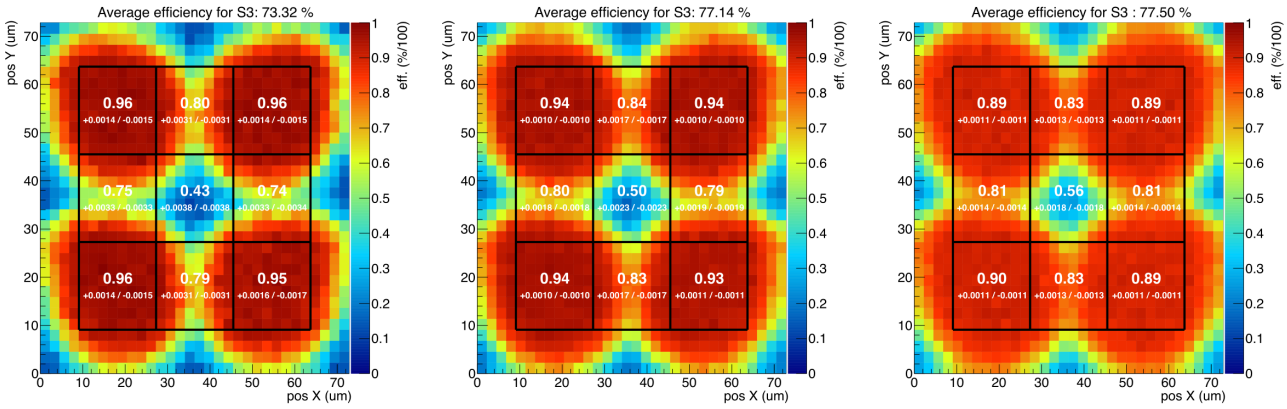

(a) Threshold of 320 e (b) Threshold of 250 e (c) Threshold of 230 e

Figure 5.13: In-pixel efficiency measurements of MALTA samples irradiated to $\phi = 1 \times 10^{15}$ $n_{\mathrm{eq}}/\mathrm{cm}^2$ with measurements from 2×2 pixel regions combined to improve statistics. The average efficiency is written above each plot, and the average efficiency of each region contained in a 3×3 grid is written on the plot.

Irradiated devices were irradiated with 1 MeV neutrons at the TRIGA reactor in Ljubliana, Slovenia [54] to fluences up to 1×10^{15} $n_{\mathrm{eq}}/\mathrm{cm}^2$. The Kartel telescope based on MIMOSA sensors was used to record tracks passing through MALTA and has a resolution of approximately 2 μm [38, 41]. The MALTA DUT was measured in a cold box and kept at -20 °C to prevent annealing and reduce the leakage current in irradiated devices. Events were reconstructed using the Proteus software package [70].

The measured in-pixel efficiencies for Sector 3 of an unirradiated sensor at three threshold levels are shown in Fig. 5.12. These in-pixel plots were made by combining the measurements from many sets of 2×2 pixels, and thus are an average of the efficiency in the entire sector. The binning corresponds to 15×15 entries per pixel. The substrate and p-well were biased at 15 V and 6 V, respectively. For the measurements with thresholds at 600 e and 400 e in Fig. 5.12(a) and 5.12(b), the efficiencies near the corner of the pixel far from the collection electrode are lower than in the center of the pixel. At a threshold of 250 e, shown in Fig. 5.12(c), the efficiency in the pixel edges improves.

For the irradiated (but not annealed) sensor with a fluence of 1×10^{15} $n_{\mathrm{eq}}/\mathrm{cm}^2$, the efficiency in these regions remains low at the same thresholds, resulting in an overall efficiency below 78 % at -15 V substrate bias as shown in Fig. 5.13. By decreasing the threshold to 230 e, the efficiency in the pixel periphery improves, but in the pixel center it is surprisingly lower than at higher thresholds as seen by comparing 5.13(a) and 5.13(b) to 5.13(c). This is due to the increase in noise at the lower threshold which results in hits being merged together in the the backup merging scheme in which the readout for simultaneous words is an OR of the two words. These corrupted words obfuscate good hits and decrease the measured efficiency since the merged hits are unlikely to pass the fiducial cuts.

At the time that these measurement were made, CMOS sensors were still being considered for installation in layer 4 of the ITk pixel barrel. However, since the required radiation hardness was 1×10^{15} $n_{\mathrm{eq}}/\mathrm{cm}^2$, hybrid pixel sensors were selected for installation in the ITk due to their superior radiation hardness, and the MALTA test beam results motivated design changes to improve the radiation hardness of MALTA and other small collection electrode CMOS sensors. These changes included modifications to the pixel and front-end design which were implemented in a miniature prototype known as MiniMALTA, the subject of the next chapter.

Chapter 6

Characterization of the MiniMALTA sensor

Following the unexpected results with the first version of MALTA in which the particle detection efficiency was below 78 % at 1×10^{15} $n_{\mathrm{eq}}/\mathrm{cm}^2$, a smaller prototype of the sensor, MiniMALTA, was made with design changes to improve its radiation hardness. MiniMALTA has a 16×64 pixel matrix, instead of the 512×512 pixel matrix and is divided into sectors with modifications to the pixel substrate and/or front-end, with one sector with the original MALTA design for comparison to other sectors as well as the results with the first version of MALTA. In test beam and laboratory measurements summarized in this chapter, the design modifications in MiniMALTA were demonstrated to result in improved efficiency (as high as 98.8 % at $\phi = 1 \times 10^{15}$ $n_{\mathrm{eq}}/\mathrm{cm}^2$ and 93.7 % at $\phi = 2 \times 10^{15}$ $n_{\mathrm{eq}}/\mathrm{cm}^2$) and the desired changes in the front-end characteristics both before and after irradiation.

6.1 Chip design

In the original design of the MALTA pixel, shown in Fig. 6.1(a), a continuous lower doped n-type layer is created in the pixel matrix by means of a low dose high energy implant. By either creating a gap in the n^- layer or including an additional deep p-well implant in that region, as shown in Fig. 6.1(c) and 6.1(b), respectively, the lateral field near the pixel edge could be

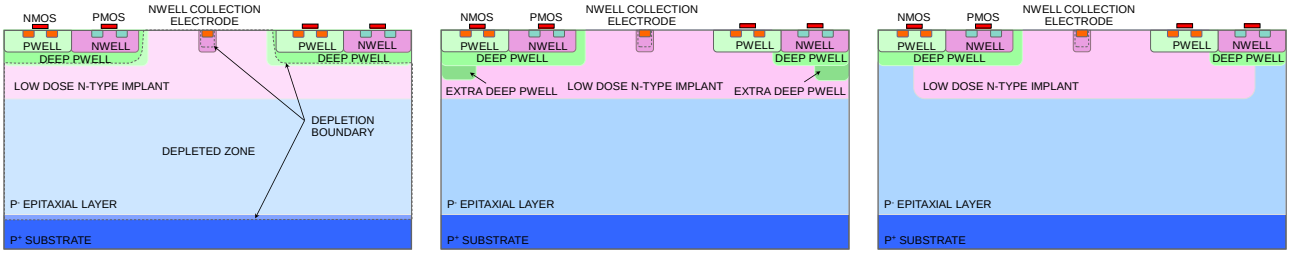

(a) The standard MALTA substrate with the continuous n^- layer.

(b) The extra deep p-well substrate.

(c) The n^- gap substrate.

Figure 6.1: Schematics of the 3 pixel substrate designs in MiniMALTA [64].

increased. Henceforth, the different pixel designs will be referred to as "n^- gap," "extra deep p-well," and "continuous n^-."

In Fig. 6.2 are Technology Computer Assisted Drafting (TCAD) [71] simulations of the electrostatic potential and corresponding electric field lines in these designs with a bias of 6 V on both the substrate and p-well from [72]. The p-well region is in the center of these plots, and the star symbol indicates the potential minimum. There is a clear increase in the lateral component of the electric field (towards the collection electrode) in the new n^- gap and extra deep p-well designs. This should lead to faster charge collection and improve the amplitude of the signal due to reduced trapping for particles that pass through and ionize the silicon beneath the deep p-well, thus improving the detection efficiency in these regions. Simulations of the generated signal current and integrated charge, shown in Fig. 6.3, demonstrate this sort of improvement both before and after irradiation to 1×10^{15} $n_{\mathrm{eq}}/\mathrm{cm}^2$. Based on simulation, the n^- gap and extra deep p-well designs were implemented in MiniMALTA. The n^- gap is achieved by a change to a mask, and the additional deep p-well is a process modification.

The analog front-end was also modified, in this case to improve the threshold behavior and gain. Initial measurements of the front-end circuit on the MALTA sensor revealed significant random telegraph signal (RTS) (or "popcorn") noise preventing lower threshold settings [73]. This was attributed to a specific transistor referred to as "M3" in the design schematic shown Fig. 5.7. The transistor size was made larger to decrease the RTS noise. Further measurements confirmed the output transconductance of this transistor was higher than expected, and caused gain degradation for the front-end. In addition it was suspected that for lower threshold settings

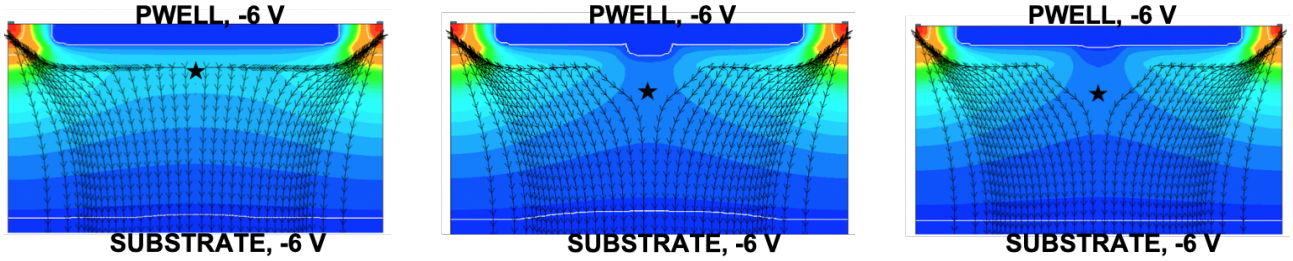

(a) The continuous n^- substrate. (b) The extra deep p-well substrate. (c) The n^- gap substrate.

Figure 6.2: TCAD simulations of electrostatic potential of the three pixel designs of MiniMALTA [72]. The figures are centered on the p-well implant, not the collection electrode, and the star marks the potential minimum. The substrate is biased to -6 V, and the collection electrode to 0.8 V.

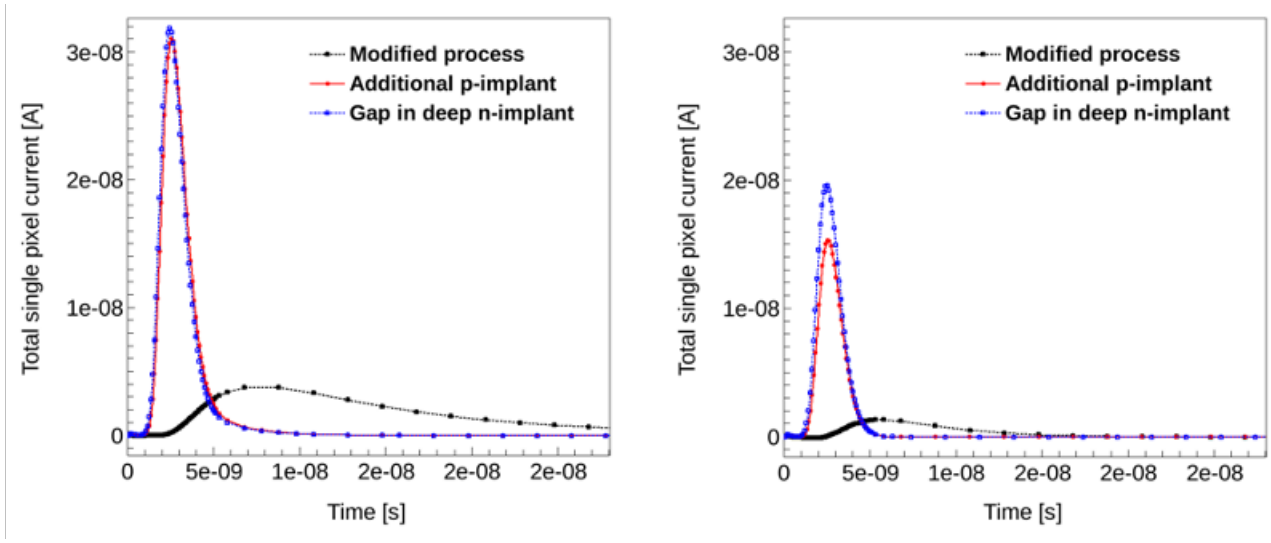

(a) Unirradiated. (b) $\phi = 1 \times 10^{15}$ $n_{\mathrm{eq}}/\mathrm{cm}^2$.

Figure 6.3: TCAD simulations of the induced current from a MIP for the three pixel designs of MiniMALTA before and after irradiation [72].

where the influence of this output conductance is larger, the spread on the gain and hence the threshold spread would be increased. In the sectors on the left half of the MiniMALTA, the M3 transistor size is enlarged relative to the original front-end (and the right half of the chip) for improved noise performance, threshold dispersion, and gain.

The MiniMALTA sensor, a photograph of which is in Fig. 6.4(b), features a 16×64 pixel matrix divided into two columns of four sectors of 8×16 pixels. Each sector has pixels with a different sensor and front-end design as shown in Fig. 6.4(a) of the chip as read out. The four sectors on the left half of the chip have the enlarged transistors on the front-end of the chip,

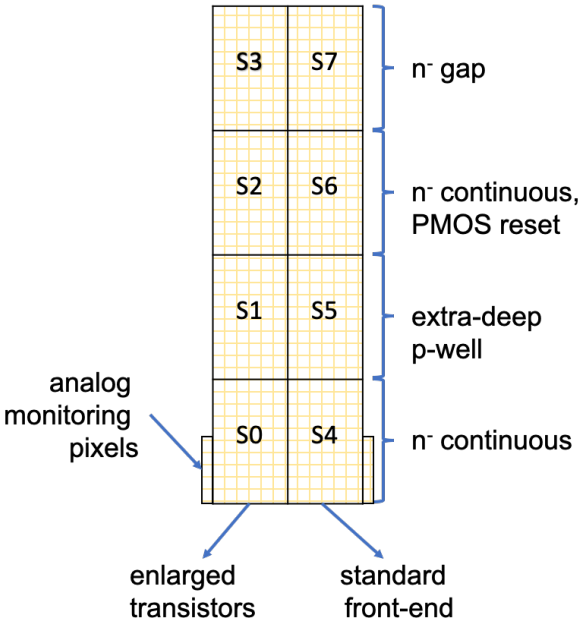

(a) Read-out layout of the 8 different sectors and monitoring pixels of MiniMALTA.

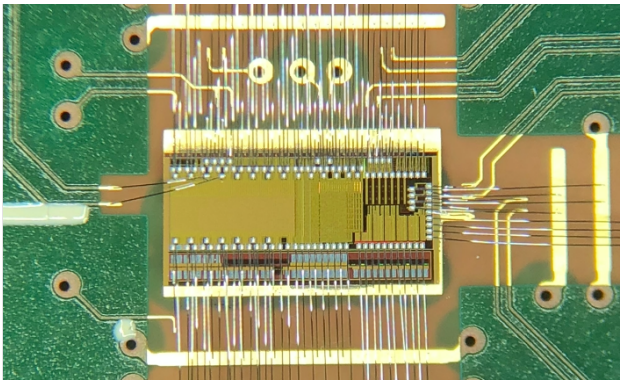

(b) Photograph of chip.

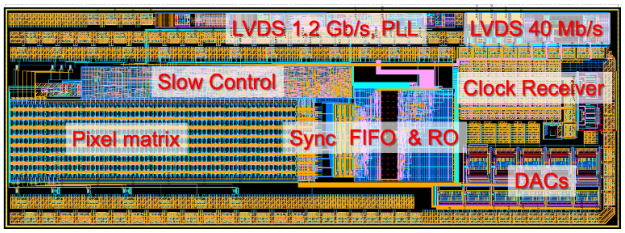

(c) Chip schematic.

Figure 6.4: The MiniMALTA chip.

while the right half has the standard transistor. Starting from the top of the chip for reference: the second and fourth rows (S2, S6, S0, S4) have the standard substrate with the continuous n-layer, the first row (S3, S7) has the n- gap, and the third row (S1, S5) the extra deep p-well. It was not possible to operate the PMOS reset sector and the others simultaneously, and for this reason test results on this sector are not presented in this thesis. The p-well implant is similar to the asymmetric medium p-well implant used for specific sectors of MALTA.

Importantly, the Slow Control was operable on the MiniMALTA device, allowing for much more convenient setting of DAC values, which were controlled with external power supplies when operating the original MALTA. For the measurements presented here, the "slow" readout mode with the data serialised at 40 Mb/s has been used, since the 1.2 Gb/s readout was found to require further firmware development to ensure stability.

6.2 Front-end measurements

Measurements of the threshold, noise, and gain were made to determine the effects of the design changes to the front-end. The re-designed front-end was expected to have higher gain while maintaining a similar noise level, and also to decrease the threshold dispersion and the number of noisy pixels due to RTS noise [73].

Threshold measurements confirmed that the larger transistors significantly decreased the threshold dispersion and the number of noisy pixels, both before and after irradiation. Fig. 6.5(a) and 6.5(b) show measured charge threshold distributions and illustrate the lower threshold dispersion for the front-end with the larger transistors at all fluences: the σ from a Gaussian fit to the threshold distribution is between 22 e and 30 e for the modified front-end and 49 e and 50 e for the unmodified. The mean of the measured ENC is comparable between the modified and standard front-end, however, there are fewer pixels with high noise in the modified sector. These improvements were maintained after irradiation, with less threshold dispersion in the modified front-end than the standard and comparable noise between the modified and standard front-ends in spite of the lower thresholds in the new front-end. The improved threshold dispersion and the decrease in noisy pixels are important for setting a consistent threshold across the chip and operating at lower thresholds without noisy pixels that make the readout busy and lead to hit corruption and challenging track reconstruction. The detection efficiency of the original MALTA device was limited by noise after irradiation (apart from the poor lateral depletion), and this should be improved with the modified front-end with smaller threshold dispersion and fewer noisy pixels.

For both front-end designs, the threshold and noise measurements also had a dependence on the level of irradiation. For the same sensor configuration (DAC settings), relative to an unirriadated sample, there was a decrease in the mean threshold from 292 e to 161 e and an increase in the ENC from approximately 10 e to 20 e measured in neutron irradiated samples with fluences up to 2×10^{15} n_{eq}/cm^2. This irradiation dependence was suspected to be related to changes in capacitance of the irradiated sensor substrate. In Equation 5.1.1, with sensor

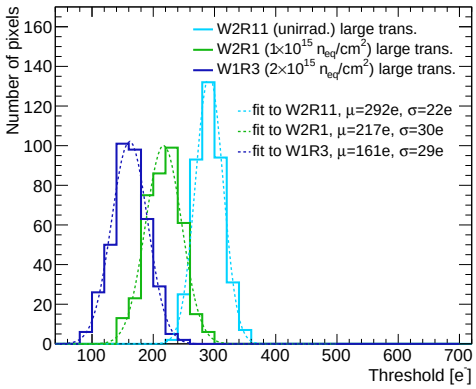

(a) Threshold distribution of the modified front-end [73]

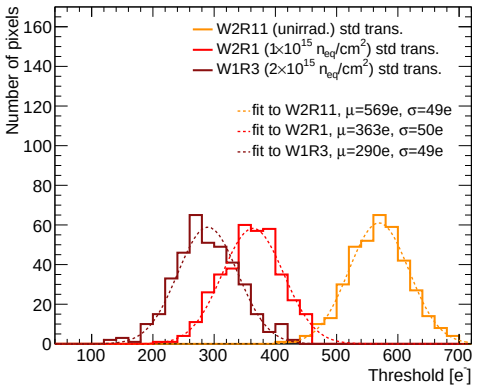

(b) Threshold distribution of the standard front-end [73]

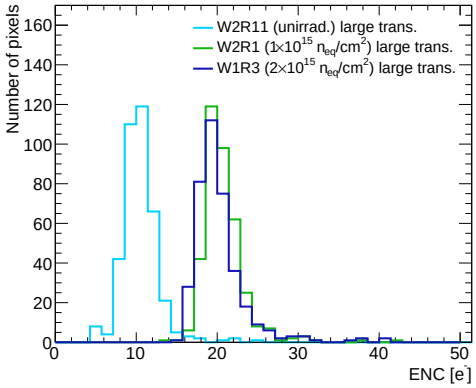

(c) ENC distribution of the modified front-end [73].

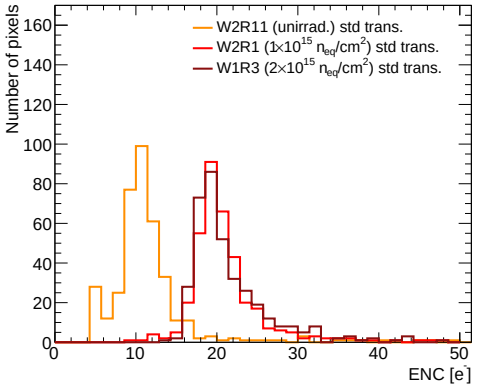

(d) ENC distribution of the standard front-end [73].

Figure 6.5: Measurements from threshold scans.

capacitance C_{IN} the injected charge for the calibration is modeled as:

$$Q_{CAL} = C_{IN}\Delta V_{IN} = C_{IN}\frac{C_C}{C_{IN}+C_C}\Delta V_{DAC} \approx C_C(V_{HIGH} - V_{LOW}) \tag{6.1}$$

To increase Q_{CAL} for a given setting of V_{DAC} and thus measure a lower threshold, C_{IN} would have to have increased after irradiation. This is possible with changes in the doping concentration and impurities that lead to smaller depletion regions and thereby higher capacitance.

In addition to improvements in the threshold performance, the larger NMOS size in the modified front-end was measured to result in a significantly higher gain. The gain of the front-end was measured with an ^{55}Fe source which emits has k-α and k-β X-rays with energies of 5.9 and 6.5 keV, respectively, with the k-α X-rays expected to form the dominant spectral

peak. The measured amplitude spectra for the two front-end designs before irradiation are shown in Fig. 6.6. The k-α peaks of the standard and modified front-ends are at 304.5 mV and 523.9 mV and correspond to gains of 186 μV/e and 320 μV/e, respectively, showing that there is nearly double the gain with the enlarged transistor [73]. Considering threshold measurements show similar pixel noise between the two front-ends, the higher gain of the modified front-end should lead to better detection efficiency at the same threshold. In the irradiated samples the gain is slightly higher than in the unirradiated devices, as was measured in the TowerJazz Investigator [44]. That the Investigators contained only the sensor component and did not have their own front-end electronics, suggests this increase in gain may not be related to the front-end but instead to changes in only the sensor such as the capacitance. As shown in Eqn. 5.1.1, the gain can be modeled as

$$g = \frac{C_S}{C_{OUT_A}} \frac{Q_{IN}}{C_{IN}} \tag{6.2}$$

and a decreased sensor capacitance C_{IN} after irradiation would imply an increased gain, as is measured. However, this contradicts the threshold measurements, which suggested an increase in sensor capacitance. Also, the changes to the gain after irradiation are much less drastic in the gain than in the threshold measurements. It seems there must be other factors at play than just C_{IN}. One possibility is that the change after irradiation may also be related to the between 1 and 2 MRad of TID, which was measured to have similar effects on the gain and threshold in MiniMALTA in [74].

In spite of these unexpected radiation dependencies of the gain and threshold, laboratory measurements of MiniMALTA showed that the modified front-end had increased gain, lower thresholds with less dispersion, and better noise characteristics than the standard front-end. In order to demonstrate that these design changes improved the efficiency and charge collection in the pixel edges and corners (and overall) after irradiation, MiniMALTA was measured in test beams with 3 to 5 GeV e^- at DESY and the Electron Stretcher system at the Physics Institute of the Rheinische Friedrich-Wilhelms-Universität Bonn (ELSA). To probe the pixel response with better spatial resolution than feasible with a relatively low energy electron beam, MiniMALTA was also measured with a focused X-ray beam at Diamond (Sec. 6.4).

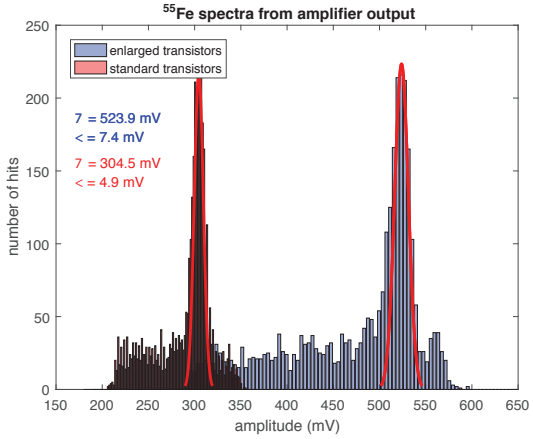

(a) Amplitude spectrum of ^{55}Fe measurements of the standard and modified front-ends [73].

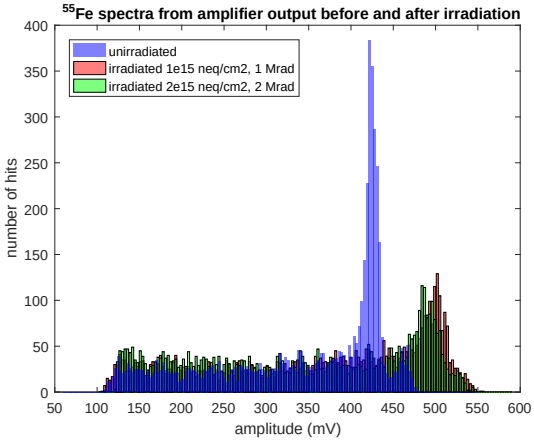

(b) Amplitude spectrum of ^{55}Fe measurements of the modified front-end of unirradiated and irradiated samples [73]. Peculiarly, the gain is greater in the irradiated sample, possibly due to a change in the input capacitance.

Figure 6.6: ^{55}Fe measurements of MiniMALTA.

6.3 Efficiency Measurements in e⁻ test beams

Following the encouraging front-end measurements with MiniMALTA, the sensor was measured in test beams with 3 to 5 GeV electrons at DESY and ELSA.

6.3.1 Development of the MALTA telescope

For measurement at test beams, a telescope composed of MALTA sensors was developed [73]. Beginning from November 2018 through 2020, (the bulk of the author's time as a PhD student, and almost all his time on-site at CERN), CERN beamlines were unavailable due to the second Long Shutdown (LS2) of the LHC for upgrades of the machine and parts of the experiments. During this time other test beam facilities had to be used. For efficiency measurements, the most practical beams were of 3 to 5 GeV electrons, which have significantly more multiple scattering than the 180 GeV pions used to measure the original MALTA at SPS. To determine if this would impact the telescope design and track reconstruction, simulation studies were undertaken.

Simulation of the MALTA telescope was done in AllPix^2, a software framework that uses

GEANT4 for simulation of the interaction of particles with matter and in particular beam telescopes [75, 76]. The simulation studies were used to determine if the MALTA telescope geometry used at SPS would yield comparable results in a beam of 3 GeV electrons. In AllPix^2 a set of configuration files are used to describe sensors and their electronic characteristics for simulation in GEANT4, including the electric field in the pixel substrate (though a simple linear model of the electric field was used for this work). There are also configurations for support structures and their relative geometry to sensors, the incident radiation, and global parameters such as the number of events to simulate. The simulation output includes the sensor response for each event along with truth information that can be used for event reconstruction, as was done with Proteus reconstruction software for these studies [70]. The reconstruction consists of a clusterization followed by iterative track alignment and reconstruction procedures that rely on correlations between sensors and minimzing track fitting parameters.

The geometry of the original MALTA telescope design is shown in Fig. 6.7(a) and consists of two "arms" of 3 MALTA sensors each and a DUT in the center in a cold box. A rendering of the AllPix^2 simulation with this geometry is shown in 6.7(b). By placing planes closer together, particles that scatter from the incident trajectories have less distance to deviate from that incident trajectory before reaching the next plane and tracks can be reconstructed with less uncertainty. The distance between planes was limited by several practical considerations such as the size of the cold box, the height of components on the MALTA carrier board, and the geometry of support structures. Hence, in simulations, the minimum distance between planes was set to be 2 cm and some of the simulated geometries were not necessarily achievable, but still served to provide insight for the telescope design.

For reconstruction of 180 GeV pions at SPS, a simple linear fit between the cluster intercepts was used since this was sufficient with the minimal scattering and also all that was available in the software at the time. However, test beams with electron beams motivated the addition of General Broken Lines (GBL), a Kalman filter approach to minimizing track uncertainties with significant multiple scattering, to Proteus, and this is included in these simulation studies [77].

In Fig. 6.8 are the distributions of track residuals in the x-direction (parallel to the columns

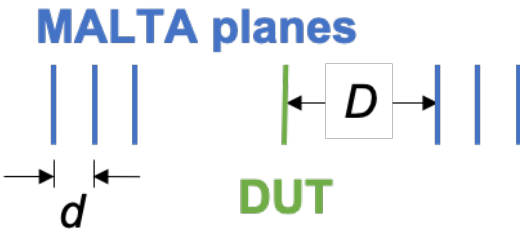

(a) Geometry of the MALTA telescope.

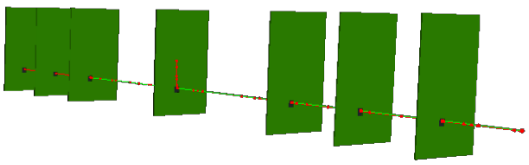

(b) Simulation of a 3 GeV electron passing through the MALTA telescope .

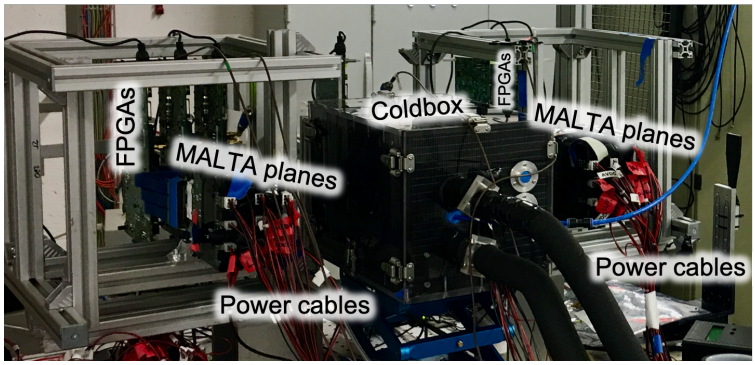

(c) Photograph of the MALTA telescope at the ELSA test beam. The DUT is inside the coldbox, which can hold two MALTA sensors.

Figure 6.7: The MALTA telescope in simulation and data acquisition.

of MALTA). The track residual is the distance between the cluster center on the DUT and the intercept of the reconstructed track and the DUT. The 11 μm σ of the Guassian fit with the original geometry and 180 GeV pions shown in Fig. 6.8(a) matches the measured results at SPS. However, as shown in Fig. 6.8(b) with 3 GeV electrons, the same geometry results in a residual with a σ of 87 μm, more than twice the pixel pitch of MALTA. Such a large residual would limit the ability to measure efficiencies, and more so the precision in reconstructing efficiency maps, especially the in-pixel maps. Hence, other geometries were simulated for use in electron test beams.

The results of the simulations with 3 GeV electrons for various geometries and with 180 GeV pions with the original MALTA telescope geometry are shown in Table 6.1. The σ of the residual was determined as the σ of Gaussian fits to the track residuals in the x and y-directions. The results with 3 GeV electrons show a strong dependence on the distance between arms and the distance between planes, but do not show that there is a significant difference between using

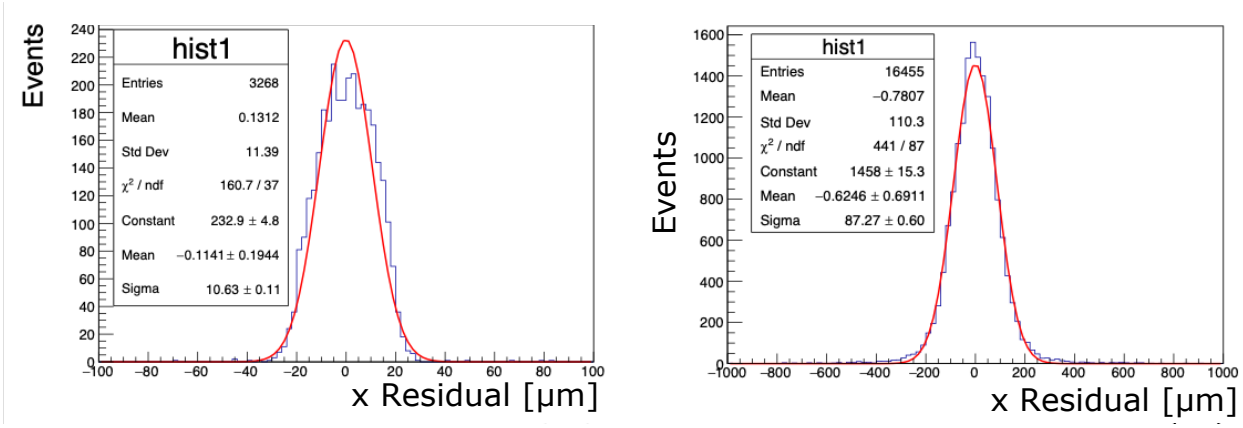

(a) Residuals in simulations of 120 GeV pions. .

(b) Residuals in simulations of 3 GeV e^-.

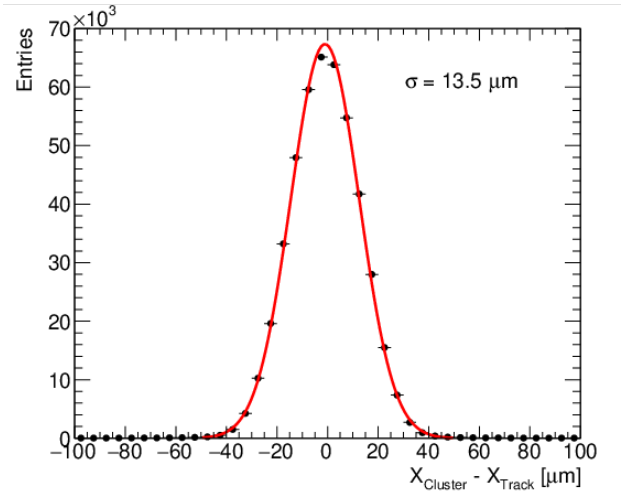

(c) Residuals in the ELSA test beam with 3 GeV e^- [73].

Figure 6.8: Residuals in AllPix^2 simulations of the MALTA telescope.

four or six planes. Hence, the MALTA telescope was redesigned to minimize these distances as much as practically possible. One significant constraint was the coldbox used for the DUT. The coldbox is relatively large (∼20 cm thick), as shown in Fig. 6.7(c) of the telescope at ELSA, and much of the space inside is taken up by insulation and the cold jig itself, so it was not practical to construct a telescope with two sensors close to the DUT prior to test beams. However, in test beams, where only one tracking sensor was in the coldbox (in addition to the DUT), this was found to have little impact. For the ELSA test beam, the final geometry used for tracking reconstruction consisted of four tracking planes: two in front of the DUT and two behind (though six planes and a single DUT were used for acquisition). The residuals for one

run of the data acquisition are shown in Fig. 6.8(c) and have $\sigma = 13.5$ μm, which is comparable to the simulated value of 10 to 20 μm and the simulation results with two tracking planes near the DUT.

Particle	Number of planes	Distance between planes, d [cm]	Distance to DUT, D [cm]	Residual σ [μm]
180 GeV π	6	12	25	10.68
3 GeV e^-	6	12	25	87.27
3 GeV e^-	6	5	5	18.45
3 GeV e^-	6	5	2	16.43
3 GeV e^-	6	2	20	28.61
3 GeV e^-	6	2	5	14.18
3 GeV e^-	4	5	5	12.01
3 GeV e^-	4	5	2	10.59
3 GeV e^-	4	2	20	21.8
3 GeV e^-	4	2	5	9.56

Table 6.1: Summary of the AllPix^2 simulation results for the MALTA telescope. The parameters D and d are for the distances shown in the diagram in 6.7(a).

The MALTA telescope is triggered on coincidences between three MALTA planes, and the asynchronous readout of a MALTA plane can send hits at any time. When they arrive from a specific region of interest (ROI) (in the center of the chip), the signal is passed from the FPGA to the trigger logic unit (TLU), in this case a set of Nuclear Instrumentation Module (NIM) modules in a crate. The FPGA pipelines the hits to a buffer with first in, first out (FIFO) logic, where they are stored until the FIFO is saturated. When a trigger signal arrives at the FPGA from the TLU, all hits in a 500 ns window of time are sent to the another FIFO for output which is read out through IPbus [78] from the data acquisition software. Originally, and for the results in this chapter, the trigger logic was done with NIM electronics but since then a custom TLU has been developed which is far more practical [79].

6.3.2 Efficiency results

Using the MALTA telescope, efficiencies were measured with MiniMALTA in 3 to 5 GeV electron beams. Fig. 6.9 shows a map of the efficiency of a neutron irradiated ($\phi = 1 \times 10^{15}$ $n_{\mathrm{eq}}/\mathrm{cm}^2$) MiniMALTA sample as measured at ELSA in which each bin corresponds to a single pixel. The

pixels on the edges of sectors have been excluded due to edge effects between the different sectors and multiple scattering which would naturally result in lower efficiency measurements in the pixels on the edge of the sensor and convolute the results between the neighboring sectors. The mean efficiency of 78.8% in the sector with the unmodified sensor and front-end is comparable to the results from the SPS with the original MALTA device, as expected. The blank sectors feature a PMOS reset instead of a diode reset, and could not be operated simultaneously with the other sectors. The efficiencies in the sectors on the left half of the chip with the enlarged transistor are greater than those on the right half, and the rows with the extra deep p-well and n^- gap pixels have better efficiencies than those with the standard MALTA substrate in the bottom row. Furthermore, the efficiency of irradiated samples is above 98% in the sectors with both the substrate and front-end modifications.

Fig. 6.10(a) shows the efficiencies as a function of the threshold of two sensors, W2R1 and W4R2, both after a fluence of 1×10^{15} $n_{\mathrm{eq}}/\mathrm{cm}^2$. For points at the same threshold, the efficiency improves with either one of the front-end or pixel modifications, and the best efficiencies are achieved when both are implemented. The efficiency of the two sensors is comparable independent of the sensor thickness, which is 25 μm for W4R2 and 30 μm for W2R1.

The efficiency results for the two samples, W5R3 and W1R3, with a fluence of 2×10^{15} $n_{\mathrm{eq}}/\mathrm{cm}^2$ are plotted in Fig. 6.10(b) as a function of the threshold. The efficiency is > 90 % for these most efficient sectors at low thresholds. The thinner, 25 μm sensor, W5R3, has lower threshold and better efficiency, however, with the same threshold settings as the 30 μm sensor, W1R3, has slightly better efficiencies in the modified sectors. As with the sensors irradiated to 1×10^{15} $n_{\mathrm{eq}}/\mathrm{cm}^2$, a significant dependence on the thickness of the epitaxial layer is not apparent.

Fig. 6.11 shows the reconstructed in-pixel efficiency maps for the various sectors of MiniMALTA. Each pixel is divided into a grid of 5×5 bins. The efficiency in the pixel centers is better than in the periphery as in the results with MALTA at SPS. However, the resolution of these results is not comparable to that achieved at SPS, as may be expected based on the AllPix^2 simulations. To probe the pixel response with greater precision, MiniMALTA was

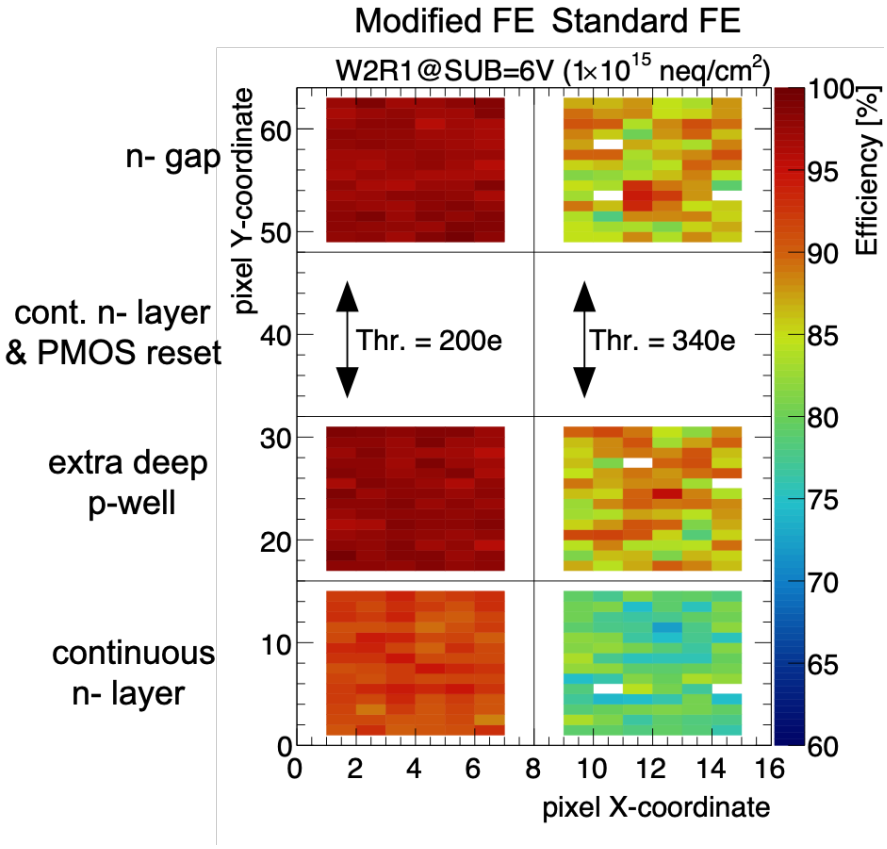

Figure 6.9: Efficiency measurements in the different sectors of MiniMALTA sample W2R1 with $\phi = 1 \times 10^{15}$ $n_{\text{eq}}/\text{cm}^2$ [73]. Each bin corresponds to a single pixel.

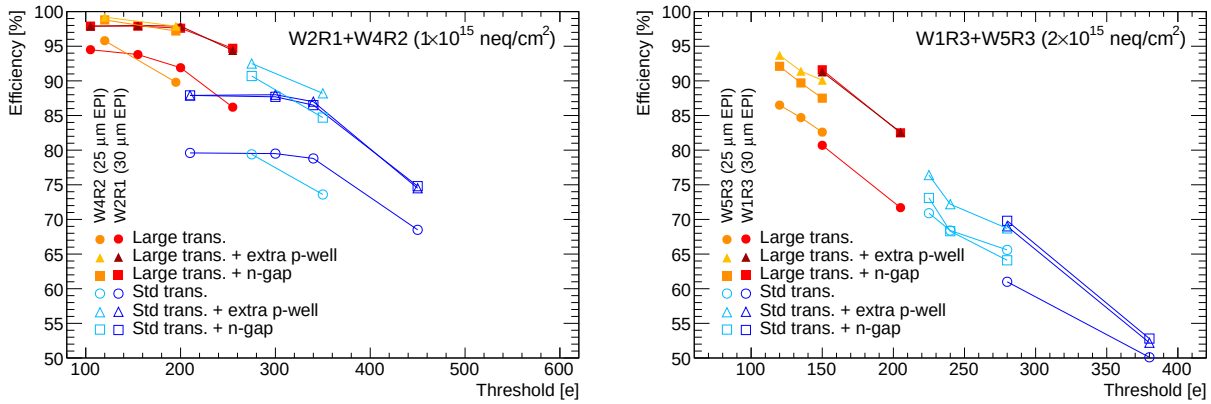

(a) $\phi = 1 \times 10^{15}$ $n_{\text{eq}}/\text{cm}^2$ (b) $\phi = 2 \times 10^{15}$ $n_{\text{eq}}/\text{cm}^2$

Figure 6.10: Efficiency measurements of MiniMALTA as a function of threshold [73].

measured with a focused photon beam at Diamond Light Source as summarized in the next section.

The efficiency results for MiniMALTA are summarized in Table 6.2. Overall, the new modifications to the pixel design and front-end yield improved efficiencies following irradiation. The modified front-end allows for operation at lower thresholds, and furthermore at the same thresholds the modified substrates and front-end result on better efficiencies. Both modifications result in an improvement on their own, but the best efficiencies are achieved in sectors with both types of modification.

Sample	Epitaxial thickness [μm]	Fluence [n_{eq}/cm^2]	Process modification	Modified FE efficiency [%] /threshold [e]	Standard FE efficiency [%]/threshold [e]
W2R11	30	None	n^- gap	99.6± 0.1 / 200	99.1± 0.1 / 380
			extra deep p-well	99.6± 0.1 / 200	98.9± 0.1 / 380
			n^- continuous	99.6± 0.1 / 200	97.9± 0.1 / 380
W2R1	30	1×10^{15}	n^- gap	97.6± 0.1 / 105	86.5± 0.1 / 210
			extra deep p-well	97.9± 0.1 / 105	87.0± 0.1 / 210
			n^- continuous	91.9± 0.1 / 105	78.8± 0.2 / 210
W4R2	25	1×10^{15}	n^- gap	98.8± 0.1 / 120	90.7± 0.1 / 275
			extra deep p-well	99.2± 0.1 / 120	92.5± 0.1 / 275
			n^- continuous	95.8± 0.1 / 120	79.4± 0.1 / 275
W5R3	25	2×10^{15}	n^- gap	92.5± 0.1 / 120	73.1± 0.3 / 230
			extra deep p-well	93.7± 0.1 / 120	76.4± 0.3 / 230
			n^- continuous	86.5± 0.1 / 120	70.9± 0.3 / 230

Table 6.2: Table of average efficiencies and thresholds measured in MiniMALTA. The uncertainties are statistical and assume a binary distribution.

6.4 Photon Test Beams

MiniMALTA samples were measured at the Diamond Light source with precision focused X-rays. The experimental setup at the Diamond B16 beam line included a focused X-ray beam and a set of motion stages with which the detector response was measured with μm-level precision.

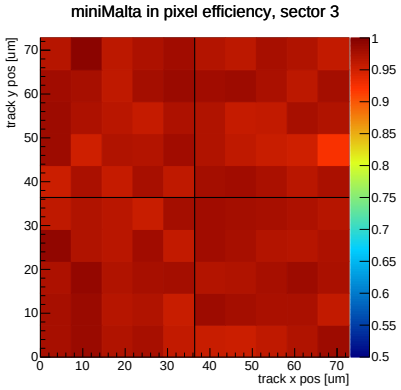

(a) Modified front-end, n$^-$ gap. Average efficiency: 97.6± 0.1%; threshold: 105 e.

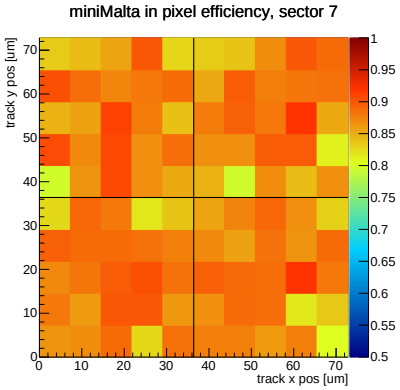

(b) Standard front-end, n$^-$ gap. Average efficiency: 86.5± 0.1%; threshold: 210 e

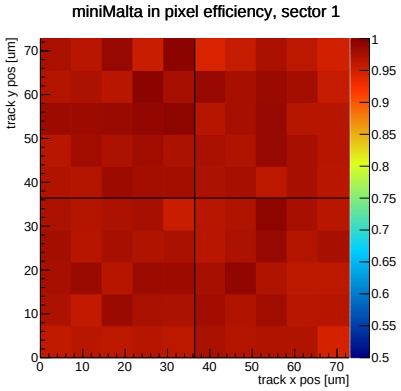

(c) Modified front-end, extra deep p-well. Average efficiency: 97.9± 0.1%; threshold: 105 e

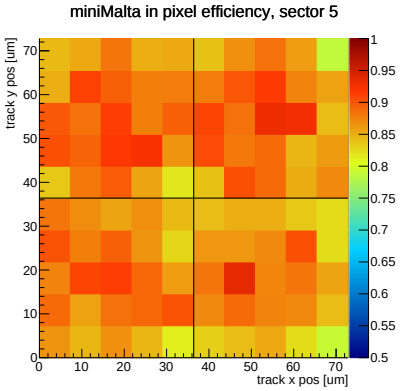

(d) Standard front-end, extra deep p-well. Average efficiency: 87.9± 0.1%; threshold: 210 e

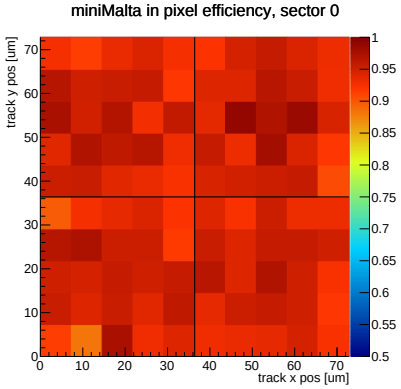

(e) Modified front-end, n$^-$ continuous blanket. Average efficiency: 91.9± 0.1%; threshold: 105 e

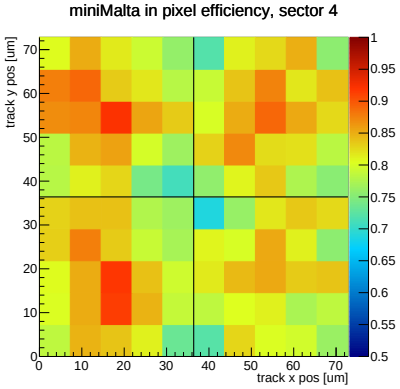

(f) Standard front-end, n$^-$ continuous blanket. Average efficiency: 78.8± 0.2%; threshold: 210 e

Figure 6.11: In-pixel efficiency measurements of sample W2R1 irradiated to 1×10^{15} $n_{\mathrm{eq}}/\mathrm{cm}^2$ with measurements from 2×2 pixel regions combined to improve statistics.

Unlike MIPs such as high-energy pions or electrons, a photon does not deposit charge along the entire length of a track passing through the sensor, but instead deposits energy via the photoelectric effect in a relatively localized position in the depleted region. Without tracks, it is not possible to measure efficiencies and no beam telescope was necessary. Instead, such an experiment is useful as it allows for the measurement of the relative response of different regions of the pixel to photons with high spatial precision. Of particular interest is the response in the edges of the pixels relative to the center since in 2018 test beams at SPS of the original MALTA sensor, the efficiency was lower in the pixel edges relative to the center region. Furthermore, it was expected that sensors with the extra deep p-well and n^- gap process modifications would have better relative photon pixel response in the periphery based on simulation and the efficiency results in electron test beams. The unmodified continuous n^- sector was expected and did show a lower pixel response in these regions, matching the in-pixel efficiency measurements of MALTA.

In addition to unirradiated sensors and a neutron-irradiated sensor with $\phi = 1\times10^{15}$ $n_{\mathrm{eq}}/\mathrm{cm}^2$, proton-irradiated devices were tested at Diamond with fluences up to 5×10^{15} $n_{\mathrm{eq}}/\mathrm{cm}^2$ and TID of 70 MRad. Sensors were irradiated at the MC40 cyclotron at the University of Birmingham with special modifications for operating MiniMALTA inside the cold box remotely and shielding the readout electronics. The irradiations were made in scanning mode due to the large area of MALTA ($2 \times 2.2\mathrm{cm}^2$) compared to the beam size of 1×1 cm^2. Having the chip operational during irradiation allowed for biasing of the substrate and electronics to mitigate TID damage and also allowed for monitoring of the sensor and periodic testing throughout the irradiation. While proton irradiated MALTA devices of any version have not been studied in test beams, the results with devices at Diamond may be a good indicator of the performance of proton-irradiated devices relative to unirradiated and neutron-irradiated devices, and at a bare minimum demonstrate that MiniMALTA can be operated after a TID of 70 MRad, nearly the 80 MRad requirement for the ATLAS ITk (as has also been demonstrated in [74] with photon-irradiated samples and with a sample irradiated to 91 MRad in [65]).

Mini-MALTA sensors were tested with an 8 keV X-ray beam with a full width half maximum

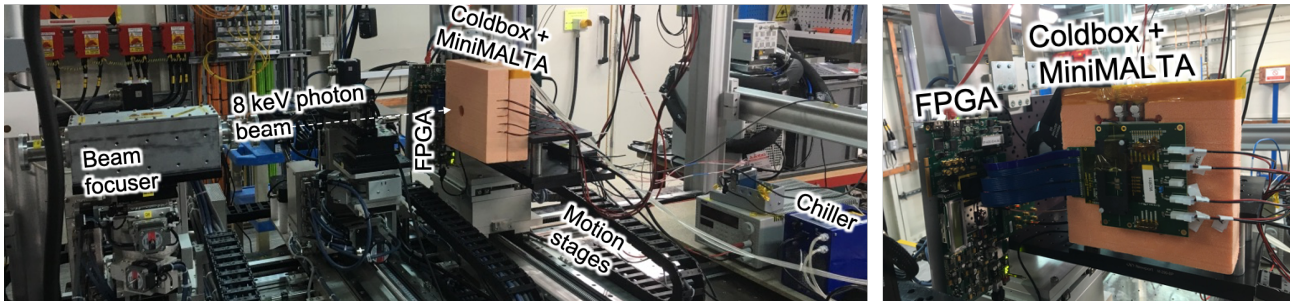

(a) Beam focuser and motion stages for the coldbox and MiniMALTA.

(b) The coldbox, specifically designed for MiniMALTA.

Figure 6.12: Experimental setup at the Diamond test beam.

of 2 μm. As shown in Fig. 6.12 of the test beam setup, a MiniMALTA sensor was mounted in a cold box on a two-dimensional 400 nm precision motion stage. The sensor was precisely moved perpendicular to the beam and measured at each point to map the sensor response. Scans were made over a 100×100 μm^2 area with 2 μm steps to ensure that at least one entire pixel is contained in each scan. The cold box was cooled with a cooling chuck attached to a 10 °C water chiller and a peltier. Nitrogen gas was fed into the cold box, and temperature and humidity were monitored and kept stable. The temperature for testing was -15 to -10 °C.

The beam energy was selected based on an estimate of how much energy a MIP would deposit in the depletion region of Mini-MALTA. The stopping power for a MIP in silicon is [23]:

$$\left\langle \frac{dE}{dx} \right\rangle = 3.88 \, \frac{\text{MeV}}{\text{cm}}. \tag{6.3}$$

The epitaxial substrate in MiniMALTA is produced to be either 25 or 30 μm thick, depending on the wafer, though the effective depletion depth is likely a few μm less. For an approximate thicknesses of 20 to 25 μm, a MIP will deposit a mean energy of 7.8 to 9.0 keV in the sensor. Hence 8 keV was selected for the beam energy.

Three sectors were studied on each chip: the continuous n$^-$ sector with the standard front-end, and the n$^-$ gap and p-well sectors with the enlarged transistors. The two modified sectors were selected since they performed best in the ELSA and DESY test beams and the standard sector as to have an experimental control.

6.4.1 Analysis Methods

Hit maps were reconstructed by merging data from the motion stage and MiniMALTA readout. For each position on the stage, a trigger was sent to MiniMALTA and it then collected data for 1 s. The times of the MiniMALTA data packets and stage positions were synchronized in order to reconstruct hit maps of the photon pixel response, though there were some cases of desynchronization between the motion stage data and MiniMALTA readout. As a result, there were more stage positions than data packets recorded in each run. Presumably, this is due to a trigger from the stages which is somehow "missed" by the FPGA for MiniMALTA. The result of this is "holes" in the reconstructed hit maps where there is no data. In the results presented, the values at these points are interpolated.

Normalized hit maps were reconstructed from each scan to compare the relative response of MiniMALTA to the 8 keV photons, and are called "photon pixel response" maps. Each map was constructed with only hits from a set of 5×5 adjacent pixels that were in the beam line to ensure that the maps were not corrupted by hits from a noisy pixel far from the beam spot. To account for variations in the intensity of the beam, the number of hits at each stage position was scaled by the beam monitor measurement during the test beam. If the number of hits in a pixel was below 7% of the maximum number of hits in any pixel at the stage position, these were considered noise and excluded from the hit map.

For the estimation of the mean photon pixel response for a given pixel, the pixel was normalized relative to itself, not the entire hit map. As shown in Fig. 6.13(a), to define the center position of each pixel used for the normalization, as well as the edges of each pixel, the unnormalized hit map was projected along the x and y axes and fit with a function of the form

$$p_0 * \left[\mathrm{Erf}\big((x - p_1)/p_2\big) + \mathrm{Erf}\big((p_3 - x)/p_4\big)\right] + p_5 \tag{6.4}$$

where Erf is the error function and p_n are the fit parameters. That is, the sum of error function, an error function reflected about y-axis, and a constant to account for background

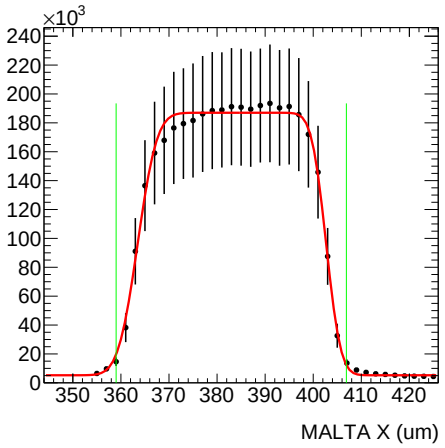

(a) Projection of the pixel hit map , fit with Eqn. 6.4.1. The green lines mark the point at which the photon pixel response falls below 5% of the peak value as determined from the fit.

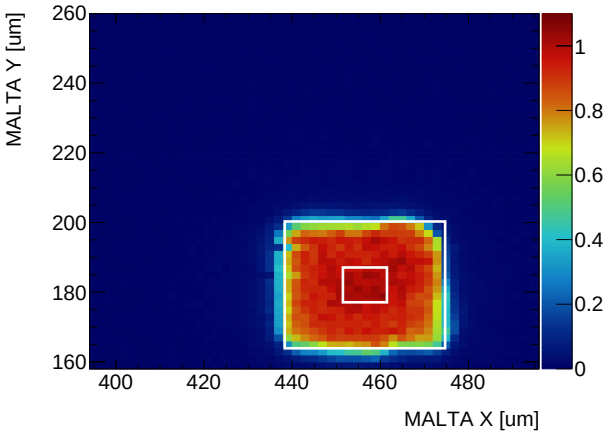

(b) Hits from a single pixel, normalized to the pixel center.

Figure 6.13: Illustration of methods to determine the pixel boundaries.

noise. The 5% limits of the charge sharing, x_{min} and x_{max}, are defined as the points at which the normalized intensity fell to 5% of the maximum value. The extent is defined as the average distance beyond the pixel edges these limits are, and is calculated as

$$x_{extent} = \frac{x_{max} - x_{min} - 36.4\ \mu\text{m}}{2} \tag{6.5}$$

for the 36.4 μm pixel pitch in MALTA sensors.

Fig. 6.13(b) shows a photon pixel response map for a single pixel. The pixel region is defined by a $36.4 \times 36.4\ \mu\text{m}^2$ square (the larger white rectangle in the figure), with the center defined by the mean of the 5% charge sharing limits. The number of hits is normalized to the mean number of hits in a $10 \times 10\ \mu\text{m}^2$ square in the center of the pixel, shown as the smaller white rectangle in the figure. The average of the response values (with the maximum contribution from a single point set to 1) is called the mean photon pixel response and is a single quantity between 0 and 1 to evaluate the performance of a pixel, analogous to the mean efficiency. Only pixels which were fully contained within the scan and had reasonable fits for the pixel edges were considered in calculations.

The appropriate algorithm in Proteus was used for clustering and to create maps of the

average cluster size. The clustering algorithm takes a set of pixel coordinates and creates clusters from adjacent pixels iteratively. Diagonal pixels are not considered to be adjacent, and repeated coordinates are ignored as opposed to counted as a separate cluster. A MALTA word (containing up to 16 hits in an 8-row double column) was considered to be potentially clustered with another word if the time difference between the two was less than four bunch crossings, equivalent to 100 ns. This long duration is due to the time stamping occurring after the output FIFO, which is following synchronization at 40 MHz, and the time information (BCID) contained in the hits being merged at the periphery of the chip, which allows for time walk and propagation time in the pixel matrix. Hence, the time when a hit is actually created in MiniMALTA cannot be resolved better than a few 25 ns clock cycles. There is a cut on the pixel coordinates so that only hits from a set of 5×5 pixels near the beam were used in creating the hit maps. The pixel coordinates of the cluster were simply set to be the coordinates of the first pixel present in the cluster. Since the ordering of the hits is arbitrary, this does not bias the clustering results.

6.4.2 Results

Mean photon pixel response

The photon pixel response maps from MiniMALTA are shown in Fig. 6.14. The 2×2 set of larger white rectangles outlines the limits used for the in-pixel calculations, and the smaller rectangle outlines the area to which one of the pixels is normalized. The entire map is normalized to the mean of the pixel centers, of which there are between one and four as can be seen. In Table 6.3 are the mean photon pixel responses for each of the sectors in each of the sensors, corresponding to the plots in Fig. 6.14. The error values are calculated as the standard deviation of the mean of the response values in the 10×10 μm^2 square in the center of the pixel. The mean values in the table follow the same trend as the efficiency results in Section 6.3, with the values of the sectors with the modified front-end and extra deep p-well and n^- gap being comparable to the sectors with the standard front-end and continuous n^- before irradiation, and decreasing

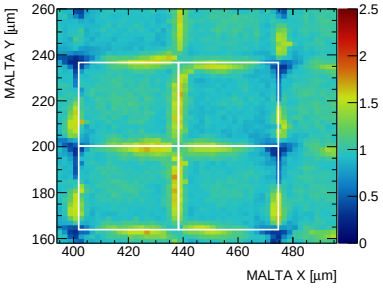

(a) W2R11 continuous n$^-$, standard front-end, unirradiated

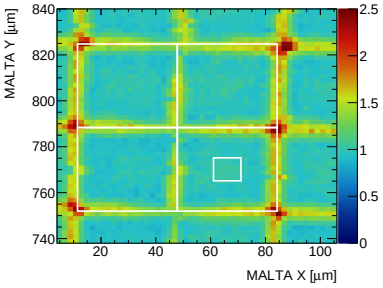

(b) W2R11 extra deep p-well, modified front-end, unirradiated.

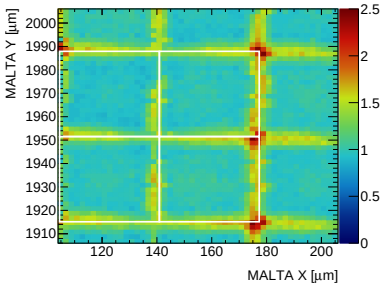

(c) W2R11 n$^-$ gap, modified front-end, unirradiated.

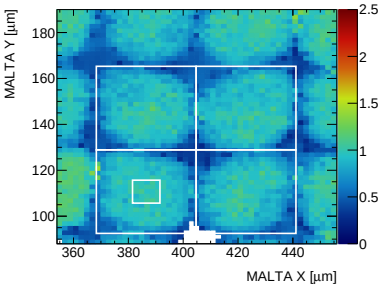

(d) W2R1 continuous n$^-$, standard front-end, 1×10^{15} n_{eq}/cm^2.

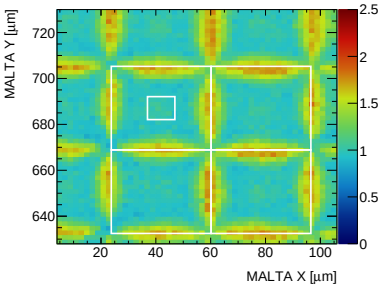

(e) W2R1 extra deep p-well, modified front-end, 1×10^{15} n_{eq}/cm^2.

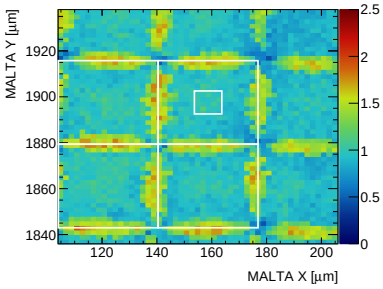

(f) W2R1 n$^-$ gap, modified front-end, 1×10^{15} n_{eq}/cm^2.

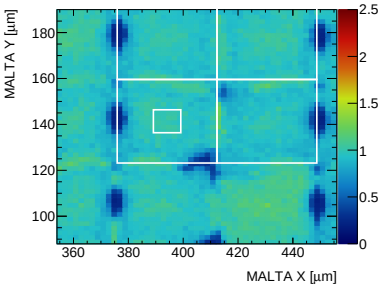

(g) W5R9 continuous n$^-$, standard front-end, 6 $\times 10^{14}$ n_{eq}/cm^2, 70 MRad

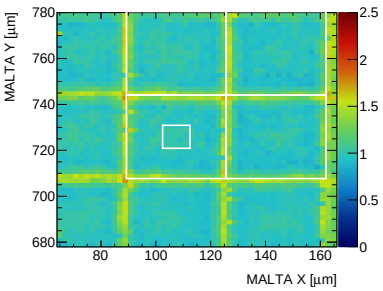

(h) W5R9 extra deep p-well, modified front-end, 6 $\times 10^{14}$ n_{eq}/cm^2, 70 MRad.

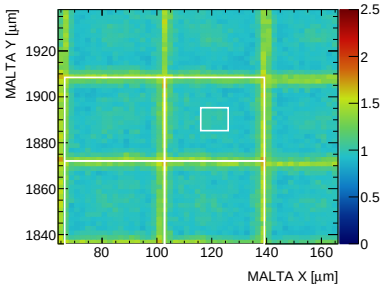

(i) W5R9 n$^-$ gap, modified front-end, 6 $\times 10^{14}$ n_{eq}/cm^2, 70 MRad.

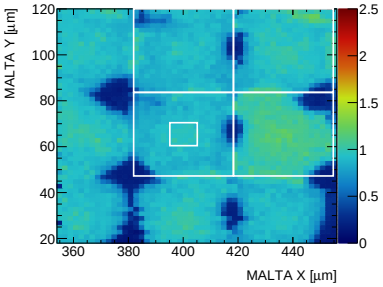

(j) W4R9 continuous n$^-$, standard front-end, 7×10^{13} n_{eq}/cm^2, 9 MRad

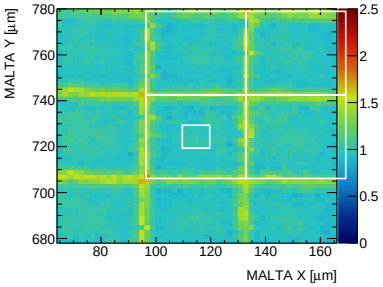

(k) W4R9 extra deep p-well, modified front-end, 7×10^{13} n_{eq}/cm^2, 9 MRad n_{eq}/cm^2.

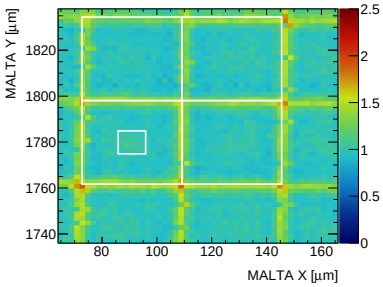

(l) W4R9 n$^-$ gap, modified front-end, 7×10^{13} n_{eq}/cm^2, 9 MRad n_{eq}/cm^2.

Figure 6.14: Relative photon pixel response maps for the different MiniMALTA samples. Each row of maps has the results for the three pixel designs for a sensor and level of irradiation. Starting from the left, the pixel designs are: the continuous n$^-$ substrate with the standard front-end, the extra deep p-well with the modified front-end, and the n$^-$ gap with the modified front-end.

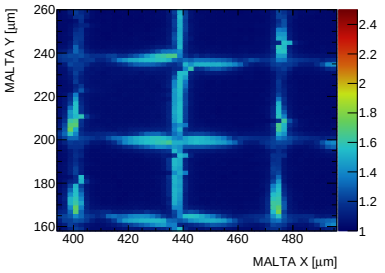

(a) W2R11 continuous n$^-$, standard front-end, unirradiated

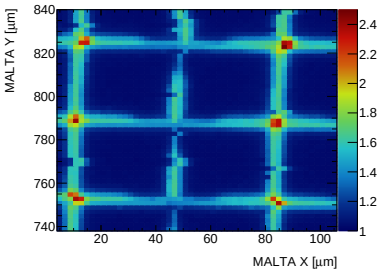

(b) W2R11 extra deep p-well, modified front-end, unirradiated.

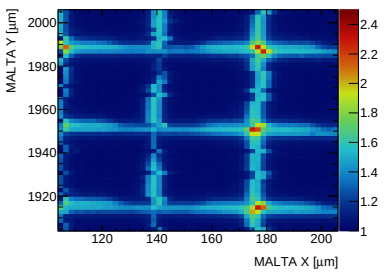

(c) W2R11 n$^-$ gap, modified front-end, unirradiated.

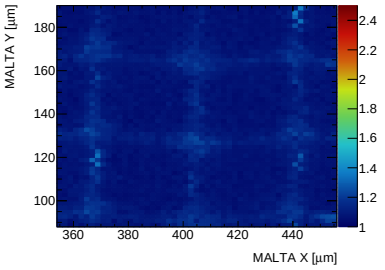

(d) W2R1 continuous n$^-$, standard front-end, 1×10^{15} n_{eq}/cm^2.

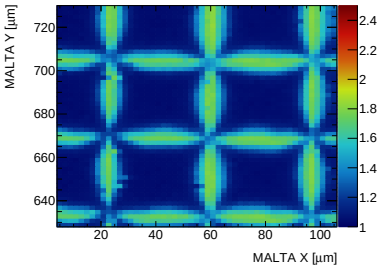

(e) W2R1 extra deep p-well, modified front-end, 1×10^{15} n_{eq}/cm^2.

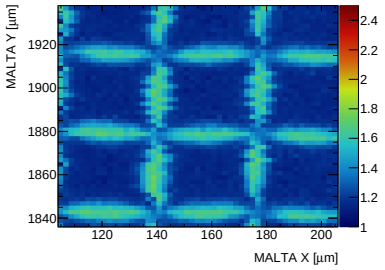

(f) W2R1 n$^-$ gap, modified front-end, 1×10^{15} n_{eq}/cm^2.

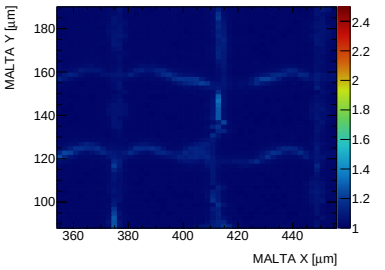

(g) W5R9 continuous n$^-$, standard front-end, 6 $\times 10^{14}$ n_{eq}/cm^2, 70 MRad.

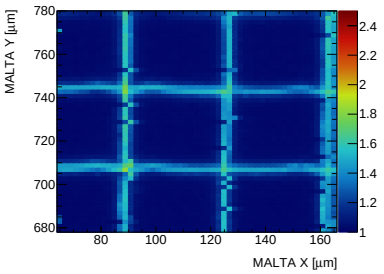

(h) W5R9 extra deep p-well, modified front-end, 6 $\times 10^{14}$ n_{eq}/cm^2, 70 MRad .

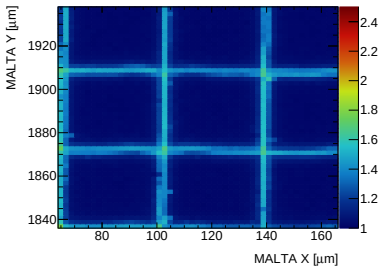

(i) W5R9 n$^-$ gap, modified front-end, 6 $\times 10^{14}$ n_{eq}/cm^2, 70 MRad.

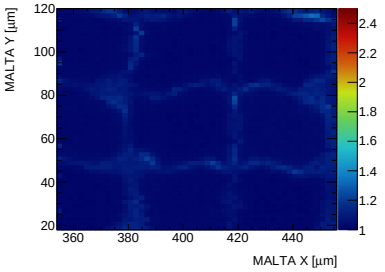

(j) W4R9 continuous n$^-$, standard front-end, 7×10^{13} n_{eq}/cm^2, 9 MRad

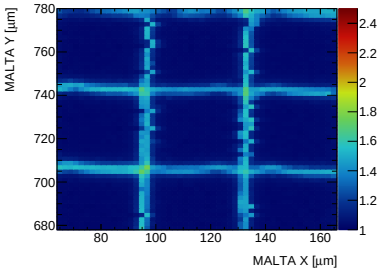

(k) W4R9 extra deep p-well, modified front-end, 7×10^{13} n_{eq}/cm^2, 9 MRad n_{eq}/cm^2.

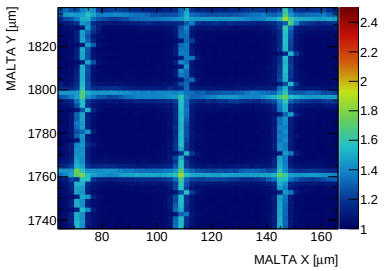

(l) W4R9 n$^-$ gap, 7×10^{13} n_{eq}/cm^2, 9 MRad n_{eq}/cm^2.

Figure 6.15: Average cluster size maps for the different samples and sectors. For each sample and row, the results are shown for three pixel designs, starting from the left: the continuous n$^-$ substrate with the standard front-end and the extra deep p-well and n$^-$ gap with the modified front-end.

significantly at $\phi = 1 \times 10^{15}$ $n_{\mathrm{eq}}/\mathrm{cm}^2$ for the n^- continuous layer design but only moderately for the n^- gap and extra deep p-well designs with the modified front-end. In particular, the region near the edges of the pixels with the continuous n^- layer has lower relative photon pixel response than the redesigned sectors, which decreases with irradiation, whereas this region in the n^- gap and p-well sectors remain relatively unchanged. In these new pixel designs, the mean number of hits near the edges is actually above 1, meaning that on average there is more than one hit, and in the corners of pixels in the unirradiated, nearly three hits on average. However, at 1×10^{15} $n_{\mathrm{eq}}/\mathrm{cm}^2$, the photon pixel response falls below 1 in the corners even in the new pixel designs, as we might expect from the in-pixel efficiency maps in Fig. 6.11 which show a similar degradation after irradiation. Notably, in Fig. 6.14(d) the shape of the region of increased response in the pixel center matches the shape of the hole in the p-well implantation well as shown in Fig. 6.16(c) where a schematic of the p-well implant has a been superimposed over the same response map.

Cluster size

In Fig. 6.15 are maps of the average cluster size. These closely match the photon pixel response maps in Fig. 6.14 with the exception that the minimum average cluster size must be 1. After irradiation, the extra deep p-well and n^-gap designs still have a large cluster size in the periphery, though not in the pixel corners. For the continuous n^- sector, the cluster size is close to 1 even in the periphery after irradiation, even to a relatively moderate level of 7×10^{13} $n_{\mathrm{eq}}/\mathrm{cm}^2$ and 9 MRad. Again, the asymmetry of the p-well implant is apparent in these maps, especially those of the n^- gap sector.

Charge Sharing Extent

Charge sharing extent results from all samples are tabulated in Table 6.4. These measurements show a clear trend: pixels in the continuous n^- gap sector became less responsive with irradiation, but the responses in the sectors with the extra deep p-well and n^- gap with the modified front-end do not show significant degradation. The larger charge sharing extent in the modified

sectors may indicate a stronger lateral field and be beneficial to the detection efficiency and in track reconstruction.

Sample	Fluence (n_{eq}/cm^2)	TID (Mrad)	Std. MALTA & FE	Extra deep p-well & Modified FE	n- gap & Modified FE
W2R11	0	0	86.9 ± 0.7	88.7 ± 0.6	89.7 ± 0.6
W2R9	5.0×10^{14}	66	80.5 ± 0.9	87.6 ± 1.3	87.4 ± 1.4
W4R9	7×10^{13}	9	79.0 ± 0.8	88.1 ± 0.6	87.9 ± 0.8
W5R9	5.6×10^{14}	74	78.3 ± 0.7	88.0 ± 0.6	87.9 ± 0.6
W2R1	1×10^{15}	1	73.6 ± 1.4	88.7 ± 0.8	89.2 ± 1.2

Table 6.3: Table of mean photon pixel responses.

Sample	Fluence (n_{eq}/cm^2)	TID (Mrad)	Std. MALTA & FE	Extra deep p-well & Modified FE	n- gap [μm] & Modified FE [μm]
W2R11	0	0	5.03 ± 0.03	6.08 ± 0.03	6.29 ± 0.03
W4R9	7×10^{13}	9	4.32 ± 0.04	5.20.1 $\pm$ 0.03	5.11 ± 0.04
W2R9	5.0×10^{14}	66	4.36 ± 0.04	6.13 ± 0.06	5.64 ± 0.07
W5R9	5.6×10^{14}	74	3.77 $\pm$0.03	5.11 ± 0.03	5.00 ± 0.03
W2R1	1×10^{15}	1	2.82 ± 0.06	6.89 ± 0.06	7.14 ± 0.06

Table 6.4: Table of the mean charge sharing extent.

Voltage dependence

The 1×10^{15} n_{eq}/cm^2 neutron-irradiated sample W2R1 was tested at two different substrate biases, -6 V and -20 V. In Table 6.5 are the mean photon pixel response values for the different sectors and in Fig. 6.16 are the photon pixel response maps at the two biases voltages for the n^- continuous sector. An increase in the substrate voltage increases the field in the depleted region of the sensor, and so decreases collection times and possibly increases signal amplitude and thereby the number of hits above threshold and photon pixel response. However, the results in all three sectors suggest an increase in voltage leads to a decrease in the mean relative

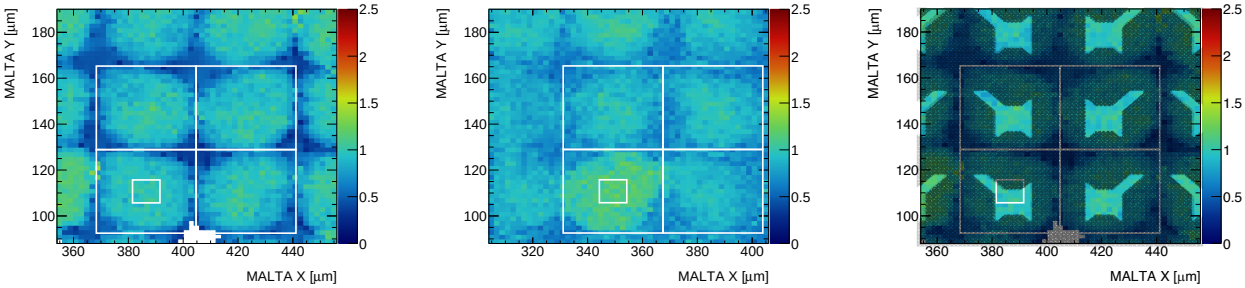

(a) Substrate bias of -6 V.

(b) Substrate bias of -20 V.

(c) Substrate bias of -6 V, with an outline of the p-well implant superimposed. The areas of low response correspond with areas where the p-well is present.

Figure 6.16: Photon pixel response maps of the continuous n^- sector of W2R1 1×10^{15} n_{eq}/cm^2 with the substrate biased at -20 V and -6 V.

response in all three sectors. Though the pixel response in the periphery is greater at -20 V, the relative response elsewhere is slightly lower leading to an overall lower mean value. Efficiency measurements with MALTA Cz in Chapter 7 show a similar decrease with bias voltage in the epitaxial samples, as do the simulations in [72]. The sharp increase in leakage current with the substrate bias in measurements in 7.2.1 may also be a factor in the degraded performance of MiniMALTA and MALTA as a function of bias voltage. In studies with full-size sensors in the Chapter 7, the maximum efficiency was measured at between -9 and -12 V, depending on the sensor and fluence.

Bias Voltage	Fluence (n_{eq}/cm^2)	TID (Mrad)	Std. MALTA & FE	Extra deep p-well & Modified FE	n- gap & Modified FE
-6	1×10^{15}	1	73.6 ± 1.4	88.7 ± 0.8	89.2 ± 1.2
-20	1×10^{15}	1	70.5 ± 1.2	86.3 ± 1.3	87.2 ± 1.2

Table 6.5: Average photon pixel response at different bias voltages.

Summary of measurements at Diamond

From the measurements of MiniMALTA with 8 keV photons at Diamond there were several key findings:

The photon pixel response of the n^- continuous sector in the pixel periphery decreases relative

to the response in the center with irradiation, as evidenced by the photon pixel response and cluster size maps of the unirradiated and irradiated samples. The mean response of the entire pixel showed only a modest decrease with irradiation in the n^- gap and extra deep p-well sectors, unlike the n^- sector which had a sharp decrease.

The charge sharing extent was measured to increase with fluence in the n^- gap and extra deep p-well sectors, and decreases in the n^- sector.

The results with the 1×10^{15} $n_{\text{eq}}/\text{cm}^2$ sample, W2R1, suggest that the photon pixel response decreases as the bias voltage is increased. In studies with MALTA Cz, it was of interest to study the dependence of the sensor's performance as a function of bias voltage and similar trends were observed.

In all, Diamond Light source provided a powerful tool for high-precision probing of the photon pixel response, and the measurements are a strong complement to the results with lower energy electron beams which have limited spatial precision in track reconstruction.

6.5 Conclusions

From the laboratory measurements and test beams with electron and photons, the MiniMALTA device was extensively characterized up to fluences of 2×10^{15} $n_{\text{eq}}/\text{cm}^2$. For the sectors with both the redesigned substrate and front-end, the efficiency was measured to be above the ATLAS requirement of 97 % at 1×10^{15} $n_{\text{eq}}/\text{cm}^2$, and above 90 % at 2×10^{15} $n_{\text{eq}}/\text{cm}^2$, while the results for the unmodified sector matched those with the previous version of the device, discussed in Section 5.2.

The apparent cause of this improved radiation tolerance is an increase in the gain of the modified front-end, as measured with an ^{55}Fe X-ray source, an improvement in threshold performance due to the decreased transconductance of the enlarged M3 transistor, and the improved lateral field at pixel boundaries in the n^- gap and extra deep p-well designs.

The measurements at Diamond confirmed the pixel structure and correlate well with the efficiency results. The response in the pixel periphery in the n^- gap and extra deep p-well

designs with the modified front-end is far superior to that in the n^- continuous design with the standard front-end.

These results with MiniMALTA demonstrated that the front-end and pixel substrate modifications in MiniMALTA both lead to improved radiation hardness and motivated implementation of these modifications in later versions of MALTA. The pixel design changes were implemented in a full-scale version of the sensor, MALTA Cz, the subject of the next chapter, and the latest version of the device, MALTA 2, has both front-end and the sensor changes (and is produced on both epitaxial and Czochralski substrates).

Chapter 7

Characterization of MALTA Cz

With the characterization of MiniMALTA as radiation tolerant to 1×10^{15} $n_{\text{eq}}/\text{cm}^2$, the extra deep p-well and n^- gap sensor modifications were implemented in full-scale (512×512 pixels) versions of MALTA. However, the front-end modifications were unfortunately unable to be included in this design, and due to time constraints of test beam schedules and wire-bonding facilities, only the continuous n^- and n^- gap designs were characterized for the epitaxial samples. The sensors were also produced with Czochralski silicon with a 300 μm thick substrate which would result in larger collection volume and a higher amplitude signal than the 25 to 30 μm epitaxial silicon. The production run of these full-scale MALTA sensors, including the samples made from Czochralksi silicon, is referred to as MALTA Cz. The production of MALTA Cz gave the opportunity to demonstrate similar radiation tolerance to that seen in MiniMALTA in a full-scale device, characterize the n^- gap and extra deep p-well sensor designs in more detail, and demonstrate advantages of the thicker collection region possible with MALTA Cz.

7.1 Chip design

MALTA devices with the continuous n^- layer, extra deep p-well and n^- gap substrates were produced on 300 μm Czochralski silicon wafers with a bulk resistivity of $\sim$800 kΩ-cm. In the epitaxial devices, the low resistivity wafers, the p^{++} region shown in Fig. 7.1(a), does not deplete, and only the 25 to 30 μm eptitaxial layer is depleted. In the Czochralski sensors,

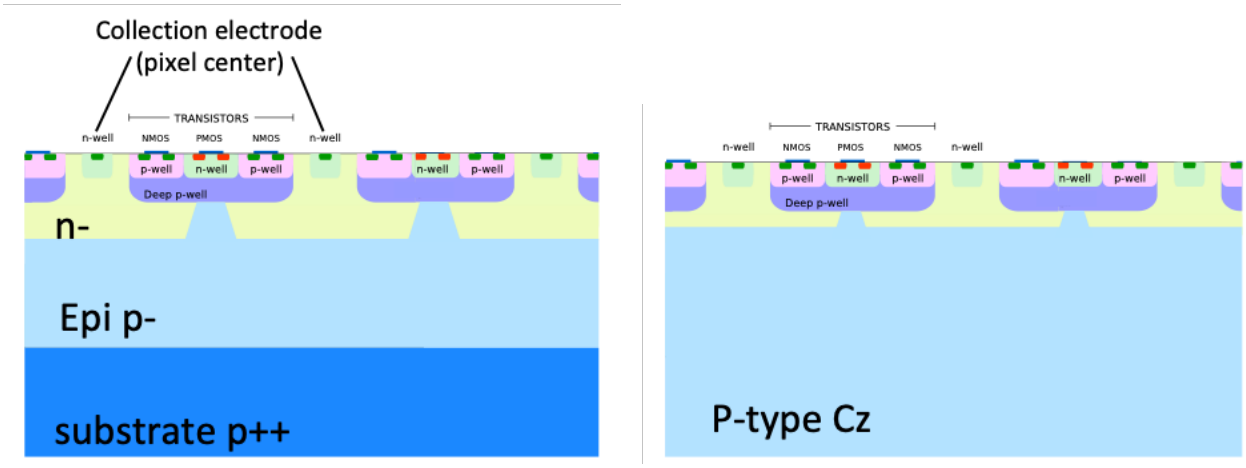

(a) Cross section of the n^- gap sensor design in epitaxial silicon. The highly doped p^{++} backside serves as an ohmic contact.

(b) Cross section of the n^- gap sensor design in Czochralksi silicon. The substrate is 300 μm thick, allowing for a larger depleted volume than the epitaxial sensors.

Figure 7.1: Cross sections of the n^- gap sensor design in epitaxial and Czochralksi silicon.

the depletion region can be made to be the full 300 μm depth of the substrate given sufficient reverse bias. This would result in a MIP generating many more electron hole pairs than in the 25 to 30 μm of depleted silicon in an epitaxial layer and a proportionately larger signal. However, depleting this much silicon of this resistivity requires significantly more voltage than to deplete the 25 to 30 μm of 1 kΩ-cm epitaxial silicon in other MALTA devices. Using a planar model for the sensor, the depletion voltage for 300 μm is estimated from Equation 3.17 to be:

$$V_{full\ depletion} = \frac{D^2}{2\epsilon\mu\rho} = \frac{(300\ \mu\text{m})^2}{2\epsilon(1500\ \text{cm}^2/\text{V}\cdot\text{s})(800\ \Omega\cdot\text{cm})} = 423\ \text{V} \tag{7.1}$$

While this is approximate, $V_{full\ depletion}$ is two orders of magnitude greater than the depletion voltage of epitaxial devices in the TowerJazz modified process, which is a few volts.

Czochralski silicon is a type of silicon which is widely used in industry to grow large ingots of silicon crystal. Typically, for particle physics applications, sensors have been made with float zone silicon which has a much lower concentration of impurities that results in higher resitivities which can be depleted at low voltage. However, high-resistivity silicon can be difficult to manufacture, and with TowerJazz and their partners in industry, the production of thicker Czochralski samples was possible in a practical time frame. MALTA Cz is made with the same

process as MiniMALTA for the n^- gap and extra deep p-well designs but the same masking and front-end as the original MALTA. A newer version of the sensor, MALTA 2, is a full-size sensor with both the front-end and pixel modifications. It is currently being characterized at CERN, however, results are preliminary and it was not available on the timescale of this PhD thesis.

7.2 Laboratory Measurements

These full-size versions of the MALTA sensor allowed for more stringent testing of the n^- gap and extra deep p-well designs than the MiniMALTA samples, and also required characterization due to the different type of silicon and depletion depth that could and did lead to differences in operation and output. Since IV measurements of MiniMALTA were made in [64], with 8 different pixel designs and a small current due to the small number of pixels, there was some ambiguity that could be resolved with IV measurements of full-scale devices with one pixel design per sensor. With many more pixels than MiniMALTA, the readout architecture had to cope with many more hits and higher data rates. The larger matrix also presents a limitation in threshold scans. Because of the OR merger in MALTA, hits from multiple places on the martrix at the same time can cause corruption, and due to this only small regions of MALTA can be measured in threshold scans at a time. For this reason, the scans are limited to areas of around 100×100 pixels. The full-size matrices allowed for characterization of the uniformity of pixel response across the entire pixel matrix, and comparison of the 8 Sectors (Fig. 5.2) with different p-well implant and collection electrode designs. MALTA Cz was also easier to operate than the original full-size version due to the correction of a design flaw of the original MALTA that allowed for use of MALTA's Slow Control, essential for setting the DACs on MALTA. In the original MALTA, DAC values were set with external power supplies connected to the DAC override lines on the right side of the MALTA carrier board as shown in Fig. 5.11(a).

The laboratory measurements of MALTA Cz are discussed in greater detail than those of MiniMALTA in this chapter due to the greater potential of and need for the measurements,

as described above, and improved methods for testing MALTA sensors that allowed for more systematic characterization.

7.2.1 Current-Voltage Measurements

Current-voltage (IV) measurements are an important tool for characterizing electronic devices, including the silicon sensors used in particle physics. They determine the power consumption of a sensor and its operational limit in terms of bias voltage. As an example, for the outer pixel layers of the ATLAS ITk, the overall power consumption is required to be below 500 mW/cm^2 [36]. For CMOS sensors, typically most of the consumption is in the digital and analog front-end electronics, and not the pixel substrate, which typically consumes less than 20 mW/cm^2 in CMOS sensors. IV measurements of the MALTA Cz sensors show differences in operational limits and power consumption in the various pixel designs and between epitaxial and Czochralski devices. There was a significant "punch-through" current[1] between the substrate and the p-well observed in the new pixel designs (extra p-wella and n$^-$ gap) in both types of silicon (epitaxial and Czochralski) and the irradiated Czochralski continuous n$^-$ layer sensors. While the radiation tolerance of MALTA Cz was demonstrated to be above 1×10^{15} n_{eq}/cm^2 in test beams (and discussed later in this chapter), the design of future versions of MALTA and other TowerJazz modified process devices must still take into consideration the punch-through currents and operational limits, particularly given the encouraging results with the extra deep p-well and n$^-$ gap designs which have promising improvements in radiation tolerance though also have lower punch-through voltages.

7.2.1.1 Setup and Methods

Current-voltage measurements of unirradiated and irradiated samples of the MALTA Cz with epitaxial and Czochralski silicon and the extra deep p-well and n$^-$ gap modifications were made at CERN. The schematic of the measurement setup is shown in Fig. 7.2, and the biasing of the

[1] A punch-through current is usually a current between the source and drain in a MOSFET that leads to breakdown of the device, usually caused by a voltage drop between the drain and source and overlapping depletion regions in the channel. Here, "punch-through" current means the current directly between the p-well and substrate that lead to high overall current draw in MALTA.

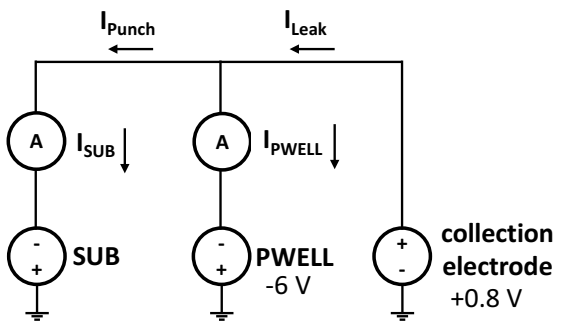

(a) Schematic of the circuit used in the IV measurement.

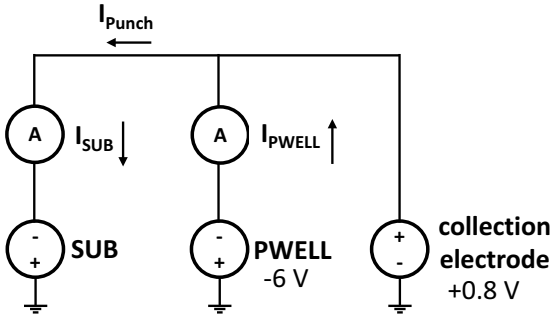

(b) Schematic of punch-through current flowing between the p-well and substrate with negligible leakage.

Figure 7.2: Schematic of the circuit used in the IV measurement. The PWELL and SUB currents are measured directly to infer the leakage and punch-through currents.

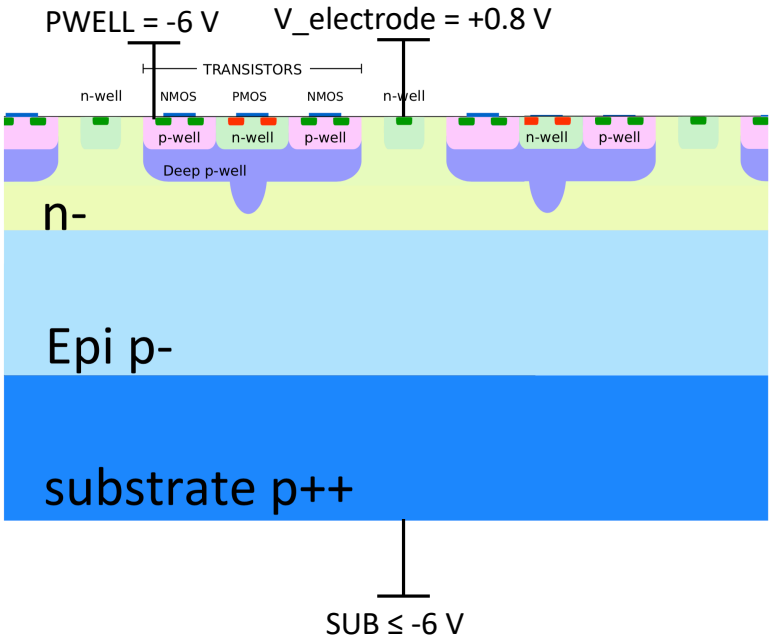

Figure 7.3: Schematic of the biasing of the pixel substrate. The electrode and PWELL voltages are kept constant, and the SUB lowered from -6 V until the operational limit with a 20 mA current compliance. The currents through the power supplies for the SUB and PWELL are measured with other supplies to act as dedicated ammeters.

of the substrate is shown in 7.3. The substrate was biased with a Keithley 2410 power supply to source voltages below -30 V and two Keithley 2410s were used to measure the current of the p-well and substrate. The p-well, analog, digital, and LVDS components were biased with TTi PL3030UD-P power supplies [80]. Unless otherwise noted, the p-well bias was -6 V for the results in this chapter. In each measurement, the voltage of the substrate was decreased from the p-well voltage in uniform steps until a current limit of 20 mA was reached in the device or the p-well power supply became unstable. The current in the p-well and substrate was measured 10 times at each voltage value and averaged. The chip was configured with the collection electrode at +0.8 V. The measurements were made in a CTS T-65/50/5 climate chamber and the temperature was measured with a 10 kΩ NTC probe attached to the MALTA carrier board [81].

The combined leakage current from the p-well and substrate is calculated as the sum of the p-well and substrate currents. In the case that there is an equal and opposite change in the p-well and substrate currents, there is a current which flows from the more positively-biased p-well to the substrate. Then if the leakage current is negligible, the punch-through current can be reliably calculated as:

$$I_{PT} = (I_{pwell} - I_{substrate})/2 \tag{7.2}$$

and the leakage is

$$I_{leakage} = (I_{pwell} + I_{substrate}) \tag{7.3}$$

Such a scenario is illustrated in 7.2(b). Notably, in an ideal measurement the current in the collection electrode would also be measured, though this was not possible due to additional circuitry in the chip which makes this impractical.

In silicon diodes, punch-through currents can be modeled as having an exponential dependence on the voltage difference between two structures, ΔV:

$$I_{PT}(V) = I_0 e^{q(V-V_{PT})/mK_BT} \tag{7.4}$$

where V_{PT} is the punch-through voltage and m is known as the non-ideality factor [82]. In this model, there is a negative temperature coefficient, that is, the current decreases as the temperature increases. This is the opposite of leakage currents, which have a positive temperature coefficient and depend on temperature as [28]:

$$I_{leakage} \, \alpha \, T^2 \exp \frac{-E_g}{2K_B T} \tag{7.5}$$

where E_g is the band gap energy for silicon.

For interpretation of these measurements, the results can generally be classified into 3 cases, as shown in Fig. 7.4:

1) There is much more punch-through than leakage current. The calculated punch-through current is accurate. See Fig. 7.4(a) and 7.4(b).

2) The punch-through is larger but the magnitude of the leakage current is comparable. In this case, the calculated punch-through current also includes a significant contribution from the leakage current, but there is still a negative p-well current. See Fig. 7.4(c) and 7.4(d).

3) The leakage current is larger than the calculated punch-through. In this case, the substrate and p-well currents flow in the same direction and there is no punch-through, i.e. $V < V_{PT}$. See Fig. 7.4(e) and 7.4(f).

7.2.1.2 Unirradiated devices at multiple temperatures

In Fig. 7.5 and Fig. 7.6 are the IV measurements at different temperatures for unirradiated devices with the calculated punch-through and leakage currents. The error bars in these plots are calculated as the sample standard deviation of the mean of 10 measurements of the current. Since the leakage currents are sums of the p-well and substrate currents the errors are added quadrature and the error can be greater than the magnitude of the calculated leakage current.

For the samples with the continuous n^- layer in Fig. 7.5, the chip can be operated with a significant potential difference between the p-well and substrate, $\Delta V > 20$ V. For the epitaxial sensor, there is a punch-through current that begins to dominate near ΔV=23 V as shown

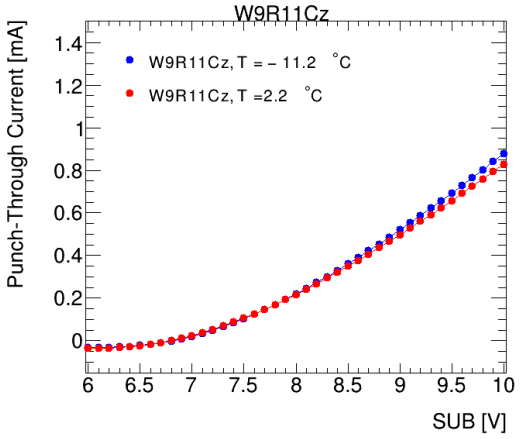

(a) Case 1, punch-through current. Punch-through dominates.

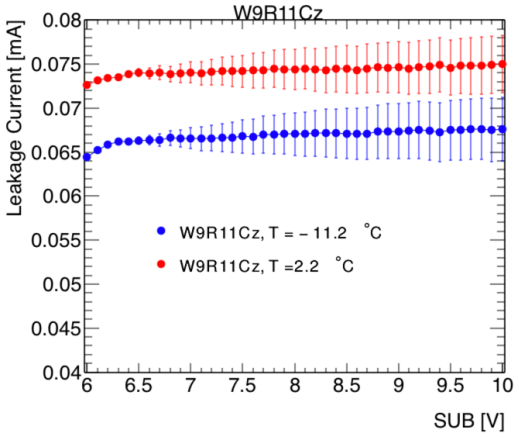

(b) Case 1, leakage current. Punch-through dominates.

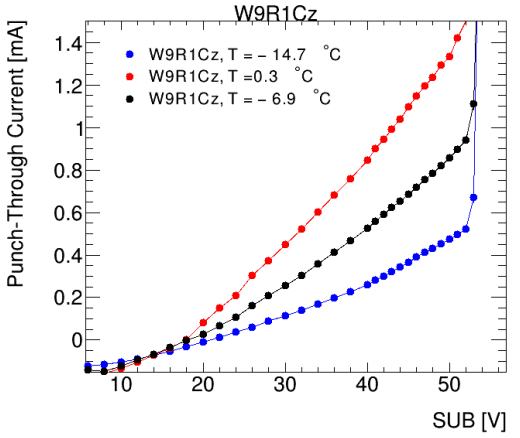

(c) Case 2, punch-through current. Leakage and punch-through are comparable.

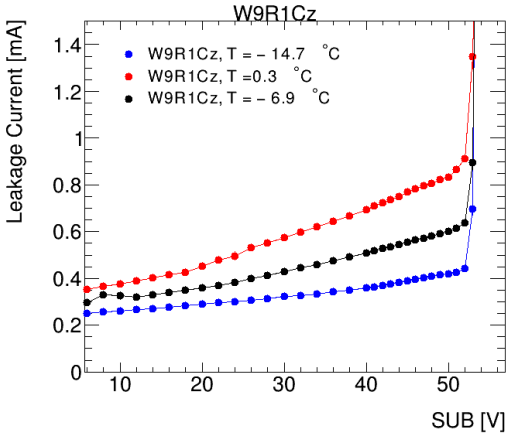

(d) Case 2, leakage current. Leakage and punch-through are comparable

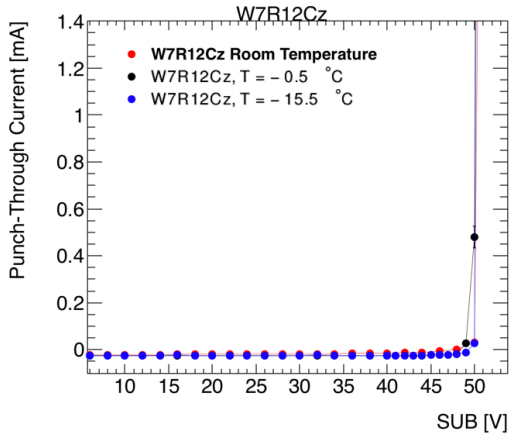

(e) Case 3, punch-through current. Leakage dominates.

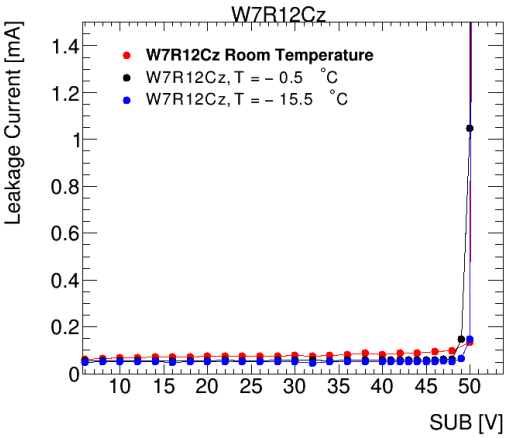

(f) Case 3, leakage current. Leakage dominates.

Figure 7.4: Examples of the 3 cases of the current-voltage measurements.

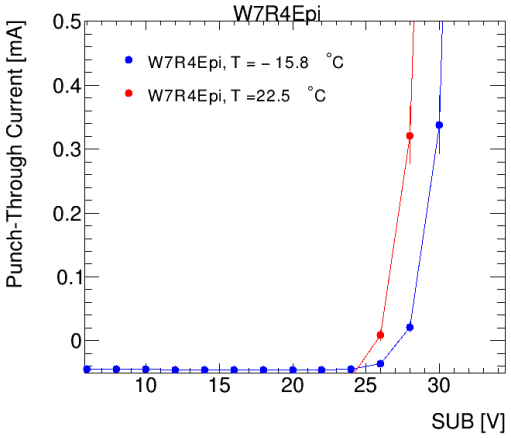

(a) Punch-through current for continuous n⁻ epitaxial

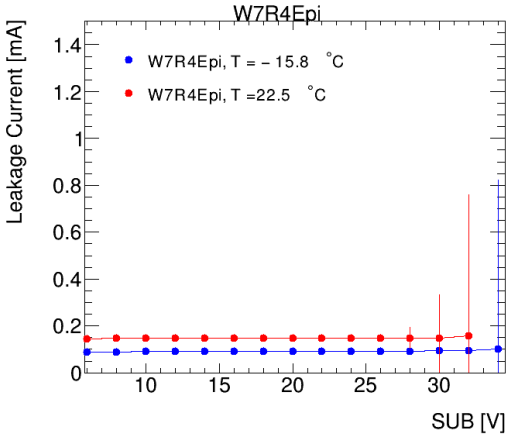

(b) Punch-through current for continuous n⁻ epitaxial

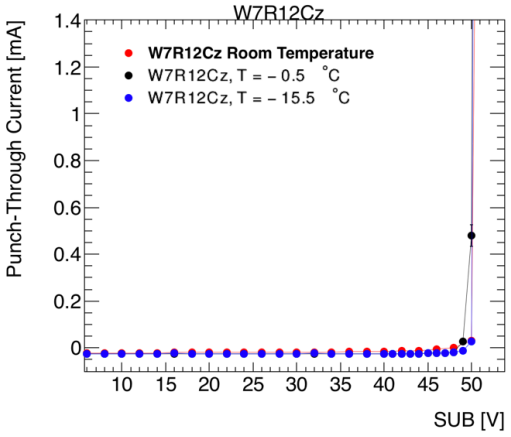

(c) Punch-through current for continuous n⁻ Czochralski

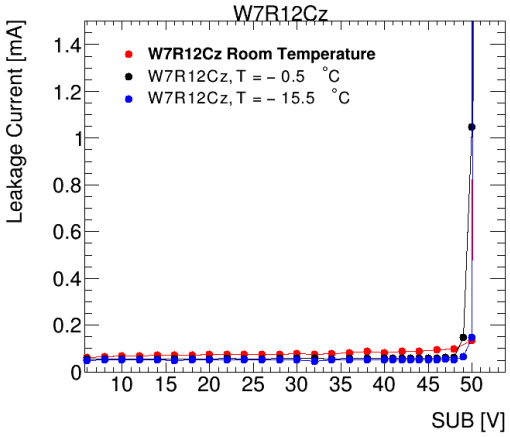

(d) Leakage current for continuous n⁻ Czochralski

Figure 7.5: Current-voltage measurements for the unirradiated samples with the continuous n⁻ substrate at different temperatures.

in Fig. 7.5(a) and 7.5(b). For the Czochralski, shown in Fig. 7.5(c) and 7.5(d), however, the punch-through current is never significant. Instead, there is an increase in the leakage current and breakdown near a substrate bias of 50 V.

For the measurements of the devices with the n⁻ gap and the extra deep p-well with epitaxial and Czochralski silicon, shown in Fig.7.6, the punch-though current dominates. Notably, this punch-through current decreases with rising temperature, contrary to the behavior for a bulk current. For the leakage current, there is the characteristic dependence on $\sqrt{V}$, and the error bars are large due to the methodology for calculating them. The leakage current has a smaller absolute value than the p-well and substrate currents that are used to estimate the errors

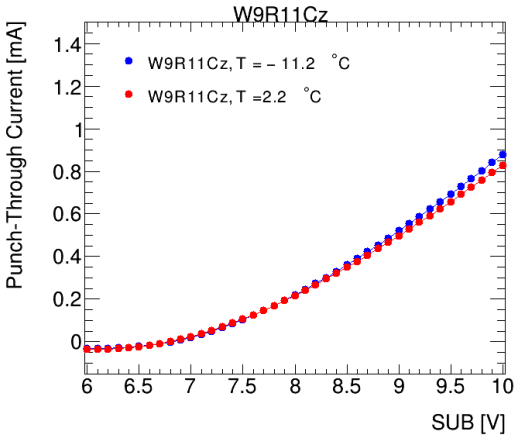

(a) Punch-through current for Czochralski n⁻ gap

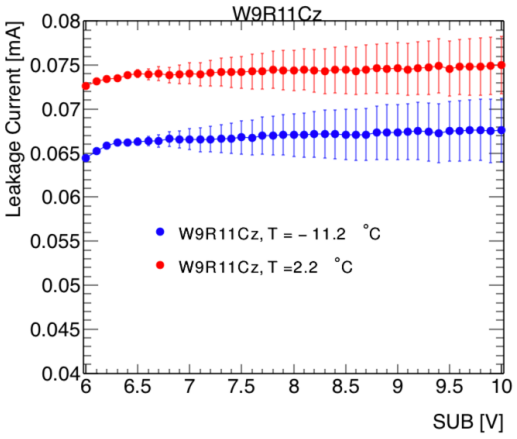

(b) Leakage current for Czochralski n⁻ gap

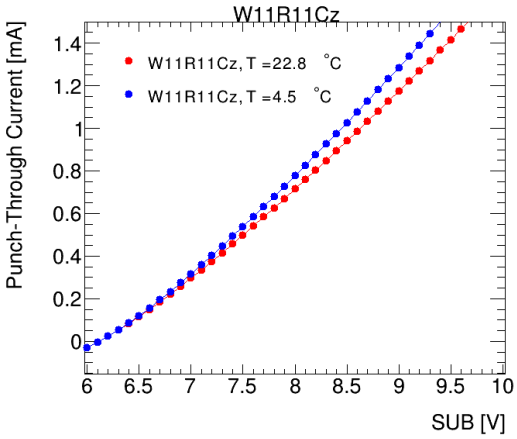

(c) Punch-through current for Czochralski extra deep p-well

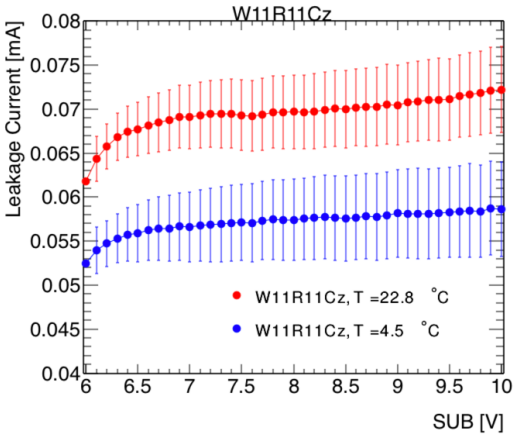

(d) Leakage current for Czochralski extra deep p-well

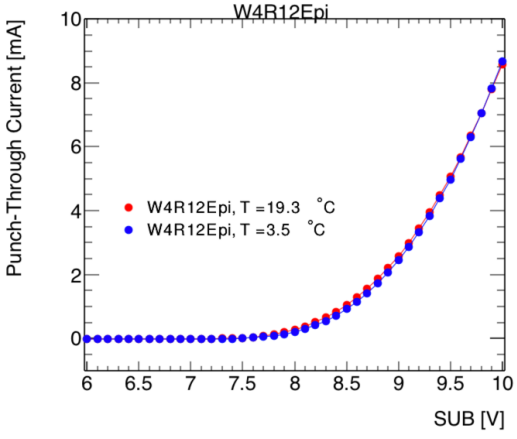

(e) Punch-through current for epitaxial n⁻ gap

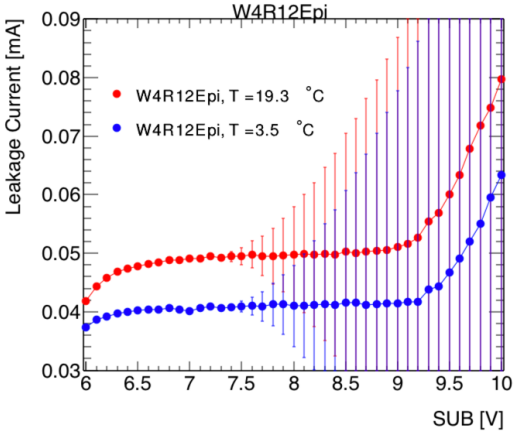

(f) Leakage current for epitaxial n⁻ gap

Figure 7.6: Current-voltage measurements for the unirradiated samples with the n⁻ gap or extra-deep p-well substrates at different temperatures.

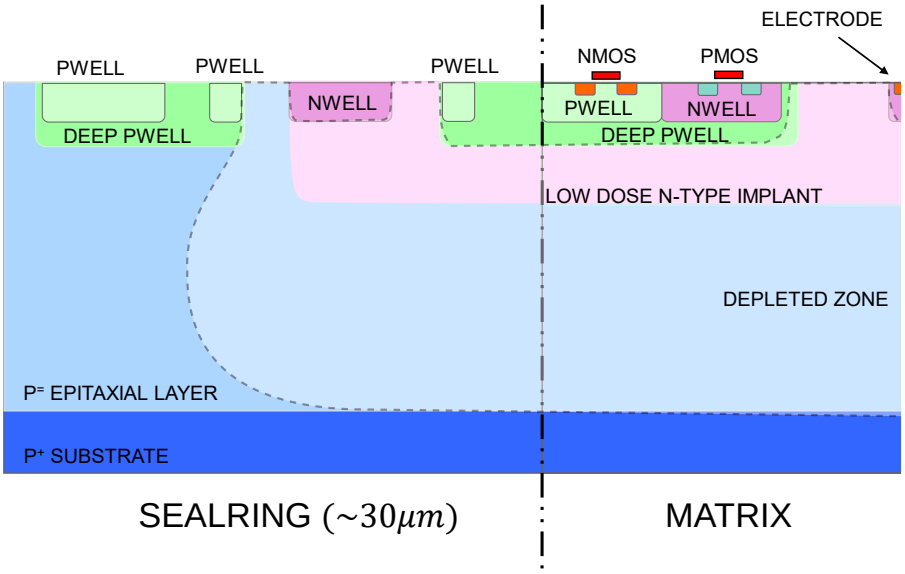

Figure 7.7: Schematic of seal ring structure at the edge of the pixel matrix, from [64].

calculated as the sum of two larger values, the p-well and substrate currents, in quadrature, which assumes the two values are independent when they are not. The actual variance of the leakage current is much less than suggested by the magnitude of the error bars in the plots.

In the measurements of the unirradiated devices, the temperature dependence of the punch-through currents is not characteristic of current flowing through bulk silicon, but instead of some sort of surface current. One possible route is through the seal ring structure around the pixel matrix, which is designed as a guard ring to collect current from outside of the matrix and is shown in Fig. 7.7 [64]. A single epitaxial continuous n^- device was tested which was diced from its wafer with a laser instead of a diamond saw to have a thinner periphery around the pixel matrix. The IV curve is shown in 7.8. The width of the region outside the seal ring was decreased from between 21 and 27 μm to between 4 and 6 μm. The sensor was measured to have a 1 mA punch-through with $\Delta V =\sim 32$ V, 9 V higher than the δV of 23 V measured in sensors with the standard dicing. It would be interesting to investigate the effects of dicing widths and techniques on the punch-through as potential methods to mitigate the punch-through and understand the underlying cause.

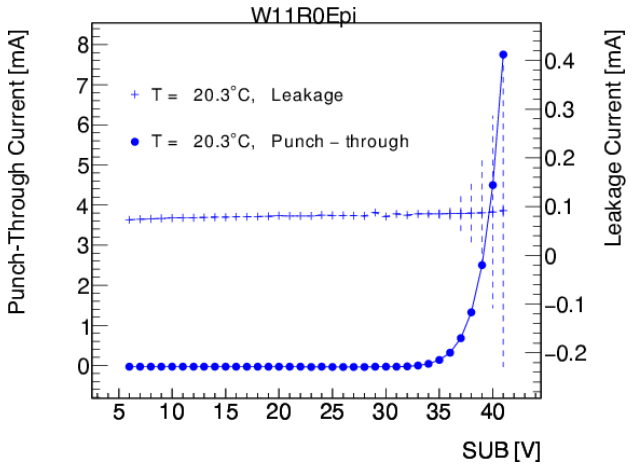

Figure 7.8: IV measurement of an epitaxial continuous n^- MALTA sensor with laser (instead of diamond saw) dicing to reduce the area of the periphery. The punch-through voltage is about 9 V lower in the diamond saw-diced samples.

7.2.1.3 Unirradiated samples at multiple PWELL biases

Fig. 7.9(a) shows the punch-through and leakage currents of an unirradiated Czochralski n^- gap sample, W9R11 as a function of substrate voltage. For each curve the sensor is biased with a different p-well voltage: 2, 4, or 6 V. The punch-through voltage is calculated as the voltage at which the punch-through current is greater than an arbitrarily chosen value of 1 mA. This is illustrated in Fig. 7.9(a) as the intersection of the IV curves and the horizontal line. In Fig. 7.9(c) and 7.10 are the punch-through currents for the unirradiated sensors as a function of the p-well voltage with linear fits of the data from each sensor. The resulting y-intercepts of the fits are tabulated in 7.1, and are the approximate voltage difference (ΔV) limit for operation of these sensors. The linearity of the data suggests that the punch-through current depends on this difference between the substrate and p-well biases as is expected, and not solely on the magnitude of the substrate bias.

In the Czochralski devices, there is initially a dominant punch-through current, then near the operational limits the leakage current becomes comparable in magnitude to the punch-through as shown in 7.9(b). In fact, one effect observed during these measurements was that at high substrate biases, the p-well current flows with the same polarity as the substrate current instead of "punching-through" to the substrate, which results in the p-well power supply further decreasing the voltage beyond the set value. This was measured by monitoring the TTi power

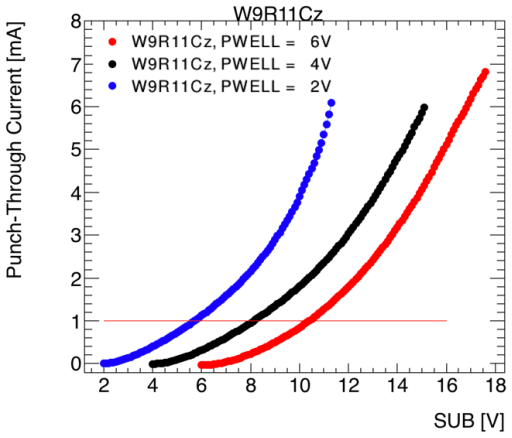

(a) Punch-through current and line at 1 mA to calculate the punch-through voltage.

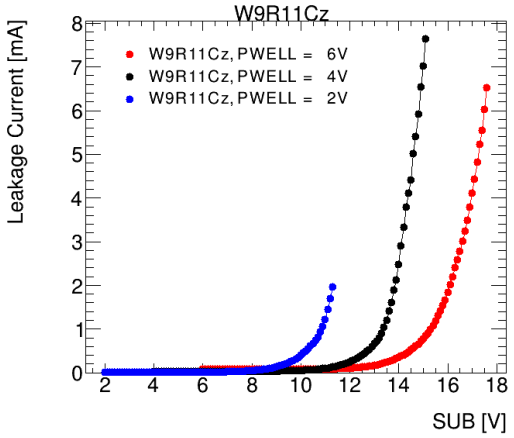

(b) Leakage current at the three p-well voltages.

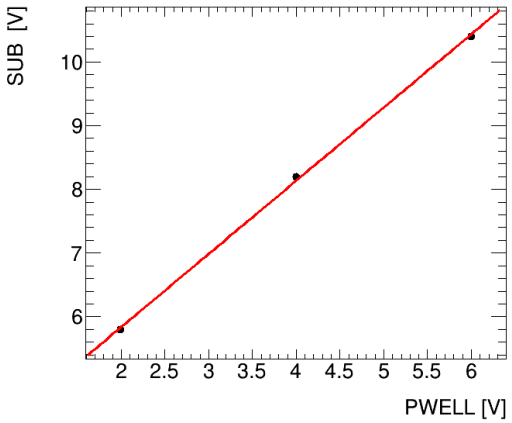

(c) Punch-through voltages

Figure 7.9: Current-voltage measurements for an unirradiated n^- gap Czochralski sensor, W9R11 at p-well biases of 2, 4, and 6 V.

Silicon	Pixel Design	ΔV =SUB - PWELL
Czochralski	cont. n^-	none, leakage breakdown at 45 V
Czochralski	n^- gap	3.54 V
Czochralski	extra deep p-well	1.88 V
Epitaxial	cont. n^-	22.7 V
Epitaxial	n^- gap	2.21 V

Table 7.1: Difference between the sub and p-well at which the punch-through reaches 1 mA as calculated from the linear fits in Fig. 7.10

supply via RS232 serial communication, and also with a digital voltmeter. This is problematic for the operation of the device since the p-well bias influences the behavior of the device, as is

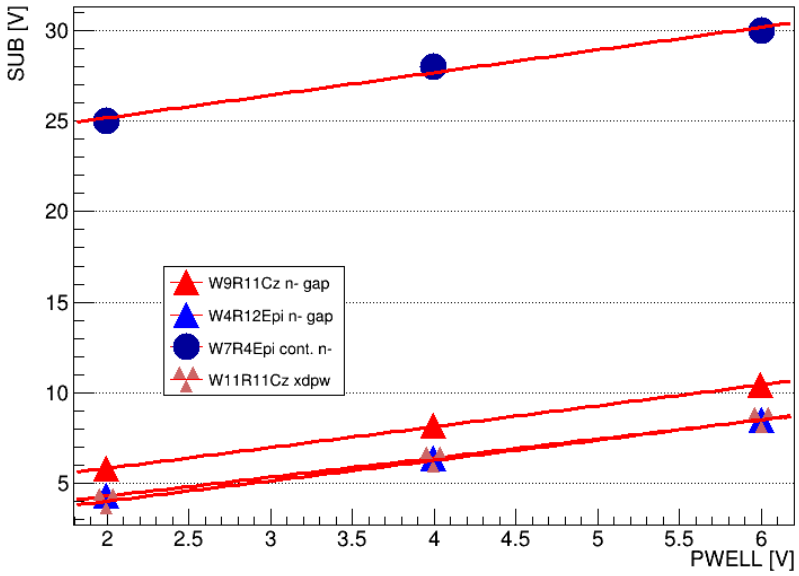

Figure 7.10: Linear fits of the difference between substrate and p-well bias at which there is 1 mA of punch-through current for different MALTA samples.

evident in these measurements and since it serves as the bulk of the NMOS transistors in the electronics. In the curves shown in this section, the p-well bias is within 50 mV of the intended value to avoid this effect.

A similar increase in leakage current also was observed in epitaxial devices. Near 9 V (with a p-well bias of 6 V) the leakage current begins to grow quickly as shown in Fig. 7.6(f). However, it did not reach the magnitude of the punch-thorough current before the overall operational limits of ∼12 V bias of the substrate was reached.

7.2.1.4 Irradiated samples

Neutron-irradiated samples

Samples were irradiated at the Triga nuclear reactor in Slovenia [54] with 1 MeV neutrons to fluences of 1×10^{15} and 2×10^{15} n_{eq}/cm^2 with TIDs of 1 and 2 MRad, respectively. Fig. 7.11 shows IV measurements for the Czochralski devices with the continuous n^- pixel and Fig. 7.12 and 7.13 show those for the remaining pixel designs with Czochralski silicon. In comparison to the unirradiated samples, the leakage current has increased and the punch-through component has

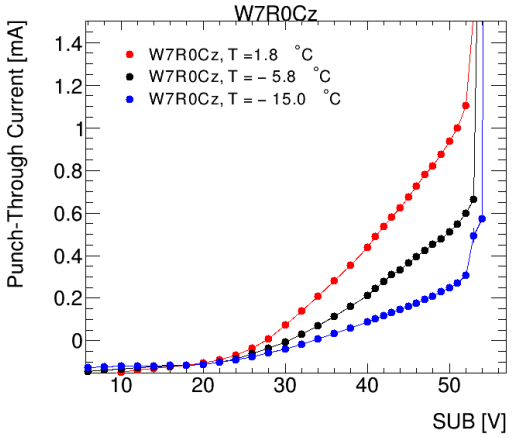

(a) Punch-through current for Czochralski continuous n^-.

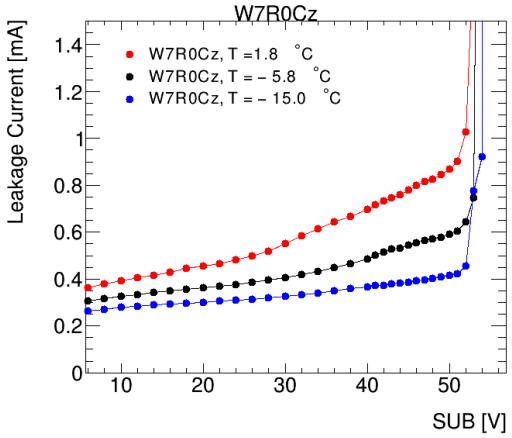

(b) Leakage current for Czochralski continuous n^-.

Figure 7.11: Current-voltage measurements for the irradiated Czochralski continuous n^- samples at different temperatures.

decreased. The calculated punch-through current is not significantly greater than the leakage current, and the overall current is less than prior to irradiation. With a 20 mA compliance, irradiated Czochralski samples were operable up to and above 50 V. Both currents have a positive temperature coefficient, unlike in the unirradiated devices, suggesting that current flows through bulk silicon as opposed to along the surface of a structure.

The epitaxial devices have similar characteristics before and after irradiation. There is a punch-through current that dominates with only a small ΔV, and there is insignificant temperature dependence, suggesting that it is not a current through bulk silicon.

That irradiated Czochralski chips can be operated up to and above 50 V is a key aspect for operation as there is deeper depletion and therefore more signal at 50 V than at 12 V. Further evidence for the deeper depletion is provided by cluster size and efficiency measurements in the DESY test beams and these are discussed later in this chapter.

Proton-irradiated samples

Two samples, an epitaxial n^- gap and a Czochralski extra deep p-well, were irradiated while cooled to -27 °C and under bias with a beam of 23 MeV protons at the MC40 Cyclotron facility at the University of Birmingham [62]. Both samples were irradiated to approximately 8×10^{14} n_{eq}/cm^2 with a total ionizing dose of 100 MRad and an uncertainty of 20% for both

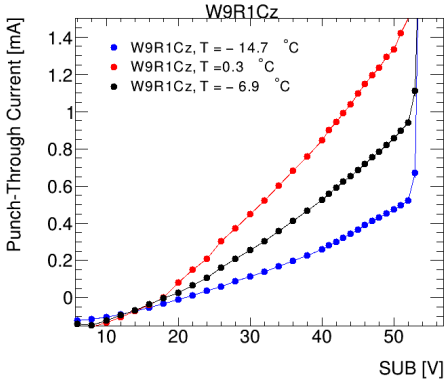

(a) Punch-through current for Czochralski n^- gap.

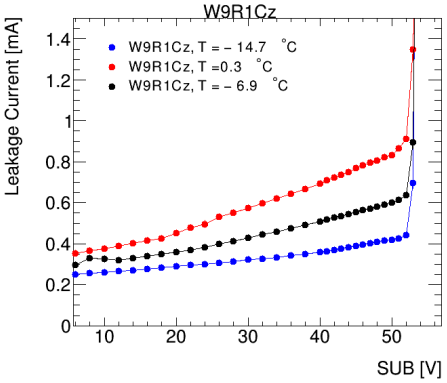

(b) Leakage current for Czochralski n^- gap.

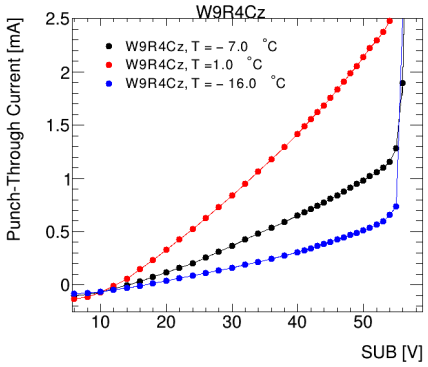

(c) Punch-through current for Czochralski n^- gap at 2×10^{15} n_{eq}/cm^2

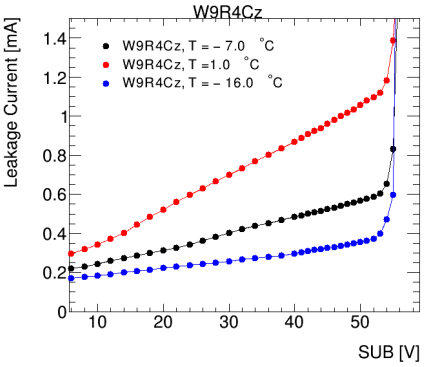

(d) Leakage current for Czochralski n^- gap at 2×10^{15} n_{eq}/cm^2

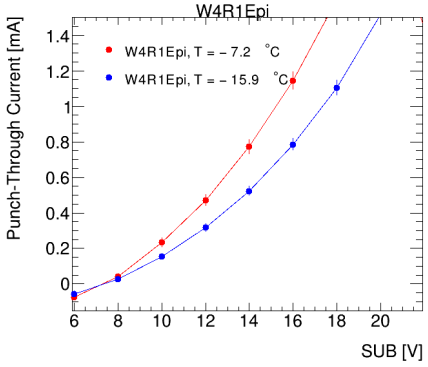

(e) Punch-through current for epitaxial n^- gap

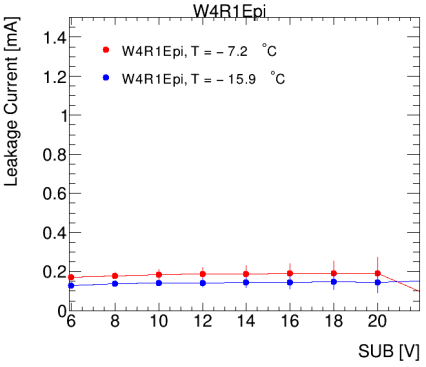

(f) Leakage current for epitaxial n^- gap

Figure 7.12: Current-voltage measurements for the irradiated samples with the n^- gap substrate at difference temperatures. The fluence is 1×10^{15} n_{eq}/cm^2 except for a single n^- gap sample.

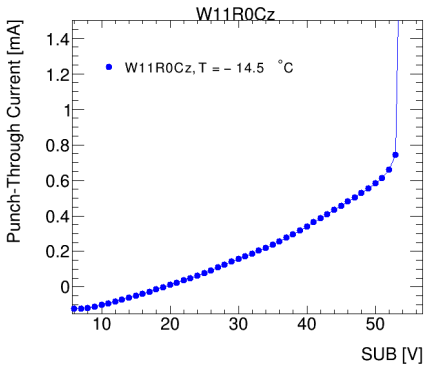

(a) Punch-through current for Czochralski extra deep p-well

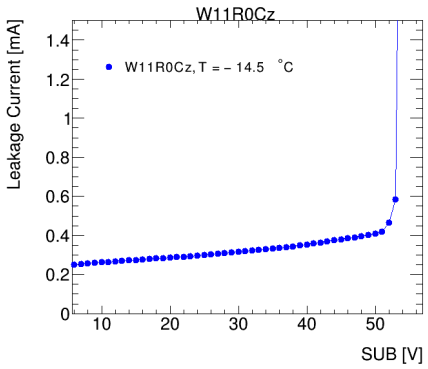

(b) Leakage current for Czochralski extra deep p-well

Figure 7.13: Current-voltage measurements for the irradiated samples with the n^- gap or extra deep p-well substrate at difference temperatures. The fluence is $1{\times}10^{15}$ n_{eq}/cm^2 except for a single n^- gap sample. [Continued from previous figure.]

values. The limited number of samples is due to the time constraints and logistical challenges in powering and operating a MALTA chip from the MC40 beam line.

The current voltage-measurements are plotted in Fig. 7.14. Here we can see that the proton-irradiated samples behave comparably to the neutron-irradiated samples irradiated to 1×10^{15} n_{eq}/cm^2 and 1 MRad. The Czochralski sample can be biased above 50 V and above this point the leakage current dominates. In the epitaxial n^- gap sample, there is a punch-through current which dominates, though it is not as large as in the neutron-irradiated device with the same pixel design.

7.2.1.5 IV Results Summary

The results of the IV measurements are summarized in Table 7.2 where the approximate operational limits and type of current are tabulated for unirradiated and irradiated sensors of the various designs. These limits were determined by the 20 mA current limit in the power supplies, or the limits of stable p-well biasing, and are accurate to approximately 2 volts.

For the unirradiated devices, the Czochralski and epitaxial samples have similar IV characteristics. For the modified process with a continuous n^- layer in epitaxial silicon, MALTA sensors have a significant punch-through current between the substrate and p-well with around 23 V of difference in bias between the substrate and p-well. The Czochralski sensors have a

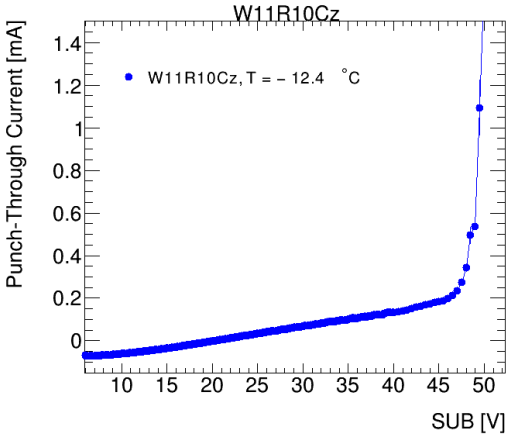

(a) Punch-through current for Czochralski extra deep p-well

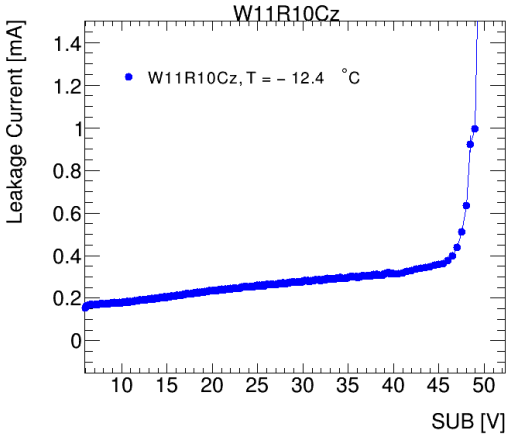

(b) Leakage current for Czochralski extra deep p-well

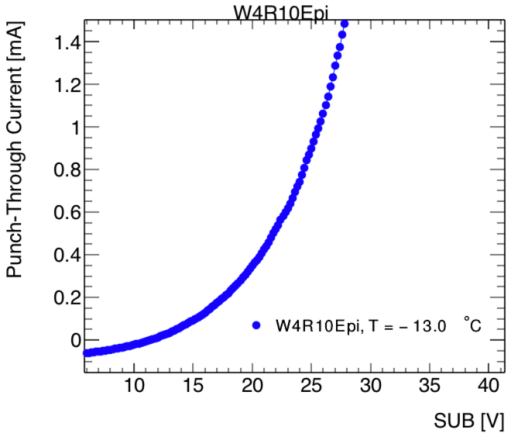

(c) Punch-through current for epitaxial n^- gap

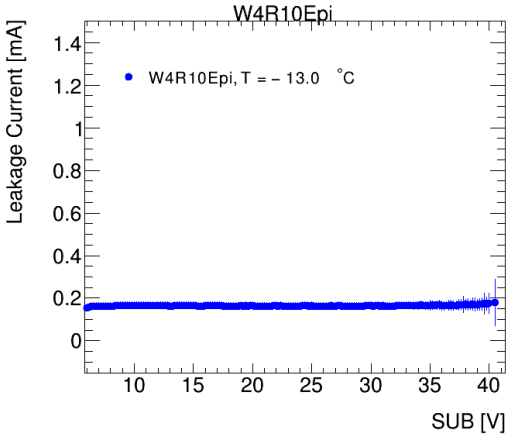

(d) Leakage current for epitaxial n^- gap

Figure 7.14: Current-voltage measurements for the proton irradiated samples with a fluence of $8{\times}10^{14}$ n_{eq}/cm^2 and TID of 100 Mrad.

breakdown in the leakage current near 50 V of bias, independent of the p-well voltage. For unirradiated epitaxial and Czochralski silicon, the new n^- gap and extra deep p-well designs to improve the radiation hardness of the chip draw a large punch-through current with only a small difference in bias voltage. This current has a negative temperature dependence. In the measurements at various p-well voltages, the punch-through voltage has a linear dependence on the p-well bias.

After irradiation (with either protons or neutrons), the Czochralski devices have significantly less punch-through current and can be operated above 50 V before the leakage current becomes too high. Furthermore, for the modified pixel designs, the higher the neutron-equivalent dose,

the higher the operational voltage. The irradiated epitaxial devices behave similarly to the unirradiated: there is a punch-through current that dominates with only a small ΔV (voltage drop between the p-well substrate), and there is insignificant temperature dependence of this current.

Silicon	Pixel design	Unirradiated limit [V] (mode)	1×10^{15} n_{eq}/cm^2 limit [V] (mode)	2×10^{15} n_{eq}/cm^2 limit [V] (mode)	8×10^{14} n_{eq}/cm^2 limit [V] (mode)
Cz	cont. n^-	50 (leakage)	55 (leakage)	N/A	N/A
Cz	n^- gap & extra deep p-well	17 (punch-through)	50 (leakage)	55 (leakage)	45 (leakage)
Epi	cont. n^-	30 (punch-through)	32 (punch-through)	N/A	N/A
Epi	n^- gap	12 (punch-through)	20 (punch-through)	N/A	25 (punch-through)

Table 7.2: Operational limits and the modes of current that dominate at the limit of MALTA Cz sensors with the p-well bias at 6 V. Uncertainties are 10%.

The IV measurements show that the limits of the operational voltage are well below the predicted full depletion voltage of 423 V, with the highest operational voltages near 50 V in the samples with the n^- continuous substrate. A planar diode model would suggest a depletion depth of approximately 104 μm at 50 V bias, meaning that the expected signal is about 8 ke and the full capabilities of the 300 μm of silicon are not being exploited and also that comparable results can be achieved with thinned sensors, which have the advantage of less material budget and resultant multiple scattering.

7.2.2 Gain measurements

The gain of MALTA devices was measured with an ^{55}Fe source targeted on the monitoring pixels of the MALTA and readout to a high bandwidth Lecroy WaveRunnner 9254 2.5 GHz digital oscilloscope using a Lecroy AP034 Active Differential Probe, similar to the measurements of MiniMALTA described in Section 6.2 [83]. Measurements were made to correspond to the settings used in test beams. To this end, measurements were made on the monitoring pixels

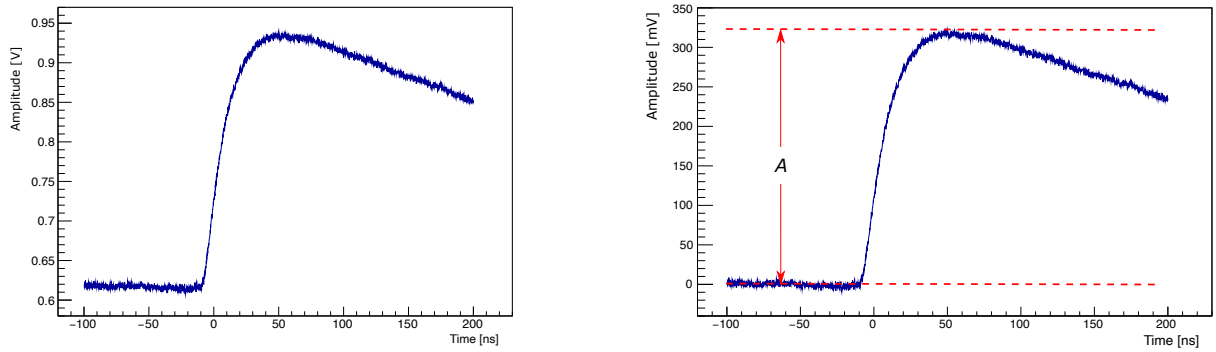

(a) Analog pulse from one of the monitoring pixels in MALTA

(b) Analog pulse from one of the monitoring pixels in MALTA after baseline subtraction. A is the pulse amplitude, the maximum voltage value after correction.

Figure 7.15: Output from a MALTA monitoring pixel with an ^{55}Fe X-ray source.

with the diode reset and with the DACs and bias voltages set to the same values as in the test beam. Both irradiated and unirradiated samples were tested in a climate chamber with the PCB cooled to -15 °C. Czochralski devices measured at higher bias voltages are expected to have more depletion and therefore less input capacitance, which is expected to affect the gain according to Equation 5.1.1. However, with the small collection electrode, a parallel plate model is not a good approximation of the behavior and the capacitance should not vary much even if the depletion depth does and the gain should remain relatively constant for a wide range of bias voltage drops between the substrate and collection electrode. The epitaxial sensors are fully depleted at the lowest operating voltage of 6 V and therefore a change in gain is not expected as the substrate voltage is increased above 6 V.

The ^{55}Fe isotope has two decays used to measure the gain of the sensor and front-end: the k-α decay in which 5.9 keV photons are emitted, and the less common k-β decay in which 6.49 keV photons are emitted. The ratio of these decay rates is expected to be 10:1, though the absorption length in silicon is slightly longer for the 6.49 keV photons, further skewing the ratio for the actual measurement. In silicon, an electron-hole pair is generated for every 3.6 eV of energy deposited, so the collected charge is expected to be 1640 e and 1800 e for the two photons, respectively. The gain is measured as the voltage output per collected charge, and has units of μV/e.

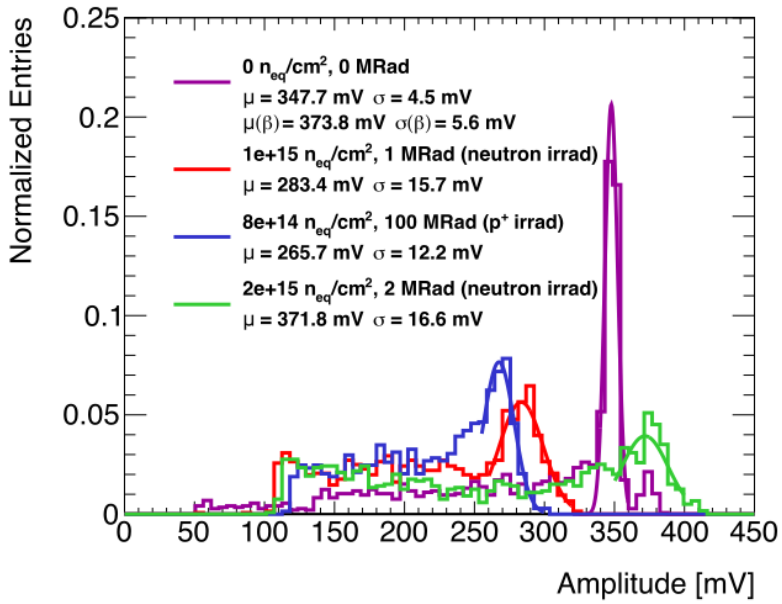

Figure 7.16: Amplitude spectra from ^{55}Fe of different MALTA devices.

Amplitude spectra are calculated from offline analysis of the individual waveforms. Fig. 7.15 shows the digital oscilloscope output of a monitoring pixel of MALTA and this signal after correction. The voltage measurements prior to the leading edge of the pulse are used to calculate the noise pedestal, which is subtracted in Fig. 7.15. The pulse amplitude is simply the maximum voltage value after subtracting the pedestal value. An amplitude distribution was formed from measurements of events in each of the four monitoring pixels on a sensor. Fig. 7.16 shows the amplitude spectra of single pixels for four samples, one unirradiated, two neutron irradiated to 1×10^{15} and 2×10^{15} $n_{\mathrm{eq}}/\mathrm{cm}^2$, and one proton-irradiated to 8×10^{14} and 100 MRad. A Gaussian fit was applied for each of the two peaks and the means of these fits were extracted. The measured amplitudes and corresponding gain are tabulated in Table 7.3. For irradiated sensors, it was difficult to fit the k-β peak so the k-α is used to determine the sensor gain. In the cases in which more than one pixel was used in the measurement, the gain is the mean of the gain of the individual pixels. The σ values are the σ values from the Gaussian fits, and are averaged for multiple pixels as well.

In Fig. 7.17(a) and 7.17(b) the gain is plotted as a function of the NIEL damage and TID. The mean gain value does not show a dependence on either the type of silicon or the pixel design, based on comparisons of the mean gain at the same level of irradiation. As tabulated in Table 7.3

Fluence [n_{eq}/cm^2]	Silicon type	Pixel design	k-α μ [mV]	k-α σ [mV]	k-β μ [mV]	k-β σ [mV]	Gain [μV/e]
None	Epi	n$^-$ gap	351.6±4.4	4.8± 0.2	378.5±4.8	5.1±0.2	214.5±2.7
	Cz	n$^-$ cont.	326.2±4.9	5.7± 0.3	350.3±5.0	5.8± 0.9	206.8±3.4
	Cz	n$^-$ gap	338.9±5.6	5.1± 0.4	364.0±6.2	5.8± 1.3	214.5±2.7
Neutron 1×10^{15}	Epi	n$^-$ gap	294.2±3.2	17.4± 0.63			179.5±2.0
	Cz	n$^-$ cont.	282.4±15.2	9.6±0.8			172.3±9.3
	Cz	n$^-$ gap	304±6.2	13.6± 1.41			185.5±3.8
	Cz	extra deep p-well	321.3±5.3	10.7± 0.4			196.0±3.3
Neutron 2×10^{15}	Epi	n$^-$ gap	362.4± 7.4	16.2± 0.3			221.1±4.5
	Cz	n$^-$ gap	376.0±4.8	15.8± 1.6			229.4±7.0
Proton 8×10^{14}, 100 MRad	Epi	n$^-$ gap	264.0±10.5	12.5± 0.2			161.1±6.4
	Cz	n$^-$ gap	265.6±11.7	11.0± 0.2			162.1±7.1

Table 7.3: Average of fit results to amplitude spectra of MALTA Cz samples. The analog signal is measured at the outputs of the preamplifiers of four monitoring pixels with the diode reset.

and shown in Fig. 7.17(a) and 7.17(b), the gain is less for the 8×10^{14} and 1×10^{15} n_{eq}/cm^2 samples, and greater at 2×10^{15} n_{eq}/cm^2 than prior to irradiation, and the σ values are much greater after irradiation due to the wider distributions in Fig. 7.16. These results are similar to those in MALTA and the TowerJazz Investigator in which the gain is greater at 2×10^{15} n_{eq}/cm^2 (though also at 2×10^{15} n_{eq}/cm^2) than for the unirradiated sensor [45], and the peak width is greater in the irradiated devices, presumably due to more electronics noise.

7.2.3 X-ray scans

To check for a uniform response across the entire pixel matrix of MALTA and the masking of pixels, The MALTA sensors were tested in an X-ray chamber at CERN. A micro X-ray source provided a spatially-uniform beam of X-rays with peaks at energies of 5.4 and 8.0 keV due to

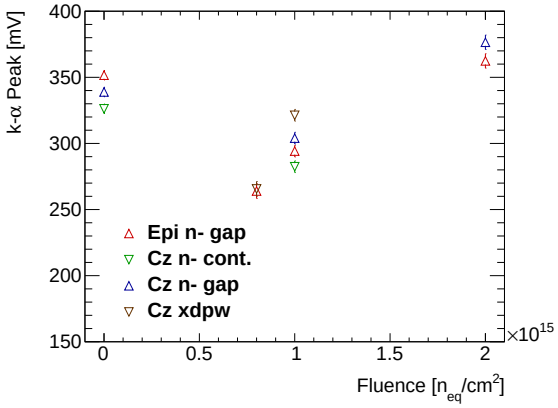

(a) Mean value of the amplitude of the k-α peak as determined from a Gaussian fit as a function of NIEL damage.

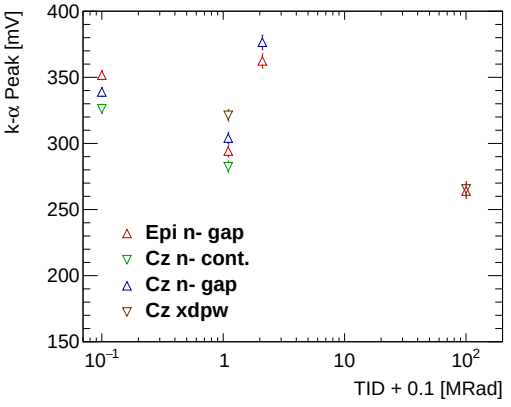

(b) Mean value of the amplitude of the k-α peak as determined from a Gaussian fit as a function of TID. The TID values have been increased by 0.1 MRad in order to use a log scale.

Figure 7.17: Average amplitude of the k-α peak in ^{55}Fe measurements.

the presence of chromium and copper, respectively.

Samples were measured at room temperature, and due to this, only unirradiated devices were measured. The X-ray source was placed on a stage above the MALTA carrier board. The MALTA chip was triggered from the FPGA board to read out hits in a set number of 500 ns windows. Pixels with a hit rate above 10 kHz were masked. The setup is shown in the photograph in Fig. 7.18(a). In Fig. 7.18(b), the spectrum of the X-ray beam is shown as measured in a monitoring pixel of MALTA with an active probe and digital oscilloscope, along with the spectrum for ^{55}Fe for comparison. The two bumps in the X-ray spectrum, one below the 5.9 keV k-α peak in ^{55}Fe and one above the k-β 6.9 keV, correspond to the chromium and copper target energies.

Mask type	Column	Row	Diagonal= row-column
Intentional	0	100	**100**
Intentional	0	**101**	101
Intentional	**1**	100	99
Ghost	**1**	**101**	**100**

Table 7.4: Example of how a coincidence in the intentionally masked rows, columns and diagonals results in "ghost" masking.

The masking in MALTA is achieved by masking all pixels in entire double columns or by

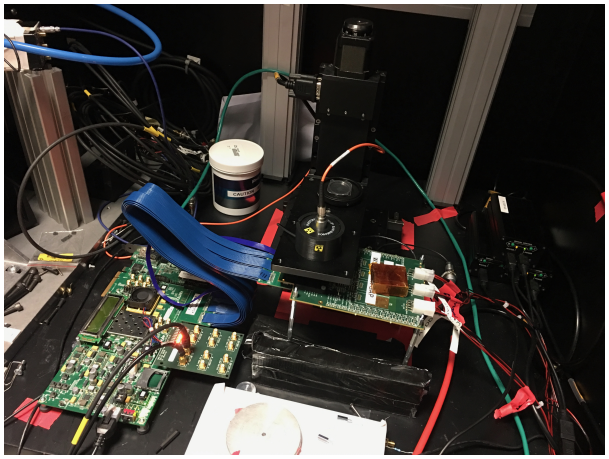

(a) The X-ray measurement setup.

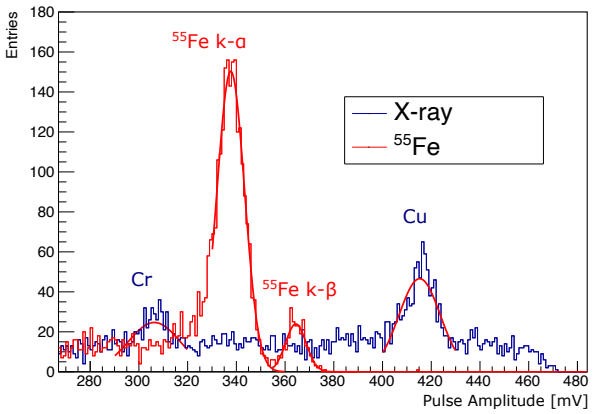

(b) The amplitude spectrum of the X-ray source as measured by MALTA with the spectrum of an ^{55}Fe source for comparison. The peaks corresponding to the copper and chromium targets and the ^{55}Fe source are labeled.

Figure 7.18: The X-ray setup and amplitude spectrum.

masking single pixels by setting the provided address lines to ground. There are 512 lines each for columns, rows, and diagonals. A diagonal is defined as a set of pixels such that the difference between the row and column number is a constant. A pixel is masked if all three of the corresponding row, column, and diagonal lines are masked (or if the entire double column is masked). A consequence of masking with this method is that in addition to masking the desired pixels, any other pixels which have all 3 of the row, column, and diagonal masked will be masked. As an example, consider masking the three pixels in Table 7.4 with column-row coordinates of (0,100), (0, 101), and (1, 100). To mask these, rows 100 and 101 and columns 0 and 1 must be masked, as well as diagonals 100, 101, and 99. This results in the unintended masking of a fourth pixel (1, 101) on the 100^{th} diagonal. These unintentionally masked pixels due to coincidences in masked rows, columns, and diagonals are known as "ghost" pixels. They can limit the detection efficiency when the number of ghost pixels becomes significant, and hence only limited number of pixels can be intentionally masked before there is a significant decrease in efficiency. The ratio of ghosts pixels to intentionally masked depends on the specific set of pixels masked, but in general becomes larger as more pixels are masked (assuming a small portion of the pixels are masked intentionally). To investigate the effectiveness of the masking, noise scans of MALTA were run to identify noisy pixels. After each scan, the noisiest

Sensor	Type	Masked pixels	Masked pixels and ghosts	Successfully masked pixels	Average number of hits	Average hits in zombies	Dead pixels
W4R12	Epi n^- gap	132	3202	2289	42	145	8
W7R12	Cz n^- cont.	57	319	251	39	1	0
W9R11	Cz n^- gap	65	487	283	42	2567	0
W11R11	Cz xdpw	74	687	475	22	2761	411
W11R0	Epi n^- cont.	40	131	103	36	1	0

Table 7.5: Table of masking statistics from X-ray scans at a substrate bias of 6 V.

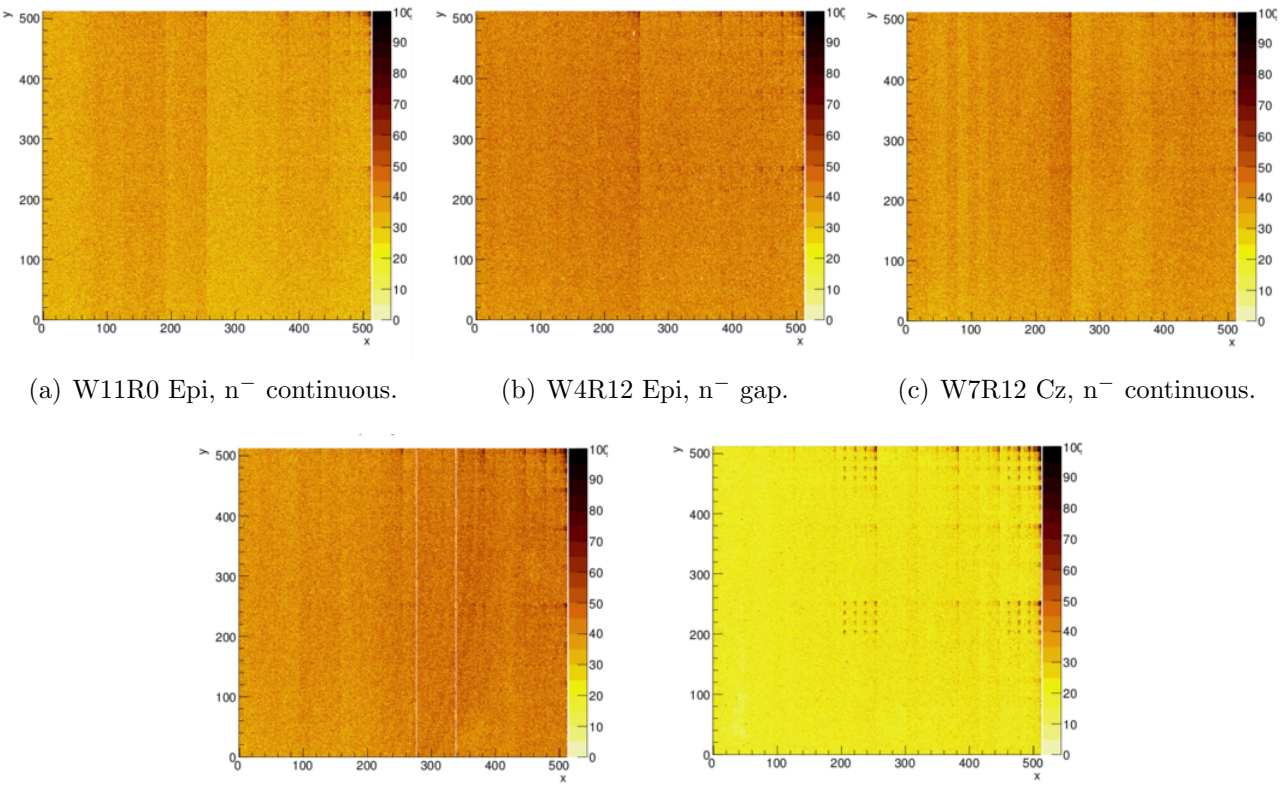

(a) W11R0 Epi, n^- continuous. (b) W4R12 Epi, n^- gap. (c) W7R12 Cz, n^- continuous.

(d) W9R11 Cz, n^- gap. (e) W11R11 Cz, extra deep p-well.

Figure 7.19: Occupancy as measured in the X-ray scans with the bias at 6 V.

pixel is masked until no single pixel had a noise rate above 10 kHz. A similar procedure was used in preparation for test beams. The number of hits in the masked pixels is compared to the number of hits in the other pixels from occupancy plots shown in Fig. 7.19. The response across

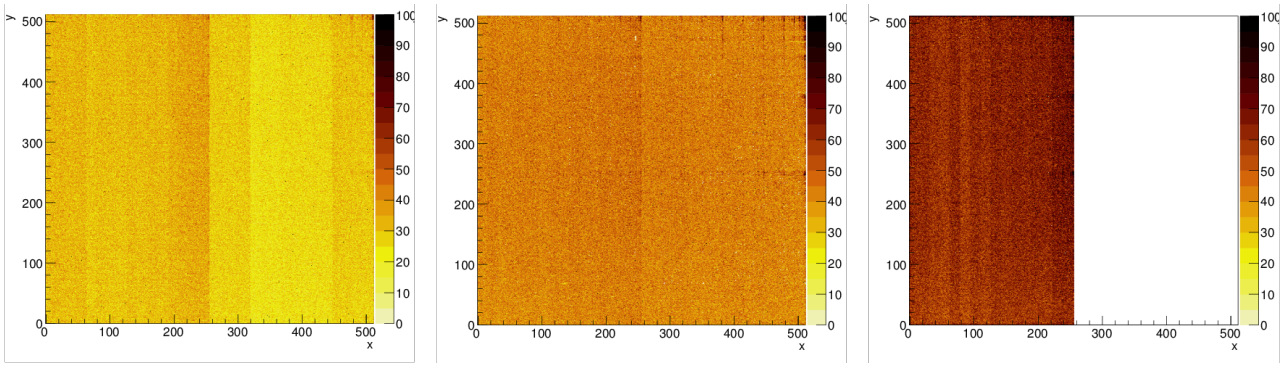

(a) W11R0 Epi, n^- continuous with 40 V substrate bias.

(b) W4R12 Epi, n^- gap with 11 V substrate bias.

(c) W7R12 Cz, n^- continuous with 50 V substrate bias.

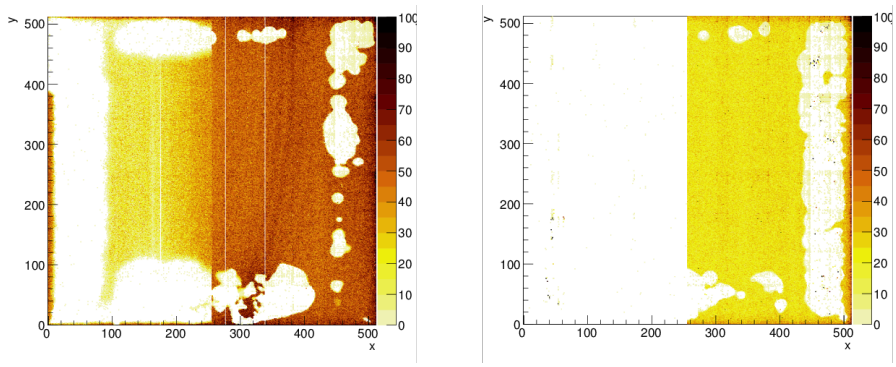

(d) W9R11 Cz, n^- gap with 15 V substrate bias.

(e) W11R11 Cz, extra deep p-well with 14 V substrate bias.

Figure 7.20: Occupancy as measured in the X-ray scans near the operational limit of the substrate bias.

the pixel matrix is uniform, with the exception of some aliasing of hits due to the OR merger, as is most apparent in Fig. 7.19(e). There is some variation between columns, possibly due to the difference in pixel design in the different sectors of MALTA in addition to the OR merging. The results from the X-ray scans with a substrate bias of 6 V are tabulated in Table 7.5. While most pixels are successfully masked, some are not, which are called "zombie" pixels. In some cases, such as in the sensor W7R12 with the epitaxial silicon and n^- continuous layer, there are few hits in the zombie pixels relative to the number of hits elsewhere in the pixel, suggesting that the pixels were actually masked. The small number of hits in these zombie pixels may be due to corruption of words when read out due to the OR merging in the column drain buffer or at the end of column. In other sensors, such as W9R11 and W11R11 with Czochralski silicon and the extra deep p-well and n^- gap pixel designs, these zombie pixels were not successfully masked and have hundreds of thousands of hits over the duration of the entire scan which was

2 s. Future versions of MALTA will have a masking scheme in which individual pixels can be masked without ghost pixels.

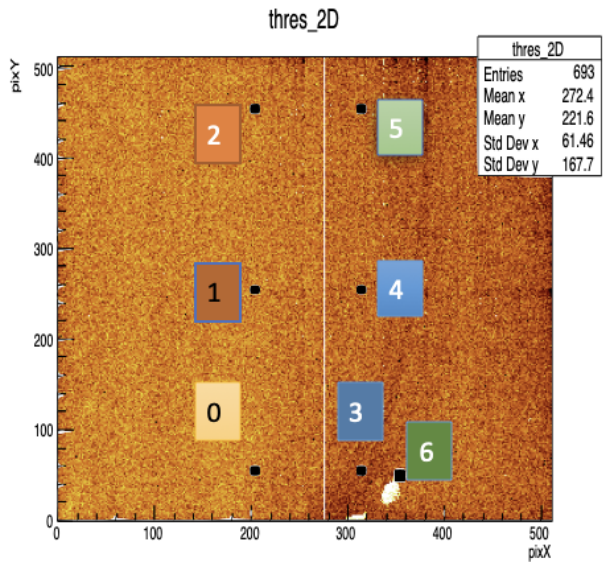

(a) W9R11 Cz, n^- gap, substrate bias of 9 V. Threshold scans were measured at the black mark next to the colored numbers.

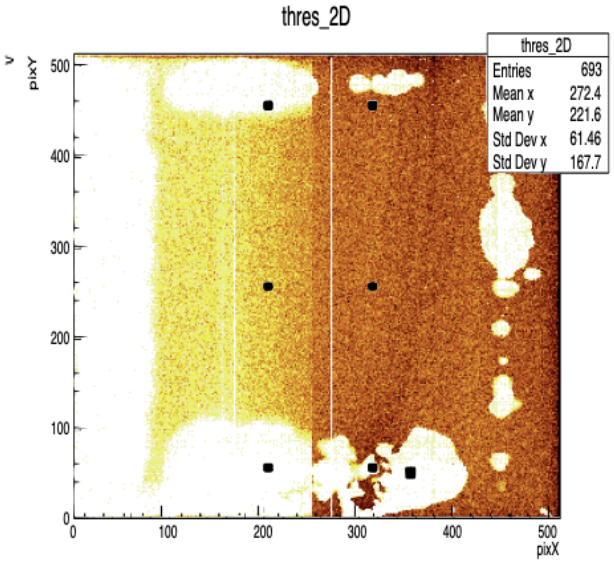

(b) W9R11 Cz, n^- gap, substrate bias of 15 V. Threshold scans were measured at the black mark next to the colored numbers.

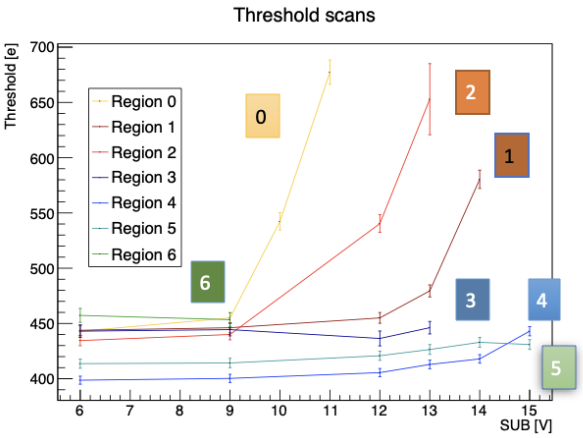

(c) Thresholds as measured as a function of substrate bias voltage in the regions numbered and colored in Fig. 7.21(a) and 7.21(b).

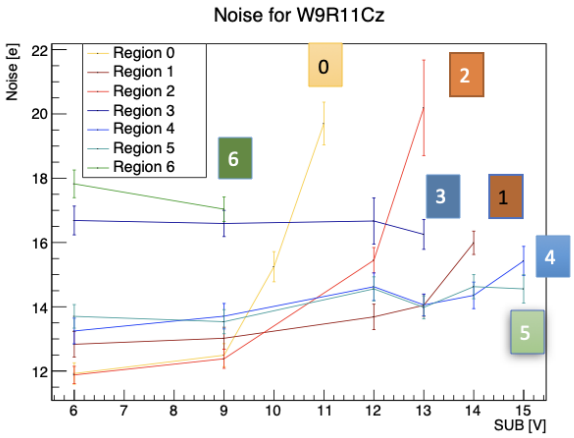

(d) Noise as measured in threshold scans as a function of substrate bias voltage in the regions numbered and colored in Fig. 7.21(a) and 7.21(b).

Figure 7.21: Occupancy as measured in the X-ray scans near the operational limit of the substrate bias.

At higher substrate voltages near the operational limits of the devices, the number of hits in specific regions of the sensors decreased as shown in the X-ray scans plotted in Fig. 7.20. These regions coincide with the areas of the sensor that are coupled with conductive glue to the carrier board which is biased with negative voltage to bias the substrate. These glue-like

patterns only appeared in the Cz sensors with the n⁻ gap and extra deep p-well, and not in sensors with the n⁻ continuous layer or the epitaxial sensors.

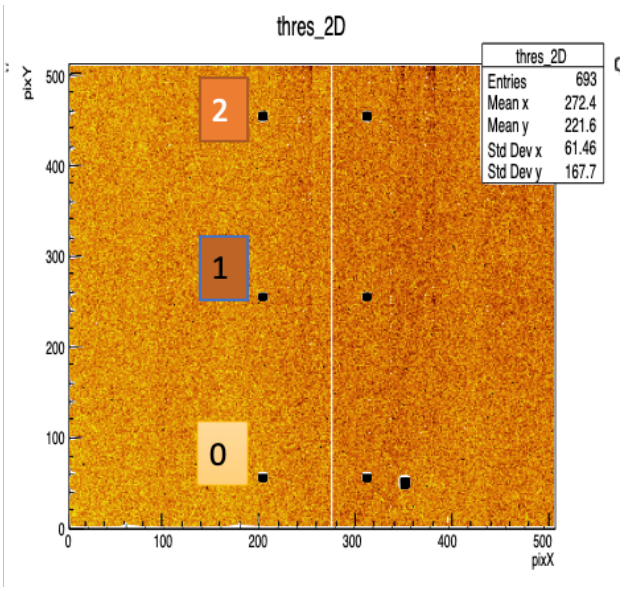

(a) W9R11 Cz, n⁻ gap, substrate bias of 6 V. Threshold scans were measured at the single black mark next to the colored numbers (at three marks in total).

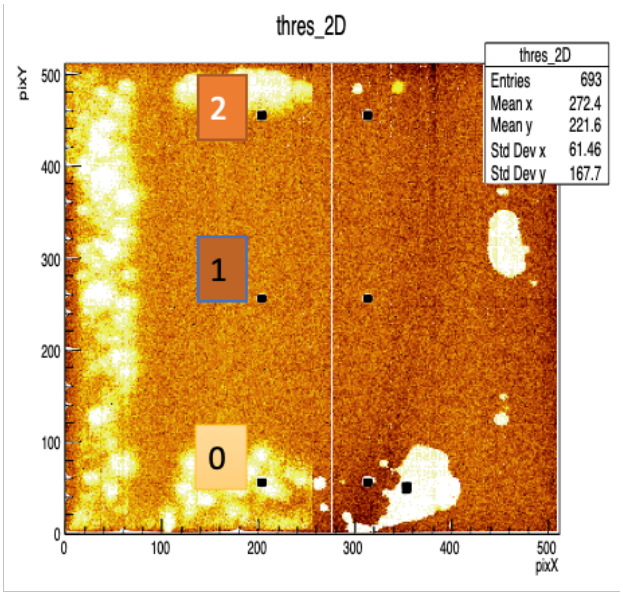

(b) W9R11 Cz, n⁻ gap, substrate bias of 13 V. Threshold scans were measured at the single black mark next to the colored numbers (at three marks in total).

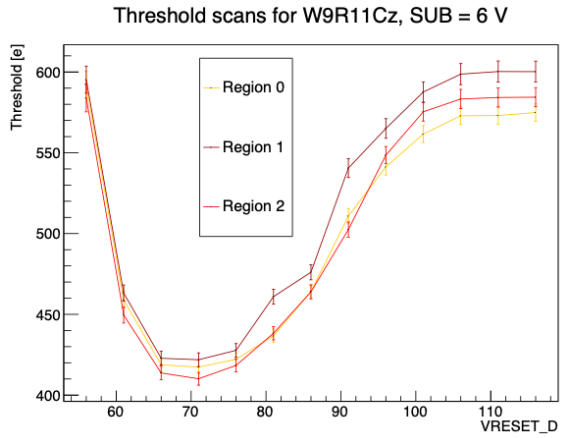

(c) Threshold measured as a function of the VRESET DAC at a substrate bias of 6 V in the regions numbered and colored in Fig. 7.22.

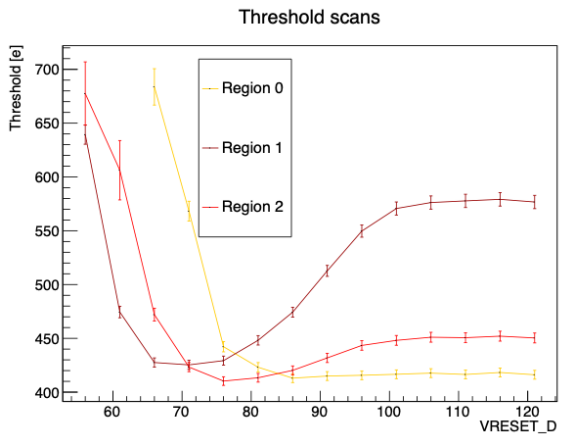

(d) Threshold measured as a function of the VRESET DAC at a substrate bias of 13 V in the regions numbered and colored in Fig. 7.22.

Figure 7.22: Occupancy as measured in the X-ray scans near the operational limit of the substrate bias.

Further investigation showed that the front-end behavior changed in the regions with glue. The mean threshold and noise were measured in the regions of MALTA illustrated in Fig. 7.21(a) with the substrate bias scanned from 6 to 15 V in 1 V steps. The resulting threshold and noise values are plotted in 7.21(c) and 7.21(d), respectively. As the substrate bias was increased,

the threshold and noise increased and fewer pixels could be successfully measured in threshold scans. Furthermore, measurements of the threshold in different regions with various values of the VRESET_D DAC, which sets the bias of the collection electrode, plotted in Fig. 7.22, show that there is a different operational value of VRESET_D to minimize the threshold in these different regions. At a substrate bias of 13 V, for region 1 in the plot, the ideal VRESET_D values is near 70, for region 2 it is 75, and for region 0 it is 90 or above. Future versions of the MALTA sensor with Czochralski silicon would benefit from careful design to ensure the substrate biasing is uniform across the entire pixel matrix to avoid large discrepancies when operating in or near this regime.

7.3 Efficiency measurements

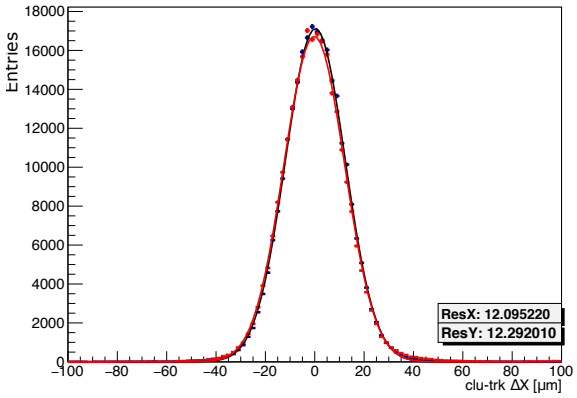

Figure 7.23: Track residuals of 3 GeV electrons as measured in Proteus with the MALTA telescope and the MALTA Cz DUT.

The efficiency of irradiated samples of MALTA Cz and full-scale epitaxial samples was measured in test beams of 3-5 GeV electrons at DESY. As with the MiniMALTA measurements, the MALTA telescope was used for data acquisition and track reconstruction was done with Proteus software and GBL. In Fig. 7.23 are distributions of the residuals measured in a MALTA Cz device, the σ of the Gaussian fits is 12 μm in each cardinal direction. With the full-scale MALTA chips instead of MiniMALTA, the telescope was triggered on a 1×1 cm^2 region of interest such that tracks passed through the 1×1 cm^2 window in the carrier board of the DUT.

Particles passing through the telescope planes in this region were less likely to go through the PCB and therefore pass through fewer radiation lengths of material and undergo less multiple scattering. As a result, the in-pixel plots show more detail for MALTA Cz than MiniMALTA with a comparable beam energy. Sectors 2 and 3 were measured, which have the larger 3 μm collection electrode and the medium and large p-well implant, respectively. The efficiency is generally slightly higher in the measurements of Sector 2, which is not surprising given the smaller p-well implant.

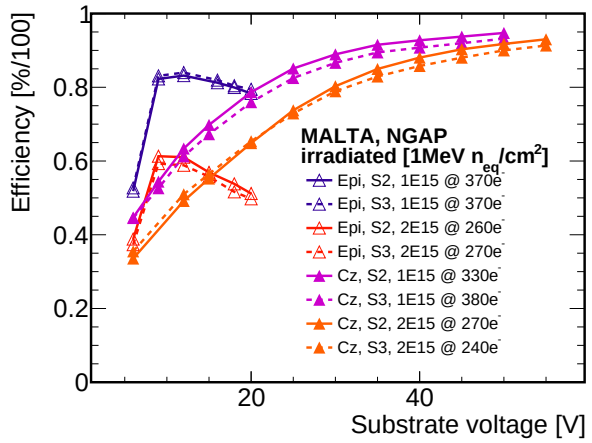

(a) Efficiency of neutron-irradiated n$^-$ gap samples.

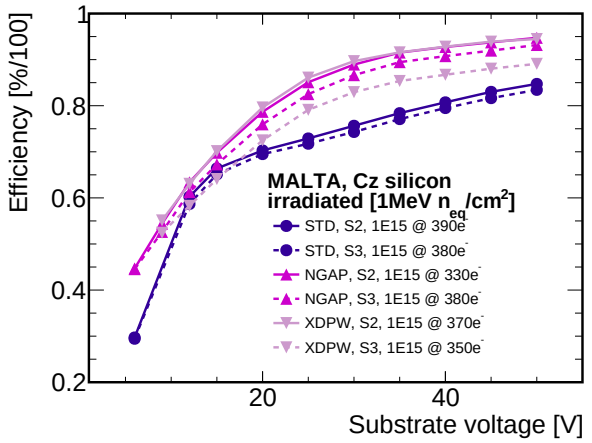

(b) Efficiency of neutron-irradiated Czochralski silicon samples, ϕ =1×10^{15} n_{eq}/cm^2.

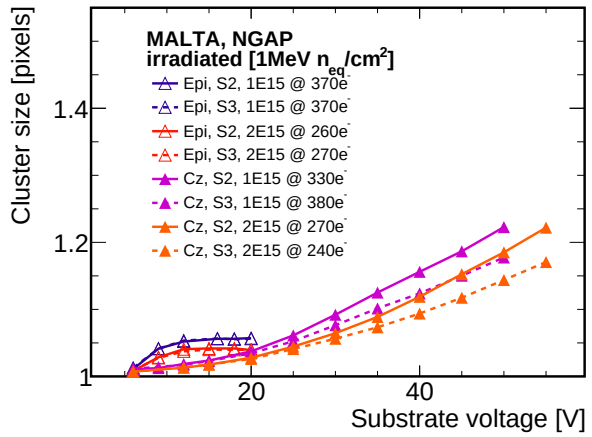

(c) Cluster size of neutron-irradiated n$^-$ gap samples.

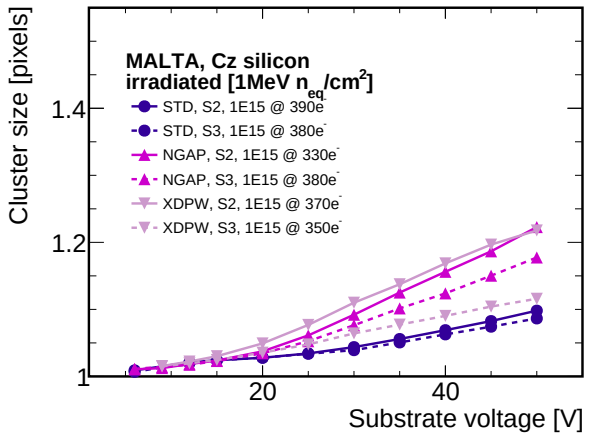

(d) Cluster size of neutron-irradiated Czochralski silicon samples, ϕ =1×10^{15} n_{eq}/cm^2.

Figure 7.24: Efficiency and cluster size measurements of MALTA Cz as a function of substrate bias. The thresholds are listed on the legend.

Fig. 7.24 shows the efficiency and cluster size of the MALTA Cz samples as measured at

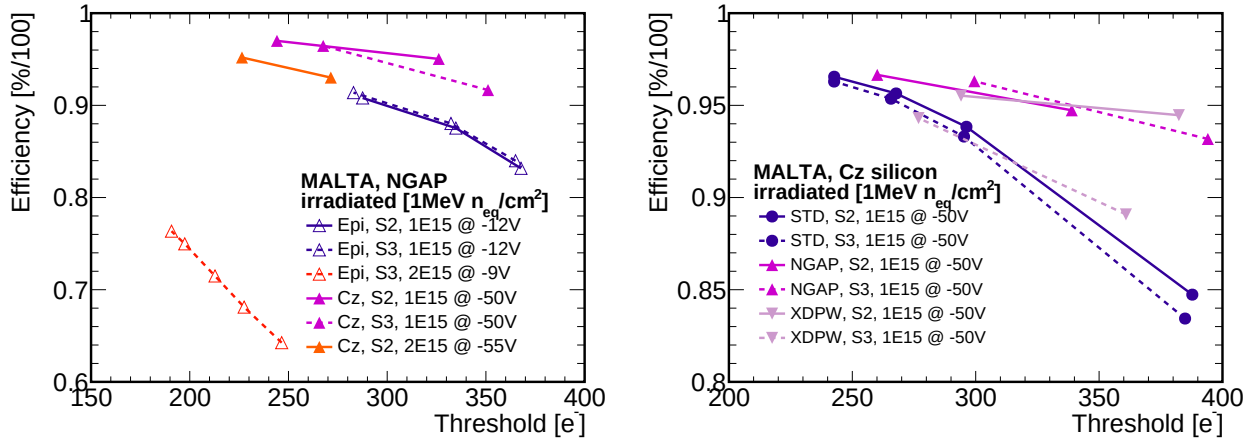

(a) Efficiency of neutron-irradiated n$^-$ gap samples.

(b) Efficiency of neutron-irradiated Czochralski silicon samples, ϕ =1×10^{15} n_{eq}/cm^2.

Figure 7.25: Efficiency measurements of MALTA Cz as a function of threshold.

DESY test beams as a function of substrate bias voltage. In order to demonstrate the best detection efficiency, at the bias voltage with the highest efficiency the front-end settings of the sensor were varied to achieve a lower threshold. The thresholds were measured at CERN after the test beam. In Fig.7.25, the efficiencies are plotted as function of the threshold.

In Fig. 7.24(a) the efficiency is plotted for n$^-$ gap samples irradiated to 1 ×10^{15} (magenta/blue markers) and 2 ×10^{15} (orange markers) n_{eq}/cm^2 as a function of bias voltage. For the epitaxial samples (empty markers), there is a maximum efficiency at 9 or 10 V. For the Czochralski samples (filled markers), the maximum efficiency is greater and achieved at 50 V, where more signal is expected due to the deeper depletetion. This is even the case when similar thresholds are achieved in the epitaxial samples, as shown in Fig. 7.25(a). For the Czochralksi sensors, the maximum efficiency is above 96% at 1 × 10^{15} n_{eq}/cm^2 and above 95% at 2 × 10^{15} n_{eq}/cm^2. Comparable efficiencies were measured with the Czochralski extra deep p-well sample irradiated to 1 × 10^{15} n_{eq}/cm^2 in Fig. 7.24(b). The efficiency for the Czochralski sensors is maximized at the operational limit of the device, as is the cluster size in Fig. 7.24(c) and 7.24(d). The increase in cluster size and efficiency suggests that the depletion depth is also increasing with the bias voltage, as we would expect given the resistivity and depth of silicon in Czochralski samples. Since the cluster size is also much larger than in the epitaxial samples, presumably more signal is generated and more than 30 μm of silicon, the maximum thickness of the epitaxial samples, is

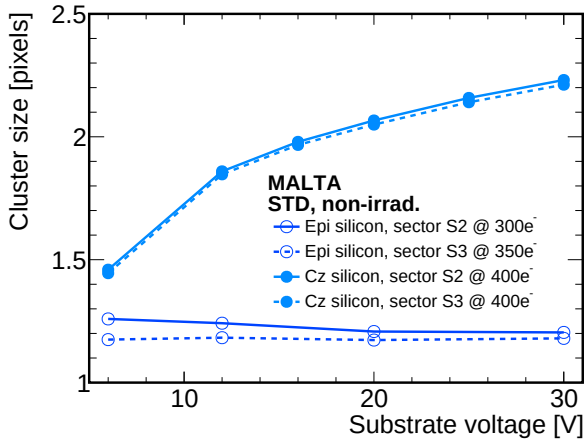

Figure 7.26: Cluster size of an unirradiated n^- continuous Czochralski sensor as a function of substrate bias.

depleted. In the unirradiated Czochralski samples, the cluster size in the Czochralski samples increases drastically with the bias voltage, as shown in Fig. 7.26. At 30 V, it is above 2.5. The n^- gap and extra deep p-well samples were limited by the large punch-through currents described in Sec. 7.2.1, and so such a measurement is not as suitable for demonstrating an increase in depletion.

In-pixel efficiency maps with the best efficiency for the n^- gap and continuous n^- substrates on Cz are shown in Fig. 7.27 [67]. The efficiency drops in the corners of the sample with the continuous n^- layer (Fig. 7.27(a)) more drastically than in the sensors with the modified pixel (Fig. 7.27(b)) at approximately the same threshold and bias. In the continuous n^- sample, however, the efficiency near the pixel center is slightly higher.

For samples with fluences of 1×10^{15} $n_{\mathrm{eq}}/\mathrm{cm}^2$, the efficiency is comparable at the same bias voltages and threshold settings, as shown in 7.25(b) and also Table 7.6 which summarizes the highest measured efficiencies in MALTA Cz. Unfortunately, wire-bonded extra deep p-well and n^- continuous sensors were not available at test beams with fluences at 2×10^{15} $n_{\mathrm{eq}}/\mathrm{cm}^2$ and so a comparison between the three pixel designs can only be made at 1×10^{15} $n_{\mathrm{eq}}/\mathrm{cm}^2$. Future test beams should characterize all three pixel designs at and above 2×10^{15} $n_{\mathrm{eq}}/\mathrm{cm}^2$.

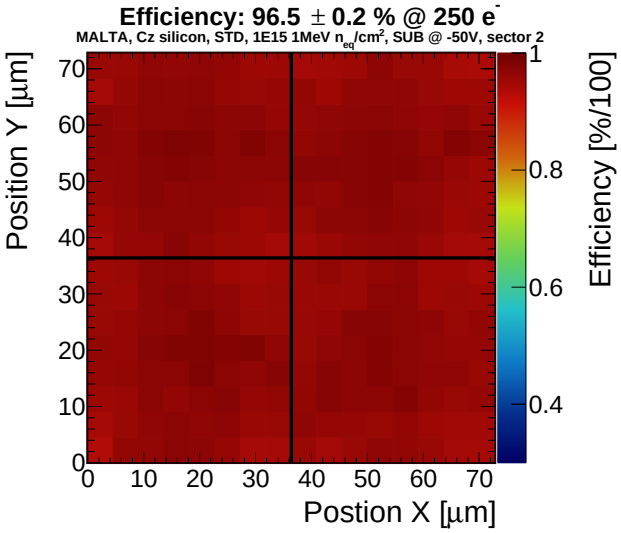

(a) Czochralski n$^-$ continuous pixel, ϕ =1e15.

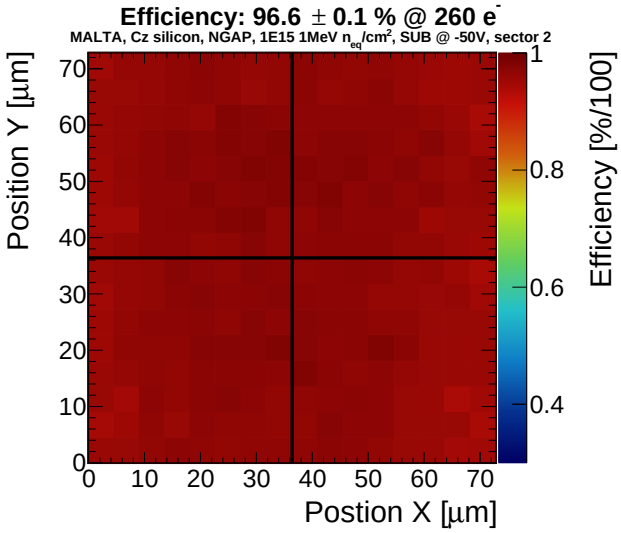

(b) Czochralski n$^-$ gap pixel, ϕ =1e15.

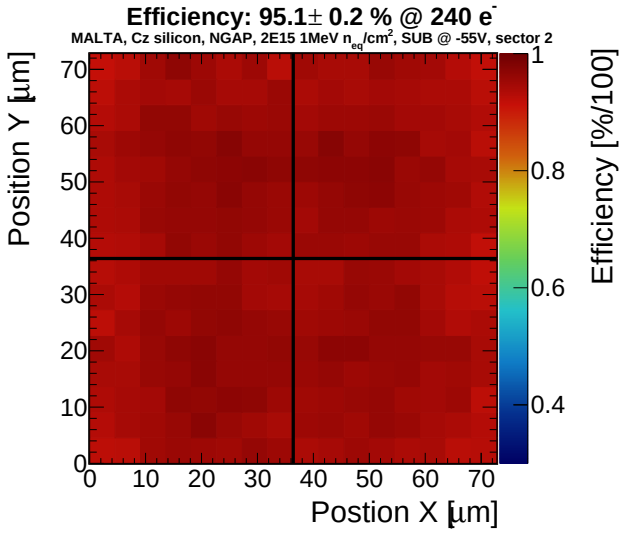

(c) Czochralski n$^-$ gap pixel, ϕ =2e15.

Figure 7.27: In-pixel efficiency maps of irradiated Cz samples [67].

7.4 Results summary, comparison of prototypes

The test beam and laboratory measurements demonstrate that MALTA sensors with Czochralski silicon are radiation tolerant to 1×10^{15} $n_{\text{eq}}/\text{cm}^2$ and approaching similar performance at 2×10^{15} $n_{\text{eq}}/\text{cm}^2$. This is achieved without any modifications to the front-end that were present in MiniMALTA and helped to improve the efficiency. The n$^-$ gap Czochralksi sample with $\phi = 2 \times 10^{15}$ $n_{\text{eq}}/\text{cm}^2$ had an efficiency above 95% and based on the comparable results at 1×10^{15} $n_{\text{eq}}/\text{cm}^2$, it is expected that the other two pixel designs may have comparable efficiency

Silicon type/thickness [μm]	Fluence [n_{eq}/cm^2]	Substrate modification	Efficiency [%]	Threshold [e]	Bias [V]
Epi / 25	0	continuous n^-	97.8± 0.3	320	-6
Epi / 30		n^- gap	99.1± 0.1	380	-6
Cz / 300		continuous n^-	98.4± 0.2	430	-6
Cz / 300		n^- gap	98.6± 0.1	360	-6
Cz / 300		extra deep p-well	97.9± 0.1	390	-6
Epi / 30	1×10^{15}	n^- gap	90.7± 0.2	290	-12
Cz / 300		continuous n^-	96.5± 0.2	250	-50
Cz / 300		n^- gap	96.6± 0.1	260	-50
Cz / 300		extra deep p-well	96.5± 0.1	300	-50
Epi / 30	2×10^{15}	n^- gap	76.6± 0.5	180	-10
Cz / 300		n^- gap	95.1± 0.2	240	-55

Table 7.6: Table of best efficiencies and thresholds measured in MALTA Cz in Sector 2 at different fluences. The uncertainties are statistical and assume a binary distribution.

at 2×10^{15} n_{eq}/cm^2 as well. If the front-end modifications in MiniMALATA were implemented in a new sensor along with a Cz substrate, this would likely make the sensor operational at lower thresholds and potentially improve the radiation hardness to unprecedented fluences for small collection electrode CMOS devices.

Table 7.7 summarizes the measurements completed for the various types of MALTA sensors. The laboratory results should help inform the design and operation of future versions of the MALTA sensors. The punch-through currents (Sec. 7.2.1) and loss of hits near the conductive glue (Sec 7.2.3) are certainly phenomena that ideally would be mitigated or avoided entirely. They would need to be resolved for implementation of MALTA in a physics experiment. However, the issues are not factors which have prevented the demonstration of crucial improvements to the sensor and its radiation tolerance. With the results of MiniMALTA in mind, there are three types of design modification to be explored in combination which would likely result in further improvements to the radiation tolerance: pixel substrate design, substrate thickness, and front-end modifications.

Silicon type/thickness [μm]	Fluence [n_{eq}/cm^2]	TID [Mrad]	Substrate modification	Efficiency test beam	^{55}Fe	IV	X-ray scan
Epi / 25	0	0	continuous n^-	✓	✓	✓	✓
Epi / 25 (laser diced)			continuous n^-			✓	
Epi / 30			n^- gap	✓	✓	✓	✓
Cz / 300			continuous n^-	✓	✓	✓	✓
Cz / 300			n^- gap	✓	✓	✓	✓
Cz / 300			extra deep p-well	✓		✓	✓
Epi / 30	1×10^{15}	1	n^- gap	✓	✓	✓	
Cz / 300			continuous n^-	✓	✓	✓	
Cz / 300			n^- gap	✓	✓	✓	
Cz / 300			extra deep p-well	✓	✓	✓	
Epi / 30	2×10^{15}	2	n^- gap	✓	✓	✓	
Cz / 300			n^- gap	✓	✓	✓	
Epi / 30	8×10^{14}	100	n^- gap		✓	✓	
Cz / 300			extra deep p-well		✓	✓	

Table 7.7: Table of measurements completed with different types of MALTA samples that are presented in this chapter. The check mark indicates the measurement was completed, the lack of a check indicates it was not. The X-ray scans could not be completed for the irradiated sensors due to lack of a cooling setup for this measurement. The proton-irradiated devices with $\phi = 8 \times 10^{14}$ n_{eq}/cm^2 were not irradiated prior to the DESY test beam and so did not have efficiency measurements. The unirradiated extra deep p-well sample was not available for ^{55}Fe measurement due to its use in other setups.

Chapter 8

Digital Electromagnetic Calorimetry for Future Colliders

In addition to use in tracking applications, monolithic active pixels have been proposed for use in construction of a digital high-granularity electromagnetic calorimeter see *e.g.* [84–87], where the high granularity of the pixel sensors is advantageous for reconstruction of objects in dense environments such as jets. This chapter presents the concept of digital electromagnetic calorimetry, and both new simulation studies and measurements. The simulations explore the performance of a MAPS-based calorimeter when implemented as a variant of the general-purpose detector CLICdet [17] introduced in Sec. 2.2. The new measurements are made using DECAL prototype pixel sensors in the TowerJazz 180 nm (standard and modified) imaging processes, with readout logic designed for calorimetry.

8.1 High-Granularity Digital Electromagnetic Calorimetry

8.1.1 Motivation for particle flow approaches

For the next generation of particle physics experiments, including the ILC, CLIC, CEPC, and FCC-ee, FCC-hh, precision measurements and new searches will depend on the analysis of final states containing hadronic jets, where reconstruction is challenging due to the track density in high p_T jets and, in hadron colliders, also multiple overlapping interactions, giving rise to very high local detector hit densities. Particle flow algorithms seek to identify and measure the energy and momentum of each individual particle in a collision, with a focus on hadronic jets. In order to achieve high precision using particle flow techniques, both high-granularity calorimeters and sophisticated software to exploit the granularity are required, and are the subject of ongoing development.

As described in [88], in traditional approaches to calorimetry, jet energies have typically been measured by summing the energy in the hadronic and electromagnetic calorimeters, and resulted in jet energy resolutions of the form

$$\frac{\sigma_E}{E} = \frac{a}{\sqrt{E(\text{GeV})}} \oplus b \tag{8.1}$$

with $a = 60\%$ and b at the percent level. To make precise measurements with center-of-mass energies in the range of 100's of GeV, a jet energy resolution with $a < 30\%$ is required, but not likely achievable with traditional approach of simply summing the energy in the hadronic and electromagnetic calorimeters. The limitation is the energy resolution of the hadronic calorimeter ($55\%/\sqrt{E(GeV)}$) that is used to measure most of the jet energy. As shown in Table 8.1, in a typical jet about 60% of the energy is from charged particles that are observed as a track in the tracker, 30% is from photons, which are measured in the electromagnetic calorimeter, and 10%

is from neutral hadrons, the only portion of the jet that must be measured exclusively by the hadronic calorimeter. If the momenta of charged particles can be measured in the tracker and these tracks associated to hits in the calorimeters, then the hadronic calorimeter would only be used to measure the remaining 10% of the energy and thus the jet energy resolution could be improved, given the relatively poor intrinsic resolution of hadronic calorimeters compared to all other subdetectors. While this gives a general idea of the potential of a particle flow approach to calorimetry, in practice it will not be possible to reconstruct every particle perfectly. To approach this ambitious goal will require the development of both new calorimeters with superior spatial resolution and new software to take advantage of these devices.

Particle type	Fraction of Jet Energy	Detector	Energy Resolution
Charged particles	0.6	Tracker	$10^{-4}E^2$
Photons	0.3	ECal	$0.15/\sqrt{E}$
Neutral hadrons	0.1	HCal	$0.55/\sqrt{E}$

Table 8.1: Typical jet composition and energy resolution of detectors for the various jet components [88].

8.1.2 High-granularity calorimetry

In pursuit of high-granularity calorimetry with particle flow analysis, the CALICE collaboration has explored several approaches for developing prototypes for both hadronic and electromagnetic calorimeters, with different sensing mediums and readout schemes [49]. A calorimeter is designed to measure the energy of specific types of particles: hadronic calorimeters measure hadronic components from particles such as neutrons, protons, and kaons, while electromagnetic calorimeters measure charged particles and photons. Calorimeters are made to absorb and measure the entire energy of particles within the length of the calorimeter and are constructed from materials that absorb a large amount of the particles' energy in a short distance, though they must also detect the particles from the resulting particle showers. In homogeneous calorimeters, a single material is used for both absorption and detection, whereas in sampling calorimeters alternating layers of passive absorbing material and active detectors are used.

As shown in Fig 8.1, the work of the CALICE collaboration is divided into five exploratory

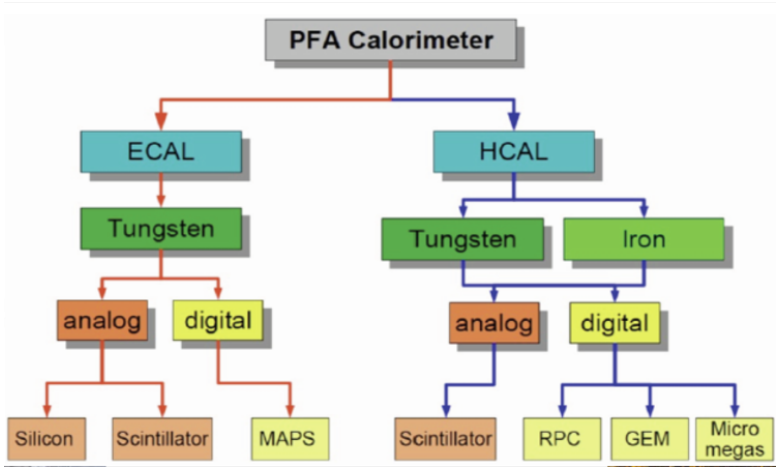

Figure 8.1: The various branches of development of Particle Flow calorimetry of the CALICE collaboration.

branches: development of an ECAL with tungsten absorbers and scintillators with analog readout (ScECAL) or with analog (SiW ECAL) or digital (SiW DECAL) silicon detectors, and development of analog (AHCAL) and digital (DHCAL) hadronic calorimeters. For hadronic calorimetry, both steel and tungsten [89] have been considered as absorbing materials by CALICE, and for sensing materials analog scintillators and digital approaches have been developed. The work of this thesis and the development of the DECAL prototype sensors is in exploration of the possibility of a digital SiW calorimeter.

In addition to advantages in granularity, a SiW calorimeter allows for construction of a more compact calorimeter (and therefore overall detector) than the liquid argon calorimeters that have been used in the ATLAS experiment and are considered a "baseline" technology for some future experiments such as FCC-hh. In proposed SiW designs, the absorbing layers of tungsten are several mm thick and sensing layers of silicon detectors less than 500μm thick, whereas in ATLAS, the liquid argon used as sensing material is 2 mm thick and comparable to the thickness of the absorbing layers of lead which ranges from 1.1 to 2.2 mm, as shown in the cross-sections in Fig. 8.2. Since the relative sensing volume of the SiW design is much smaller than that of the ATLAS LAr, the same radiation length can be achieved with a shallower calorimeter. The LAr is 53 cm thick in the barrel region to achieve 24 radiation lengths of attenuation, and in proposed SiW calorimeters, 22 radiation lengths would be achieved in approximately 20 cm. This would allow all systems outside of the calorimeter to be smaller. For detector designs with

the calorimeter inside of a magnetic solenoid, such as the CLICdet design for the proposed CLIC experiment and simulation work presented in this chapter, a compact SiW calorimeter decreases the size of the solenoid, a key driver for the cost of a detector [17]. A High-Granularity Calorimeter (HGCAL) using silicon pads for the ECAL and utilizing concepts from CALICE, is planned for installation in CMS during Long Shutdown 3.

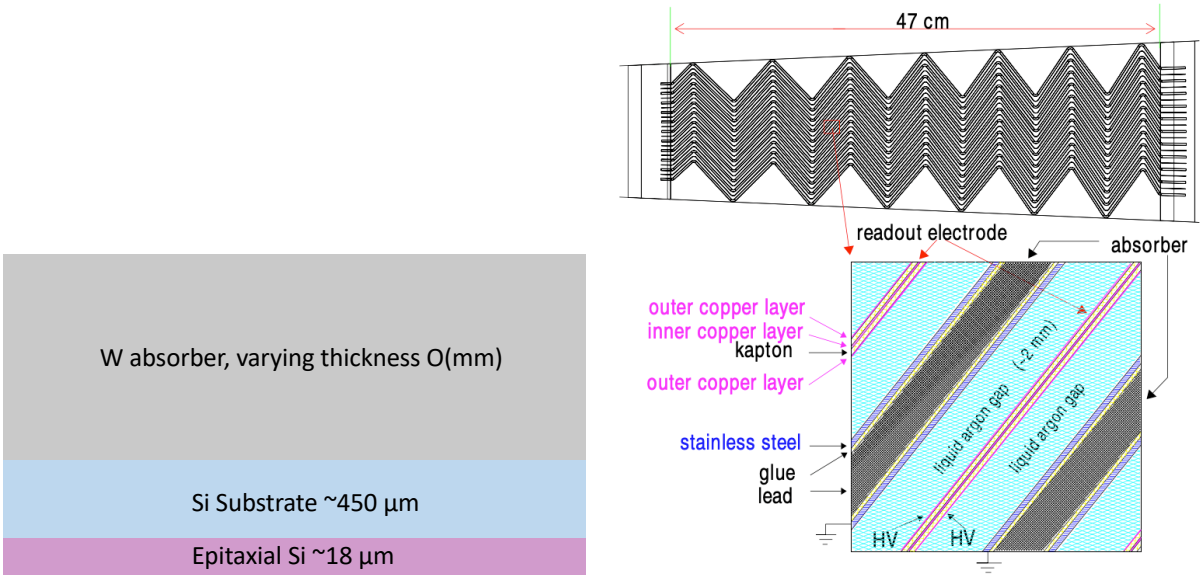

(a) Schematic of a layer in a digital SiW calorimeter with a monolithic sensor.

(b) Schematic of the accordion layout and cross section of the ATlAS LAr calorimeter.

Figure 8.2: Layers in the ATLAS LAr and proposed digital SiW calorimeters.

8.1.3 Digital electromagnetic calorimetry

In the digital version of electromagnetic calorimetry, the energy of a shower is estimated from the number of pixels that register a hit in a high granularity sensor. This differs from the analog approach where the energy is estimated from the signal pulse heights in larger (5×5 mm^2) analog pads. For the digital case, to estimate accurately the number of particles in the shower and thereby the total energy, it is necessary to have a small pixel size to avoid multiple particles passing through a single pixel and being effectively recorded as one, a problem known as saturation.

This digital version of calorimetry is motivated by several factors. It allows the use of MAPS, which may reduce production and assembly costs and complexity for a large experiment. The

improved granularity in the digital case may offer improved particle tracking and reconstruction while maintaining comparable energy resolution, and to this end simulation of integration of a digital SiW calorimeter into a full detector shows promising results in single particle events, which are the subject of Sec. 8.3. The radiation hardness of CMOS sensors is maturing, which increases their potential applications. DECAL prototype sensors have been produced in the TowerJazz 180 nm CMOS imaging sensor modified process, which has demonstrated radiation hardness at 10^{15} $n_{\mathrm{eq}}/\mathrm{cm}^2$ with MALTA as described in detail in Chapters 5, 6, and 7.

8.2 The DECAL chip

The DECAL prototype, shown in Fig. 8.3(a), is a sensor fabricated in the TowerJazz 180 nm CMOS imaging process with an 18 μm thick high resistivity epitaxial layer and a 64×64 matrix of 55×55 $\mu\mathrm{m}^2$ pixels [90]. As its name implies, DECAL is intended for digital electromagnetic calorimetry and reads out the total number of pixels hits at a rate of 40 MHz. The DECAL sensor can be configured to readout in "strip mode" for tracking and pre-shower layers or "pad mode" for pixel counting to give a measure of the total shower energy in regions deeper in the ECAL where the higher granularity is no longer advantageous for reconstruction and is a challenge to readout. In strip mode the total number of hits in each strip is summed, with up to three hits per strip. In pad mode the matrix is divided into four pads of 16 strips each as shown in Fig. 8.4 and up to 15 hits can be summed from each strip for a total of 240 from a pad and a maximum occupancy of 960 hits out of 4096 pixels.

In Fig. 8.3(b), a GDS file of a single pixel in DECAL is shown. The pixel is designed with four small collection electrodes in the corners to have low capacitance and crosstalk, unlike the MALTA pixel which as a single collection electrode in the pixel center. Each pixel contains a pre-amplifier, shaper, discriminator and a 5-bit calibration DAC to tune the threshold.

The biasing of DECAL is somewhat different than that on MALTA. Instead of having a negative voltage applied to the substrate and p-well (usually -6 V) and the collection electrode held slightly above ground (around +0.8 V), for DECAL, the p-well and substrate are held at

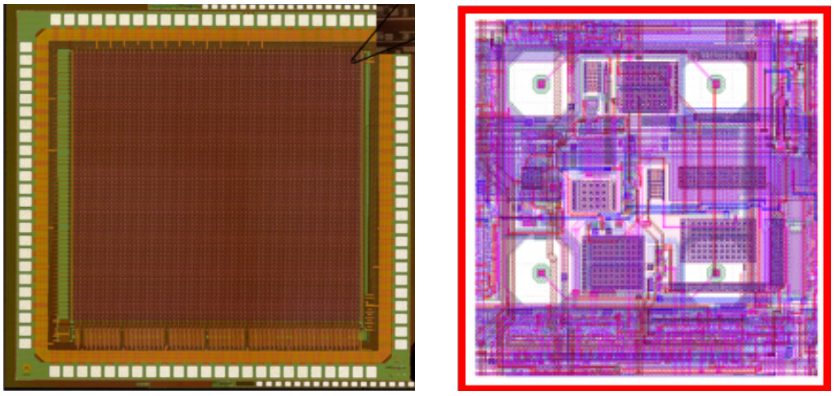

(a) The DECAL sensor.

(b) GDS file of a single pixel in DECAL.

Figure 8.3: The DECAL sensor.

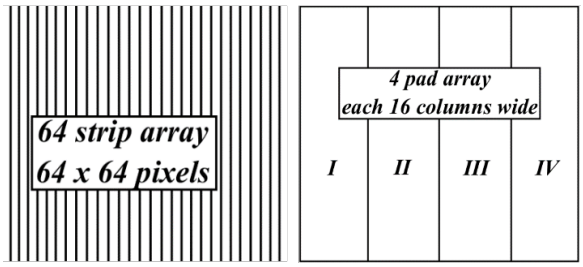

Figure 8.4: Schematic of the strip and pad modes in DECAL.

0 V and the collection electrode is biased, typically at +3.3 V, but as high as +6.5 V. The setting of +3.3 V should be above the depletion voltage of the sensor, and this is supported by ^{55}Fe measurements at various bias voltages in this section. While the DECAL biasing results in a comparable relative bias for MALTA and DECAL between the p-well and collection electrode, the biasing of the p-well is significantly different between the two devices. The p-well serves as the bulk for the NMOS transistors in the p-well, and the -6 V bias in MALTA affects their operation and is near the limit for transistor operation. There is also a difference between the p-well and substrate biases in MALTA, which can lead to punch-through currents as discussed and measured in Chapter 7.

A schematic of the in-pixel analog front-end is shown in Fig. 8.5. The front-end consists of a pre-amplifier coupled to a shaper connected to a comparator along with the threshold voltage of the chip. The amplifier is capacitively coupled to the discriminator through C5 in the figure and a voltage DAC biases C5 to allow for tuning of the offset of the shaper's output

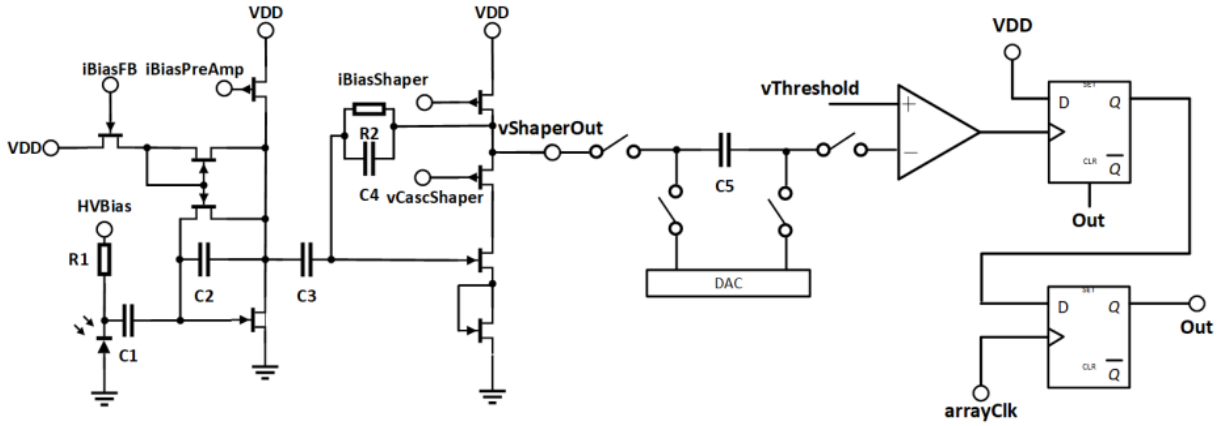

Figure 8.5: Schematic of the DECAL front-end.

to the comparator. The voltage of this DAC can be sampled with either polarity, depending on a specific bit of the DAC: positive to effectively increase the pixel threshold, or negative to decrease it. Unlike the MALTA and other CMOS sensors, DECAL does not have an injection circuit to measure the threshold. Instead, the noise of the shaper must be used to trigger the comparator when doing threshold measurements as described in Sec. 8.2.2. For measurements of the analog front-end, DECAL has a monitoring pixel from which the pre-amplifier and shaper signal can be read out on separate SMA connections.

DECAL in the TJ Modified process

A second version of the device, known as DECAL FD, with "FD" indicating "full depletion," has also been produced. Unlike the original DECAL in the standard Tower Jazz 180 nm process, DECAL FD is in the modified process with n^- gap substrate as in MALTA to improve the lateral depletion of the device for applications in high radiation environments and high rate experiments.

Measurements of the digital and analog sectors of both DECAL and DECAL FD devices were made. The DECAL readout system is shown in Fig. 8.6(b). The sensor was mounted on a custom-built PCB carrier board shown in Fig. 8.6(a) and connected to a second custom PCB, the DECAL motherboard, which was connected via FMC to a NEXYS Video board and allowed for readout and powering with ITSDAQ software [11, 91, 92].

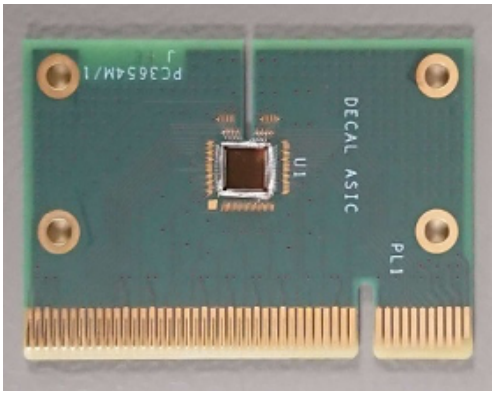

(a) DECAL wire bonded to its carrier board.

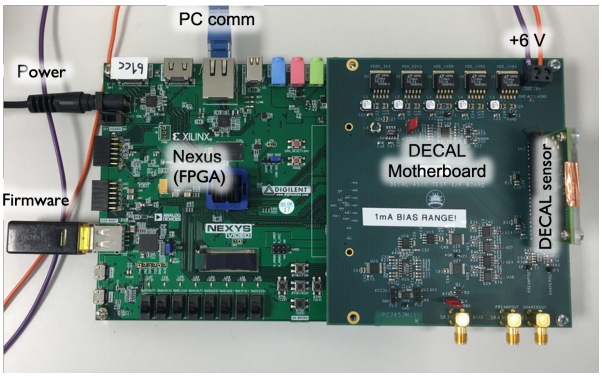

(b) The DECAL readout system: carrier board, motherboard, and Nexys FPGA.

Figure 8.6: The DECAL readout system.

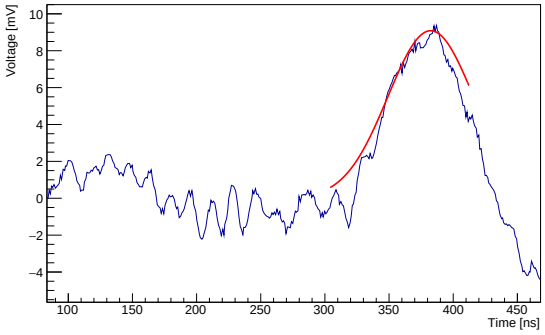

Figure 8.7: Example of Gaussian fit to a waveform from ^{55}Fe X-rays on DECAL FD.

8.2.1 Analog pixel measurements

Measurements were made on the output of the analog front-end of the monitoring pixel of DECAL and DECAL FD. A radioactive source was placed above the sensor and waveforms of the preamplifier and shaper output were recorded with a DRS4 500 MHz digital oscilloscope [93]. The DRS4 was triggered on the shaper output with the trigger level such that no hits were recorded over a duration of approximately 30 seconds when the source was absent. Waveforms were analyzed offline with a modified version of the analysis used for the ^{55}Fe measurements of MALTA Cz. As shown in the plotted waveform of ^{55}Fe acquisition in Fig. 8.7, a Gaussian fit to the leading edge was used to calculate the pulse maximum and rise time. The noise and offset were calculated as the standard deviation and mean of the voltage values in the time before the leading edge, respectively.

The 40 MHz clock was turned off during measurements since this resulted in the removal of a significant oscillation in the monitoring pixel readout. In Fig. 8.8(a) is a waveform from the shaper output of the monitoring pixel of DECAL FD with no radioactive source and the clock on, in 8.8(c) the clock has been turned off, in Fig. 8.8(b) the clock is on during ^{55}Fe acquisition, and in Fig. 8.8(d) the clock is off during acquisition, which is the mode used for the results in this thesis. In Fig. 8.8(e), 8.8(f), 8.8(g), and 8.8(h), are the waveforms for the original DECAL under the same conditions. In both versions of the device, the 40 MHz clock is coupled to the shaper (and preamplifer) output lines, and for reasonable measurement of waveform characteristics, had to be turned off. The clock had to remain on during threshold measurements in order to communicate with the sensor digitally. In the original DECAL, there is also another oscillation with approximately a 17.5 ns period.

In Table 8.2 are the measurements of the rise time, amplitude, and noise from ^{55}Fe and ^{90}Sr injection with DECAL and DECAL FD. The values are determined from fits to the distributions in Fig. 8.9. The signal-to-noise is at a level which leads to questionable detection efficiency, however, this relatively low pulse amplitude and gain of approximately 6 μV/e may be due to the buffering of the monitoring pixel output. In simulation, the attenuation factor has been approximately 2, however, it may be greater in reality. The currents for biasing the preamplifer, shaper, and buffer for the monitoring pixel were varied between 0 and 1 mA, but at no point was a significant increase in the signal amplitude observed. To more accurately measure the amplitude that is seen by the comparator, the analog and digital outputs should be measured simultaneously with a source with a sufficiently high rate and energy. Previous measurements with the old DECAL device in an X-ray tube at Rutherford Appleton Laboratory (RAL) measured a gain of 32 μV/e, however, the results need to be checked and both the old results should be reproduced as well as measurements taken for the DECAL FD. Further measurements must be made to resolve the apparent conflict between the previous measurements and those in this section. Plans were in place to measure DECAL in a high-flux X-ray tube at RAL, but unfortunately, due to a series of delays, the measurement was pushed beyond the scope of this work.

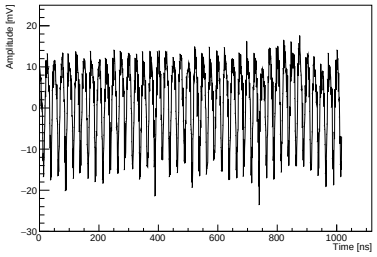

(a) DECAL FD shaper output with the clock on and no source.

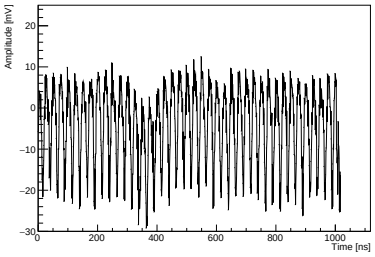

(b) DECAL FD shaper output from ^{55}Fe with the clock on.

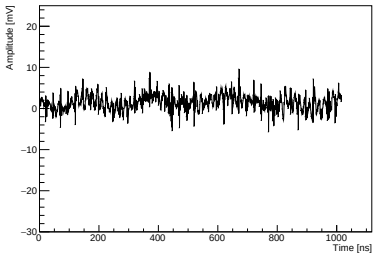

(c) DECAL FD shaper output with the clock off and no source.

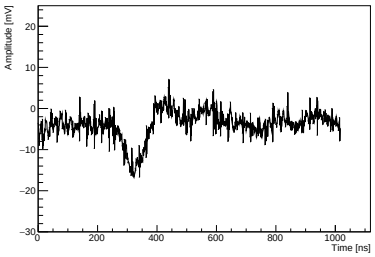

(d) DECAL FD shaper output from ^{55}Fe with the clock off. This mode was used for measurement.

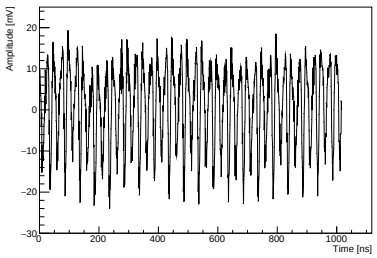

(e) DECAL shaper output with the clock on and no source.

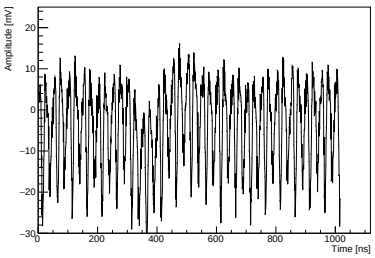

(f) DECAL shaper output with the clock on and an ^{55}Fe source.

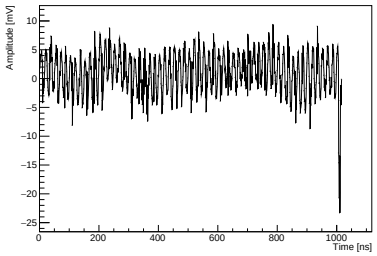

(g) DECAL shaper output with the clock off and no source.

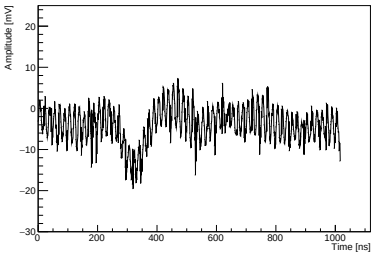

(h) DECAL shaper output with the clock off and an ^{55}Fe source.

Figure 8.8: Waveforms from DECAL and DECAL FD with the clock on and off and an ^{55}Fe source present or not. Turning off the clock removes the 40 MHz oscillation, and there is a negative polarity signal from the source.

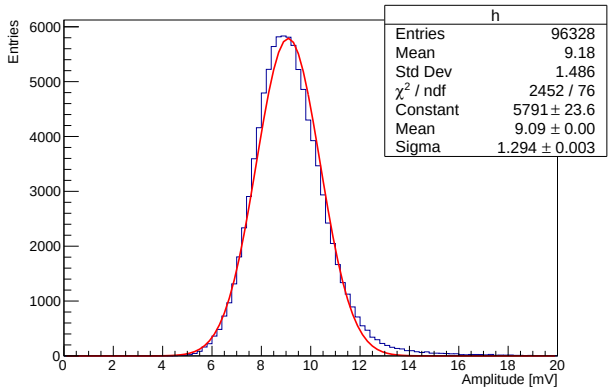

(a) Amplitude of DECAL FD with an ^{55}Fe X-ray source.

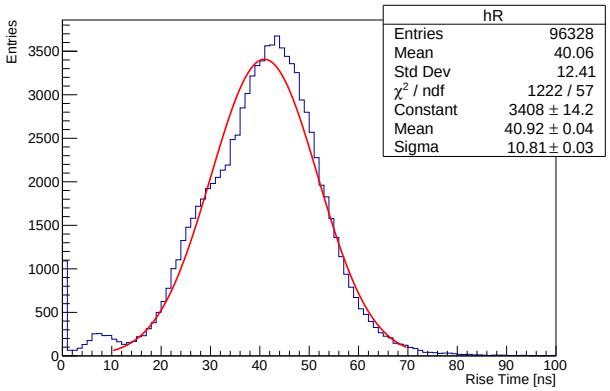

(b) Rise time of DECAL FD with an ^{55}Fe X-ray source.

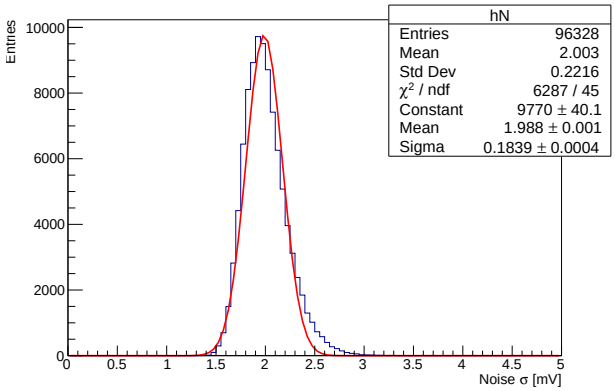

(c) RMS of DECAL FD with an ^{55}Fe X-ray source.

Figure 8.9: Fits to distributions of pulse measurements.

Pulse Measurement	Source	DECAL	DECAL FD
Amplitude [mV]	^{55}Fe	11.47 ± 0.04	9.090 ± 0.004
Noise [mV]	^{55}Fe	3.43 ± 0.01	1.988 ± 0.0001
Rise time [ns]	^{90}Sr	53.01 ± 0.04	40.92 ± 0.04

Table 8.2: Measurements of DECAL and DECAL FD waveforms with ^{55}Fe and ^{90}Sr. Measurements are determined from Gaussian fits to distributions as in Fig 8.9.

The bias voltage of the DECAL collection electrode can be sourced from an external power supply and allows for higher bias voltage values than 3.3 V. In Table 8.3 are the acquisition rate and pulse amplitude as measured with DECAL FD and ^{55}Fe at various collection electrode bias voltages. The amplitude does not increase much with the bias since the deposition of charge from an X-ray occurs in a small region in the silicon, while the acquisition rate does increase,

presumably due to increasing depletion depth. This measurement suggests that DECAL is fully depleted by around 3 V. The rise times decrease with bias, presumably since the sensor is fully depleted and the field in the depletion region increases along with the carrier drift velocity.

Collection electrode bias [V]	Acquisition Rate [Hz]	k-α amplitude [mV]	Rise Time [ns]
0.5	0.71 ± 0.02	8.21 ± 0.03	44.5 ± 0.5
1	1.32 ±0.04	8.45 ± 0.04	42.7± 0.4
2	1.92 ±0.05	8.67±0.04	42.6±0.04
3	2.19±0.07	8.82±0.04	41.9±0.04
4	2.42±0.08	8.97±0.04	40.4±0.04
5	2.51±0.08	9.08±0.04	40.2±0.04
6	2.57±0.08	9.27±0.04	39.9±0.03

Table 8.3: Measurements with X-ray source at different substrate voltages of DECAL.

8.2.2 Threshold Measurements

Measurements of the digital sector confirmed the counting logic and allowed for the measurement of pixel noise and pedestal levels.

As previously mentioned, the circuitry of DECAL is not equipped with a sort of calibration circuit as in many silicon sensor front-ends such as the one in MALTA. Due to this, a typical threshold scan in which a threshold DAC is set on the sensor and the calibration charge is varied is not possible. Instead, the threshold setting of DECAL is varied, and the noise pedestal is measured. The threshold in DECAL is a crossing threshold, meaning that the input signal must cross the threshold value to trigger the in-pixel discriminator; the shaper output voltage being above or below the threshold value will not result in hits. The in-pixel tuning DAC of DECAL is configured with five bits, four which set the voltage value for the correction, and one for the polarity of this correction.

To measure the noise pedestal of DECAL FD, the threshold voltage was varied and data was acquired with DECAL for a set number of 25 ns cycles and the number of hits at each threshold voltage was recorded. These measurements were made in the default configuration, that is with no voltage on the pixel tuning DAC. A single row of DECAL FD was enabled at a

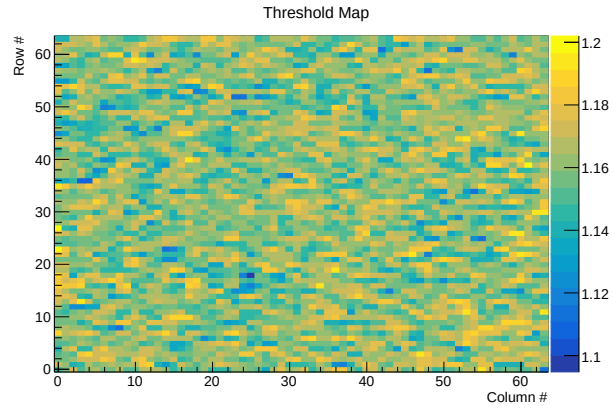

(a) Map of mean pedestal values measured in threshold scans.

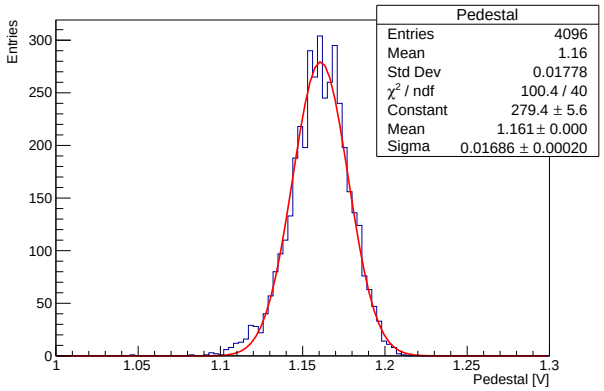

(b) Mean pedestal values for DECAL in the base configuration.

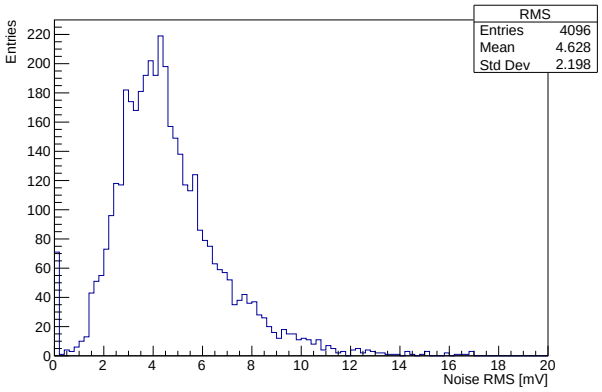

(c) RMS pedestal values for DECAL in the base configuration.

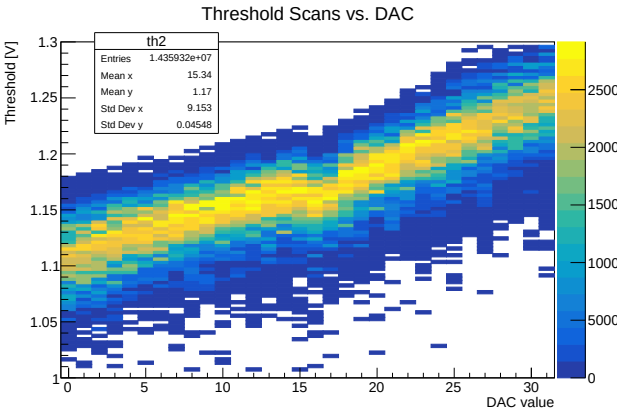

(d) Threshold measurement for the entire sensor at different tuning DAC values.

Figure 8.10: Threshold scans of DECAL.

time, so hits from a given strip corresponded to a single pixel. This was done for all rows, and combined as in Fig. 8.10(a), where the mean pedestal values are plotted for the pixel matrix of DECAL. In Fig. 8.10(b) and 8.10(c) the mean and RMS values of the single-pixel pedestals are put into a single histogram. The mean noise value of 4.6 mV suggests that the 40 MHz clock signal observed in the analog output is not propagated to the pixel matrix or front-end, since the 30 mV peak-to-peak amplitude of the clock signal would result in more than 4.6 mV of noise.

In Fig. 8.10(d), all hits from threshold scans are plotted against the value of the pixel tuning DAC and the threshold voltage. The response to the DAC is linear as intended, and has a range of approximately 150 mV. Since most pedestal values are within 150 mV of the mean pedestal

value shown in 8.10(b), in principle the DECAL sensor can be tuned to achieve a narrow overall pedestal on the sensor which would allow for the setting of a global threshold.

Digital Measurement

The counting logic was tested in previous measurements of the original DECAL by a direct injection of specific bit patterns into the test register, known as number injection. Both strip and pad mode were tested in [94]. In strip mode, up to 3 pixel hits can be counted in a single strip, and in pad mode 15 can be counted per strip, though at the cost of granularity.

In strip mode, the pattern '11' was injected into the test register. Each strip reads out 2 bits, so the total output for all 64 strips is a 128 bit word. For strip 0, the first 2 bits should be set, in strip 1, the next 2, and so on until the bits 126 and 127 are set in strip 63. This is what was measured in DECAL as shown in 8.11(a).

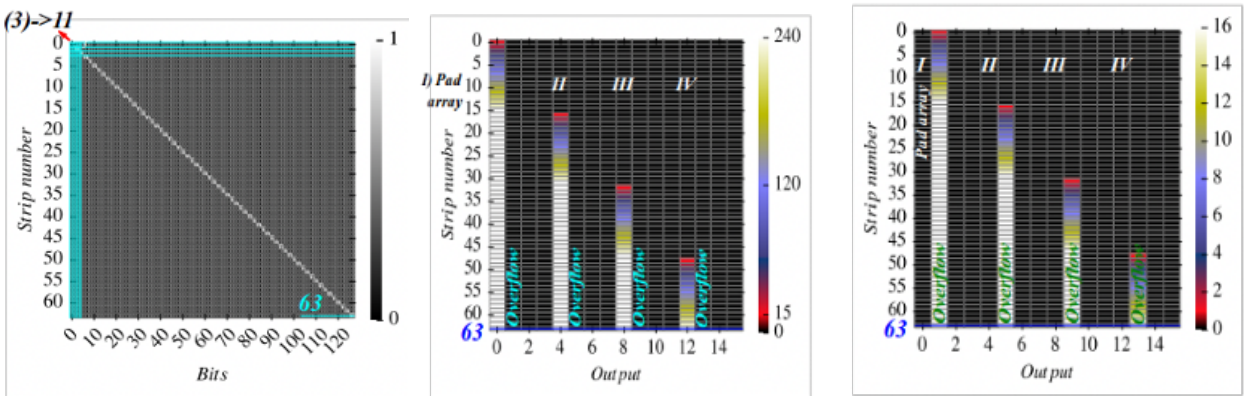

(a) Injection of '11' in strip mode. (b) Injection of 'b01111' in pad mode. (c) Injection of 'b01111' in pad mode.

Figure 8.11: Testing of the digital sector of DECAL with number injection.

For pad mode, two tests were done. In the first, the pattern '01111' was clocked into the test register, corresponding to 15 hits. As this propagates through a 16-strip pad, the total number of hits should be incremented in steps of 15 until 240 is reached in the last strip of the pad. Then the summation in the next pad should begin. This is what is measured in 8.11(b). In the second test, the pattern '10000' is clocked, corresponding to 16 hits and results in the overflow of a strip when injected in pad mode. The summation output stays at 0, but the overflow bit is set in each strip, and sums to 16 for the 16 strips in the entire pad. This is what is observed

in Fig. 8.11(c) (note the scale of the z-axis has a maximum of 16 here, and 240 in the other pad test).

8.3 Simulation Results

To estimate and compare the performance of analog and digital SiW calorimeters, simulations were made of single particle events in the CLICdet detector design for the proposed CLIC experiment [17], which is closely based on the SiD detector for the ILC. Cross-sections of the detector are shown in Fig. 8.12. This detector was selected for ease of use and applicability: previous work has been with a robust, well-maintained detector simulation and event reconstruction package, ilcsoft, and the results are applicable to other detectors of similar design since the simulation is of single particles and not of TeV e^+e^- events [95]. The work in this thesis was with `ilcsoft-v02-04` (July 2019). The hit digitization and event reconstruction is performed by Modular Analysis and Reconstruction for LINear Collider (Marlin), a reconstruction framework for linear colliders, which includes implementation of the Pandora Software Development Kit and Pandora Particle Flow Analysis (PandoraPFA) [88, 96, 97] used for clustering and reconstruction. A GEANT4 particle gun was used to generate Monte Carlo samples of events and the energy deposition in the detector system was simulated with DD4HEP [76, 98].

The pixel pitch in the simulated MAPS was 50 μm and in the analog sensors 5 mm. In both cases the overall thickness of the silicon was set to 500 μm, though in the case of MAPS, sensing layers could potentially be much thinner. For example, the MALTA sensor is 300 μm thick and chips have been thinned to and operated at 100 μm.

The basic steps in PandoraPFA can be summarized as follows:

Clustering Hits in the calorimeter are clustered together, with cluster seeds potentially coming from the tracks in the tracker.

Track association Clusters are associated with tracks in the tracker. Clusters with an associated track are assumed to be from charged particles, and clusters without a track are assumed to be neutral.

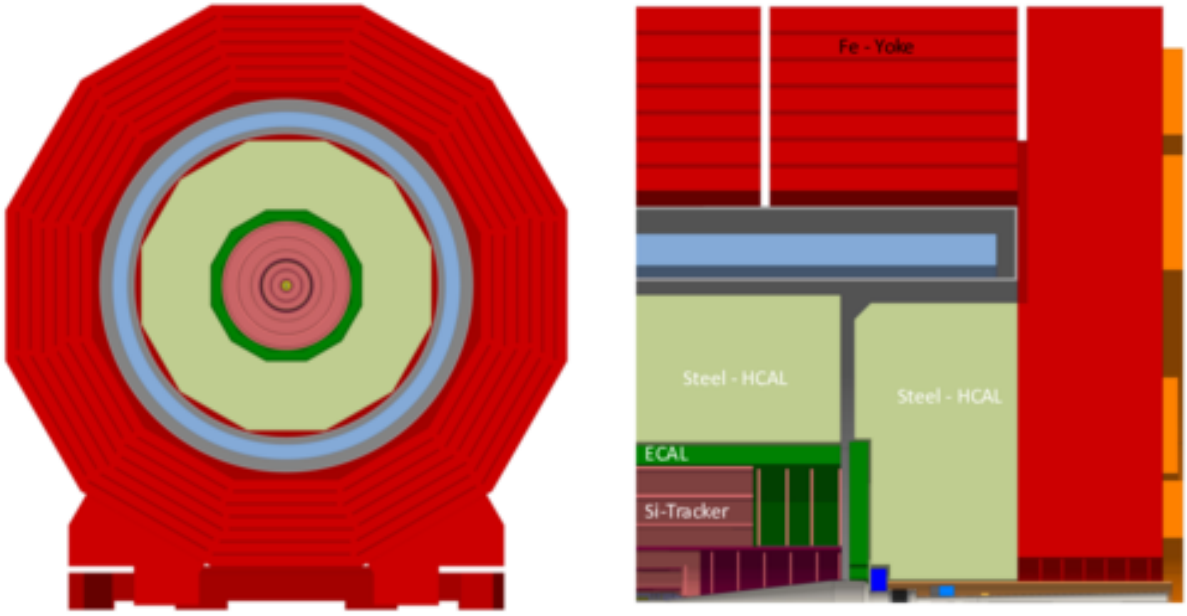

(a) Front view of CLICdet. (b) A quadrant of CLICdet.

Figure 8.12: Proposed CLICdet detector [17].

Fragment removal Small clusters called fragments are associated with larger ones, potentially using track information.

Particle flow objects Particles are reconstructed and dubbed particle flow objects. When available, tracks are used to determine particle properties.

Particle identification Particle flow objects are assigned a final identification and corresponding Particle Data Group (PDG) code.

8.3.1 Reconstruction calibration

In order to run simulations with the analog and digital calorimeters, the digital calorimeter was calibrated using single particle samples at various energies as described in a calibration procedure included in the CLIC reconstruction portion of the ilscsoft package. The procedures involved extraction of the digitization and calibration constants used for the energy in PandoraPFA for the electromagnetic and hadronic calorimeters. Two samples, one of 10 GeV γ and one of 20 GeV K_L^0, were used for the electromagnetic and hadronic calorimeters, respectively. The energies measured with the calibrated values obtained after an iterative procedure

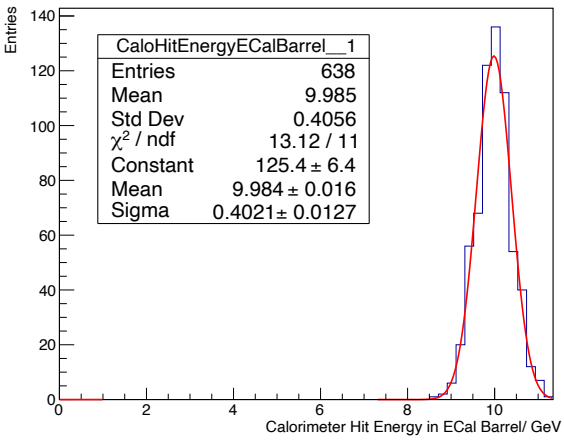

(a) Reconstructed energy of 10 GeV photons for calibration of the ECAL digitization.

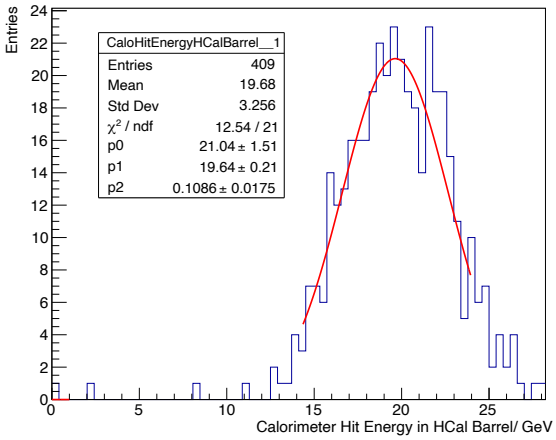

(b) Reconstructed energy of 20 GeV kLong for calibration of the HCAL digitization.

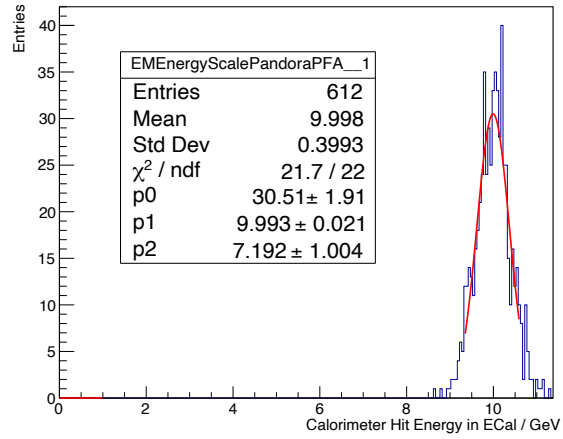

(c) Reconstructed energy of 10 GeV photons for calibration of the ECAL Pandora constants.

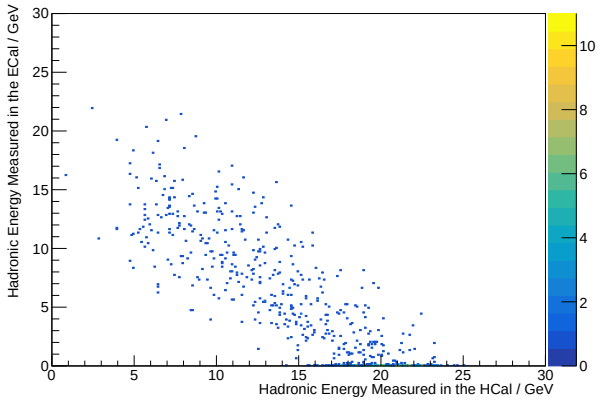

(d) Reconstructed energy of 20 GeV kLong for calibration of the ECAL and HCAL constants in Pandora.

Figure 8.13: Simulated data and corresponding fits used in the Pandora calibration procedure.

are shown in Fig. 8.13: in Fig. 8.13(a), 8.13(b), and 8.13(c), the fit values are within desired accuracy, and in Fig. 8.13(d), the conversion factors for estimating hadronic energy in the electromagnetic calorimeter and vice versa are calibrated by tuning the intercepts of a linear fit to the data at 20 GeV. The digitization calibration is 92 pixels per GeV of shower energy for a 40-layer thick calorimeter. This 40-layer geometry was selected based on the superior energy resolution in simulation results in [17] and studies similar to those in Sec. 8.3.2 as a confirmation.

8.3.2 Energy Resolution studies

Single particle events of photons and electrons were used to measure the energy resolution in the analog and digital calorimeters. The results of these studies demonstrate comparable energy resolution in the analog and digital calorimeters as did previous studies [17, 99]. For particles at a given energy, the distribution of the number of hits above threshold in the calorimeter was fit with a Gaussian, as in Fig. 8.14(a) with 50 GeV γ. The mean of these fits for samples of photons are shown in Fig. 8.14(b) and 8.14(c) as a function of the true energy, and are fit with linear and quadratic functions. The quadratic term is small and demonstrates good linearity; there is no evidence of saturation up to 100 GeV.

The energy resolution is calculated as the standard deviation of the mean number of hits as estimated from the sigma of the Gaussian distributions at each energy. In Figs. 8.14(d) and 8.14(e) the energy resolution is plotted as a function of the true energy and fit with a function of the form

$$\frac{\sigma(E)}{E} = \frac{a}{\sqrt{E}} + \frac{b}{E} + c \tag{8.2}$$

In equation 8.2 the energy resolution of measurements of electromagnetic showers is parameterized, where a is the stochastic term, representing statistical fluctuations in the shower process and sampling of energy by the detector, b is the noise term which characterizes electronic and background noise, and c is the constant term caused by calibration uncertainty and non-linearity of response. Since no additional electronic noise was included in the detector simulation, b is expected to be 0 in these simulation results. At low energies, there is little pixel saturation and the calibration term c is small and the resolution is dominated by a. As in previous studies, the energy resolution at this energy scale is comparable between the analog and digital calorimeters with $a = 0.13 \pm 0.003$ in the digital case and $a = 0.15 \pm 0.003$ for the analog.

With the energy resolution in single particle studies confirmed to be comparable between analog and digital calorimeters, it was of interest to compare the performance of the two designs in more sophisticated reconstruction tasks such as π^0 reconstruction.

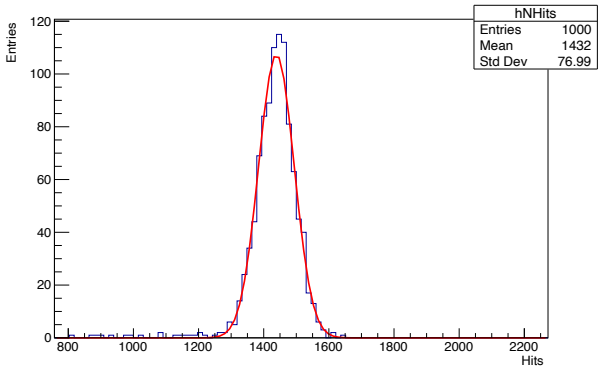

(a) Number of hits in the electromagnetic calorimeter for 50 GeV photons.

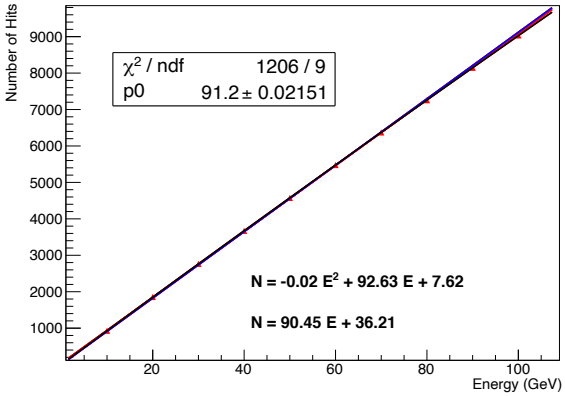

(b) Mean number of hits from single photons as a function of true energy.

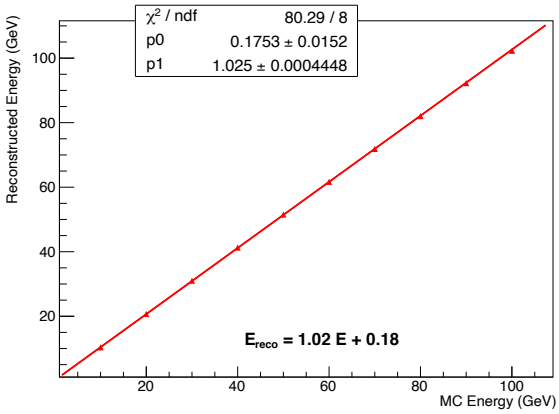

(c) Energy of reconstructed photons as a function of true energy. .

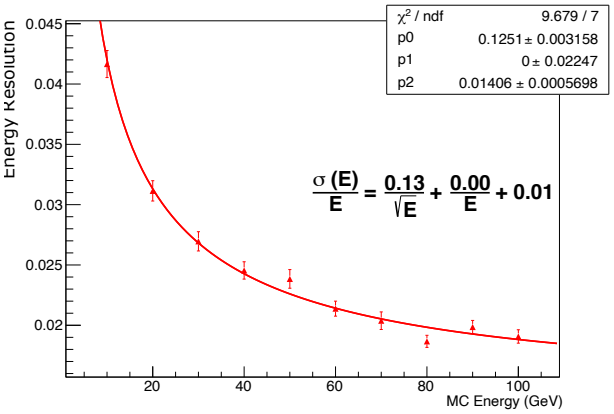

(d) Energy resolution in the digital calorimeter for single photons.

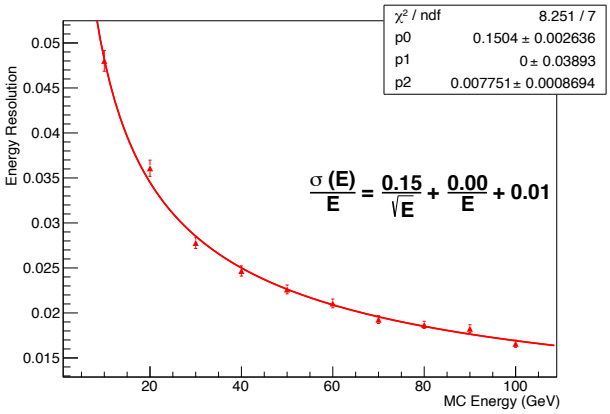

(e) Energy resolution in the analog calorimeter for single photons.

Figure 8.14: Reconstructed energy and energy resolution for single photon events the analog and digital calorimeters.

8.3.3 π^0 reconstruction studies

In order to investigate the performance of the digital calorimeter in reconstruction of spatially confined decays, reconstruction of the π^0 was studied. A π^0 decays to two photons with a branching ratio of 98.8% and mean lifetime of 8.4×10^{-17} s [23]. The invariant mass can be inferred from the measurement of two closely spaced photons as:

$$M = \sqrt{2E_1E_2(1-\cos\alpha)}, \tag{8.3}$$

where α is the angle between the two photons and E_1 and E_2 are the energies of the individual photons. Hence, to reconstruct the π^0 mass reliably, it is necessary to measure accurately the energy and direction of the two photons. The DECAL provides higher granularity with 1/100 of the pixel pitch than in the proposed SiW analog calorimeter, and therefore may allow more accurate reconstruction of photon showers and the π^0 mass.

However, the reconstruction may be limited by the characteristics of electromagnetic showers, and not the granularity of the detector. The Molière radius of a material is the radius of a cylinder which contains 90% of the energy in an electromagnetic shower generated by that material, and is found as

$$r_M = \frac{21\ \text{MeV}}{E_C}X_0, \tag{8.4}$$

where E_C and X_0 are the critical energy (at which the probability of energy loss by bremsstrahlung and ionization are equal for an electron) and radiation length of the material. For tungsten, the Molière radius is 0.9327 cm [23], already larger than the 5×5 mm pixel size proposed for the analog calorimeter in CLICdet. Therefore, there may be more benefit for resolving two nearby electromagnetic showers from the improved granularity of the DECAL before the showers have traveled deep into the calorimeter.

With the proposed calorimeter minimum radius of $r = 1.5$ m and the fact that the simulated π^0 will decay almost immediately at the interaction point, the Molière radius corresponds to

an angle of

$$\alpha_{Molière}(\text{CLICdet}) = \sin^{-1}(0.0009327/1.5) = 0.0062 \text{ rad} \tag{8.5}$$

The opening angle between the two photons is minimized when the two photons have equal energy

$$\alpha(E_1, E_2) = 2 \sin^{-1}(M_{\pi^0}/\sqrt{4E_1E_2})\alpha(E/2, E/2) = 2 \sin^{-1}(M_{\pi^0}/E) \tag{8.6}$$

and is equal to the $\alpha_{Molière}$(CLICdet) when $E = \frac{135\text{MeV}}{\sin 0.0062/2} = 43$ GeV. For π^0 with energies comparable to or above this, it may be challenging to resolve the angle between the two photons or even recognize two distinct showers in the first place.

The results of the simulations confirm the minimum angle between the two photons. Figures 8.15(a) and 8.15(b) show the true and reconstructed opening angles as a function of simulated π^0 energies, respectively, with the minimum expected opening angle indicated by the red line. In some cases the reconstructed angle differs from the MC truth and is sometimes even less than this minimum. As the π^0 energy is increased, there are fewer events in which two distinct photons are correctly identified, as expected because the separation angle decreases. However, this drop off in reconstruction at higher energies was somewhat sharper than expected, and the reconstruction efficiency at low energies also less than expected, therefore the individual steps in the π^0 reconstruction were investigated more thoroughly, and the range of a valid comparison between the two is limited to energies 10 GeV and below, and there are some unexpected results as the energy approaches 10 GeV.

Intuitively, many of the events where only a single cluster has been identified should really have two clusters. Figures 8.16(a) and 8.16(b) give 2-D histograms of the $z - y$ positions[1] of hits in the calorimeter from a 20 and a 50 GeV π^0 with the minimum photon separation angle that have been identified as single photons in PandoraPFA. In Fig. 8.16(c) and 8.16(d) are projections of hits from similar (but not the exact same) events in a single dimension perpendicular to the π^0 momentum. In both sets of figures, the hits marked in red are from the first five layers of the calorimeter. Even at the minimum angle with a π^0 energy of 50 GeV,

[1]Directions perpendicular to π^0 momentum vector.

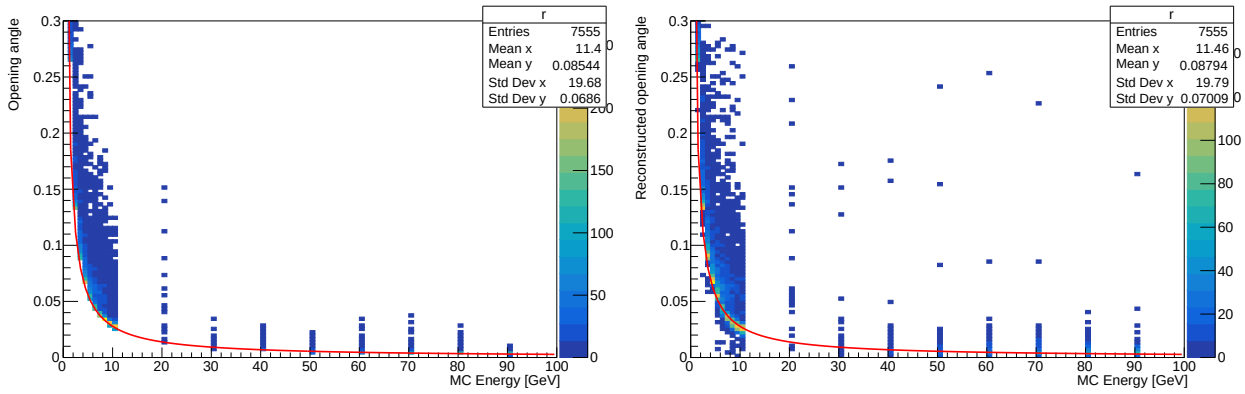

(a) True opening angles between photons as a function of π^0 true energy.

(b) Reconstructed opening angles between photons as a function of π^0 true energy.

Figure 8.15: Photon separation angles.

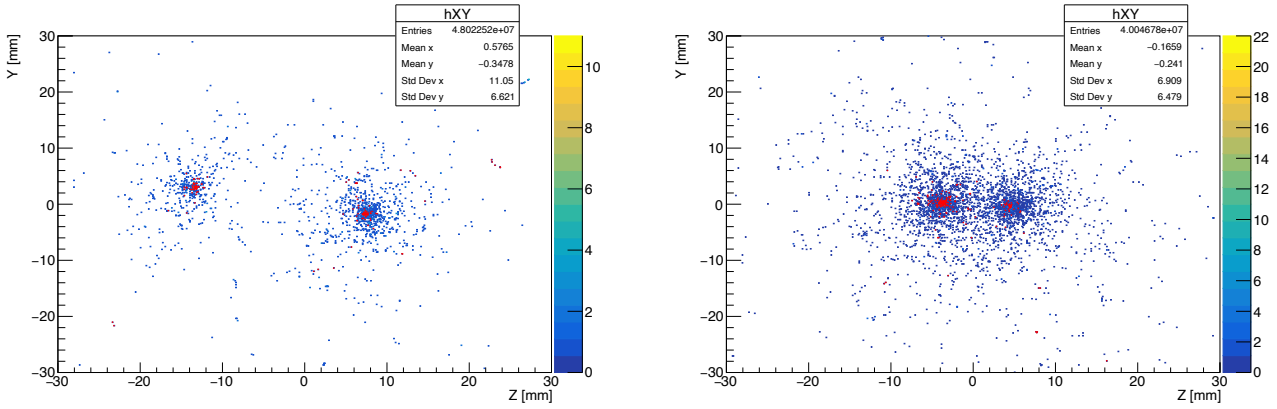

(a) Simulated hits in the DECAL from a 20 GeV π^0.

(b) Simulated hits in the DECAL from a 50 GeV π^0.

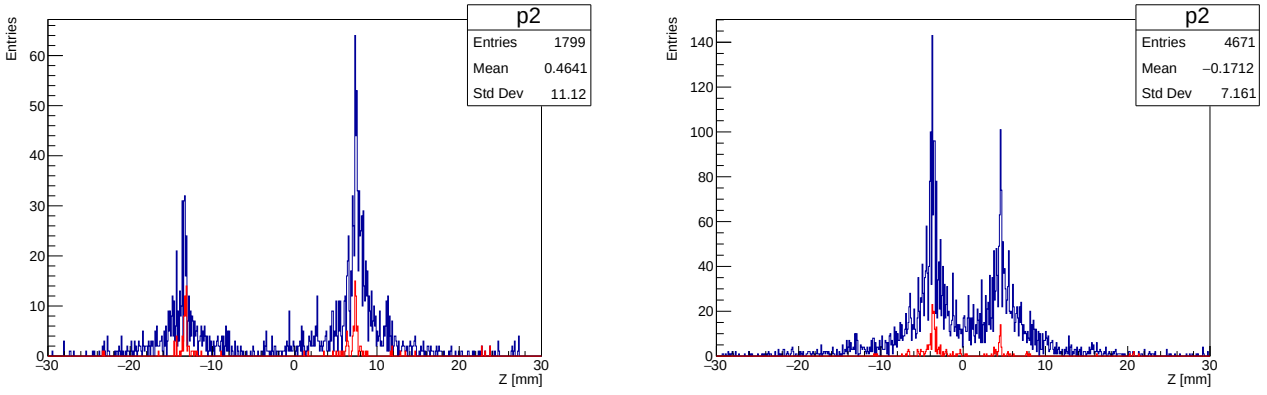

(c) Simulated hits in the DECAL from a 20 GeV π^0.

(d) Simulated hits in the DECAL from a 50 GeV π^0.

Figure 8.16: Projected DECAL hits for single 20 GeV and 50 GeV π^0. The hits in red are from the first five layers of the ECAL.

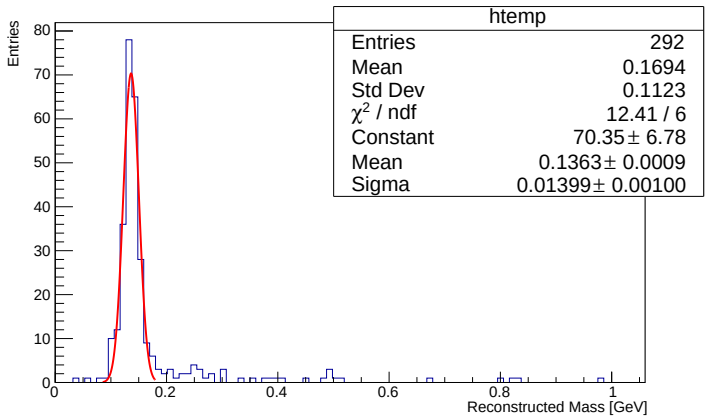

(a) Reconstructed invariant mass for 8 GeV pions with the digital calorimeter and a Gaussian fit to the data.

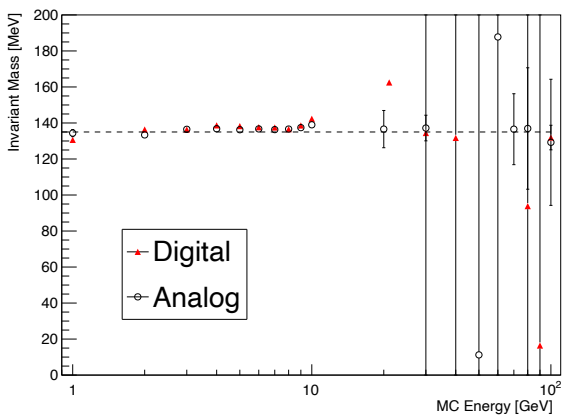

(b) Pion reconstructed mass as a function of true energy.

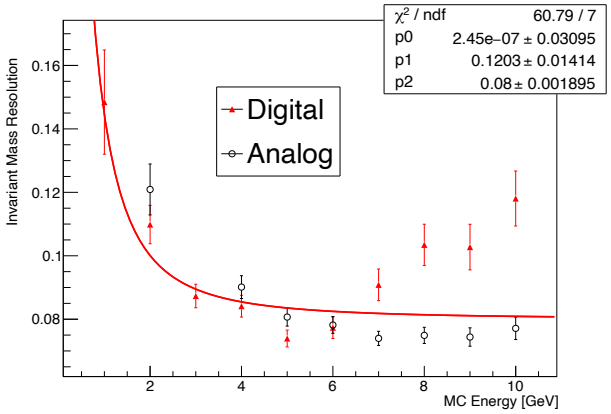

(c) Reconstructed mass resolution as a function of true energy.

Figure 8.17: Pion reconstructed mass resolution.

one would intuitively expect that two clusters could be identified from measurements such as these and the failure to do so is a shortcoming of the tuning of Pandora clustering algorithms, in particular the `ConeClustering` algorithm, for the digital calorimeter. In general, improving the photon reconstruction and clustering may require: the development of new algorithms, possibly involving emphasis on hits from the first few layers; tuning and training of both new and existing algorithms with large samples of single photons; and/or the adjustment of the settings of key parameters which are tied to assumptions about detector geometry.

Hits from even just the first five layers may be sufficient to separate clusters, and have additional benefit. If clustering can be performed in just the first few layers, there would be less stringent readout requirements for a digital calorimeter. For example, the first five layers

could be configured to read out pixel positions or strip positions on back-to-back sensors, but the remaining layers could be operated with only strip or chip-level precision readout.

For π^0 energies at and below 10 GeV, comparisons can be made between the analog and digital calorimeters. In Fig. 8.17(a), the distribution of the reconstructed mass for 8 GeV π^0 in the digital calorimeter is given. The mean value of the Gaussian fit, 136.3 MeV, is consistent with the generated π^0 mass. The reconstruction is reasonably accurate below 20 GeV, as shown in Fig. 8.17(b) by the mean values extracted from the Gaussian fits to the reconstructed mass as a function of the pion energy. Both the analog and digital calorimeters reliably reconstructed the pion mass of 135 MeV for pions up to energies near 20 GeV. At higher energies, the opening angles may be too small to reconstruct the mass reliably, and the photon reconstruction algorithm may benefit from further development or tuning as previously discussed.

The resolution of the reconstructed invariant mass, defined as $\sigma(M)/M$, is plotted in Fig. 8.17(c). Below 8 GeV, the mass resolution may be better for the digital calorimeter. This is probably due to better performance in resolving the angle between the two photons as shown in Fig. 8.18(a) of the residuals of the separation angle as a function of the π^0 energy. The residuals are extracted from Gaussian fits to the reconstructed separation angle, as shown for 5 GeV π^0 given in Figs. 8.18(b) and 8.18(c) for the analog and digital calorimeters, respectively. Above 6 GeV, the trend unexpectedly changes to the analog calorimeter having smaller residuals, likely due to shortcomings in the implementation of PandoraPFA which would take a significant effort to resolve. This improvement in resolving small angles and thereby the π^0 invariant mass is the exact type of improvement expected when using the much finer granularity of the digital calorimeter. With a project focused on the refinements to the photon algorithm, the true benefits of the ultra high-granularity digital electromagnetic calorimeter can be thoroughly explored and may provide insight for the development of the next generation of calorimeters and particle detectors.

As previously mentioned, it was found that with the existing settings and algorithms for photon reconstruction in PandoraPFA, there are some shortcomings which likely can be improved in future implementations of PandoraPFA and studies on digital high-granularity calorimetry

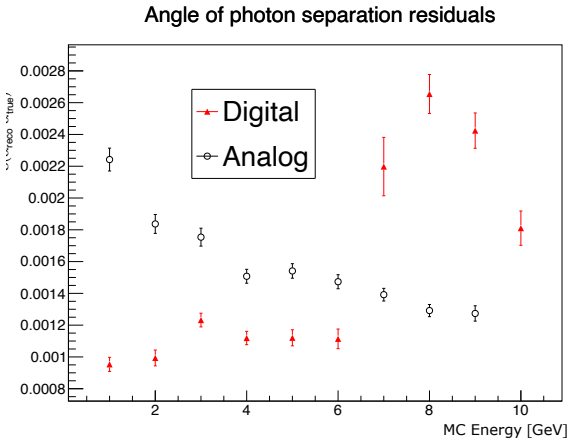

(a) Residuals of the photon separation angle with the digital and analog calorimeter as a function of true π^0 energy.

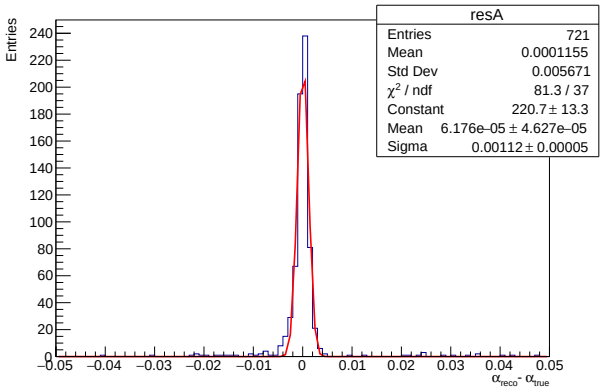

(b) Residuals of the photon separation angle with the digital calorimeter fit with a Gaussian.

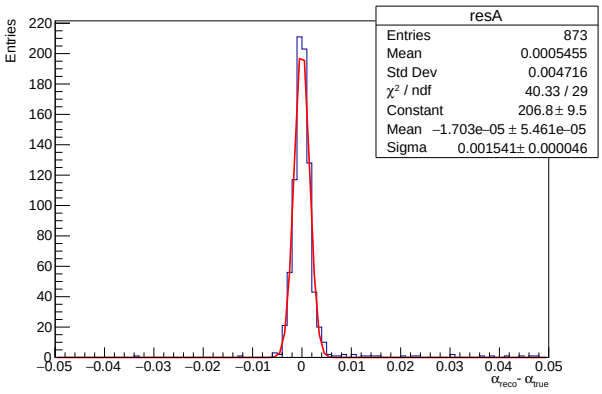

(c) [Residuals of the photon separation angle with the analog calorimeter fit with a Gaussian.

Figure 8.18: Angles between photons.

similar to this one. In general, the photon reconstruction with the digital calorimeter was not as precisely tuned as for the analog case, which had been the focus of extensive work [100]. In the π^0 reconstruction, for the digital calorimeter, photons with smaller energies ($\leq$1 GeV) are not as reliably reconstructed with the digital calorimeter since they were often misidentified as neutrons. To this end, reconstruction of single photons was explored.

The reconstruction of single photons as a function of their true energy is shown in Fig. 8.19. Figure 8.19(a) presents the fraction of single photons correctly identified, while Fig. 8.19(b) gives the fraction identified as a neutral hadrons, which is more than 70% for 1 GeV photons in the digital calorimeter. Figure 8.19(c) shows the fraction of events in which more than one photon has been reconstructed. At every energy, the performance of the analog calorimeter is

better. At low energies the tendency of photons in the digital calorimeter to be identified as neutrons is detrimental to the π^0 reconstruction. To mitigate the effects of the tuning of the current method used within Pandora and allow studies to examine the potential benefit of the small DECAL pixel size, an algorithm in Pandora known as `LCCheating` was used to assign the true particle identity to reconstructed objects in Pandora. This "cheating" algorithm does not affect the formation of clusters, only the particle identification associated with clusters, and so does not hinder the investigation of the potential advantage of the ultra high-granularity of the digital calorimeter.

In the reconstruction of π^0, two additional modifications were made to the implementation of reconstruction algorithms in Pandora. For the digital calorimeter, the `FragmentRemoval` algorithm tended to identify the cluster from the less energetic of the two photons as a fragment of the cluster from the more energetic photon and combine the two into one cluster, thus failing to reconstruct the two photons and thereby the π^0. Simply turning the `FragmentRemoval` off improves results for π^0 below 20 GeV. However, for higher energies the fragment removal is helpful to perform its intended function of combining cluster fragments to the original clusters, and without it there are false positives which lead to the seeming increase in efficiency above 50 GeV as in Fig. 8.20(a). Hence, for the results in this section, the `FragmentRemoval` is off below 20 GeV and on otherwise. The second change was to set the energy scaling of ECAL hits to be constant, since there were still a small number of hits for which a different scaling would be used due to misidentification as being from hadronic components.

Even with these simple improvements to the photon reconstruction, the clustering algorithms leave much to be desired. As discussed previously, the minimum separation angle and Moliére radius are comparable for π^0 with energies of 43 GeV and above. However, at 10 GeV the minimum separation angle is 0.027 rad, over four times $\alpha_{Moliere}(\text{CLICdet}) = 0.0062$.

In any case, in order to more deeply and reliably explore the possibilities of high-granularity digital calorimetry, it is likely that significant work must be put into the photon reconstruction in the Pandora Particle Flow analysis. In this implementation, PandoraPFA struggles with seemingly simple identification problems, and a thorough treatment of the photon reconstruc-

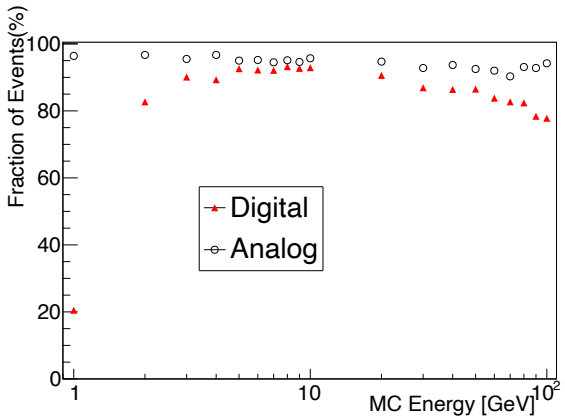

(a) Photon reconstruction efficiency as a function of true photon energy.

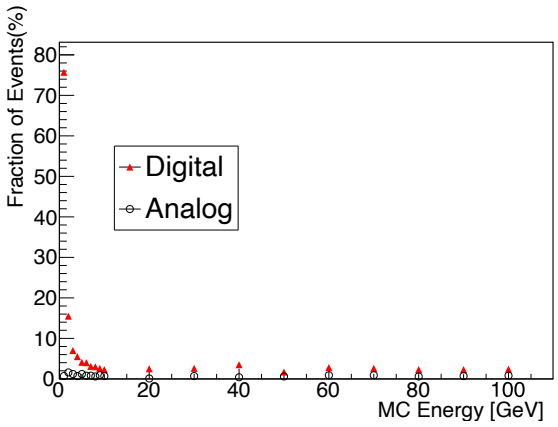

(b) Rate of misidentification of photons as neutrons.

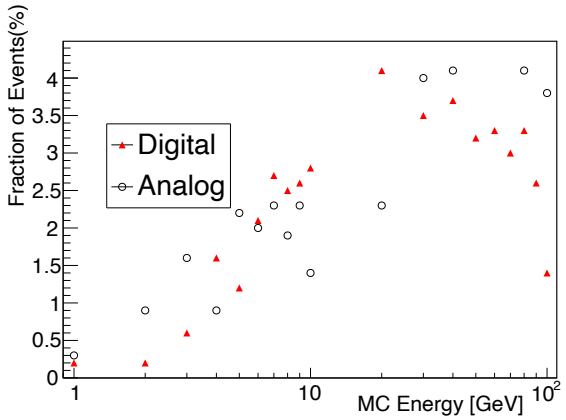

(c) Rate of misidentification of single photons as two or more photons.

Figure 8.19: Efficiency of reconstruction of single photons.

tion algorithms for the digital calorimeter may be necessary as was for the analog calorimeter in [100].

In spite of these identified areas for improvement of the photon reconstruction, with the small changes to the implementation of PandoraPFA described above (adding `LCCheating`, turning off `FragmentRemoval` below 20 GeV, and removing the scaling for hadronic energy in the ECAL) the reconstruction can be improved to be comparable to or better than the analog for certain constraints. The efficiency of the reconstruction is plotted in Fig. 8.20(a) as a function of the pion true energy, where efficiency is defined as the fraction of events in which exactly two photons are identified. In Fig. 8.20(b) are the fraction of events in which a single photon is reconstructed, that is, the two photon clusters are merged. Below 5 GeV, the

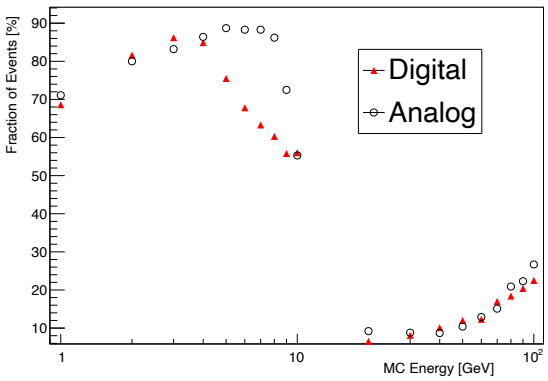

(a) Fraction of π^0 reconstructed with two photons as a function of true π energy.

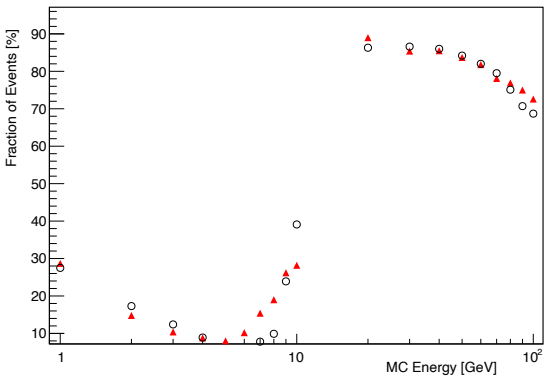

(b) Fraction of π^0 reconstructed with one photon as a function of true π energy.

Figure 8.20: Efficiency for photon identification in simulated π^0 decays.

efficiency is comparable for analog and digital, however, above this, the efficiency in the digital calorimeter drops off much more quickly. Both show significantly poorer performance above 20 GeV, suggesting there may still improvements to be made to the photon reconstruction in the analog calorimeter as well.

8.4 Conclusions

The simulation of a digital calorimeter for use in particle physics experiments has shown promising results, with comparable energy resolution to the analog calorimeter, and the potential to improve discrimination of higher energy photons from π^0 decays. In regions where the efficiency of the π^0 reconstruction algorithm is comparable in the analog and digital calorimeters, the angular resolution and thereby the mass resolution is superior in the digital calorimeter. However, it was found that the π^0 reconstruction was not effective for the digital calorimeter, and efficiency was vastly superior in the analog calorimeter due to superior performance in the photon clustering and identification. While moderate changes were made to the reconstruction to generate the results in this chapter, there is significant room for improvement to the clustering algorithms that would allow for deeper demonstration of the potential advantages (or lack thereof) of a digital electromagnetic calorimeter and potentially influence a preference for digital or analog ECAL in particle physics experiments.

With the DECAL sensor, an early prototype sensor for use in a digital ECAL, the performance of the digital and analog sectors has been demonstrated. The counting logic is functional in previous number injection studies, noise pedestals were measured at all pixel tuning DACs in threshold scans, and single pixel noise pedestals and the analog monitoring pixel were measured. In DECAL FD, the average single-pixel noise was measured as 4.6 mV, however, the gain of 6 μV/e in ^{55}Fe measurements of the monitoring pixel was surprisingly low in light of previous results in which a gain of 32 μV/e was measured [101]. Future measurement of the sensor in a high-flux X-ray tube at RAL are intended to resolve the discrepancy between the two. If the results do not confirm a gain of 32 μV/e [101], but are closer to the analog measurements, the device may be difficult to operate as an effective MIP detector. In that case, future versions of DECAL would need to modify the front-end to increase the gain and signal-to-noise in DECAL. In some other devices, like the modified MiniMALTA front-end, the gain is more than an order of magnitude higher than even the 32 μV/e, and other MAPS for MIP detection have even higher gain. Given this, and other challenges with the device, a redesign of the front-end is prudent and also feasible in the next version of DECAL in order for continued consideration of its intended use as a MIP detector.

Chapter 9

Summary and Outlook

In the work presented in this thesis, potential sensor technologies were characterized for particle physics experiments, including strip sensors for the ATLAS ITk, but with a primary focus on testing and demonstrating the suitability of MAPS technology for particle physics applications. The small collection MAPS technology offers a number of intrinsic advantages such as low-mass, low-power-consumption, low-noise, and other advantages due to the robust commercial demand for CMOS technologies. Sensors in the TowerJazz 180 nm modified CMOS imaging process were characterized and demonstrate the potential for the implementation of small collection electrode MAPS in high-radiation ($\phi > 1 \times 10^{15}$ $n_{\mathrm{eq}}/\mathrm{cm}^2$) environments as high-granularity sensors for applications in tracking and calorimetry. The results with various design modifications demonstrate a clear path for sensor research and development to achieve higher radiation tolerance.

For use in the ITk, ATLAS17 strip sensors were irradiated and characterized. The ATLAS17 strip sensors were demonstrated to have sufficient radiation hardness in terms of CCE and interstrip resistance, however, in the work, there were found to be issues with the damage seen at a given dose at the MC40 Cyclotron at Birmingham. These issues were investigated and rectified such that more recent results with irradiation of ATLAS strips have been comparable to results with sensors irradiated at other facilities, though there are still some intermittent anomalous results with the MC40 beamline and further investigation is necessary and ongoing.

Based on this CCE and interstrip resistance characterization and others like it, refined versions of the ATLAS17 sensors will be used in the construction of the ATLAS ITk Strip Detector.

For the latest prototypes of MALTA, a small collection electrode DMAPS, improved radiation hardness was demonstrated with full-efficiency (97%) measured at $\phi = 1 \times 10^{15}$ $n_{\text{eq}}/\text{cm}^2$ for MiniMALTA and MALTA Cz. This was achieved through design changes to the front-end and pixel substrate which are being further explored in MALTA 2 (not studied in this work) and future versions of the device with the combinations of and refinements to both types of design changes.

The MALTA MAPS were targeted for tracking in the ATLAS ITk, originally in the initial installation along with the rest of the ITk, but now as a potential replacement for the inner pixel layers following Run 4. The original MALTA device was expected to have radiation tolerance to $\phi = 1 \times 10^{15}$ $n_{\text{eq}}/\text{cm}^2$ based on results with the TowerJazz Investigator, however, this was shown to not be the case in the test beams which measured a peak efficiency of 78% at that fluence. The low efficiency was due to a drop in efficiency in the corners of pixels, as might be expected given the small collection electrodes.

MiniMALTA was developed to have improved radiation hardness in the pixel corners and had seven new pixel designs with modifications to the front-end, pixel substrate, or both. The front-end modifications were demonstrated to result in improved threshold and gain characteristics relative to the original front-end in laboratory measurements, and all modified pixel designs were measured to have improved radiation hardness. In the pixels with both modifications, radiation hardness was greatest and demonstrated to be above 1×10^{15} $n_{\text{eq}}/\text{cm}^2$. Measurements at Diamond with a 2-μm x-ray beam demonstrated that the pixel response in the corners was greatly improved compared to the original MALTA pixel design, as was was the efficiency in electron test beams with an overall increase in efficiency from 78% to above 98%.

The pixel substrate modifications were also implemented in full size epitaxial and Czochralski silicon versions of MALTA (which did not have the front-end modifications). The Czochralski silicon has two potential advantages: it allows for a thicker (up to 300 μm) collection volume than the epitaxial (up to 30μm), and thereby more signal, and the silicon itself has different

impurity concentrations that can improve the radiation tolerance. In both unirradiated and irradiated sensors, the cluster size was shown to increase as a function of voltage, presumably due to an increase in depletion depth that is expected at those voltages. For the irradiated sensors, the efficiency also increased as a function of bias voltage, while in the unirradiated sensors, the efficiency did not increase significantly since sensors had high efficiency even at the minimum substrate bias of 6 V. The Czochralski silicon was demonstrated to lead to radiation tolerance to 1×10^{15} $n_{\mathrm{eq}}/\mathrm{cm}^2$ with even the original MALTA pixel design. An n^- gap Czochralski sensor had 95% efficiency with $\phi = 2 \times 10^{15}$ $n_{\mathrm{eq}}/\mathrm{cm}^2$, and based on comparable results at $\phi = 1 \times 10^{15}$ $n_{\mathrm{eq}}/\mathrm{cm}^2$, the other two pixel substrate designs presumably would also have comparable results at $\phi = 2 \times 10^{15}$ $n_{\mathrm{eq}}/\mathrm{cm}^2$, if these had been available for testing.

While the improvement in radiation tolerance for MALTA devices is significant, there are other requirements for inclusion in an experiment which are of concern based on existing issues discovered throughout characterization of the device. Resolving these issues will potentially lead to improved radiation tolerance as well, for example by allowing higher operational voltages or the ability to cope with higher event and noise rates. Work is being done to fix or mitigate these sources of concern, listed below.

- The O(mA) currents are orders of magnitude higher than devices typically implemented in physics experiments, and so the punch-through currents are of great concern. The mitigation of this current is being taken into consideration for future pixel substrate design and is being investigated in TCAD simulations.

- The Czochralski sensors with these designs also demonstrate inhomogeneity in the pixel response due the presence conductive glue, which is potentially troublesome for operation. The biasing of MALTA without a conductive glue is an ongoing development.

- The merger must be fixed, since the OR merger too easily results in hit corruption. This should be fixed in future versions of MALTA.

- The pixel masking scheme of using coincidences between rows, columns, and diagonals is undesirable due to the unintentional masking of "ghost pixels" (as well as the ineffective-

ness of this masking), as is the fact the only a global threshold can be set. To rectify these concerns, designs to include in-pixel masking and in-pixel tuning have been proposed and are discussed in detail in [65].

In spite of these concerns, between MiniMALTA and MALTA Cz, there have been three types of modification demonstrated to lead to improved radiation tolerance: pixel substrate, front-end, and collection volume thickness. As of now, a combination of front-end modifications and Czochralski silicon may be most promising. This would avoid the punch-through currents and response inhomogeneity measured in sensors with the pixel modification and/or Czochralski silicon, but allow for the improved front-end and collection volume. The MALTA 2 devices, which is currently being tested, but is beyond the timescale for this thesis, features two new front-end designs which should have even higher gain than the MiniMALTA modified front-end, and in one design the ability to tune the response of the M3 transistor. The sensor has been produced with both epitaxial and Czochralski silicon in the n^- gap and extra deep p-well sensor designs. The MALTA 2 is expected to have radiation tolerance above that of MiniMALTA and further improvements to resolve the yet-addressed issues in the next version of the device, MALTA 3, and subsequent versions, could lead to even higher tolerance and broader possibilities for inclusion in particle physics experiments. The results with the MALTA sensors demonstrate the potential to greatly improve radiation tolerance in the intrinsically low-noise small collection electrode MAPS designs for ATLAS, and stimulate interest in a number of potential paths forward for development of the sensor and the TowerJazz 180 nm modified process.

Digital electromagnetic calorimtetry, a novel application of silicon sensors where DMAPS may improve performance in reconstruction with Particle Flow techniques, was investigated in simulations to compare the performance of analog and digital SiW calorimters in reconstruction of single particle events. The simulated digital calorimeter has much finer granularity than the analog (50 μm pixel pitch compared to 5 mm) that should enable more accurate event reconstruction. There is an improvement in reconstruction of π^0 due to the improved granularity, but quantifying this proved difficult due to challenges in application of the Photon Reconstruction

algorithm of the available software package developed for SiW calorimetry at CLIC. Follow-up work focused on the training and tuning of this algorithm in the Pandora Particle Flow Analysis should produce results which can more easily be quantified and more clearly motivate development of digital electromagnetic calorimetry.

The feasibility of digital ECAL was also explored with a prototype sensor with a 55 μm pixel pitch, the DECAL sensor, also in the TowerJazz 180 nm CMOS imaging process. The counting logic of the device has been demonstrated in both pad and strip modes, and the front-end was characterized in versions of the device in the standard process and modified process with the n^- gap pixel modification. While the gain is possibly too low for efficient particle detection in the current version of the front-end, this can almost certainly be rectified in future versions of the device given the results with other TowerJazz 180 nm small collection electrode devices such as MALTA and Monopix. A new version of DECAL or a similar sensor with gain characteristics comparable to those of MALTA would be potentially radiation hard to $\phi = 1 \times 10^{15}\ n_{\mathrm{eq}}/\mathrm{cm}^2$ and feature the counting logic to allow for digital calorimetry and the associated possible physics advantages. Such a sensor would be a low-mass, high granularity, low-capacitance, monolithic CMOS sensor with radiation hardness that would be suitable for a very compact calorimeter design for linear collider, circular e^+e^- and even barrel calorimetry at future hadron colliders.

Through the characterization of MALTA and DECAL, the potential for implementation of MAPS for tracking and calorimetry in high-radiation experiments has been demonstrated. If the radiation hardness can be improved even further there is the possibility to develop a fully silicon, high-granularity digital detector with low mass, low volume, low power consumption, potentially low cost, and tracking for Particle Flow Analysis from the vertex detector through the electromagnetic calorimeter. The low mass of this detector could have minimal multiple scattering in the vertex detector, allowing for precise reconstruction of impact parameters, essential for event reconstruction and the probing of matter at even finer scales in the pursuit of higher precision physics measurements and searches for new phenomena.

Bibliography

[1] R. Garoby, *Scenarios for upgrading the LHC injectors*, doi: 10.5170/CERN-2007-002.107.

[2] ATLAS collaboration, G. Aad *et al.*, *Observation of a new particle in the search for the Standard Model Higgs boson with the ATLAS detector at the LHC*, Phys. Lett. B **716** (2012) 1, arXiv:1207.7214.

[3] CMS collaboration, S. Chatrchyan *et al.*, *Observation of a New Boson at a Mass of 125 GeV with the CMS Experiment at the LHC*, Phys. Lett. B **716** (2012) 30, arXiv:1207.7235.

[4] C. Lefèvre, *The CERN accelerator complex. Complexe des accélérateurs du CERN*, 2008.

[5] ATLAS collaboration, G. Aad *et al.*, *The ATLAS Experiment at the CERN Large Hadron Collider*, JINST **3** (2008) S08003.

[6] CMS collaboration, S. Chatrchyan *et al.*, *The CMS Experiment at the CERN LHC*, JINST **3** (2008) S08004.

[7] ALICE collaboration, K. Aamodt *et al.*, *The ALICE experiment at the CERN LHC*, JINST **3** (2008) S08002.

[8] LHCb Collaboration, A. A. Alves Jr. *et al.*, *The LHCb Detector at the LHC*, JINST **3** (2008) S08005, Also published by CERN Geneva in 2010.

[9] CERN, *The High-Luminosity LHC Project. 298th Meeting of Scientific Policy Committee* , 2016. https://cds.cern.ch/record/2199189.

[10] ATLAS Collaboration, *Technical Design Report: A High-Granularity Timing Detector for the ATLAS Phase-II Upgrade* , CERN, Geneva, 2020. https://cds.cern.ch/record/2719855.

[11] ATLAS Collaboration, *Technical Design Report for the ATLAS Inner Tracker Strip Detector* , CERN, Geneva, 2017. https://cds.cern.ch/record/2257755.

[12] J. E. Augustin *et al.*, *Limitations on Performance of e+ e- Storage Rings and Linear Colliding Beam Systems at High Energy*, eConf **C781015** (1978) 009.

[13] ALEPH Collaboration, DELPHI Collaboration, OPAL Collaboration, and LEP Working Group: Higgs Boson Searches, *Search for the standard model higgs boson at lep*, Physics Letters B (2003) 61–75.

[14] *The International Linear Collider Technical Design Report - Volume 3.II: Accelerator Baseline Design*, arXiv:1306.6328.

[15] H. Aihara, P. Burrows, and M. Oreglia, *Sid letter of intent*, 2009.

[16] T. I. C. Group, *The international large detector: Letter of intent*, 2010.

[17] N. Alipour Tehrani *et al.*, *CLICdet: The post-CDR CLIC detector model*, .

[18] CLIC, CLICdp collaboration, M. J. Boland *et al.*, *Updated baseline for a staged Compact Linear Collider*, doi: 10.5170/CERN-2016-004 arXiv:1608.07537.

[19] M. Mangano and M. Mangano, *Physics at the FCC-hh, a 100 TeV pp collider*, CERN Yellow Reports: Monographs, CERN, Geneva, 2017.

[20] CEPC Study Group, *CEPC Conceptual Design Report: Volume 1 - Accelerator*, arXiv:1809.00285.

[21] CEPC Study Group, M. Dong *et al.*, *CEPC Conceptual Design Report: Volume 2 - Physics & Detector*, arXiv:1811.10545.

[22] S. Myers, *The LEP Collider, from design to approval and commissioning*, John Adams' memorial lecture, CERN, Geneva, 1991. Delivered at CERN, 26 Nov 1990.

[23] Particle Data Group, P. A. Zyla *et al.*, *Review of Particle Physics*, PTEP **2020** (2020) 083C01.

[24] J. Kemmer, *Fabrication of low noise silicon radiation detectors by the planar process*, Nucl. Instrum. Meth. **169** (1980) 499.

[25] E. H. M. Heijne *et al.*, *A SILICON SURFACE BARRIER MICROSTRIP DETECTOR DESIGNED FOR HIGH-ENERGY PHYSICS*, Nucl. Instrum. Meth. **178** (1980) 331.

[26] P. Freeman, *Performance of Ultra-Fast Silicon Detectors at the Fermilab Test Beam Facility.*, PhD thesis, University of California, Santa Cruz, 2017, `https://escholarship.org/content/qt99t4h6ch/qt99t4h6ch.pdf`.

[27] S. M. Sze, *semiconductor devices physics and technology reference citation*, Wiley, New York, 1985.

[28] H. Spieler, *Semiconductor Detector Systems*, Oxford University Press, 2005.

[29] M. Moll, *Displacement damage in silicon detectors for high energy physics*, IEEE Transactions on Nuclear Science **65** (2018) 1561.

[30] A. Chilingarov *et al.*, *Radiation studies and operational projections for silicon in the atlas inner detector*, Nuclear Instruments and Methods in Physics Research Section A: Accelerators, Spectrometers, Detectors and Associated Equipment **360** (1995) 432, Proceedings of the Sixth Pisa Meeting on Advanced Detectors.

[31] E. Barberis *et al.*, *Capacitances in silicon microstrip detectors*, Nuclear Instruments and Methods in Physics Research Section A: Accelerators, Spectrometers, Detectors and Associated Equipment **342** (1994) 90.

[32] M. Moll, *Radiation damage in silicon particle detectors: Microscopic defects and macroscopic properties*, PhD thesis, Hamburg U., 1999.

[33] R. Wunstorf, *Systematische Untersuchungen zur Strahlenresistenz von Silizium-Detektoren für die Verwendung in Hochenergiephysik-Experimenten*, dr., University of Hamburg, Hamburg, 1992.

[34] M. Moll, *Displacement damage in silicon detectors for high energy physics*, IEEE Trans. Nucl. Sci. **65** (2018) 1561.

[35] G. Lindstram, M. Moll, and E. Fretwurst, *Radiation hardness of silicon detectors- a challenge from high-energy physics*, Nuclear Instruments and Methods in Physics Research Section A: Accelerators, Spectrometers, Detectors and Associated Equipment **426** (1999) 1.

[36] ATLAS Collaboration, *Technical Design Report for the ATLAS Inner Tracker Pixel Detector* , CERN, Geneva, 2017. `https://cds.cern.ch/record/2285585`.

[37] ALICE Collaboration, *Expression of Interest for an ALICE ITS Upgrade in LS3*, .

[38] R. Turchetta *et al.*, *A monolithic active pixel sensor for charged particle tracking and imaging using standard vlsi cmos technology*, Nuclear Instruments and Methods in Physics Research Section A: Accelerators, Spectrometers, Detectors and Associated Equipment **458** (2001) 677.

[39] *The star experiment*, `https://www.star.bnl.gov//`. Accessed: 2021-08-30.

[40] J. Baudot *et al.*, *First test results of MIMOSA-26: A fast CMOS sensor with integrated zero suppression and digitized output*, .

[41] A. Gorisek, *Kartel ljubljana telescope based on m26 sensors*, `https://indico.desy.de/event/13620/contributions/13701/attachments/9247/10858/Gorisek-4thBTTBW.pdf`. Access 7 July 2021.

[42] D. Kim *et al.*, *Front end optimization for the monolithic active pixel sensor of the ALICE inner tracking system upgrade*, Journal of Instrumentation **11** (2016) C02042.

[43] N. Wermes, *Pixel detectors ... where do we stand?*, Nuclear Instruments and Methods in Physics Research Section A: Accelerators, Spectrometers, Detectors and Associated Equipment **924** (2019) 44, 11th International Hiroshima Symposium on Development and Application of Semiconductor Tracking Detectors.

[44] W. Snoeys *et al.*, *A process modification for cmos monolithic active pixel sensors for enhanced depletion, timing performance and radiation tolerance*, Nuclear Instruments and Methods in Physics Research Section A: Accelerators, Spectrometers, Detectors and Associated Equipment **871** (2017) 90.

[45] H. Pernegger *et al.*, *First tests of a novel radiation hard CMOS sensor process for Depleted Monolithic Active Pixel Sensors*, JINST **12** (2017) P06008.

[46] E. J. e. a. Schioppa, *Measurement results of the MALTA monolithic pixel detector*, Nucl. Instrum. Meth. A **958** (2020) 162404.

[47] W. Snoeys, *Monolithic cmos sensors for high energy physics*, Nuclear Instruments and Methods in Physics Research Section A: Accelerators, Spectrometers, Detectors and Associated Equipment **924** (2019) 51, 11th International Hiroshima Symposium on Development and Application of Semiconductor Tracking Detectors.

[48] K. Moustakas *et al.*, *Cmos monolithic pixel sensors based on the column-drain architecture for the hl-lhc upgrade*, Nuclear Instruments and Methods in Physics Research Section A: Accelerators, Spectrometers, Detectors and Associated Equipment **936** (2019) 604, Frontier Detectors for Frontier Physics: 14th Pisa Meeting on Advanced Detectors.

[49] CALICE collaboration, C. Adloff *et al.*, *Calorimetry for Lepton Collider Experiments - CALICE results and activities*, `arXiv:1212.5127`.

[50] M. Aleksa *et al.*, *Calorimeters for the FCC-hh*, `arXiv:1912.09962`.

[51] F. Hartmann, *Evolution of Silicon Sensor Technology in Particle Physics*, vol. 275 of *Springer Tracts in Modern Physics*, Springer, 2017.

[52] S. Wosnak, *Characterisation of Irradiated Planar Silicon Strip Sensors for HL-LHC Applications.*, PhD thesis, University of Liverpool, 2016, "https://livrepository.liverpool.ac.uk/3006162/.

[53] W. R. Leo, *Techniques for Nuclear and Particle Physics Experiments*, Springer, 1994.

[54] L. Snoj, G. Åcerovnik, and A. Trkov, *Computational analysis of irradiation facilities at the jsi triga reactor*, Applied Radiation and Isotopes **70** (2012) 483.

[55] K. Hara *et al.*, *Charge collection and field profile studies of heavily irradiated strip sensors for the atlas inner tracker upgrade*, Nuclear Instruments and Methods in Physics Research Section A: Accelerators, Spectrometers, Detectors and Associated Equipment **831** (2016) 181, Proceedings of the 10th International Hiroshima Symposium on the Development and Application of Semiconductor Tracking Detectors.

[56] CERN, *Ps-irrad proton facility*, https://ps-irrad.web.cern.ch/ps-irrad/. Accessed 24 August 2021.

[57] P. Allport *et al.*, *Experimental determination of proton hardness factors at several irradiation facilities*, Journal of Instrumentation **14** (2019) P12004.

[58] *Ortec high purity germanium radiation detectors*, https://www.ortec-online.com/products/radiation-detectors/germanium-hpge-radiation-detectors. Accessed 26 August 2021.

[59] *Alibava systems*, /https://alibavasystems.com/. Accessed: 2021-06-24.

[60] D. Baumeister, S. Löchner, and M. Schmelling, *The Beetle Reference Manual: chip version 1.2* , CERN, Geneva, 2006.

[61] K. Hara *et al.*, *Charge collection study with the atlas itk prototype silicon strip sensors atlas17ls*, Nuclear Instruments and Methods in Physics Research Section A: Accelerators, Spectrometers, Detectors and Associated Equipment **983** (2020) 164422.

[62] P. Allport *et al.*, *Recent results and experience with the birmingham MC40 irradiation facility*, Journal of Instrumentation **12** (2017) C03075.

[63] R. Cardella *et al.*, *LAPA, a 5 Gb/s modular pseudo-LVDS driver in 180 nm CMOS with capacitively coupled pre-emphasis*, PoS **TWEPP-17** (2017) 038.

[64] R. Calogero Cardella, *CMOS Detector and System Developments for LHC Detector Upgrades*, PhD thesis, Oslo U., 2019, `https://www.duo.uio.no/handle/10852/71258`.

[65] I. Berdalovic, *Design of radiation-hard CMOS sensors for particle detection applications.*, PhD thesis, Zagreb, 2019, `https://cds.cern.ch/record/2702884`.

[66] I. Peri *et al.*, *The fei3 readout chip for the atlas pixel detector*, Nuclear Instruments and Methods in Physics Research Section A: Accelerators, Spectrometers, Detectors and Associated Equipment **565** (2006) 178, Proceedings of the International Workshop on Semiconductor Pixel Detectors for Particles and Imaging.

[67] F. Dachs, *Radiation hardness characterization of CMOS sensors for the ATLAS ITK pixel at HL-LHC and Future Trackers*, PhD thesis, Technische Universität Wien, 2020, `https://doi.org/10.34726/hss.2020.28966`.

[68] R. Cardella *et al.*, *MALTA: an asynchronous readout CMOS monolithic pixel detector for the ATLAS high-luminosity upgrade*, Journal of Instrumentation **14** (2019) C06019.

[69] I. Berdalovic *et al.*, *Monolithic pixel development in TowerJazz 180 nm CMOS for the outer pixel layers in the ATLAS experiment*, Journal of Instrumentation **13** (2018) C01023.

[70] M. Kiehn, *Proteus beam telescope reconstruction*, 2019. doi: 10.5281/zenodo.2586736.

[71] *Sentarus tcad*, `https://www.synopsys.com/silicon/tcad.html`. Accessed: 2021-11-03.

[72] M. Munker *et al.*, *Simulations of CMOS pixel sensors with a small collection electrode, improved for a faster charge collection and increased radiation tolerance*, Journal of Instrumentation **14** (2019) C05013.

[73] M. Dyndal *et al.*, *Mini-MALTA: radiation hard pixel designs for small-electrode monolithic CMOS sensors for the high luminosity LHC*, Journal of Instrumentation **15** (2020) P02005.

[74] P. M. Freeman *et al.*, *Recent measurements on MiniMALTA, a radiation hard CMOS sensor with small collection electrodes for ATLAS*, PoS **Vertex2019** (2020) 020. 11 p.

[75] S. Spannagel, K. Wolters, and P. Schütze, *Allpix Squared - Generic Pixel Detector Simulation Framework*, 2021. doi: 10.5281/zenodo.4924549.

[76] S. Agostinelli *et al.*, *Geant4: simulation toolkit*, Nuclear Instruments and Methods in Physics Research Section A: Accelerators, Spectrometers, Detectors and Associated Equipment **506** (2003) 250.

[77] C. Kleinwort, *General broken lines as advanced track fitting method*, Nuclear Instruments and Methods in Physics Research Section A: Accelerators, Spectrometers, Detectors and Associated Equipment **673** (2012) 107.

[78] C. Ghabrous Larrea *et al.*, *IPbus: a flexible Ethernet-based control system for xTCA hardware*, JINST **10** (2015) C02019.

[79] I. A. Tortajada *et al.*, in *Latest Developments and Results of Radiation Tolerance CMOS Sensors with Small Collection Electrodes*, 2021. arXiv:https://journals.jps.jp/doi/pdf/10.7566/JPSCP.34.010009.

[80] *Aim tti pl series power supplies*, https://www.aimtti.com/product-category/dc-power-supplies/aim-plseries. Accessed: 2021-08-26.

[81] *Temperature/climatic stress screening chambers, series ts and cs*, https://https://www.cts-umweltsimulation.de/en/products/stress-ts-cs.html. Accessed: 2021-08-26.

[82] J. Lohstroh *et al.*, *Punch-through currents in p+np+ and n+pn+ sandwich structures: Introduction and basic calculations*, Solid-State Electronics **24** (1981) 805.

[83] *Lecroy ap034 active differential probe*, https://teledynelecroy.com/probes/differential-probes-1500-mhz. Accessed: 2021-08-27.

[84] SPiDeR collaboration, P. Dauncey, *Performance of CMOS sensors for a digital electromagnetic calorimeter*, PoS **ICHEP2010** (2010) 502.

[85] A. P. de Haas *et al.*, *The FoCal prototype—an extremely fine-grained electromagnetic calorimeter using CMOS pixel sensors*, JINST **13** (2018) P01014, arXiv:1708.05164.

[86] T. Price, *MAPS technology for vertexing, tracking, and calorimetry*, Phys. Procedia **37** (2012) 932.

[87] J. A. Ballin *et al.*, *Monolithic Active Pixel Sensors (MAPS) in a quadruple well technology for nearly 100% fill factor and full CMOS pixels*, arXiv:0807.2920.

[88] M. A. Thomson, *Particle flow calorimetry and the pandorapfa algorithm*, Nuclear Instruments and Methods in Physics Research Section A: Accelerators, Spectrometers, Detectors and Associated Equipment **611** (2009) 25–40.

[89] D. Dannheim, W. Klempt, and E. van der Kraaij, *Beam tests with the CALICE tungsten analog hadronic calorimeter prototype*, .

[90] P. P. Allport *et al.*, *First tests of a reconfigurable depleted MAPS sensor for digital electromagnetic calorimetry*, Nucl. Instrum. Meth. A **958** (2020) 162654.

[91] *Nexys video board*, https://digilent.com/reference/programmable-logic/nexys-video/start. Accessed: 2021-09-08.

[92] J. Dopke, *radhard-decal-daq*, 2021.

[93] *Drs4 chip*, `https://www.psi.ch/en/drs/`. Accessed: 2021-09-08.

[94] S. Benhammadi *et al.*, *DECAL: A Reconfigurable Monolithic Active Pixel Sensor for use in Calorimetry and Tracking*, PoS **TWEPP2019** (2020) 040.

[95] F. Gaede *et al.*, *LCIO: A Persistency framework for linear collider simulation studies*, eConf **C0303241** (2003) TUKT001, `arXiv:physics/0306114`.

[96] F. Gaede, *Marlin and lccd:software tools for the ilc*, Nuclear Instruments and Methods in Physics Research Section A: Accelerators, Spectrometers, Detectors and Associated Equipment **559** (2006) 177, Proceedings of the X International Workshop on Advanced Computing and Analysis Techniques in Physics Research.

[97] F. Gaede, *Marlin and LCCD: Software tools for the ILC*, Nucl. Instrum. Meth. A **559** (2006) 177.

[98] M. Frank *et al.*, *DD4hep: A detector description toolkit for high energy physics experiments*, Journal of Physics: Conference Series **513** (2014) 022010.

[99] P. Allport *et al.*, *A reconfigurable cmos sensor for tracking, pre-shower and digital electromagnetic calorimetry*, Nuclear Instruments and Methods in Physics Research Section A: Accelerators, Spectrometers, Detectors and Associated Equipment **978** (2020) 164459.

[100] B. Xu, *Detectors and Physics at a Future Linear Collider*, PhD thesis, University of Cambridge, 2017, `https://cds.cern.ch/record/2293892`.

[101] P. Allport *et al.*, *A reconfigurable cmos sensor for tracking, pre-shower and digital electromagnetic calorimetry*, Nuclear Instruments and Methods in Physics Research Section A: Accelerators, Spectrometers, Detectors and Associated Equipment **978** (2020) 164459.